Studies of $PbWO_4$ Crystals and Construction and Tests of a compact Crystal Calorimeter for ZEUS

DISSERTATION

zur Erlangung des Doktorgrades
des Fachbereiches Physik
der Universität Hamburg

vorgelegt von
Nils Gendner
aus Bremen

I. Institut für Experimentalphysik der Universität Hamburg
Mai 2000

Gutachter der Dissertation:	Prof. Dr. K. Wick Prof. Dr. U. Strohbusch
Gutachter der Disputation:	Prof. Dr. K. Wick Prof. Dr. W. Scobel
Datum der Disputation:	22. Juni 2000
Dekan des Fachbereiches Physik und Vorsitzender des Promotionsausschusses:	Prof. Dr. F.-W. Büßer

Abstract

The ZEUS experiment at the electron(positron)/proton collider HERA is planning to replace a small electromagnetic tungsten/scintillator sampling calorimeter by a lead tungstate ($PbWO_4$) crystal calorimeter.

The "beampipe calorimeter" (BPC) directly adjacent to the beam intercepts electrons with small scattering angles. It measures the inelastic electron-proton scattering in the interesting kinematic region $0.045 \leq Q^2 \leq 0.80\,\mathrm{GeV}^2$ and $3 \times 10^{-7} \leq x \leq 10^{-3}$ where the transition from photoproduction to deep inelastic scattering occurs. An improvement of the current electromagnetic energy resolution from $17\%/\sqrt{E/GeV}$ to $5\%/\sqrt{E/GeV}$, which is expected for a $PbWO_4$ calorimeter, would result in a much higher precision of for example the proton structure function F_2 and would further extend the accessible kinematic region.

The so-called Crystal BPC has to meet stringent requirements: the size is restricted, the light yield must be very high, the scintillation light pulses have to be short (95% within 96 ns), and the crystals have to be sufficiently radiation stable. Bench tests have shown that 20 $PbWO_4$ crystals (La doped) with dimensions $200 \times 23.8 \times 23.8\,\mathrm{mm}^3$ which were received in autumn 1997 from BTCP, Bogoroditsk, Russia, fulfil the demands.

A full size calorimeter of 4×4 crystals has been built and tested in a CERN SPS beam with energies 3–100 GeV. The crystals are read out by small photomultipliers which can work in a magnetic field. A LED transmission monitoring system proved its functionality when two crystals were interchanged with irradiated crystals and the recovery was tracked.

Kurzfassung

Das ZEUS–Experiment am Elektron(Positron)–Proton–Beschleuniger HERA plant den Austausch eines kleinen elektromagnetischen Wolfram/Szintillator–Stichprobenkalorimeters durch ein Kalorimeter aus Bleiwolframatkristallen ($PbWO_4$).

Das Strahlrohrkalorimeter ("beampipe calorimeter", BPC) ist sehr nahe am HERA–Elektronenstrahl angebracht und detektiert unter sehr kleinen Winkeln gestreute Elektronen. Das Kalorimeter ermöglicht Messungen der inelastischen Elektron–Proton–Streuung in dem interessanten kinematischen Bereich $0.045 \leq Q^2 \leq 0.80\,\mathrm{GeV}^2$ und $3 \times 10^{-7} \leq x \leq 10^{-3}$, wo der Übergang von der Photoproduktion zur tief–inelastischen Streuung erfolgt. Eine Verbesserung der gegenwärtigen Energieauflösung von $17\%/\sqrt{E/GeV}$ auf den für ein $PbWO_4$–Kalorimeter erwarteten Wert von $5\%/\sqrt{E/GeV}$ würde eine sehr viel genauere Messung der Protonstrukturfunktion F_2 ermöglichen und den kinematischen Bereich der Messungen erweitern.

An das sogenannte Crystal BPC werden hohe Anforderungen gestellt: Der zur Verfügung stehende Raum ist beschränkt, die Lichtausbeute muß sehr hoch sein, die Szintillationslicht–Pulse müssen sehr kurz sein (95% innerhalb von 96 ns) und die Kristalle müssen eine hohe Strahlenhärte aufweisen. Testmessungen haben gezeigt, daß 20 $PbWO_4$–Kristalle (La dotiert) mit den Abmessungen $200 \times 23.8 \times 23.8\,\mathrm{mm}^3$, die 1997 aus Bogoroditsk, Rußland, geliefert wurden, den Anforderungen genügen.

Das Kalorimeter wurde in den endgültigen Abmessungen (4×4 Kristalle) konstruiert und am CERN in einem SPS–Teststrahl mit Teilchenenergien von 3–100 GeV getestet. Die Kristalle werden von Miniatur–Photomultipliern ausgelesen, die insensitiv gegenüber Magnetfeldern sind. Ein Transmissions–Meßsystem, das mit einer Leuchtdiode arbeitet, bewies seine Funktion anhand von Messungen, wo zwei Kristalle durch bestrahlte Kristalle ausgetauscht wurden und die Ausheilung beobachtet wurde.

für Ortrud

...versuch' zu leben, nicht zu eilen!
Manch' einer ackert still und stumm,
erblindet für das um ihn 'rum.
Deiner Augen Blick sei weit—
bist für des Zaubers Spiel bereit?

Contents

1 Introduction **1**

2 Theoretical Background **2**

2.1 The Standard Model of particle physics 2

2.2 Lepton–nucleon–scattering 3

2.3 Kinematic variables 4

2.3.1 Reconstruction of the kinematic variables 6

2.4 The cross–section formalism 10

2.5 Proton structure functions 11

2.6 Virtual photon–proton scattering 12

2.7 The Quark–Parton model 12

2.8 Quantum Chromodynamics 14

2.9 Physics in the transition region 15

2.9.1 Vector Dominance Model 16

2.9.2 Regge theory 16

2.9.3 Models describing the low x and low Q^2 region 17

3 HERA **19**

4 The ZEUS detector **21**

4.1 The ZEUS coordinate system 21

4.2 Components of the ZEUS–detector 21

4.3 Luminosity measurement 24

5 Basics of calorimetry **26**

5.1 Calorimeter design 26

5.2 Electromagnetic showers 27

5.3 Hadronic showers 29

5.4 Energy resolution 30

6 The Beampipe Calorimeter **31**

6.1 BPC II and BPT 32

6.2 The Crystal BPC as an upgrade of BPC II 35

6.3 Estimation of the effect on physics measurements 35

6.4 Improvements by the 1997 analysis 38

7 $PbWO_4$ as scintillator **40**

7.1 Chemical and physical properties 40

7.2 The complex refractive index of $PbWO_4$ 40

7.3 The scintillation mechanism 42

8 Bench tests of $PbWO_4$ crystals **45**

8.1 Transmission measurements 45

8.1.1 Calculation of Fresnel losses 46

8.1.2 Transverse transmission 46

8.1.3 Longitudinal transmission 47

8.2 Measurements of the intrinsic light yield 49

8.3 Optimization of the light collection efficiency 50

8.3.1 Optimization of the optical couplings 50

8.3.2 Measurements with single crystals 53

8.4 Measurements of the scintillation spectra of $PbWO_4$ crystals 55

8.4.1 The measurement setup 55

8.4.2 Typical scintillation spectra 57

8.4.3 Dependence on the azimuthal orientation 57

8.5 Decay time of the scintillation signal 59

9 Radiation damage effects of $PbWO_4$ 62

9.1 Radiation damage processes in $PbWO_4$ 62

9.2 Online–Measurements of the radiation damage 63

9.2.1 The Online–Measurement setup 63

9.2.2 Dosimetry 65

9.2.3 First measurements 66

9.2.4 Systematic study of the radiation damage 66

9.2.5 Annealing of the radiation damage during irradiation 72

9.3 Radiation damage at high doses 74

9.4 Radiation damage by neutrons 75

9.5 Effect of irradiation on scintillation 75

10 Measurements with the Crystal BPC prototype 77

10.1 Description of the prototype 77

10.2 Measurements at the DESY II test beam 78

10.2.1 Energy resolution 79

10.2.2 Uniformity 79

10.2.3 Temperature effect 80

10.2.4 Radiation damage monitoring system 80

11 Description of the Crystal BPC 83

11.1 Mechanical Design of the Crystal BPC 83

11.2 Magnetic field 86

11.3 The radiation damage monitoring system 86

11.4 The temperature system 88

11.4.1 Measurements of heat conduction in the Crystal BPC 88

11.5 Shower development in the Crystal BPC 91

12 Test Beam Measurements at the CERN SPS **93**

12.1 The CERN SPS X5 test beam facility 93

12.2 The test beam setup 96

12.3 The readout system 97

12.4 Reconstruction 98

12.4.1 Pedestal subtraction 98

12.4.2 Channel-to-channel calibration 100

12.4.3 Temperature correction 101

12.4.4 Correction for longitudinal leakage 105

12.5 Measurements 105

12.5.1 Electron identification 105

12.5.2 Energy Resolution 106

12.5.3 Linearity 108

12.5.4 Uniformity 108

12.5.5 Position and shower reconstruction 110

12.5.6 Test of the radiation damage monitoring system 114

12.5.7 Hadron rejection 115

13 Conclusions **116**

A Overview of Crystal BPC channels **118**

B Scintillation spectra of $PbWO_4$ crystals **120**

C Longitudinal transmission spectra of $PbWO_4$ crystals **125**

D Measurements of LED spectra **130**

E ADC calibration in units of photoelectrons **132**

F The data analysis program "cernnt.c" **133**

Chapter 1

Introduction

HERA is the electron/proton collider located in Hamburg, Germany. It collides electrons or positrons of 27.5 GeV on protons of 920 GeV. The ZEUS detector is a large, general purpose detector situated in the South Hall of the HERA accelerator. The beampipe calorimeter (BPC) is a ZEUS subsystem which is positioned to intercept electrons emanating from the interaction point at small angles (18-32 mrad). The beampipe tracker (BPT) is a small silicon tracker in front of the BPC with a position resolution of 0.1 mm.

BPC II, which is presently installed, is a tungsten/scintillator sampling calorimeter with an energy resolution of $17\%/\sqrt{E/GeV}$. A description can be found in [mon98] and [sur98]. It was planned to replace BPC II by the so-called Crystal BPC, which is the third in a series of BPCs, each with improving energy resolutions. The lead tungstate ($PbWO_4$) crystals used are a development of BTCP, Bogoroditsk and CMS [cms97]. Their excellent properties seem to make possible a compact calorimeter with an energy resolution of $5\%/\sqrt{E/GeV}$. This would result in a much higher precision of the measurement of for example the proton structure function F_2 and would further extend the accessible kinematic region.

The thesis is organized as follows: In the second chapter, some principles of the physics relevant for this thesis are presented. In the third and fourth chapter, respectively, the HERA collider and the ZEUS detector are described. The fifth chapter presents basic principles of calorimetry. In the sixth chapter, a description of the Beampipe Calorimeter is given. The seventh and eighth chapter present properties of $PbWO_4$ crystals and several measurements which were performed on these crystals. The ninth chapter deals with measurements concerning the radiation damage of $PbWO_4$ crystals. The Crystal BPC prototype, which was built at DESY and tested at a DESY test beam, is presented in chapter ten. Chapters eleven and twelve, finally, give a description of the Crystal BPC and present measurements performed at the CERN SPS test beam.

Chapter 2

Theoretical Background

This chapter deals with the theoretical background of the physics relevant for this thesis. After an introduction to the Standard Model, some aspects of lepton–nucleon scattering are presented, followed by the description of theoretical approaches to electron–proton scattering in the low x and low Q^2 region. Some of the models, which make the attempt to explain the experimentally measured phenomena, are briefly introduced.

Throughout this thesis, the natural system of units is used: $\hbar \equiv 1$ and $c \equiv 1$.

2.1 The Standard Model of particle physics

The Standard Model (SM) of particle physics describes the organization of elementary particles and their interactions.

According to the SM, interactions between pointlike fundamental particles, leptons and quarks, all of them fermions, are mediated by the exchange of virtual gauge bosons. These are photons (γ) in case of the electromagnetic (em) interaction, Z^0 and $W^{\pm}$ bosons in case of the weak interaction, and gluons (g) in case of the strong interaction.

Leptons can be observed as free particles. Hence their properties have been studied in great detail in many experiments. The electron[1] is the best known lepton. The muon and the tau differ from the electron in a higher mass. Each of these three leptons carry electric charge. The other three leptons, called neutrinos, have no electric charge and very little, if any, mass. There is one type of neutrino corresponding to each of the three types of charged leptons.

Quarks have never been observed as free particles but only as constituents of composite particles, the hadrons. As a consequence, the existence of quarks and their properties can only be derived from inelastic scattering experiments. There are two classes of hadrons: Baryons, such as the proton and the neutron, contain three quarks, while mesons contain one quark and one antiquark.

Only the quarks feel the effects of the strong nuclear force. The quarks and the leptons are subject to the weak nuclear force. All particles that have electric charge, including

[1] The term *electron* is used in this thesis for both electrons and positrons unless denoted otherwise.

	charge	fermions					
quarks	$+2/3$	up	u	charm	c	top	t
	$-1/3$	down	d	strange	s	bottom	b
leptons	0	e-neutrino	ν_e	μ–neutrino	ν_μ	τ–neutrino	ν_τ
	-1	electron	e	muon	μ	tau	τ

bosons		
electromagnetic interaction	photon	γ
weak interaction	$Z^0, W^\pm$	
strong interaction	gluon	g

Table 2.1: Fundamental particles in the Standard Model

the $W^\pm$ bosons, feel the electromagnetic force. The fundamental fermions and bosons in the Standard Model are listed in Tab. 2.1.

2.2 Lepton–nucleon–scattering

Scattering experiments, where particles are accelerated to high energies and then brought to collision, are an established method to gain information about the nature of particles and their interactions. In the beginning of the twentieth century, Rutherford, together with Geiger and Marsden, scattered α–particles on a thin gold foil. The interpretation of the results led to the atomic model named after him. According to this model, the atom consists of a very small nucleus with positive charge and negatively charged electrons circulating around the nucleus [rut11].

Leptons do not participate in the strong interaction. Hence, they are able to penetrate deeply into nucleons, and it is possible to test the inner structure of nucleons by lepton–nucleon scattering experiments.

In the early 1950s, elastic electron–proton scattering experiments were performed shooting an electron beam on a proton target at rest. It was shown that the proton is not a structureless point–like object but has an extended structure and a size of about 1 fm [hof53, hof55, hof57]. As a consequence of these experiments, efforts were made to increase the electron beam energy and therefore the available momentum transfer.

At very large momentum transfer between the scattered particles, the scattering process is referred to as deep inelastic. Deep inelastic electron–proton scattering experiments showed that the structure functions W_1 and W_2, which describe the structure of the proton [dre64], only depend on the Bjœrken scaling variable x (see sections 2.3 and 2.7). Bjœrken predicted that this behaviour of the deep inelastic structure functions, known as scaling, follows from the scattering of electrons off free point–like objects within the proton [bjo67, bjo69]. It was assumed that protons consist of point–like constituents which were called partons [fey69]. Later, the partons were identified with the quarks

proposed by Gell–Mann and Zweig [gel64a, zwe64]. Thus, deep inelastic electron–proton scattering can be described as scattering of electrons off quarks.

The final state of a deep inelastic electron–proton scattering process consists of the scattered lepton and the hadronic final state, which originates from the proton's constituents and consists to first order of two hadronic jets. The current jet is associated to the fragmentation of the quark in the proton which took part in the interaction. The proton remnant jet originates from the fragmentation of the remaining quarks and escapes through the beampipe close to the direction of the initial proton.

There are two categories of scattering experiments. In a fixed–target experiment, a particle is accelerated to a high energy and then scattered on a stationary target. In a collider experiment, both scattering particles are accelerated and then brought to collision. Taking electron–proton scattering as example, the center–of–mass energies squared s for both types of experiment are given by the following expressions:

$$\text{fixed–target experiment:} \quad s = 2\,E_e\,m_P \tag{2.1}$$

$$\text{collider experiment:} \quad s = 4\,E_e\,E_P \tag{2.2}$$

In case of a fixed–target experiment, the center–of–mass energy squared is proportional to the incident electron energy E_e and the target proton mass m_P. The center–of–mass energy which can be achieved in a collider experiment is significantly larger because it depends on the product of both particle energies E_e and E_P. Due to this fact, the center–of–mass energy at the electron–proton collider HERA (see chapter 3) is about an order of magnitude higher than in all previous comparable experiments. At HERA, electrons are scattered off unpolarized protons. This process is in first order perturbation theory described by the exchange of a Standard Model electroweak gauge boson.

As shown in Fig. 2.1, there are two classes of events in deep inelastic electron–proton scattering which are distinguished by the type of the exchanged gauge boson. In a neutral current (NC) event, $ep \to eX$, the final state lepton is an electron, and the interaction is mediated by the exchange of a virtual photon γ^* or a Z^0 boson (left figure). In a charged current (CC) event, $ep \to \nu_e X$, the exchanged gauge boson is a $W^\pm$ boson carrying electric charge, and the final state lepton is an (anti)neutrino (right figure). The (anti)neutrino does not interact in the detector and thus escapes undetected. For this thesis, only NC events are of interest.

2.3 Kinematic variables

This section briefly describes the kinematic variables used to describe NC scattering of unpolarized electrons on unpolarized protons. The considered process is

$$e(k) + P(p) \longrightarrow e(k') + X(p') \tag{2.3}$$

The Feynman diagram of this process to first order in perturbation theory is shown in Fig.2.1 (left). The electron e and the proton P in the initial state are denoted by their four–momenta k and p, respectively:

$$k = (E_e, \vec{k_e}) \tag{2.4}$$

$$p = (E_P, \vec{P}) \tag{2.5}$$

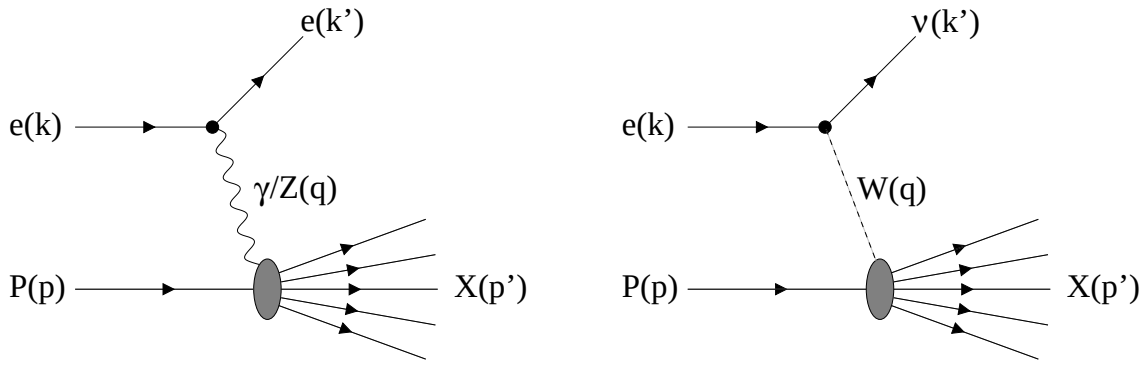

Figure 2.1: Lowest–order Feynman diagrams of neutral current (left) and charged current (right) deep inelastic electron–proton scattering.

The final state consists of the scattered electron e and the hadronic final state X characterized by their four–momenta k' and p', respectively:

$$k' = (E'_e, \vec{k'_e}) \tag{2.6}$$
$$p' = (E_X, \vec{p_X}) \tag{2.7}$$

For a NC event, the energy and direction of both the scattered electron and the hadronic final state system are measured. At fixed beam energy, two of these four independently measured quantities are sufficient to reconstruct the event kinematics. The choice of the two measured quantities used for reconstruction depends on the covered kinematic region and the detectors used. In case of CC events, where the (anti)neutrino cannot be detected, only the information of the hadronic final state system can be used (see section 2.3.1 for details).

The unpolarized inelastic electron–proton event kinematics are described in a relativistic–invariant way using the following kinematic variables (m_P denotes the proton mass):

$$s = (k+p)^2 \cong 4\,E_e E_P \tag{2.8}$$
$$t = (p-p')^2 \tag{2.9}$$
$$Q^2 = -(k-k')^2 = -(p-p')^2 = -t = -q^2 \leq s \tag{2.10}$$
$$x = \frac{Q^2}{2\,p\cdot q} = \frac{Q^2}{2\,m_P\,\nu} \qquad 0 \leq x \leq 1 \tag{2.11}$$
$$y = \frac{p\cdot q}{p\cdot k} \qquad 0 \leq y \leq 1 \tag{2.12}$$
$$W^2 = (p+q)^2 = (p')^2 = m_P^2 + \frac{Q^2}{x}(1-x) \tag{2.13}$$
$$\nu = \frac{p\cdot q}{m_P} \tag{2.14}$$

s is the square of the center–of–mass energy of the electron–proton system.

t denotes the four–momentum transfer squared at the proton vertex.

Q^2 is the negative square of the momentum transfer q. $Q^2 = 0$ corresponds to real photon–proton scattering. The largest possible value of the momentum transfer is given by $Q^2_{max} \cong s$.

x is the Bjœrken scaling variable. In the Quark–Parton model it can be interpreted as the fraction of the proton momentum which is carried by the struck parton.

y is the fraction of the initial electron energy which is transferred between the electron and the hadronic system in the proton rest frame.

W^2 is the square of the invariant mass of the hadronic final state X, or the squared center–of–mass energy of the proton–gauge boson system. Small values of x correspond to large values of W, whereas $x = 1$ corresponds to the elastic case with $W = m_P$.

ν in the proton rest frame denotes the energy of the exchanged gauge boson, which represents the energy transfer from the electron to the proton.

The kinematic variables Q^2, x, y, s are related by the following equation, neglecting electron and proton masses:

$$Q^2 \cong s \cdot x \cdot y \tag{2.15}$$

A common choice of two independent kinematic variables for the description of inelastic electron–proton event kinematics are x (or y) and Q^2. In case of elastic electron–proton scattering ($x = 1$), the kinematics can be described by only one variable.

The momentum transfer $\sqrt{Q^2}$ determines the wavelength λ of the exchanged virtual gauge boson by Heisenberg's uncertainty principle:

$$\lambda = \frac{1}{|\vec{q}|} = \frac{1}{\sqrt{Q^2 + \nu^2}} \tag{2.16}$$

$$\approx \frac{1}{\nu} = \frac{2\, m_P\, x}{Q^2} \qquad \text{for} \quad \nu^2 \gg Q^2 \tag{2.17}$$

The size Δ of an object which can be resolved in a scattering process is, in analogy to an optical microscope, limited by the wavelength λ of the exchanged boson: To resolve objects of size Δ, λ must be smaller than Δ. Better resolution thus requires smaller wavelengths λ of the exchanged boson. This can be achieved at large momentum transfers Q^2.

2.3.1 Reconstruction of the kinematic variables

Precision measurements at HERA require an accurate determination of the relativistic–invariant variables describing the event kinematics. In case of NC events, the energy and direction of both the scattered electron and the hadronic final state system can be used for the reconstruction of the event kinematics. Because just two of these four independently measured quantities are sufficient, several reconstruction methods exist, each of them based on a subset of two or more of the four measured quantities. The choice of the reconstruction method used for a certain analysis depends on the covered kinematic region and the detectors used. A detailed review of the different reconstruction methods used at HERA is given in [bas97].

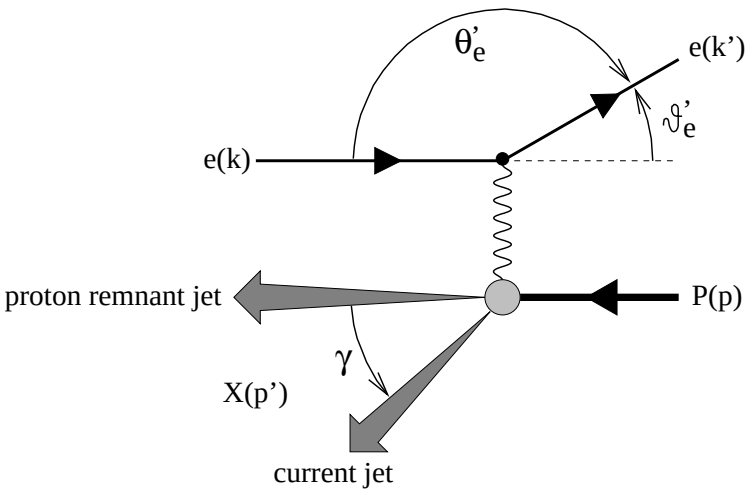

Figure 2.2: The final state in NC electron–proton scattering. It consists of the scattered electron and the hadronic final state, the latter in first order divided into current jet and proton remnant jet.

In the right–handed Cartesian ZEUS coordinate system, the four–momenta of the initial and the final state of the process

$$e(k) + P(p) \longrightarrow e(k') + X(p')$$

are given as follows:

$$k = \begin{pmatrix} E_e \\ 0 \\ 0 \\ -E_e \end{pmatrix} \quad k' = \begin{pmatrix} E_e^{'} \\ E_e^{'} \sin\theta_e^{'} \cos\phi_e^{'} \\ E_e^{'} \sin\theta_e^{'} \sin\phi_e^{'} \\ E_e^{'} \cos\theta_e^{'} \end{pmatrix} \quad p = \begin{pmatrix} E_P \\ 0 \\ 0 \\ E_P \end{pmatrix} \quad p' = \begin{pmatrix} \sum_h E_h \\ \sum_h p_{X,h} \\ \sum_h p_{Y,h} \\ \sum_h p_{Z,h} \end{pmatrix} \tag{2.18}$$

In these equations, E_e and E_P denote the energy of the initial state electron and proton, respectively. E_e', θ_e', and ϕ_e' are the energy, polar angle, and azimuthal angle of the scattered electron. The expressions $\sum_h E_h$ and $(\sum_h p_{X,h}; \sum_h p_{Y,h}, \sum_h p_{Z,h})$ denote the energy and momentum of the hadronic final state system X, obtained by a summation over all hadronic final state particles h.

Furthermore, the transverse hadronic momentum

$$p_{T,h}^2 = (\sum_h p_{X,h})^2 + (\sum_h p_{Y,h})^2 \tag{2.19}$$

and the difference of the energy and the longitudinal momentum of the hadronic final state

$$\delta_h = (E - P_Z)_h = \sum_h (E_h - p_{Z,h}) \tag{2.20}$$

can be used to define the energy F and the polar angle γ of a massless object which describes the hadronic final state:

$$F = \frac{p_{T,h}^2 + \delta_h^2}{2\,\delta_h} \tag{2.21}$$

$$\gamma = \arccos\left(\frac{p_{T,h}^2 - \delta_h^2}{p_{T,h}^2 + \delta_h^2}\right) \tag{2.22}$$

In the Quark–Parton model (see section 2.7) the energy F and the polar angle γ correspond to the energy and polar angle of the struck quark. The angle γ can therefore be associated with the angle of the current jet. Fig. 2.2 shows a sketch of the scattering process together with the relevant variables.

In the following, some reconstruction methods used in electron–proton scattering experiments are briefly introduced.

Electron method: The electron method [ben92] is the prime method of reconstruction in NC electron–proton scattering experiments. It relies solely on the energy E'_e and the scattering angle θ'_e of the final state electron and is thus applicable to NC events only.

The kinemactic variables are calculated as follows:

$$Q_e^2 = 2\,E_e\,E'_e\,(1+\cos\theta'_e) \tag{2.23}$$

$$y_e = 1 - \frac{E'_e}{2\,E_e}\,(1-\cos\theta'_e) \tag{2.24}$$

$$x_e = \frac{Q_e^2}{s\,y_e} \tag{2.25}$$

The relative measurement error in y_e is given by [bas94] [2]:

$$\frac{\Delta y_e}{y_e} = \frac{1-y_e}{y_e} \cdot \left(\frac{\Delta E'_e}{E'_e} \oplus \frac{\Delta\theta'_e}{\tan\frac{\theta'_e}{2}}\right) \tag{2.26}$$

It depends on the energy resolution $\Delta E'_e/E'_e$ and the angular resolution $\Delta\theta'_e/\theta'_e$ of the measurement of the final state electron.

Due to the $1/y_e$ dependence of the measurement error in y_e, the electron method degrades rapidly with decreasing y_e. For a given detector with energy resolution $\Delta E'_e/E'_e$, this leads to a lower bound in y_e for the use of the electron method.

Jacquet–Blondel method: This method, proposed by Jacquet and Blondel [jac79], uses information from the hadronic final state only to reconstruct the kinematic variables, namely the transverse momentum $p_{T,h}^2$ and the difference of the energy and the longitudinal momentum δ_h:

$$Q_{\mathrm{JB}}^2 = \frac{p_{T,h}^2}{1-y_{\mathrm{JB}}} \tag{2.27}$$

$$y_{\mathrm{JB}} = \frac{\delta_h}{2\,E_e} \tag{2.28}$$

$$x_{\mathrm{JB}} = \frac{Q_{\mathrm{JB}}^2}{s\,y_{\mathrm{JB}}} \tag{2.29}$$

[2] We define $A \oplus B \equiv \sqrt{A^2+B^2}$

The method is insensitive to the loss of final state particles in dead areas of a particular detector in the initial proton direction such as beam pipe holes because these particles do not contribute to $p_{T,h}^2$ and δ_h. It is also insensitive to the final state fragmentation process.

For very small and very large current jet angles $\gamma \longrightarrow 0°, 180°$, the resolution of the reconstructed variables is dominated by the angular resolution. This makes a precise angular measurement of the hadronic final state at low Q^2 necessary.

At low values of y, the Jacquet–Blondel method is superior to the electron method as there is no divergence in x or y for $y \longrightarrow 0$. It can therefore be used at lower values of y if the angular resolution is sufficient. The resolution in x_{JB} and Q^2_{JB} diverges for $y_{\mathrm{JB}} \longrightarrow 1$.

Double Angle method: The Double Angle method [ben92] uses the angle θ'_e of the scattered electron and the angle γ of the current jet for the reconstruction of the kinematic variables:

$$Q^2_{\mathrm{DA}} = 4\,E_e^2 \cdot \frac{\sin\gamma\,(1+\cos\theta'_e)}{\sin\gamma + \sin\theta'_e - \sin(\gamma+\theta'_e)} \tag{2.30}$$

$$y_{\mathrm{DA}} = \frac{\sin\theta'_e\,(1-\cos\gamma)}{\sin\gamma + \sin\theta'_e - \sin(\gamma+\theta'_e)} \tag{2.31}$$

$$x_{\mathrm{DA}} = \frac{E_e}{E_P} \cdot \frac{\sin\gamma + \sin\theta'_e + \sin(\gamma+\theta'_e)}{\sin\gamma + \sin\theta'_e - \sin(\gamma+\theta'_e)} \tag{2.32}$$

The use of this method is restricted by the limited acceptance of a particular detector for very small and very large angles $\theta'_e, \gamma \longrightarrow 0°, 180°$.

Sigma method: The Sigma method [bas94] uses the energy and angular information of the scattered electron and the difference of the energy and the longitudinal momentum

$$\Sigma = \sum_h (E_h - p_{Z,h}) = \delta_h \tag{2.33}$$

of the hadronic final state. It tries to combine the very good resolution of the electron method at high y and the good resolution of the Jaquet–Blondel method at low y:

$$Q^2_\Sigma = \frac{(E'_e\,\sin\theta'_e)^2}{1-y_\Sigma} \tag{2.34}$$

$$y_\Sigma = \frac{\Sigma}{\Sigma + E'_e(1-\cos\theta'_e)} \tag{2.35}$$

$$x_\Sigma = \frac{Q^2_\Sigma}{s\,y_\Sigma} \tag{2.36}$$

Consequently, neither the divergence in y for $y \longrightarrow 0$ as in the electron method nor for $y \longrightarrow 1$ as in the Jaquet–Blondel method appear.

Mixed Sigma method: The Mixed Sigma method [bas94] is a mixture of the electron and the Sigma method. y is reconstructed using the Sigma method while for the reconstruction of Q^2 the electron method is used, resulting in an optimal use of the available resolution:

$$Q^2_{m\Sigma} = Q^2_e \tag{2.37}$$

$$y_{m\Sigma} = y_\Sigma \tag{2.38}$$

$$x_{m\Sigma} = \frac{Q^2_{m\Sigma}}{s\, y_{m\Sigma}} \tag{2.39}$$

Electron–Sigma method: Like the Mixed Sigma method, the Electron–Sigma method [bas94] is a mixture of the electron and the Sigma method. In addition, y_Σ is rescaled:

$$Q^2_{e\Sigma} = Q^2_e \tag{2.40}$$

$$y_{e\Sigma} = y_\Sigma \frac{Q^2_e}{Q^2_\Sigma} \tag{2.41}$$

$$x_{e\Sigma} = \frac{Q^2_{e\Sigma}}{s\, y_{e\Sigma}} \tag{2.42}$$

At high y, the resolution of the Electron–Sigma method is superior to the Mixed Sigma method, while the two methods become indistinguishable at low y.

2.4 The cross–section formalism

Derived from the famous Rutherford experiment, the cross–section formalism was developed to describe quantitatively the interaction probability of two scattering particles. The cross–section is formally given by

$$\sigma_{tot} = \frac{\dot{N}}{\mathcal{L}} \tag{2.43}$$

Here, $\dot{N}$ denotes the number of interactions per time interval, i.e. the event rate, and $\mathcal{L}$ is the product of the number of incident particles per time interval and the number of scattering centers per area. In storage ring experiments like HERA, $\mathcal{L}$ is called luminosity. With the numbers of electrons N_e and protons N_P per bunch, the number of bunches j, the velocity of the particles v, the accelerator circumference U and the beam cross–section at the interaction point A, the luminosity can be calculated to be:

$$\mathcal{L} = \frac{N_e\, N_P\, j\, v}{U\, A} \tag{2.44}$$

In general, a particular detector only covers a fraction of the solid angle, and only the appropriate fraction of scattering events is detected. Hence, the differential cross–section $d\sigma/d\Omega$ is defined. According to Eq.(2.43), the detected event rate is proportional to the luminosity delivered by the accelerator, the differential cross–section, and the covered solid angle $\Delta\Omega$:

$$\dot{N} = \mathcal{L} \cdot \frac{d\sigma}{d\Omega} \cdot \Delta\Omega \tag{2.45}$$

If the energy E' of the scattered particle is measured in the experiment, the double–differential cross–section $d^2\sigma/dE'd\Omega$ is obtained. The total cross–section is calculated from this result by integrating over the complete solid angle and all scattering energies:

$$\sigma_{tot} = \int_0^{E'_{max}} \int_0^{4\pi} \frac{d^2\sigma}{dE'd\Omega}\, d\Omega\, dE' \tag{2.46}$$

2.5 Proton structure functions

In the single boson exchange approximation, the double–differential cross–section for deep inelastic electron–proton scattering, see Eq.(2.46), can be factorized into a leptonic tensor $L_{\mu\nu}$ and a hadronic tensor $W^{\mu\nu}$:

$$\frac{d^2\sigma}{dE'_e d\Omega} = \frac{\alpha^2}{q^4}\frac{E'_e}{E_e} L_{\mu\nu} W^{\mu\nu} \tag{2.47}$$

Neglecting the electron mass, the leptonic tensor $L^{\mu\nu}$ is given by

$$L_{\mu\nu} = \frac{1}{2} Tr(\not{k}'\gamma_\mu \not{k}\gamma_\nu) = 2(k'_\mu k_\nu + k_\mu k'_\nu + \frac{q^2}{2} g_{\mu\nu}) \tag{2.48}$$

where $g_{\mu\nu}$ is the metric tensor, which is symmetric in μ and ν.

The hadronic tensor $W_{\mu\nu}$ parametrizes the substructure of the proton which takes part in the interaction. It cannot be calculated from first principles as can the leptonic tensor. $W_{\mu\nu}$ is a second-rank tensor and only depends on the four-momentum of the initial proton p and the momentum transfer q. The most general form is given as follows [hal84]:

$$W_{\mu\nu} = -W_1\, g^{\mu\nu} + \frac{W_2}{m_P^2} p^\mu p^\nu + \frac{W_4}{m_P^2} q^\mu q^\nu + \frac{W_4}{m_P^2}(p^\mu q^\nu + p^\nu q^\mu) \tag{2.49}$$

The scalars W_i depend on q^2 and $p \cdot q$. Four–current conservation can be used to reduce the number of independent scalars. Usually, W_4 and W_5 are replaced by

$$W_4 = \left(\frac{p\cdot q}{q^2}\right)^2 \cdot W_2 + \frac{m_P^2}{q^2} \cdot W_1 \tag{2.50}$$

$$W_5 = \frac{p\cdot q}{q^2} \cdot W_2 \tag{2.51}$$

$W_{\mu\nu}$ can then be expressed in terms of only two scalar functions W_1 and W_2. The double-differential cross-section in Eq.(2.47) can now be written as follows:

$$\frac{d^2\sigma}{dE'_e d\Omega} = \left(\frac{d\sigma}{d\Omega}\right)_{MOTT} \cdot \left[W_2(\nu, Q^2) + 2\, W_1(\nu, Q^2) \tan^2\left(\frac{\theta}{2}\right)\right] \tag{2.52}$$

$$with \quad \left(\frac{d\sigma}{d\Omega}\right)_{MOTT} = \frac{4\alpha^2 E'^2_e \cos^2\frac{\theta}{2}}{q^4} \tag{2.53}$$

The Mott cross section according to Eq.(2.53) describes the scattering of electrons on a pointlike particle with infinite mass, not taking into account the spin and the anomalous

magnetic momentum of the proton. The formula describing the scattering of a spin–1/2 electron on a spin–1/2 proton with an extended structure was introduced by Rosenbluth [ros50].

The functions $W_i(\nu, Q^2)$ are the structure functions of deep inelastic electron–proton scattering. They depend on two relativistic–invariant variables, which in this case were chosen to be ν and Q^2. The behaviour of these functions reflect the dynamics of the strong interaction. Usually, the functions are transformed into the dimensionless proton structure functions $F_i(x, Q^2)$:

$$F_1(x, Q^2) = m_P \cdot W_1(\nu, Q^2) \quad (2.54)$$

$$F_2(x, Q^2) = \nu \cdot W_2(\nu, Q^2) \quad (2.55)$$

In addition, there exists a third structure function $F_3(x, Q^2)$ which is small in the low and medium Q^2 range and describes the parity violation contribution due to $(\gamma^* - Z^0)$–interference.

2.6 Virtual photon–proton scattering

The process of deep inelastic scattering of an electron off a proton by the exchange of a virtual photon can be interpreted as the scattering of a virtual photon off the proton. In this picture, the initial electron serves as the source of a virtual photon probing the proton.

If the lifetime of the virtual photon is large compared to the interaction time, the differential electron–proton scattering cross–section may be interpreted as the product of the virtual photon flux and the total photon–proton cross section $\sigma_{tot}^{\gamma^* P}$ [dre64, han63, gil72].

In the observed kinematic region, where x is much smaller than 1, the total photon–proton cross section can be related to the proton structure function F_2 in a simple way:

$$\sigma_{tot}^{\gamma^* P} \equiv \sigma_T^{\gamma^* P} + \sigma_L^{\gamma^* P} \approx \frac{4\,\pi^2\,\alpha}{Q^2} \cdot F_2(x, Q^2) \quad (2.56)$$

Here, $\sigma_T^{\gamma^* P}$ and $\sigma_L^{\gamma^* P}$ denote the cross–sections for the scattering of transversally respectively longitudinally polarized virtual photons off protons, as virtual photons are either transversally or longitudinally polarized.

2.7 The Quark–Parton model

Two models were developed independently to describe the structure of the proton and other hadrons.

The Quark model by Gell–Mann and Zweig [gel64a, zwe64] was introduced to explain the classification of observed hadrons proposed by Gell–Mann and Ne'eman and is known as the Eightfold Way [gel62, gel64b, nee61].

Feynman's parton model [fey69] describes the proton as consisting of quasi–free point–like objects called partons. Each parton i carries a fraction $\xi_i\, P$ of the proton momentum P, where $0 \leq \xi_i \leq 1$. The inelastic electron–proton cross section is given by the incoherent sum of quasi–elastic electron–parton scattering.

As mentioned in section 2.3, the momentum transfer Q^2 determines the resolving power of the scattering process. In 1968, Bjœrken made a prediction for the behaviour of the structure functions based on the following assumption: If the partons were indeed point–like and non–interacting, one would expect that even with increasing resolving power at rising Q^2 no new details would be visible. Hence, for the high energy limit $Q^2 \longrightarrow \infty, \nu \longrightarrow \infty$, but $x = Q^2/2\, m_P\, \nu$ finite, the structure functions would only depend on the dimensionless scaling variable x:

$$F_1(x, Q^2) \;\rightarrow\; F_1(x) \tag{2.57}$$
$$F_2(x, Q^2) \;\rightarrow\; F_2(x) \tag{2.58}$$

This behaviour, known as scaling, was experimentally confirmed, and x was called the Bjœrken scaling variable. In the infinite momentum frame of the proton, x can be interpreted as the fraction ξ of the proton momentum which is carried by the struck parton, neglecting the parton mass m_x and the proton mass m_P:

$$\begin{aligned} m_P^2 &= (\xi p + q)^2 = \xi^2 p^2 - Q^2 + 2\,\xi p\, q = m_x^2 - Q^2 + 2\,\xi p\, q \\ \Rightarrow \qquad \xi &= \frac{1}{2\, p \cdot q} \cdot (m_P^2 - m_x^2 + Q^2) \approx \frac{Q^2}{2\, p \cdot q} = x \end{aligned} \tag{2.59}$$

In 1969, Bjœrken and Paschos suggested that the partons and quarks are identical, introducing the Quark–Parton model (QPM).

The structure functions F_1 and F_2 in the QPM are related to the sum of the parton distribution functions $f_i(x)$ of the partons confined in the proton:

$$F_1(x) = \frac{1}{2} \sum_i e_i^2\, f_i(x) \tag{2.60}$$
$$F_2(x) = x \sum_i e_i^2\, f_i(x) \tag{2.61}$$

Here, e_i is the charge of parton i in units of the proton charge e. The partons are treated as spin 1/2 particles. This result reproduces the Bjœrken scaling behaviour because the proton is assumed to contain free point–like constituents.

$F_1(x)$ and $F_2(x)$ are related through the Callan–Gross relation [cal69] as a consequence of the Parton model ansatz and the treatment of partons as spin 1/2 particles:

$$F_2(x) = 2\, x\, F_1(x) \tag{2.62}$$

This relation has also been confirmed experimentally in a restricted kinematic region.

Although the QPM was very successful explaining some of the early results of electron–proton scattering experiments, some problems of this model became apparent. For example, the fact that no free quarks were observed, which is known as quark confinement, could not be explained. As a consequence, a new field theory of the strong interaction, the Quantum Chromodynamics, was formulated, which for $Q^2 \longrightarrow \infty$ reproduces the QPM.

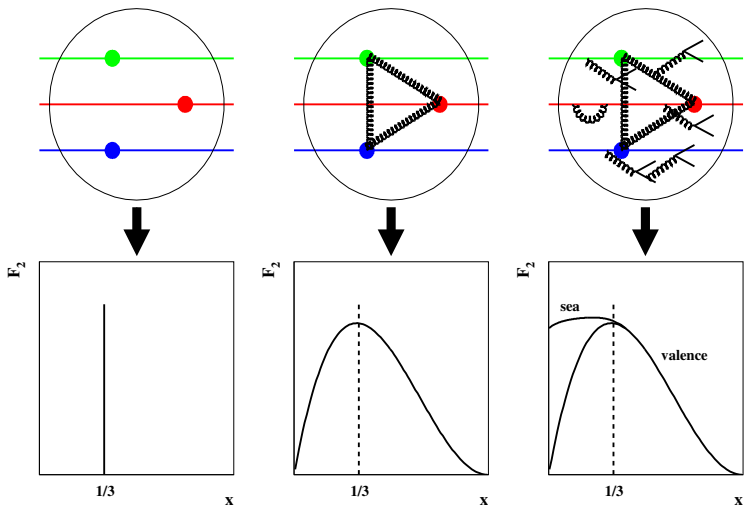

Figure 2.3: Expected form of F_2 for several assumptions for the substructure of the proton [sur98]: Three valence quarks (left), three valence quarks bound by gluon exchange (middle) and valence quarks with QCD dynamics (right).

2.8 Quantum Chromodynamics

The Quantum Chromodynamics (QCD) is the gauge theory of the strong interaction. It describes the interactions between quarks. It is a non–Abelian gauge theory based on a SU(3) symmetry group.

According to QCD, quarks carry an additional quantum number, the colour charge, with three degrees of freedom: red (r), green (g) and blue (b) respectively anti–red ($\overline{r}$), anti–green ($\overline{g}$) and anti–blue ($\overline{b}$) for the antiquarks. The three coloured quarks of one flavour form a triplet.

The gauge bosons of QCD are the eight gluons, which were experimentally observed in 1979 through three–jet events at the PETRA collider at DESY [wu84]. In contrast to the gauge bosons of the weak and electromagnetic interactions, the gluons themselves carry a combination of colour and anti–colour. As a consequence, they are able to interact with each other.

In QCD, the effective coupling, i.e. the colour charge, decreases for large momentum transfers (small distances), which explains the quasi–free behaviour of the quarks inside a nucleon. On the other hand, it increases for small momentum transfers (large distances), which allows the description of the absence of free quarks in nature (quark confinement).

The QCD coupling constant $\alpha_s(Q^2)$ is given in the leading order approximation by

$$\alpha_s(Q^2) = \frac{4\pi}{(11 - 2\,n_f/3) \cdot \ln(Q^2/\Lambda^2)} \tag{2.63}$$

Here, n_f is the number of quark flavours, and Λ is a free scale parameter which has to be determined experimentally. Measurements resulted in values of Λ between 100 and 300 MeV [bar96].

For large momentum transfers $Q^2 \gg \Lambda^2$, α_s is small and increases logarithmically with decreasing Q^2. The quarks are quasi–free and can be described by perturbative calculations according to the perturbative QCD (pQCD). For small Q^2, α_s is large, and perturbative calculations are not valid beyond a certain minimum of Q^2. This is the regime of the non–perturbative QCD. The pQCD was found to be applicable in the region $Q^2 \geq 1\,\mathrm{GeV}^2$ [bre97].

Fig. 2.3 shows the expected qualitative behaviour of F_2 as a function of x for different parton compositions of the proton. In the case of only three valence quarks without Fermi motion (left picture), the proton momentum is expected to be divided equally between them, and F_2 would have a single peak at $x = 1/3$. For three valence quarks bound by gluon exchange (middle picture), we expect a somewhat broadened distribution. Including the whole QCD dynamics (right picture), i.e. the reactions of gluon splitting ($g \to gg$), quark–gluon radiation ($q \to qg$), and pair production of so–called sea quarks ($g \to q\bar{q}$), F_2 is expected to rise at low x. This is caused by the large quark density in the low x region, which is populated by gluons and sea quarks.

At low $Q^2 = Q_0^2$, the resolution is low, and the sea quarks can not be resolved. The measured distribution is $q(x, Q^2) = q(x, Q_0^2)$. Going to higher Q^2, where the resolution increases, more and more sea quarks can be resolved. Hence, the measured distribution is $q(x, Q^2) > q(x, Q_0^2)$, and F_2 rises in the region of small x. Due to the reason mentioned above, the rise of F_2 increases with increasing Q^2.

The region of large x is dominated by valence quarks only, hence the quark density is small. Here, F_2 decreases with increasing Q^2 due to gluon radiation.

The resulting logarithmic dependence of F_2 as function of Q^2 at fixed x is known as scaling violation. Both the rapid rise of F_2 at small x as well as the scaling violation have been observed by the HERA experiments H1 and ZEUS [der93, abt93].

2.9 Physics in the transition region

As mentioned above, pQCD was found to be applicable in the region $Q^2 \geq 1\,\mathrm{GeV}^2$ only. In the region between the regime of pQCD and the photoproduction limit at $Q^2 \approx 0\,\mathrm{GeV}^2$, the so–called transition region with $0\,\mathrm{GeV}^2 \leq Q^2 \leq 1\,\mathrm{GeV}^2$, non–perturbative concepts have to be applied to describe the experimentally observed rise of F_2. Any model attempting to interpret the phenomena in the transition region must provide a consistent behaviour of F_2 transiting from perturbative to non–perturbative QCD.

The BPC (see chapter 6) was built and installed in ZEUS to explore experimentally this very interesting kinematic region. The motivation for the construction of the Crystal BPC, a calorimeter with superior energy resolution compared to BPC II, was the improvement of measurements in the transition region.

Several phenomenological models have been proposed to describe the transition region. Most of them are based on the concepts of the Vector Dominance Model and Regge theory. Detailed descriptions of these models and concepts can be found in [ame99, fri99, mnc98, mon98, sur98].

2.9.1 Vector Dominance Model

Photon–hadron type interactions to a certain extent show analogies to pure hadron–hadron type interactions. This experimental result leads in the Vector Dominance Model (VDM) to the formulation of the photon as a superposition of the bare photon $|\gamma\rangle_{bare}$ and a hadronic component $|\gamma\rangle_{hadronic}$:

$$|\gamma\rangle = |\gamma\rangle_{bare} + |\gamma\rangle_{hadronic} \tag{2.64}$$

The hadronic component appears as a fluctuation of the bare photon into a quark–antiquark pair, thus a vector meson, with the same quantum numbers. The vector meson must be one of the three lightest vector mesons, ρ^0, ω or ϕ, as they possess the same quantum numbers as the bare photon. Hence, the hadronic component is given by a sum over these three vector mesons [sak60]:

$$|\gamma\rangle_{hadronic} \propto \sum_{V=\rho^0,\omega,\phi} \frac{1}{f_V} \left(\frac{m_V^2}{m_V^2 + Q^2} \right) |V\rangle \tag{2.65}$$

Here, m_V are the vector meson masses. The coupling constants f_V, which were determined experimentally in γp and e^+e^- reactions, denote the strength of the individual $\gamma \leftrightarrow V$ coupling.

The VDM assumes that in a photon–hadron interaction only the hadronic component of the photon interacts with the hadron. This ansatz is valid if the fluctuation time, which can be estimated using the uncertainty principle, is large compared to the interaction time.

Using the ansatz from Eq.(2.65) for $|\gamma\rangle_{hadronic}$, expressions for the total longitudinal and transversal cross–sections of virtual photon–proton scattering can be derived, from which a VDM representation of the proton structure function F_2 can be obtained.

Although experimental results confirm the validity of the VDM ansatz in general, several observations from inelastic electron–proton scattering are not reproduced by this model. Consequently, the generalized Vector Dominance Model (GVDM) [sak72] was introduced, which is an extension of the VDM approach. Here, not only the three lightest vector mesons, but also the contributions of all higher mass states are included.

2.9.2 Regge theory

Regge theory was introduced long before the formulation of QCD to describe hadronic two–particle scattering processes. Here, only a short overview is given. A detailed introduction of Regge theory can be found in [col70].

Before the introduction of Regge theory, a simple ansatz was made to describe hadronic two–particle scattering with the one–particle exchange model. In this model, the total cross–section σ_{tot} for the exchange of a single particle with spin j was found to depend on the center–of–mass energy of the virtual photon–proton system $s = W^2_{\gamma^* P}$ like

$$\sigma_{tot} \propto s^{2\,(j-1)} \tag{2.66}$$

For exchanged particles with spin $j > 1$, the cross–section thus would increase with s, which would violate unitarity.

In Regge theory, the two–particle scattering process is described by the exchange of several particles instead of a single particle exchange [reg59]. The scattering amplitude of a two–particle process is decomposed into partial waves. Resonances in the partial wave amplitudes correspond to the exchange of particular particles, e.g. vector mesons $(\rho^0, \omega, \phi, \ldots)$.

If the spins j of all possible exchanged particles of given isospin and strangeness are plotted versus the square of the corresponding particle masses m_j^2, the particles join in a line of the simple form $\alpha(t) = \alpha(t=0) + \alpha' t$. These lines are called Regge trajectories or Reggeons. The term $\alpha(t=0)$ is called intercept of the trajectory. Each set of particles with the same quantum numbers apart from their spin defines a particular Regge trajectory.

In the high energy Regge limit $s \gg Q^2$, the following expression is obtained for the total cross–section:

$$\sigma_{tot} \propto s^{\alpha(t=0)-1} \tag{2.67}$$

The intercept of the highest Regge trajectory for meson exchange is given by $\alpha(t=0) \approx 0.5$. Consequently, the total cross–section is proportional to $s^{-0.5}$ and decreases with increasing center–of–mass energy s, which conserves unitarity.

The predictions from Regge theory and the experimentally measured cross–sections for hadron–hadron interactions are in good agreement for $W < 10\,\mathrm{GeV}$. Measurements at higher W show a slow rise of the cross–section with W, which cannot be generated by the known trajectories since here $\alpha(t=0) < 1$. In order to describe the rise, an additional trajectory with $\alpha(t=0) > 1$, the Pomeranchuk trajectory or Pomeron, was introduced. The Pomeron is not an observed particle but a mathematical construct which was invented to account for the observed rise of the total cross–section. It is required to possess the quantum numbers of the vacuum. The intercept of the Pomeron was determined to be $\alpha_{Pomeron}(t=0) \approx 1.08$.

As the Pomeron is a hypothetical particle, it is not understood how it can be explained in terms of Standard Model particles. Some models consider it to be composed of two gluons [abr96] because it is expected to be colourless.

The Regge ansatz not only describes nucleon–nucleon scattering, but, under certain conditions, also photon–hadron and lepton–hadron interactions. This is illustrated by the possible fluctuations of photons into hadrons, which were described in section 2.9.1.

2.9.3 Models describing the low x and low Q^2 region

There are several models with different approaches trying to describe the phenomena observed in the low x and low Q^2 region.

Some models are based on a Regge ansatz, such as Abramowicz et al. [abr97], who include pQCD expectations at high Q^2 and parameterize F_2 by a fit with 23 free parameters to experimental data, or Capella et al. [cap94], who provide a simple parametrization of F_2 for $0 \leq Q^2 \leq 5\,\mathrm{GeV}^2$ by assuming a bare pomeron which interpolates between the

effective soft pomeron and the effective hard pomeron. Donnachie and Landshoff [don92] fitted all total cross sections for pp, $p\bar{p}$, $\pi^{\pm}p$, $K^{\pm}p$, and $\gamma\,p$ scattering by the sum of two terms, which account for the Pomeron exchange and for the exchange of a conventional trajectory.

Other models are based on the generalized Vector Dominance Model. Badelek and Kwiecinski [bad90] describe F_2 as a sum of a vector meson part, summing over the three lightest vector mesons, and a partonic part. Schildknecht and Spiesberger [sch97] formulated explicit expressions for the virtual photon–proton cross–sections and performed a fit to F_2.

Another author, Haidt [hai99], proposes a parametrization for F_2 based on the experimental result that F_2 in the low x region is linear in terms of an empirical variable ξ.

See [ame99] and [fri99] for a more complete list of models and more detailed descriptions.

Chapter 3

HERA

HERA[1] is the world's first electron–proton collider located at DESY[2] in Hamburg, Germany. It was approved in 1984, first electron–proton collisions were observed in 1991, and physics operation started in 1992. The collider consists of two separate storage rings of 6.3 km circumfence for electrons and protons, respectively, which are located 10 to 25 m below ground. For the proton storage ring, superconducting magnets are used, while the electron storage ring is equipped with normal conducting magnets.

HERA was designed to provide beams to four separate experiments located in four experimental halls (North, South, East, West). The two colliding experiments, H1 [abt97] and ZEUS (see chapter 4), are located in the North respectively South experimental hall. At the appropriate interaction points, electrons and protons collide head–on at zero crossing angle.

Two fixed–target experiments, HERMES [her93] and HERA–B [her95], are installed in the East respectively West experimental hall. The HERMES experiment is designed to explore the spin structure of the nucleon by scattering longitudinally polarized positrons on polarized gas targets and thus only makes use of the HERA electron beam. The HERA–B experiment aims to study $\mathcal{CP}$–violation in the $B^0\bar{B}^0$ system using the interaction of the proton beam halo with wire targets to produce B mesons.

An overview of the HERA accelerator complex is shown in Fig. 3.1. The left figure shows the complete HERA ring with the four experimental halls. In the right figure, the system of pre–accelerators used for HERA is shown.

The proton injection procedure starts with a 50 MeV linear accelerator for negatively charged hydrogen ions (H^-–Linac). After the electrons have been removed by a stripping target, the remaining protons are injected into DESY III, accelerated to an energy of 7.5 GeV and transferred to the PETRA storage ring. Here, the protons are accelerated to 40 GeV and finally transferred to HERA, where they are accelerated to their final energy of 920 GeV.

The electron injection process begins in a 450 MeV linear accelerator (Linac). The electrons are accumulated in a small storage ring (PIA), transferred to DESY II, accelerated

[1] Hadron–Elektron–Ring–Anlage
[2] Deutsches–Elektronen–Synchroton

Figure 3.1: The HERA accelerator complex. The left figure shows an overview. Four experiments are located in the experimental halls North (H1), South (ZEUS), East (HERMES) and West (HERA–B). In the right figure, the system of pre–accelerators used for HERA is shown.

to 7 GeV and injected into PETRA. In PETRA, the electrons are accelerated to an energy of 14 GeV and transferred to HERA where the acceleration to the final energy of 27.5 GeV takes place.

In 1998, the energy E_P of the HERA proton beam was raised from 820 GeV to 920 GeV. Together with an electron beam energy of $E_e = 27.5\,\mathrm{GeV}$, a center–of–mass energy of $\sqrt{s} = 318\,\mathrm{GeV}$ is obtained. The maximum energy transfer is given by $\nu_{max} = s/(2\,m_P) = 54\,\mathrm{TeV}$.

Chapter 4

The ZEUS detector

The ZEUS detector is a large, general purpose detector situated in the South Hall of the HERA accelerator. It started operation in 1992. In the following, the main components of the ZEUS detector are described. A detailed description of ZEUS can be found in [zeu93].

4.1 The ZEUS coordinate system

The coordinate system of the ZEUS detector is a right–handed Cartesian coordinate system. The origin $(X, Y, Z) = (0, 0, 0)$ is located at the nominal interaction point. The X axis points horizontally towards the center of HERA, the Y axis points upwards, and the Z axis points to the proton beam direction, where the $+Z$ direction is referred to as the forward direction and the $-Z$ direction as the backward or rear direction. The polar angle θ is defined relatively to the $+Z$ direction, whereas the azimuthal angle ϕ is measured relatively to the $+X$ axis.

4.2 Components of the ZEUS–detector

Central Tracking Detector: The Central Tracking Detector (CTD) [fos93] is a cylindrical drift chamber which surrounds the beampipe at the interaction point. Its active volume has a length of 205 cm, an inner radius of 18.2 cm and an outer radius of 79.4 cm covering a polar angle of $15° \leq \theta \leq 164°$ and the full range of the azimuthal angle ϕ.

The CTD provides a high–precision measurement of the direction and momentum of charged particles and of the interaction point of each specific event. The latter is measured with a resolution of 0.1 cm in X and Y and 0.4 cm in Z direction. In addition, the identification of individual particles is possible by measuring the mean energy loss dE/dx of charged particles within the CTD.

The Solenoid, a superconducting magnet which produces an axial magnetic field of 1.43 T, encloses the CTD, in order to measure the particle momentum from its track curvature in the magnetic field.

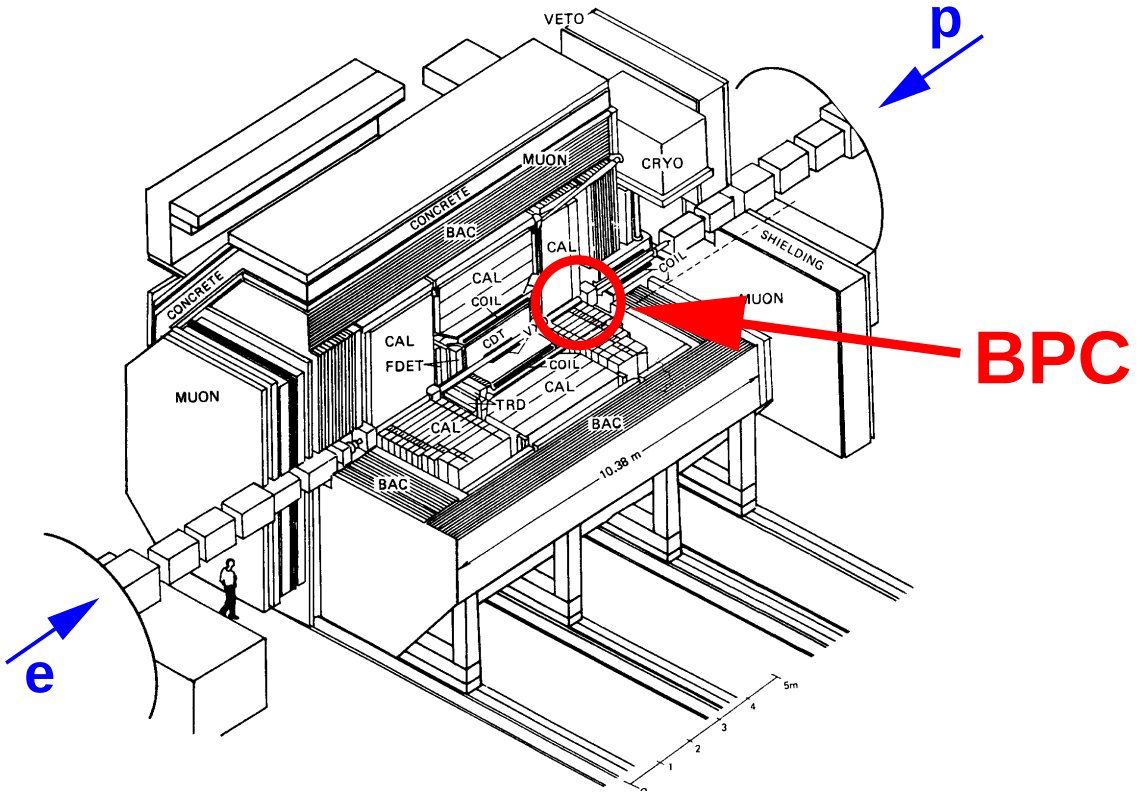

Figure 4.1: Overview of the ZEUS detector. The HERA beam pipe is running from the bottom left to the top right corner of the picture. The directions of electrons respectively protons are indicated by arrows. The interaction vertex is located in the center of the picture. It is surrounded by the Central Tracking Detector (CTD), the Calorimeter (CAL) and the Backing Calorimeter (BAC). The location of the Beampipe Calorimeter (BPC) is marked by a circle.

Forward and Rear Tracking Detector: These detectors provide additional tracking information in the forward respectively backward direction. The Forward Tracking Detector (FTD) consists of three sets of planar drift chambers with transition radiation detectors (TRD) in between. The Rear Tracking Detector is constructed as a single planar drift chamber with three layers.

Calorimeter: The ZEUS calorimeter (CAL) [and91, der91, ber93] is a compensating uranium–scintillator sandwich sampling calorimeter. It consists of three parts: the planar forward and rear calorimeters FCAL in the proton direction and RCAL in the electron direction and the cylindrical barrel calorimeter BCAL.

FCAL and RCAL are divided into 23 modules which are arranged side by side and consist each of up to 23 calorimeter towers stacked one upon the other. The BCAL consists of 32 wedge–shaped modules, each divided in 14 towers. The construction of an FCAL module is shown in Fig. 4.2.

Each calorimeter tower consists of alternating layers of 3.3 mm thick plates of depleted uranium as passive absorber encapsulated in stainless steel sheets and 2.6 mm thick plates of plastic scintillator (SCSN–38) [kam83] as active detector layer. The uranium/scintillator

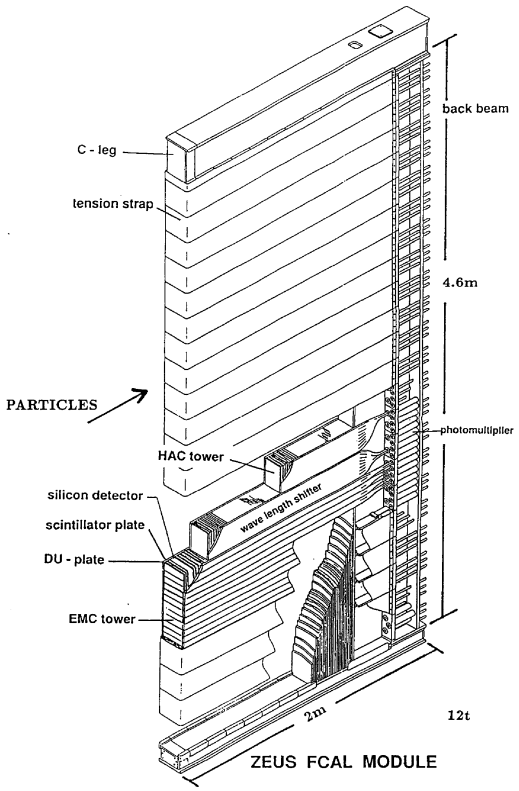

Figure 4.2: Sketch of an FCAL module. The vertical subdivision of the module into calorimeter towers stacked one upon the other is visible. Also, the construction of the towers of alternating scintillator and depleted uranium (DU) plates can be observed.

ratio was tuned to achieve compensation, i.e. the same calorimeter response for both electrons and hadrons of the same energies, which improves the hadronic energy resolution.

The scintillator plates are read out by wavelength shifter bars which run along the calorimeter towers on two sides and lead the scintillation light to photomultipliers where it is detected and converted into an electrical signal. The independent readout on two sides of the calorimeter allows to reconstruct the transverse position of a shower by measuring the imbalance of both signals. Furthermore, a certain redundancy is achieved, which makes the calorimeter less sensitive to failures of the readout system.

The RCAL and FCAL towers are divided longitudinally into electromagnetic (EMC) sections with a depth of $1\,\Lambda$ and hadronic (HAC) sections with a depth of $3\,\Lambda$. See section 5.3 for the definition of the interaction length Λ.

The RCAL consists of one EMC section subdivided into two cells which are each 20 cm wide and 10 cm high and one HAC section with transverse dimensions $20 \times 20\,\mathrm{cm}^2$. The FCAL consists of one EMC section subdivided into four cells which are each 20 cm wide and 5 cm high and two consecutive HAC sections with transverse dimensions $20 \times 20\,\mathrm{cm}^2$. Hence, the RCAL has an overall depth of $4\,\Lambda$ whereas the FCAL has an overall depth of $7\,\Lambda$. The BCAL is $5\,\Lambda$ deep. This asymmetry of the calorimeter's construction is due to the fact that the centre of mass of ep scattering moves in proton direction. The calorimeter covers 99.8% of the full solid angle, i.e. a polar angle θ from 2.6° to 176.1°.

Beampipe Calorimeter: The Beampipe Calorimeter (BPC) is installed in the backward direction close to the beampipe and serves to detect electrons under very small scattering angles. A detailed description is given in chapter 6.

Forward Plug Calorimeter: The Forward Plug Calorimeter (FPC) is installed in the beam pipe hole of the FCAL surrounding the beampipe. It extends the calorimetric coverage of the ZEUS detector and increases the physics potential for diffraction in deep inelastic scattering [bam99].

Backing Calorimeter: The calorimeter is surrounded by an iron yoke which serves as return path for the solenoid magnetic field flux. In addition, it is equipped with proportional chambers for the measurement of energy leakage from the calorimeter and thus serving as the so–called Backing Calorimeter (BAC).

Veto Wall: The so–called Veto Wall composed of iron and scintillator strips is installed outside the detector in the backward direction at $Z = -7.3\,\mathrm{m}$. It is used to reject background events which are dominated by proton–beam gas reactions.

Proton Remnant Tagger: The Proton Remnant Tagger (PRT) consists of three groups of lead/scintillator counters which are installed in the forward direction and serve to detect fragments of the dissociated proton.

Leading Proton Spectrometer: The Leading Proton Spectrometer (LPS) is located in the forward direction very close to the beam. It consists of six stations of silicon strip detectors and is used to measure longitudinal and transverse momentum of quasi-elastically forward scattered protons.

Forward Neutron Calorimeter: The Forward Neutron Calorimeter (FNC) is a lead/scintillator sandwich calorimeter. It is installed in the forward direction at $Z = 105.6\,\mathrm{m}$ and is used to detect neutrons scattered in the forward direction.

4.3 Luminosity measurement

As shown in section 2.4, the cross–section of a scattering process is closely related to the luminosity $\mathcal{L}$ delivered by the accelerator. Hence, the exact measurement of the luminosity is crucial for the precise determination of cross–sections and structure functions.

At ZEUS, the luminosity is measured via the well–known Bethe–Heitler bremsstrahlung process [bet34]

$$eP \longrightarrow eP\gamma \tag{4.1}$$

whose cross–section σ_{BH} is known from QED to an accuracy of 0.5% [gae89]. According to Eq.(2.43), the integrated luminosity $\mathcal{L}_{int}$ can thus be determined by integrating over the photon rate $\dot{N}_{BH}$ from the Bethe–Heitler process:

$$\mathcal{L}_{int} = \int \frac{\dot{N}_{BH}}{\sigma_{BH}}\, dt \tag{4.2}$$

Photons from the Bethe–Heitler process are emitted under very small angles with respect to the electron beam direction. They are detected by a separate electromagnetic calorimeter (LUMIG) [and92, pio93], which is located far from the main ZEUS detector in the HERA tunnel in the electron direction at $Z = -107\,\mathrm{m}$.

A second electromagnetic calorimeter (LUMIE), located at $Z = -35\,\mathrm{m}$, was initially designed to measure the final state electron of the Bethe–Heitler process simultaneously to the photon measurement. This was found not to be necessary in order to obtain a precise luminosity measurement.

Chapter 5

Basics of calorimetry

This chapter deals with the basic principles of the energy measurement of high energetic electromagnetic particles using calorimeters. First, some important categories of calorimeters are presented. Then, the principles of energy loss of electromagnetic particles and, for completeness, of hadronic particles are outlined. Finally, the factors which contribute to the energy resolution are discussed for the electromagnetic case.

5.1 Calorimeter design

The principle of calorimetry is based on the absorption of a particle's energy in matter and the conversion of at least a part of this energy into a measurable signal.

Two major calorimeter designs are commonly is use. A homogenous calorimeter, also called a total absorption calorimeter, consists of one homogenous medium which serves both as absorber and as the active medium which produces a measurable signal. Common materials are heavy scintillating crystals such as $PbWO_4$, BGO ($Bi_4Ge_3O_{12}$) or NaI as well as lead glass, where Čerenkov light is produced. Homogenous calorimeters reach very good energy resolutions only limited by intrinsic shower fluctuations and photoelectron statistics.

In a sampling calorimeter, two different materials are used for the energy dissipation and the measurement. The absorber material typically consists of a heavy element, for example lead, tungsten or uranium. A common choice for the active material is scintillator, for example plastic scintillator, which offers a good light yield together with a fast time response. The energy resolution of sampling calorimeters in general is inferior to homogenous calorimeters, as sampling fluctuations, which are caused by the varying ratio of energy deposited in the scintillator and in the absorber, have a large contribution.

There are several types of sampling calorimeters: In sandwich–type calorimeters such as the ZEUS calorimeter and BPC II, absorber and scintillator plates are arranged in alternating layers, the latter read out by wavelength shifter bars running along the calorimeter sides. Shashlik–type calorimeters also show a sandwich structure, but here the readout is performed by wavelength shifting fibers located in holes in the absorber and scintillator plates. In spaghetti–type calorimeters, finally, scintillating fibers are arranged in grooves in a block of absorber material and usually read out directly.

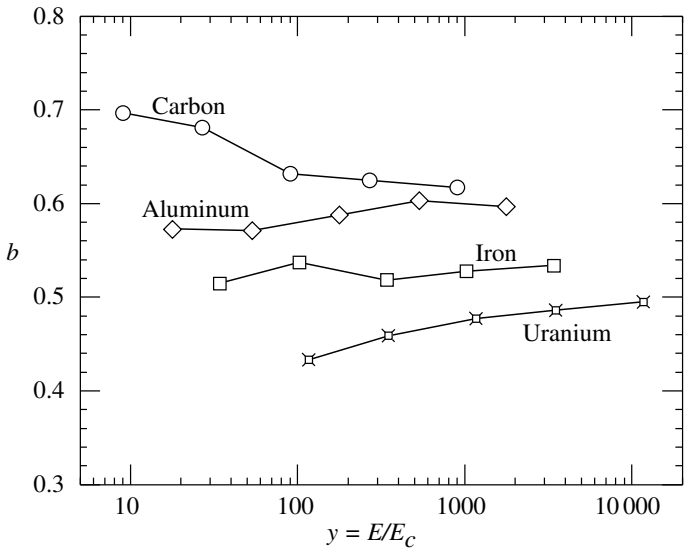

Figure 5.1: Fitted values of the scale factor b for energy deposition profiles obtained with EGS4 for several elements (from [cas98]).

5.2 Electromagnetic showers

Travelling through matter, electromagnetic particles such as electrons and photons lose energy due to several processes.

In case of electrons at high energies above 100 MeV, the main process of energy loss is bremsstrahlung in the Coulomb field of a nucleus

$$e + \text{nucleus} \longrightarrow e' + \gamma + \text{nucleus} \tag{5.1}$$

Below 100 MeV, electrons mainly lose energy due to ionization, although other processes, such as positron annihilation $e^+e^- \to \gamma\gamma$, Møller scattering $e^-e^- \to e^-e^-$ and Bhabha scattering $e^+e^- \to e^+e^-$, also contribute.

In case of high energetic photons with energies above 100 MeV, the dominating effect of energy loss is pair production in the Coulomb field of a nucleus

$$\gamma + \text{nucleus} \longrightarrow e^+e^- + \text{nucleus} \tag{5.2}$$

Going to lower energies, first Compton scattering $e\gamma \to e\gamma$ and then photoelectric effect $\gamma + \text{atom} \to \text{atom}^+ + e^-$ become dominant.

Due to these processes, a high energetic electron or photon in matter initiates a particle cascade which consists of an increasing number of secondary particles with decreasing energy. Hence, an electromagnetic shower is formed around the incident direction of the primary particle. The mean energy loss of an electron due to bremsstrahlung is given by the following formula:

$$\frac{dE}{E} = -\frac{dx}{X_0} \quad \Longleftrightarrow \quad E(x) = E_0\, e^{-x/X_0} \tag{5.3}$$

Here, x denotes the thickness of the material, and E_0 the electron impact energy. The radiation length X_0 is the distance over which an electron loses all but $1/e$ of its initial energy by bremsstrahlung.

The dependence of the radiation length of a particular material on its atomic number Z and atomic weight A can be parametrized by a fit to the experimental data [cas98]:

$$X_0 = \frac{716.4\,\mathrm{g\,cm^{-2}} \cdot A}{Z(Z+1)\,\ln(287/\sqrt{Z})} \tag{5.4}$$

where X_0 is given in units of $\mathrm{g/cm^2}$.

For a compound of several elements, the effective atomic number can be calculated:

$$Z_{eff} = \sum_i w_i\, Z_i \tag{5.5}$$

where the factors w_i denotes the fraction by weight of the i^{th} element with the atomic number Z_i.

The critical energy E_c according to [ros52] denotes the energy at which the ionization loss per radiation length is equal to the electron energy. Below the critical energy, the electron energy losses are dominated by ionization and not by bremsstrahlung. As a consequence, no new bremsstrahlung photons are produced, and the shower dies out. According to [cas98], the critical energy is given by the following expressions:

$$\text{for solids and liquids:} \quad E_c = \frac{610\ \mathrm{MeV}}{Z + 1.24} \tag{5.6}$$

$$\text{for gases:} \quad E_c = \frac{710\ \mathrm{MeV}}{Z + 0.92} \tag{5.7}$$

It is convenient to express the distance in units of the radiation length X_0 and the energy in units of the critical energy E_c by introducing the scale variables

$$t = x/X_0 \tag{5.8}$$

$$y = E_0/E_c \tag{5.9}$$

The mean longitudinal profile of an electromagnetic shower can be described by a gamma distribution [lon75]:

$$\frac{dE}{dt}(t) = E_0\, b \cdot \frac{(b\,t)^{(a-1)}\, e^{-bt}}{\Gamma(a)} \tag{5.10}$$

The scale factor b is determined from simulations, as shown in Fig. 5.1. The parameter a can be calculated from the following expression for the location of the shower maximum t_{max}:

$$t_{max} = \frac{a-1}{b} = \ln y + C_j\,, \qquad j = e, \gamma \tag{5.11}$$

Here, $C_e = -0.5$ for electron induced showers and $C_\gamma = +0.5$ for showers induced by photons. For the energy dependent value of a we obtain

$$a(y) = b \cdot (\ln y - 0.5) + 1 \tag{5.12}$$

In section 11.5, Eq. 5.10 is used to simulate longitudinal shower shapes in the Crystal BPC for different energies.

The transverse shower development is described by the Molière radius [nel66, bat70]

$$R_M = X_0 \cdot \frac{E_s}{E_c} \tag{5.13}$$

with the scale energy $E_s = \sqrt{4\pi/\alpha}\, m_e\, c^2 = 21.2\,\mathrm{MeV}$. On the average, 90% of the shower energy is deposited within a cylinder with radius R_M, and about 99% is contained within $3.5\,R_M$ [cas98].

5.3 Hadronic showers

A hadronic shower is the result of the inelastic interaction of an incident hadron with a nucleus. In this process, secondary particles are produced. These are mainly charged and neutral pions and, with lower multiplicities, kaons, nucleons and other hadrons.

The longitudinal propagation of a hadronic shower in a particular material after the shower maximum is described by the interaction length Λ:

$$E(x) = E_0\, e^{-x/\Lambda} \tag{5.14}$$

The interaction length of a particular material is significantly larger than its radiation length in the electromagnetic case, resulting in a much larger longitudinal extension of a hadronic shower compared to an electromagnetic shower. In addition, hadronic showers also show a broadened distribution in the lateral dimension due to the transverse momentum transfer in nuclear interactions.

A considerable fraction of the secondary particles produced in hadronic showers are neutral pions. These decay into two high–energetic photons and so initiate subordinate electromagnetic showers. The production of neutral pions is subject to large fluctuations, depending on the energy of the incident hadron and other factors. Hence, a hadronic shower in general has an indeterminate electromagnetic component.

In contrast to electrons and photons, whose energy is fully transferred into a measurable signal in a calorimeter, about 20% of the energy of an incident hadron escapes detection. This is due to processes such as breakup and excitation of nuclei, which do not contribute to the measured signal. Furthermore, stable neutral particles like slow neutrons, neutrinos and muons may leave the calorimeter and reduce the measured energy. All these effects result in a reduced hadron response of a calorimeter compared to the electron response. Having in mind the above mentioned hadronic and electromagnetic components of a hadronic shower, this leads to an inferior hadronic energy resolution.

In order to achieve an optimal energy resolution, a ratio of the hadron response to the electron response of $e/h = 1$, which is called compensation, is necessary. Slow neutrons which are produced in nuclear interactions will split target nuclei producing additional neutrons and high–energetic photons. In the case where uranium is used as absorber in a sampling calorimeter, this fission process is exothermic, and the additionally produced neutrons and photons may contribute to the calorimeter's hadronic response. Hence, in case of a careful calorimeter design, compensation can be achieved.

5.4 Energy resolution

The energy resolution of a calorimeter, that is the uncertainty of the energy measurement, is determined by several contributions.

The statistical term dominates the energy resolution over much of the calorimeter's useful energy range:

$$(\sigma(E)/E)_{statistic} \propto 1/\sqrt{E/GeV} \tag{5.15}$$

It is caused by statistical processes such as shower development and photoelectron statistics. In sampling calorimeters, the statistical term is dominated by sampling fluctuations, whereas in homogenous calorimeters, where this effect is not present, photoelectron statistics dominate.

The noise term is due to rather energy–independent instrumental effects such as electronics noise:

$$(\sigma(E)/E)_{noise} \propto 1/(E/GeV) \tag{5.16}$$

As its relative contribution decreases with E, it may limit the calorimeter performance at low energies.

The constant term is caused by calibration errors, non–uniformities and non–linearities in the energy deposition and the calorimeter readout:

$$(\sigma(E)/E)_{const} = const. \tag{5.17}$$

In case of hadronic calorimeters, non–compensation also contributes to the constant term. It is not dependent on energy, therefore becomes dominant at very high energies and sets the performance limit there.

Finally, there are fluctuations due to increasing longitudinal shower leakage with increasing energy [gru93]:

$$(\sigma(E)/E)_{leakage} \propto \ln(E/GeV) \tag{5.18}$$

Although this effect is usually considered as a contribution to the constant term, it may be useful to examine it separately because of its energy dependence.

To obtain the full energy resolution, all contributions must be added in quadrature:

$$\left(\frac{\sigma(E)}{E}\right)^2 = \left(\frac{\sigma(E)}{E}\right)^2_{statistic} + \left(\frac{\sigma(E)}{E}\right)^2_{noise} + \left(\frac{\sigma(E)}{E}\right)^2_{const} + \left(\frac{\sigma(E)}{E}\right)^2_{leakage} \tag{5.19}$$

In order to achieve an energy measurement with optimal precision, it is desirable that the energy resolution of a calorimeter be as good as possible.

Chapter 6

The Beampipe Calorimeter

The Beampipe Calorimeter (BPC) is a subsystem of the ZEUS detector. It consists of two separate modules located on either side of the beampipe, referred to as BPC North and BPC South according to their position with respect to the HERA collider. This thesis only deals with the North module, which is the main component for physics analysis. The South module is not used for physics analysis because its acceptance for electrons, determined by the size of the beampipe exit window, is significantly smaller. Hence, the term BPC in general denotes the North module only until explicitely stated otherwise.

The BPC is installed between the RCAL and the ZEUS compensator magnet very close to the beampipe and extends from about $Z = -2.9\,\mathrm{m}$ to $Z = -3.2\,\mathrm{m}$. The distance of the inner edge (oriented towards the beampipe) of the BPC North module housing to the HERA electron beam is about 39 mm. The distance of the inner edge of the active area to the electron beam is 44 mm. The location within the ZEUS detector is shown in Fig. 4.1.

The location of the BPC inside the ZEUS detector directly next to the beampipe entails certain requirements and constraints. First, there is very little free volume. The North module must fit in a very limited space of about 150 mm and 180 mm in X respectively Y direction, determined by the surrounding RCAL modules and the beampipe, and 300 mm in Z direction. Thus, a very compact calorimeter design is necessary. In addition there is a magnetic field at the level of several 100 Gauss caused by the ZEUS solenoid and compensator magnet. This might cause problems if photomultipliers, which in general are sensitive to a magnetic field, are used for the detection of the scintillation light. Furthermore, high radiation doses of up to 12 kGy per year in 1995 and 10 kGy in 1996 were observed in the BPC area. The doses decreased to 2 kGy per year in 1997 after improving the dumping procedure for the HERA electron beam [sur98]. Finally, temperature changes at the level of 2 K have been observed in the BPC area inside ZEUS.

The BPC is used to detect electrons scattered under very low angles, corresponding to the low Q^2 region $Q^2 \leq 1\,\mathrm{GeV}^2$ and the very low x region $x \leq 10^{-3}$. The angular acceptance for scattered electrons ranges from polar angles of $\theta'_e = 178.2°$ to $179.0°$ corresponding to scattering angles $\vartheta'_e = 32\,\mathrm{mrad}$ to $18\,\mathrm{mrad}$ (see Fig. 2.2 on page 7).

A modified beampipe was installed in the rear detector area in 1994 [loh96]. It is shown in Fig. 6.1 together with the two BPC modules. In order to enable electrons scattered under low angles to reach the BPC, two exit windows are installed at a distance of

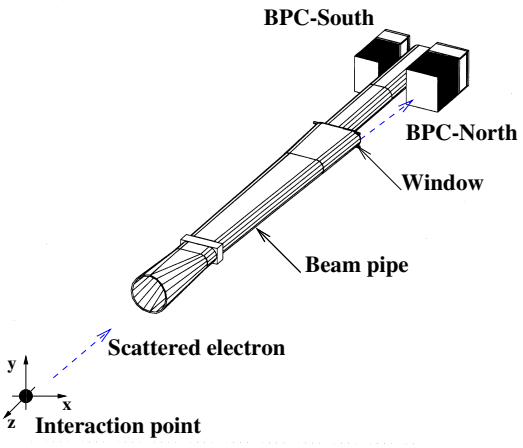

Figure 6.1: Overview of the rear beampipe together with the two BPC modules located at both sides of the beampipe.

$Z = 2498\,\mathrm{mm}$ from the interaction point on both sides of the beamipe in front of the corresponding calorimeter modules. They are made of 1.5 mm thick aluminium which corresponds to 0.016 radiation lengths, enabling the electron to leave the beampipe with minimal interference. The projection of the beampipe exit window on the calorimeter front face defines the size of the fiducial volume of the appropriate BPC module, where electrons from the interaction point can hit traversing the beampipe window. The border of the fiducial volume towards the beampipe is determined by evaluating the effect that transverse losses of the electromagnetic shower degrade the quality of the measurements. This effect increases approaching the calorimeter edges.

The BPC has been subject to a certain process of evolution. The first BPC was a tungsten–silicon calorimeter [loe94]. The passive layers consisted of tungsten with a thickness of two radiation lengths, whereas the active layers were built of silicon diodes. Its energy resolution was measured to be $28\%/\sqrt{\mathrm{E/GeV}}$. In front of the calorimeter, two silicon strip detectors were located to obtain information about the position of the incoming particles. In 1995, the first BPC was replaced by BPC II, which is further described in the next section.

It was planned to replace the BPC II North module by the Crystal BPC, a homogenous calorimeter made of $PbWO_4$ crystals with a superior energy resolution. The motivation and estimated consequences related to this project are described in the sections 6.2 and 6.3.

6.1 BPC II and BPT

BPC II was installed in ZEUS in 1995 and started data taking in the same year. The kinematic range covered in the analysis of 1995 and 1996 data is given by $0.11 \leq Q^2 \leq 0.65\,\mathrm{GeV}^2$ and $2 \times 10^{-6} \leq x \leq 6 \times 10^{-5}$. Results of the proton structure

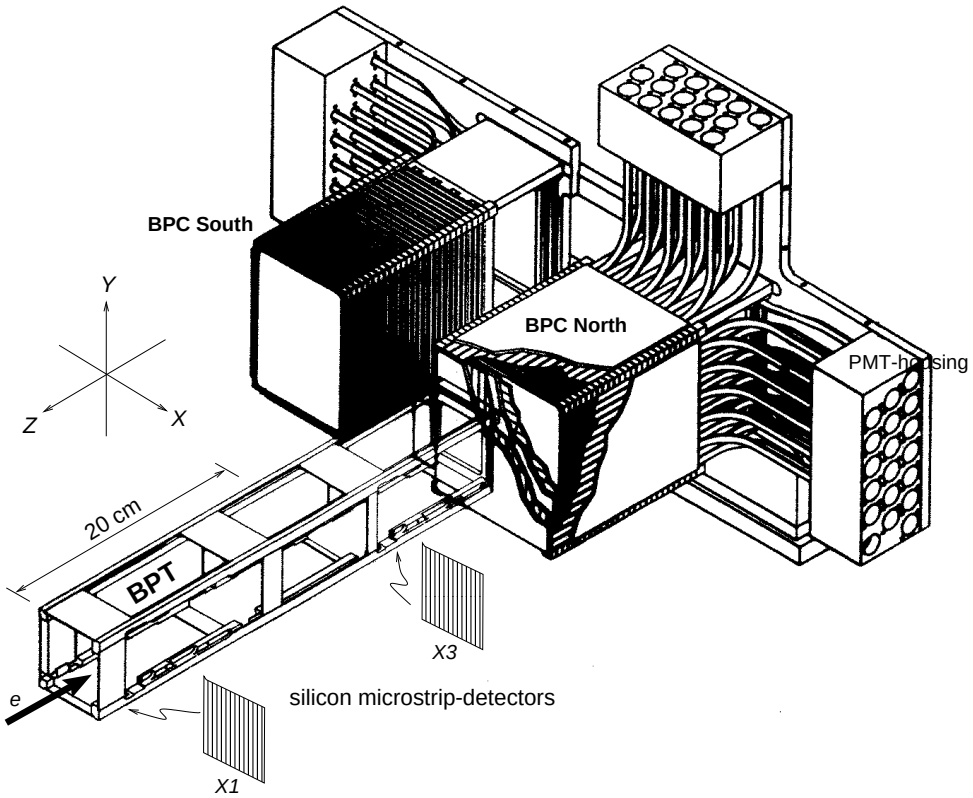

Figure 6.2: Picture of the two BPCII modules (North and South) with the BPT attached to BPC North [mnc98]. The beampipe is running between the BPC modules, not shown in the picture. Electrons from the interaction vertex emenate from the left. The BPT is shown in its 1997 configuration with two planes of silicon microstrip detectors, X1 and X3.

function F_2 and the total virtual photon-proton ($\gamma^* p$) cross-section for this kinematic range, based on 1995 data, have been published in [sur98] and [zeu97]. A study of exclusive electroproduction of ρ^0 mesons at low Q^2 using BPC II has been published in [mon98]. A cross–section measurement of the diffractive process $\gamma^* + P \to X + N$ in the low Q^2 region has been published in [inu99].

In 1997, the beampipe tracker BPT was installed in ZEUS between the frontface of the North module of BPC II and the corresponding beampipe exit window. The analysis of the 1997 data makes use of this new component, which allows an extension of the kinematic range and a reduction of the systematic errors. The kinematic range of the 1997 analysis is given by $0.045 \leq Q^2 \leq 0.80\,\mathrm{GeV}^2$ and $3 \times 10^{-7} \leq x \leq 10^{-3}$. Results of the proton structure function F_2 and the total virtual photon-proton ($\gamma^* p$) cross-section have been published in [ame99, fri99, mnc98].

BPC II is a segmented tungsten–scintillator sampling calorimeter. It was designed to measure both the energy and the impact point of the scattered electron.

The 26 passive layers of the calorimeter consist of 3.5 mm thick tungsten alloy plates (DENSIMET D18k) [pla94] with a density of $18\,\mathrm{g/cm}^3$ and a radiation length of 3.87 mm. The total radiation length of the passive layers amounts to 24 X_0.

Each of the 26 active layers consists of 7.9 mm wide and 2.6 mm thick plastic scintillator fingers (SCSN–38) [kam83] wrapped in aluminium foil to increase the light yield and achieve an optical decoupling. The scintillator fingers are arranged in alternating horizontal and vertical layers providing spatial information about the electron impact position. The horizontal layers (Y fingers) are used for the reconstruction of the Y position whereas the vertical layers (X fingers) provide the X reconstruction. Both BPC modules contain 16 channels for the Y reconstruction. The North module contains 15 channels for the reconstruction of the X coordinate, whereas the South module only has 11 X channels.

The scintillator fingers are read out by 7 mm wide and 2 mm thick wavelength shifter (WLS) bars which contain 30 ppm of the dye Y7 in PMMA. All fingers oriented the same way behind each other are read out by the same WLS bar and represent one calorimeter channel. There is no longitudinal segmentation of the readout.

Each WLS bar is bent by 90° with a radius of 30 mm away from the calorimeter and coupled to a photomultiplier tube (PMT) of the type Hamamatsu R5600–03 [ham94]. This miniature PMT type has a diameter of 16 mm and a length of 12 mm. Unlike conventional PMTs, it is rather insensitive to a magnetic field. There is no performance degradation in magnetic fields up to 100 G. To provide additional magnetic shielding, the PMTs are mounted inside a block of magnetic iron (ARMCO) [arm90].

In a test beam experiment at the DESY II test beam, the energy resolution of BPC II was measured to be $17.2\,\%/\sqrt{E/GeV}$ [sur98]. See [mon98, sur98] for a more detailed description of BPC II.

The BPT represents a tracking system which is independent of the ZEUS central tracking chambers, thus providing an independent Z vertex reconstruction. In addition, the BPT increases the position resolution of the BPC and allows to reject noise caused by fake electrons, which are mainly photons from photoproduction events [cal96]. It is installed between the BPC North module and the corresponding beampipe exit window. The BPT

consists of a carbon fiber support structure attached to the front face of BPC North. Initially is was designed to contain five planes of silicon microstrip detectors, three for the reconstruction of the X coordinate and two for Y reconstruction.

In July 1997 the first two planes, X1 and X3, were installed. Both measure the X position and thus provide a measurement of the horizontal scattering angle. The resolution of this measurement is given by the BPT resolution in X, which amounts to $\Delta X_{BPT} = 40\,\mu$m, and the resolution of the Z vertex reconstruction of the CTD (0.4 cm). From these values, the resolution of the horizontal scattering angle reconstructed with the BPT was calculated to 0.04 mrad. As the BPT in the 1997 configuration cannot provide a measurement of the Y coordinate, the vertical scattering angle has to be reconstructed using the BPC Y measurement with a resolution of $\Delta Y_{BPC} = 0.22\,\mathrm{cm}/\sqrt{E'_e/\mathrm{GeV}}$. A Monte Carlo study resulted in an angular resolution of $(\Delta\vartheta'_e)_{BPT} = 0.25$ mrad if X_{BPT} and Y_{BPC} are used for reconstruction, compared to a value of $(\Delta\vartheta'_e)_{BPC} = 0.31$ mrad if both coordinates are reconstructed using only BPC information [fri99].

More detailed information about the BPT is given in [ame99, fri99, mnc98]. An overview of the two BPC II modules together with the BPT attached to BPC North is shown in Fig. 6.2.

6.2 The Crystal BPC as an upgrade of BPC II

After the successful installation of BPC II in the ZEUS detector, some methods were proposed to further improve the quality of the measurements [cal96].

An upgrade proposal considers the improvement of the spatial resolution of BPC II by the installation of the BPT in front of the BPC.

The second proposed upgrade concerns the calorimeter itself. By improving the energy resolution of the device, a further extention of the covered kinematic range together with an improvement of the accuracy of the measurements was expected. This can be achieved by replacing the sampling calorimeter BPC II by a new, homogenous calorimeter with a superior energy resolution of $5\%/\sqrt{\mathrm{E/GeV}}$. As scintillator, $PbWO_4$ crystals were proposed, as they have unique properties for the construction of a compact high–precision calorimeter. The next section gives an estimate of the improvements which were expected.

6.3 Estimation of the effect on physics measurements

The kinematic region which is accessible by a particular detector is determined by the size of the uncertainties of the measurement. A useful measurement is only possible in regions where the measurement error is sufficiently small.

The kinematic region covered by the measurement of F_2 based on 1997 BPC II and BPT data is shown in Fig. 6.3 shaded light gray. In this region, the electron method is used for the reconstruction of the kinematic variables, which relies solely on the energy E'_e and the

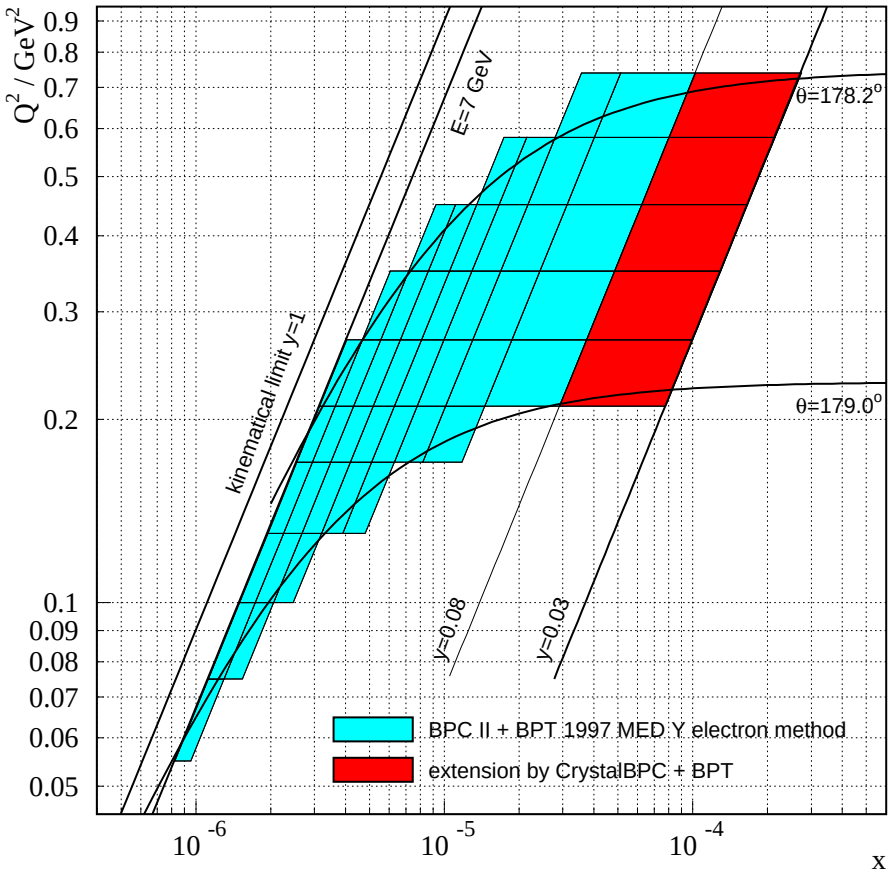

Figure 6.3: Estimated extension of the kinematic region in the Q^2–x plane by the Crystal BPC. The region covered by BPC II with BPT in the 1997 MED Y analysis using the electron method is shaded light gray. The Crystal BPC is expected to expand the kinematic region to higher x corresponding to lower values of y. The estimated additionally covered region is shaded dark gray. The curves labeled $\theta = 178.2°$ and $\theta = 179.0°$ denote the geometrical acceptance of the BPC.

scattering angle θ'_e of the final state electron (see section 2.3.1). The relative measurement error in y_e has already been quoted in Eq.(2.26):

$$\frac{\Delta y_e}{y_e} = \frac{1 - y_e}{y_e} \cdot \left(\frac{\Delta E'_e}{E'_e} \oplus \frac{\Delta \theta'_e}{\tan \frac{\theta'_e}{2}} \right) \tag{6.1}$$

Due to the $1/y_e$ dependence of the measurement error in y_e, the electron method degrades rapidly with decreasing y_e. It depends on the energy resolution $\Delta E'_e/E'_e$ and the angular resolution $\Delta\theta'_e/\theta'_e$ of the detector used.

The angular resolution is given to about 1% by the BPT. By installing the Crystal BPC, the energy resolution will be improved from about 3.4% (BPC II) to the same range of about 1% and the energy scale error to less than 0.5%. Hence the Crystal BPC is expected to further extend the kinematic region usable for reconstruction with the electron method towards lower y_e with small systematic uncertainties.

The kinematic region using the electron method covered by BPC II with BPT in the 1997 analysis extends to $y = 0.08$. The systematic error $\Delta y/y$ at low y is about 0.25 [fri98].

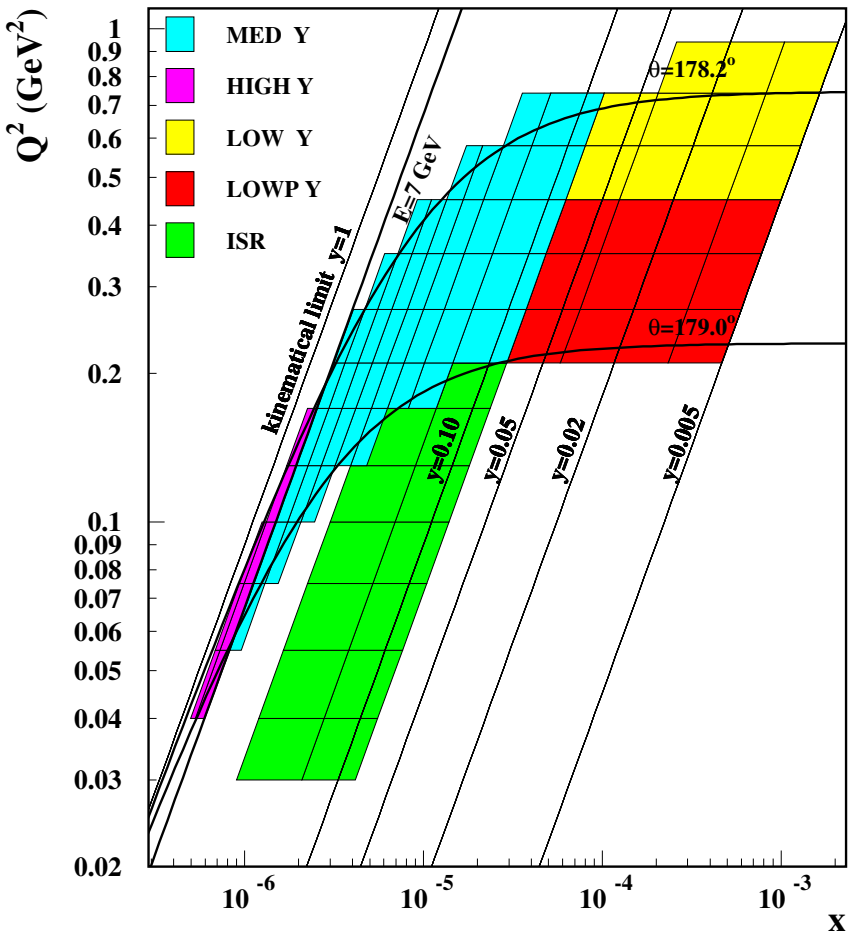

Figure 6.4: The kinematic region of BPC II and BPT in the Q^2–x plane covered in the 1997 analysis [fri99]. For the reconstruction, the electron method is used in the regions MED Y and HIGH Y, whereas the e–sigma method is used in the LOW Y and LOWP Y regions. In the region denoted as ISR only a feasability study was performed.

Assuming the same error and taking into account an improvement of the energy resolution from $17\%/\sqrt{E/GeV}$ to $5\%/\sqrt{E/GeV}$, the kinematic region of the Crystal BPC is expected to reach down to $y = 0.03$. The expected additionally accessible kinematic region is shown in Fig.6.3 shaded dark gray. The extension towards lower y is accompanied by a substantial increase in the x range covered by the measurements. As another consequence, a higher precision of the measurements can be expected, resulting in significantly reduced bin sizes in y [cal96].

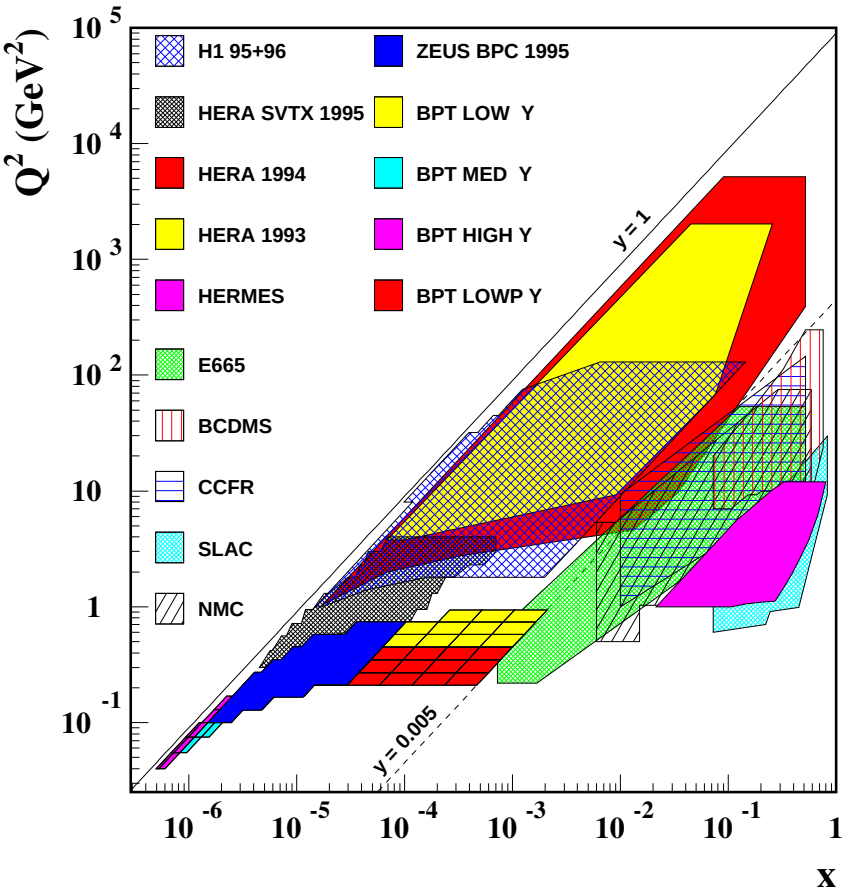

Figure 6.5: The kinematic regions in the Q^2–x plane covered by several experiments throughout the world. The overlap of the 1997 BPCII/BPT analysis with the E665 experiment is clearly visible.

6.4 Improvements by the 1997 analysis

In the previous section, an estimation of the improvements of physics measurements with the Crystal BPC was given. The study was based on the kinematic range which could be covered using the electron method for reconstruction. It was shown that the kinematic range which is accessible using the electron method could be significantly extended towards higher x.

In the 1997 analysis of the BPCII and BPT data [ame99, fri99], an effort was made to achieve an extension of the accessible kinematic range, namely the use of a different method of reconstruction.

In order to extend the kinematic range, the electron–sigma method was employed, which uses the energy and angular information of the scattered electron and the difference $\Sigma = \sum_h (E_h - p_{Z,h})$ of the energy and the longitudinal momentum of the hadronic final state (see section 2.3.1). Using this method, there is no divergence of the measurement

error in y at low y [bas94] as in case of the electron method. The resulting kinematic region covered by the 1997 analysis in shown in Fig.6.4. For the reconstruction, the electron method is used in the regions MED Y and HIGH Y, whereas the electron–sigma method is used in the LOW Y and LOWP Y regions.

In the region denoted as ISR, only a feasability study was performed [ame99]. Here, events with initial state radiation (ISR) are used to measure at higher values of x and, at the same time, lower values of Q^2 than in the nominal analysis. In this class of events, the initial electron radiates a photon which is detected in the photon calorimeter of the ZEUS LUMI system. The momentum transfer $\hat{Q}^2$ of an ISR event, compared to a nominal event, is reduced by a factor which depends on the energy of the photon.

As a result of the improvements, an overlap with the kinematic region covered by the fixed target experiment E665 [ada96] was achieved, which scattered muons of 400 to 500 GeV on fixed targets of liquid hydrogen or deuterium. The overlap can be observed in Fig.6.5, where the kinematic regions of several experiments throughout the world are summarized.

Chapter 7

$PbWO_4$ as scintillator

First investigations of $PbWO_4$ were carried out in 1948, but at that time this material was considered of low interest for calorimetry due to its low light yield at room temperature [lec94].

7.1 Chemical and physical properties

$PbWO_4$ is a crystal of the tungstate family. It has a fast but relatively low light yield scintillation due to a strong thermal quenching at room temperature which also causes a temperature coefficient of the light yield. Nevertheless it is one of the densest crystals known and has a very small radiation length and Molière radius. Hence this material allows to build very compact high resolution electromagnetic calorimeters.

$PbWO_4$ is a birefringent scheelite type crystal. Optically, it is a negative uniaxial crystal. It belongs to the space group $I4\,1/a$ with tetragonal unit cell. It is grown from a 50%/50% mixture of lead oxide (PbO) and tungsten oxide (WO_3) which melts congruently at 1123°C. Physical and chemical properties of $PbWO_4$ are given in Tab. 7.1.

7.2 The complex refractive index of $PbWO_4$

The knowledge of the refractive index of $PbWO_4$ is necessary for calculations concerning, for example, the optical readout of crystals.

In [bac97a], the ordinary and extraordinary refractive index of $PbWO_4$ crystals were measured by reflectance and transmittance measurements with polarized light at different wavelengths throughout the optical spectrum. The results are shown in Tab. 7.2. The extraordinary refractive index was found to be lower than the ordinary one. Both were found not to be affected by doping.

Density	8.28 g/cm^3
Composition	14.06% O (Z=8) 40.40% W (Z=74) 45.53% Pb (Z=82)
Effective Atomic Number	Z_{eff}=68.3
Radiation Length	0.89 cm
Interaction Length	22.4 cm
Molière Radius	2.19 cm
dE/dx per MIP	13.0 MeV/cm
Critical Energy, see Eq.(5.6)	8.8 MeV
Light Yield	7% of BGO
Decay Time	5 ns (39%) 15 ns (69%) 100 ns (1%)
Maximum of Emission	420 nm – 500 nm, dependent on crystal doping
Temperature Coefficient at Room Temperature	-2 %/K
Melting Point	1123 °C
Hardness	4 Moh
Mechanical Strength	1 kg/mm^2
Hygroscopic	no
Chemical Activity	inert
Thermal Conductivity	3300 W/K
Specific Heat	440 J/kg K

Table 7.1: Properties of $PbWO_4$ crystals [rus97, lec94, lec96, cas98].

λ / nm	n_o	n_e
375	2.452±.009	2.297±.025
400	2.393±.009	2.260±.019
425	2.353±.009	2.236±.015
450	2.323±.009	2.218±.013
475	2.301±.009	2.205±.011
500	2.284±.009	2.194±.010
525	2.270±.009	2.186±.010
550	2.259±.009	2.178±.012
575	2.250±.009	2.173±.012
600	2.242±.009	2.169±.013
625	2.236±.009	2.164±.014
650	2.230±.009	2.161±.018
675	2.226±.009	2.158±.015
700	2.221±.009	2.156±.015

Table 7.2: Ordinary (n_o) and extraordinary (n_e) refractive index of $PbWO_4$ at different wavelengths [bac97a]

7.3 The scintillation mechanism

$PbWO_4$ is known to have a complex emission spectrum consisting of several different emission bands.

blue (420 nm) The blue emission is caused by regular $(WO_4)^{2-}$ lattice centers [lum98]. It is very fast and not polarized.

green (480–520 nm) There are two independent green emission bands, which are both polarized. They are related to two types of non–equivalent (WO_3+F) defect centers, which appear dependent on oxygen non–stoichiometry and accidental impurities [kor96]. These centers consist of a WO_3 defect group, which is created by an oxygen vacancy in the first co–ordinating sphere of an W^{6+} ion, and a nearby F centre composed of two electrons in an oxygen vacancy. Apart from the (WO_3+F) centers, molybdenum contaminations of the crystal lead to the formation of $(MoO_4)^{2-}$ groups, which show a slow emission at a wavelength of 520 nm [lum98].

red The red emission is of significantly less importance compared to the blue and green emission bands. It is caused by complex defects based on heterovalent Pb^{3+} ions. These defects are created by tungsten deficiency in the crystal [lec94] and depend strongly on the purity and stoichiometry of the raw crystal material and the growth conditions [nik95].

The emission of Pb^{2+} ions in the uv spectral region, which exists in other Pb–based crystals, has not been observed for $PbWO_4$. This leads to the conclusion that scintillation in $PbWO_4$ arises due to sensitization of the emission centers mentioned above by energy

transfer processes from Pb^{2+} ions [lec94]. A scheme of the energy transfer processes in $PbWO_4$ scintillator is shown in Fig. 7.1.

Differences in the emission spectrum and the absolute light yield of different crystals can be explained by variable oxygen deficiencies depending on the conditions of crystal growth and fluctuations in the crystal purity [nik96].

The light yield of $PbWO_4$ shows a strong temperature dependence (Fig. 7.2). The temperature dependence is due to the fact that all emission bands are quenched at room temperature, which means that radiationless relaxation of the excited states occurs with increasing probability at rising temperature. The decay kinetics of the blue and green emission components have already been described in [loo75] using a three–level–excited–state model to explain observed temperature dependencies.

The radius of Lanthanum ions (La^{3+}) (1.15 Å) is very close to the radius of Pb^{2+} (1.20 Å) [kob97]. A doping of $PbWO_4$ crystals in the melt with Lanthanum significantly improves the characteristics of the crystals. The transmission in the short wavelength region is improved and the decay time is shortened.

Measurements of scintillation spectra of $PbWO_4$ crystals are described in section 8.4. The scintillation spectra of all measured crystals are shown in appendix B.

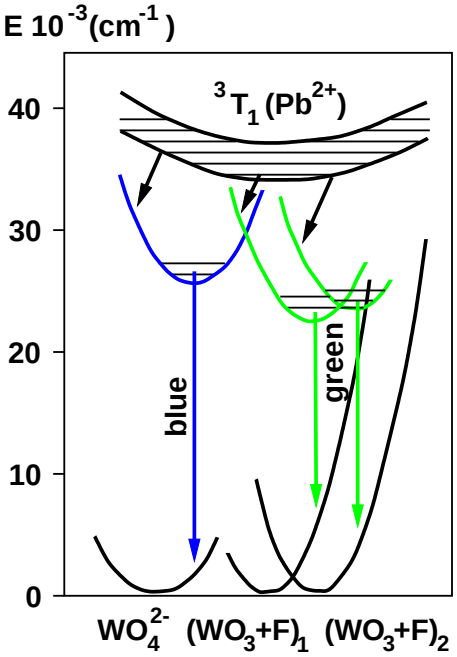

Figure 7.1: Scheme of energy transfer processes in $PbWO_4$ scintillator [lec94].

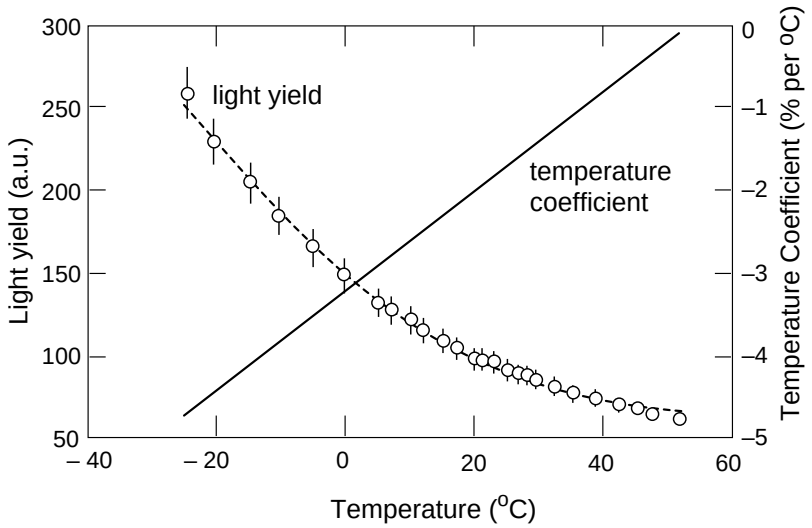

Figure 7.2: The temperature dependence of the light yield of $PbWO_4$ together with the temperature coefficient of the light yield [cms97].

Chapter 8

Bench tests of $PbWO_4$ crystals

Several bench tests were performed on two batches of $PbWO_4$ crystals [joh97, gen98a, gen99, hol99]. They were produced by BTCP, Bogoroditsk, Russia. The first batch of 10 crystals was delivered in summer 1995. The second batch, consisting of 20 crystals, was delivered in November 1997. The crystals are referred to as "1995 crystals" and "1997 crystals", respectively. The quality of the crystals has increased significantly from 1995 to 1997 due to improvements in the growth process (stoichiometric ratio of the elements, removal of impurities, doping) and post-growth annealing [cms97].

8.1 Transmission measurements

The absolute transmission $T(\lambda)$ of a sample, measured with an optical setup, is in general dependent on the wavelength λ and the sample thickness d. It is given by the product of the intrinsic transmission $T_{intr}(\lambda, d)$ of the sample, also called transmittance, and the Fresnel transmission $T_{Fresnel}(\lambda)$, which takes into account light losses at the sample surfaces due to Fresnel reflection:

$$T(\lambda, d) = T_{intr}(\lambda, d) \cdot T_{Fresnel}(\lambda) \tag{8.1}$$

$T_{Fresnel}(\lambda)$, which can be calculated according to Eq.(8.6), hereby gives an upper bound of the absolute transmission. Even if the intrinsic transmission is $T_{intr} = 1$, the absolute transmission cannot exceed the Fresnel transmission.

The absorption coefficient $\mu(\lambda)$ describes the light attenuation in a specific material independent of the sample thickness. It can be calculated from the intrinsic transmission according to

$$\mu(\lambda) = -\frac{1}{d} \ln T_{intr}(\lambda, d) \tag{8.2}$$

It is usually difficult to obtain the absorption coefficient from a transmission measurement because of the surface effects.

Both transmission measurement setups described in this thesis use the same principle of measurement. The setup consists of a sample channel where the measurement light traverses the sample, and a reference channel, where the light reaches the light detector

unaffected. The latter is used to remove variations in the light source or light detector performance. Shutters are used to switch between the channels. The pedestal of the readout chain, which causes an offset of the measurement signal, can be determined by a measurement with both shutters closed.

A set of measurements thus consists of three parts, a measurement of the light intensity in the sample channel I_S and in the reference channel I_R as well as a pedestal measurement I_0.

In addition, an independent measurement is performed, denoted by the index "100%", where the sample channel is left empty to determine the maximum amount of light available in the setup. This serves for a normalization of the measurements.

From the measured light intensities, the absolute transmission of the sample with the thickness d is calculated to

$$T(\lambda, d) = \left(\frac{I_S(\lambda) - I_0}{I_R(\lambda) - I_0}\right) \cdot \left(\frac{I_S^{100\%}(\lambda) - I_0^{100\%}}{I_R^{100\%}(\lambda) - I_0^{100\%}}\right)^{-1} \tag{8.3}$$

8.1.1 Calculation of Fresnel losses

A light ray traversing the interface between two materials with different refractive indices n_1 and n_2 will suffer from attenuation due to losses by Fresnel reflection. The Fresnel loss for perpendicular incidence of the light upon the surface is described by the reflection coefficient given by the formula

$$R_{Fresnel} = \left(\frac{1-n}{1+n}\right)^2 \tag{8.4}$$

Here, $n = n_1/n_2$ denotes the relative refractive index. The Fresnel transmission is calculated to

$$T_{Fresnel} = 1 - R_{Fresnel} \tag{8.5}$$

In the case of transmission measurements of crystals, the fact that the measuring light ray traverses the air/crystal interface twice, when entering and leaving the crystal, must be taken into account. Hence, also taking into account the wavelength dependence of the refractive index, the Fresnel transmission is obtained by the formula

$$T_{Fresnel}(\lambda) = \left[1 - \left(\frac{1-n(\lambda)}{1+n(\lambda)}\right)^2\right]^2 \tag{8.6}$$

8.1.2 Transverse transmission

Measurements of the transverse transmissions of $PbWO_4$ crystals through 20 or 23.8 mm were performed using the modified Beckman ACTA V spectrophotometer shown in Fig. 8.1. This apparatus can be used for transmission measurements in a wavelength range from 190 to 800 nm. It is equipped with two light sources, a deuterium lamp for the uv region and a tungsten lamp for the visible part of the spectrum. An adjustable

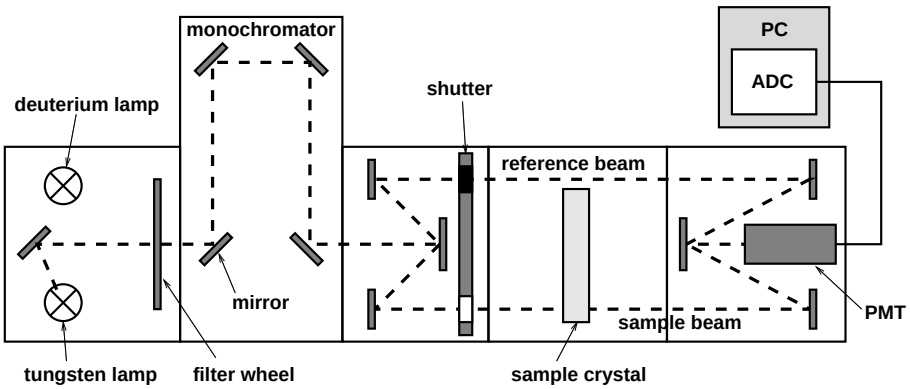

Figure 8.1: Overview of the Beckman ACTA V spectrophotometer.

mirror directs the light of the appropriate lamp to the monochromator which transmits only the desired wavelength. A filter wheel equipped with several colour filters serves for a modulation of the light intensity as well as the suppression of higher orders of diffraction. The light beam is now split in two fractions. The first fraction, referred to as the sample beam, is led through the sample chamber such that it traverses the sample. The second fraction, called the reference beam, traverses the sample chamber unaffected. A shutter allows to choose between the two beams. Both beams are then focused to a PMT where the light intensities are measured. The PMT is read out by a PC equipped with an ADC card which also controls the setup using stepping motors. The control program running under the operating system Linux was custom–made [sch94].

A special support was constructed which allows to put full–size $PbWO_4$ crystals into the sample chamber. The measurements proceed as described in section 8.1. Measurements of the transverse crystal transmission are described in section 8.4.3 in order to examine an observed dependence of the scintillation light yield on the azimuthal orientation of the crystal and in section 9.3 to determine the radiation damage of irradiated crystals.

8.1.3 Longitudinal transmission

The intrinsic absorption length of $PbWO_4$ crystals was found to be significantly larger than 1 m [cms97]. Hence, the measurement of the transverse crystal transmission where the light beam only traverses 23.8 mm of crystal material reveals little information about the intrinsic crystal transmission because the observed absorption effects are very small. Due to this fact, it is desirable to measure the crystal transmission in the longitudinal direction. Here, the measuring light beam traverses 20 cm of crystal material, resulting in a much more accurate measurement of absorption effects.

The sample chamber of the Beckman spectrophotometer described in the previous section is too small to contain a full size crystal in longitudinal direction. In addition, the light beam is too divergent for the measurement of a long sample. A special setup was built for the measurement of the longitudinal transmissions of the crystals, shown in Fig. 8.2. See [thi99] for a more detailed description.

A xenon lamp serves as light source. The light is led by an optical fiber to a monochromator, where the appropriate wavelength is adjusted, and then divided into a sample

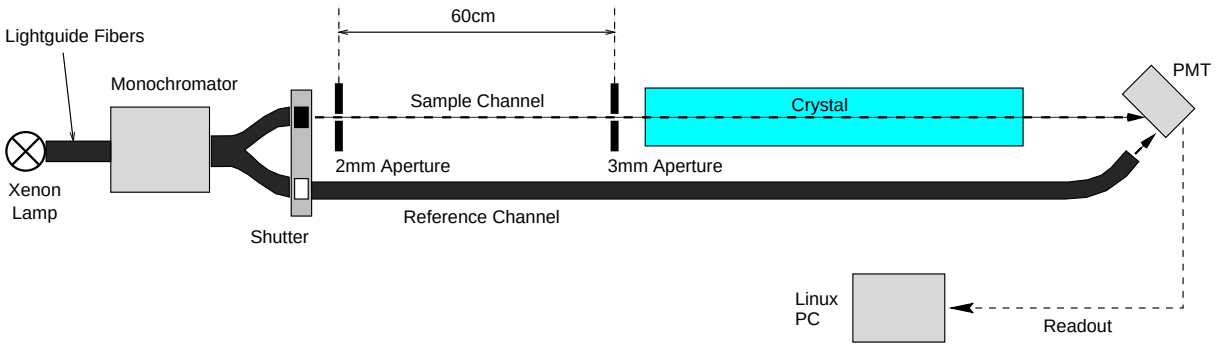

Figure 8.2: The setup used for longitudinal transmission measurements of the crystals

channel and a reference channel. The reference channel light reaches the PMT directly.

Before the sample channel light reaches the crystal, it traverses two apertures of 2 mm respectively 3 mm diameter with a distance of 60 cm. This ensures a collimated beam travelling through the crystal without reflections at the crystal side faces. Finally, the light beam reaches the PMT, where it is detected and the intensity converted into an electric signal. The beam diameter measured on the PMT front face amounts to 6 mm. The control of the setup using stepping motors as well as the readout of the PMT using an ADC card is performed by a PC. The custom–made measurement program is running under the operating system Linux [mey95].

The longitudinal transmission spectra of all twenty crystals were measured according to the procedure described in section 8.1 [thi99]. The resulting transmission curves are shown in appendix C. In the plots the Fresnel transmission is also depicted, which is calculated according to Eq.(8.6) and denotes the highest possible transmission limited by losses due to Fresnel reflections. The values for the refractive index are taken from Tab. 7.2.

The crystal transmission curves are normalized to the Fresnel transmission for wavelengths above 600 nm, assuming a very good intrinsic crystal transmission in this spectral area. This assumption was confirmed by previous measurements [zhu96], where no significant absorption bands were found for wavelengths longer than 500 nm. The normalization was performed because the measured transmission curves were found to be shifted upwards or downwards by an absolute intensity offset varying from crystal to crystal and possibly caused by a normalization problem of the setup. It was found that the offset depends to a certain extent on the azimuthal orientation of the crystal relatively to the setup, demonstrating possible surface effects or crystal impurities. Additional uncertainties in the transmission measurements arise because of the birefringent nature of $PbWO_4$. Some of the transmission curves before the normalization even exceeded the Fresnel transmission curve in parts of the spectrum.

The observed spectral shapes are formed by several absorption bands. Four different absorption centers have been identified:

Pb^{3+} centre: This centre is formed by a Pb^{2+} ion which captured a hole. These centres absorb light at a wavelength of 340–360 nm [lum98, bac97b].

$(WO_4)^-$ or O^- centre: This centre is composed of a $(WO_4)^{2-}$ group which captured a hole, causing absorption at 410–430 nm [nik96, lum98, bac97b].

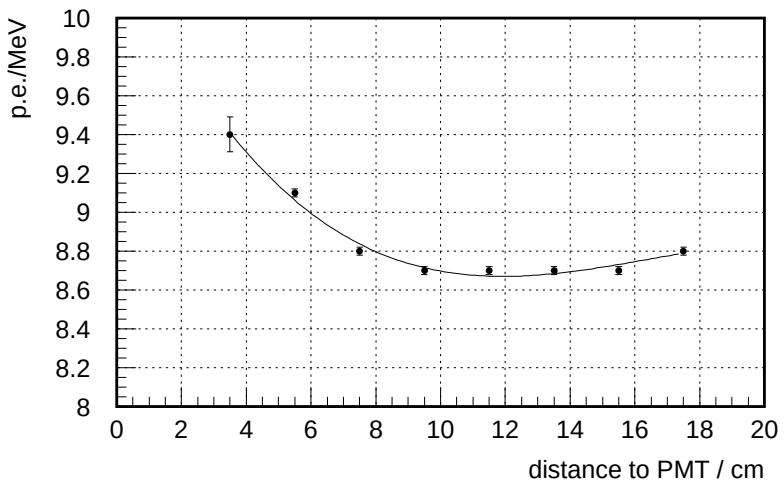

Figure 8.3: The light yield of crystal 388 in dependence of the distance from the exciting ^{60}Co source to the PMT.

F centre: This centre consists of an oxygen vacancy which captured two electrons, absorbing at 520–575 nm [lum98, bac97b].

F$^+$ centre: This centre is formed by an oxygen vacancy which captured one electron. It absorbs light at 670–740 nm [lum98, bac97b].

The contributions of each absorption band vary from crystal to crystal and are dependent on the conditions during crystal growth, such as stoichiometry and impurities.

The intrinsic transmission of $PbWO_4$ crystals can be significantly improved in the short wavelength region by doping with lanthanum. The La^{3+} ions introduce additional charge into the Pb sublattice. This diminishes the concentration of Pb^{3+} and O^- hole centers and thus causes a lower absorption in the appropriate spectral regions [lum98].

8.2 Measurements of the intrinsic light yield

The Crystal BPC is a homogenous calorimeter. Due to this fact, its energy resolution is expected to be dominated by photoelectron statistics. To attain the required energy resolution of $5\%/\sqrt{\mathrm{E/GeV}}$, at least 400 photoelectrons (p.e.) from the photomultiplier (PMT) cathode per GeV of energy deposit in the crystal, the stochastic minimum, are necessary. Hence, it is important that the intrinsic light yield of the $PbWO_4$ crystals is sufficient.

The light yield measurements were performed in November, 1997 at CERN using a setup constructed by CMS. A more detailed description of the measurement procedure is given in [mor98]. The crystal under test is wrapped in Tyvek to optimize the light yield, leaving

only the front face unwrapped. The front face is coupled to a PMT (Philips XP2262B) using optical grease. A small ^{60}Co source is moved to a defined position relative to the crystal. The emitted photons produce scintillation light in the crystal which is detected by the PMT and converted into an electrical signal read out by a multi channel analyser. For each crystal, several measurements are performed at different longitudinal source positions, beginning with a distance of 3.5 cm from the PMT. Because of the temperature dependence of the light yield of $PbWO_4$, the results are corrected for temperature changes.

All 1997 crystals and two of the 1995 crystals were measured. The results of the measurements with a distance of 15.5 cm of the source to the PMT are shown in Tab. 8.1. The mean value of the light yields of the best 16 crystals, which will be used for the construction of the Crystal BPC, and of all crystals are shown. Evidently, the light yield of the 1997 crystals, compared to the 1995 crystals, has almost doubled.

For comparison, also the results of light yield measurements by the crystal manufacturer at Bogoroditsk are shown. Both results differ by a factor of about 1.4, which is due to differences of the measurement setups, for example the use of PMTs with different photocathode sensitivities.

In Fig. 8.3, the light yield of crystal 388 in dependence of the distance of the ^{60}Co source to the PMT is shown. The measured light yield reaches its maximum if the source is located closest to the PMT. At larger distances, the light yield decreases due to light absorption in the crystal. The observed decrease of 7.4% over a distance of 8 cm corresponds to an absorption coefficient of about $0.01\,cm^{-1}$ and an attenuation length of 1 m. This value is smaller than the results of other measurements, which result in attenuation lengths of 2–3 m [cms97]. Approaching the rear crystal end opposite to the PMT, a small increase of the light yield is observed. This may give evidence for longitudinal non–uniformities of the crystal structure.

8.3 Optimization of the light collection efficiency

The optical components of the Crystal BPC such as crystals, lightguides and PMTs are subject to several mechanical constaints (overall length, crystal size, PMT type) which limit the light collection efficiency of the Crystal BPC readout. Hence, the efficiency of light collection of the Crystal BPC is far from the optimum which is achieved using a PMT with a large photocathode which covers the whole crystal front face, as is described in the previous section. In order to gain a sufficient number of photoelectrons even under these non–optimal conditions, the light collection efficiency of the optical components of the Crystal BPC has to be studied and optimized.

8.3.1 Optimization of the optical couplings

The optical readout of each Crystal BPC channel consists of a small acrylic lightguide (GS218, uv transparent) of 10 mm length which connects the rear face of the crystal to the PMT photocathode (8 mm diameter). The PMT cannot be coupled directly to the crystal because a magnetic shielding between PMT and crystal is required. Consequently,

crystal	LY_{CERN} in p.e./MeV	$LY_{Bogoroditsk}$ in p.e./MeV	factor
466	13.0	18.9	1.45
467	12.5	18.7	1.50
464	12.2	17.4	1.43
469	12.0	17.0	1.42
465	10.4	12.0	1.15
456	10.2	13.9	1.36
470	9.7	13.4	1.38
435	9.6	12.5	1.30
377	9.5	12.9	1.36
393	8.8	12.0	1.36
468	8.8	12.0	1.36
388	8.7	12.8	1.47
439	8.6	12.0	1.40
422	8.4	12.6	1.50
440	8.4	12.0	1.43
471	8.1	12.0	1.48
434	7.6	12.3	1.62
379	7.1	12.0	1.69
458	7.1	12.0	1.69
461	7.1	12.0	1.69
Mean value (16)	9.9	13.9	1.40
Mean value (20)	9.4	13.5	1.44
1202 (old)	4.9		
1209 (old)	4.7		

Table 8.1: Results of the light yield measurements at CERN. All twenty 1997 crystals as well as two 1995 crystals were tested [mor98]. The distance between the source and the PMT is 15.5 cm. For comparison, also the results of light yield measurements by the crystal manufacturer at Bogoroditsk are shown.

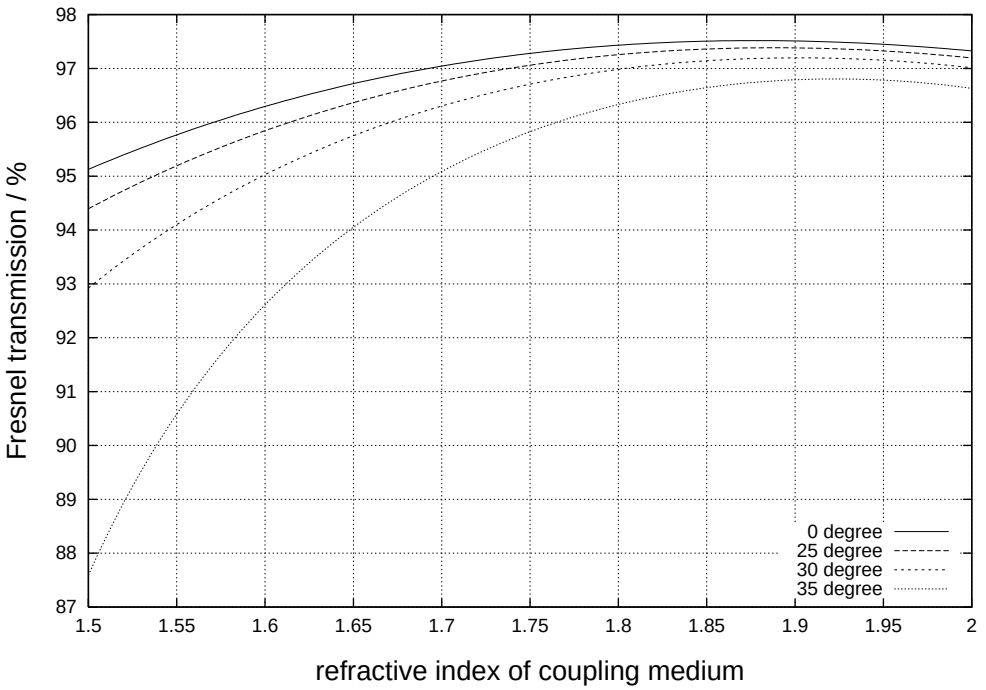

Figure 8.4: Fresnel transmission of the crystal–lightguide interface in dependence of the refractive index of the coupling medium for different angles of light incidence.

scintillation light produced in the crystal must first traverse the crystal–lightguide interface and then the lightguide–PMT interface, degrading the light intensity due to Fresnel reflection losses at each traversal.

A study of the influence of different coupling media on the optical transmission of the crystal–lightguide interface was performed. See [thi99] for a more detailed description. The calculations are performed for light at a wavelength of 420 nm, which is the emission peak of the $PbWO_4$ crystals. The refractive indices of $PbWO_4$ and GS218 at this wavelength amount to $n_{PWO} = 2.35$ and $n_{GS218} \approx 1.5$.

The Fresnel transmission of the crystal–lightguide interface for normal light incidence, assuming a coupling medium with refractive index n_c in between, is given by [jac82]

$$T_{Fresnel} = \frac{16 \cdot n_{PWO} \cdot n_{GS218} \cdot n_c^2}{[(n_{PWO} + n_c) \cdot (n_c + n_{GS218})]^2} \tag{8.7}$$

The transmission reaches its maximum if the refractive index of the coupling medium is given by

$$n_c = \sqrt{n_{PWO} \cdot n_{GS218}} \approx 1.88 \tag{8.8}$$

The results of simulations for angles of light incidence of $0°, 25°, 30°$ and $35°$ are shown in Fig. 8.4. The maximum of transmission is reached at the value of n_c calculated above. The curves clearly show the transmission losses for refractive indices varying from the optimal value, which become even more emphasized for non–perpendicular light incidence.

As coupling medium optical glue Cargille Meltmount Mounting Media with the highest available refractive index of $n_c = 1.7$ was chosen. The improvement of the optical transmission with respect to conventional optical grease with a refractive index of about 1.5

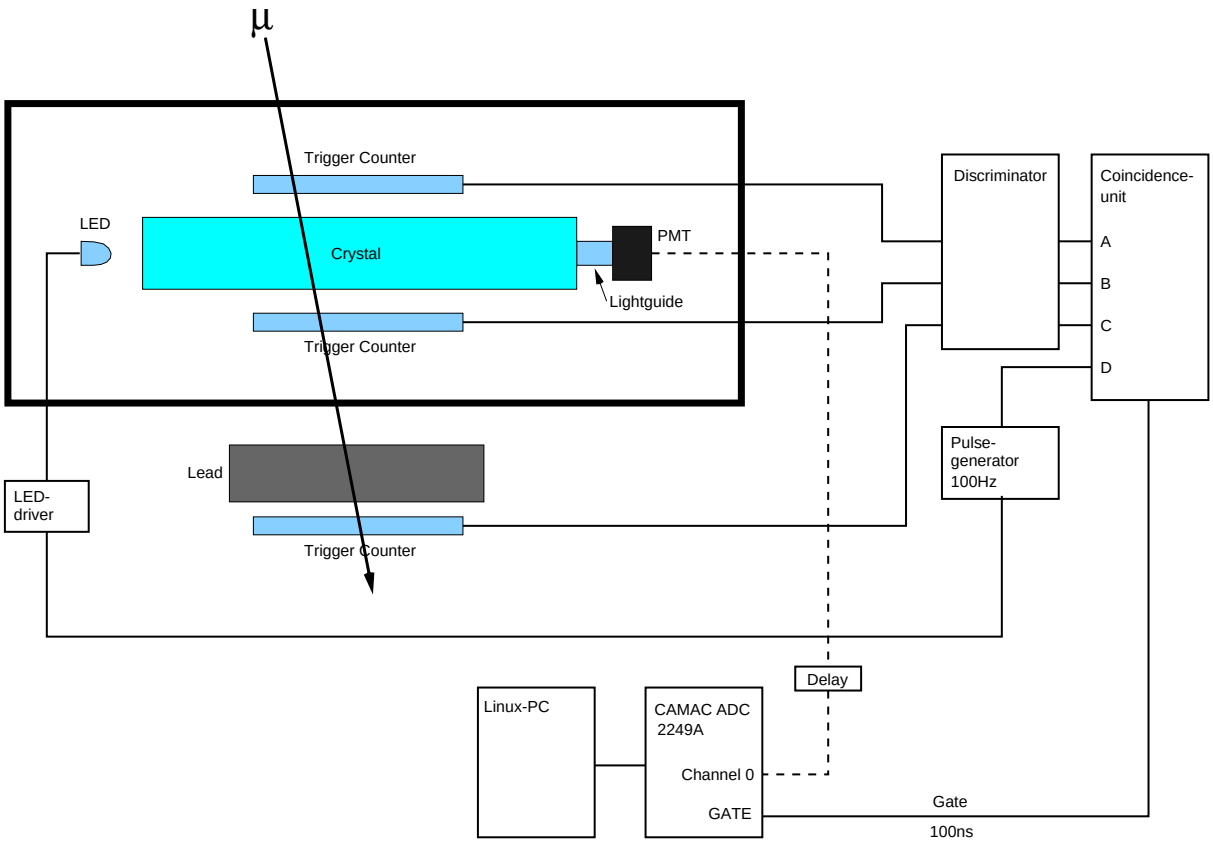

Figure 8.5: The single crystal setup used for studies of the light collection optics.

was estimated to 3.4%. This result was confirmed by transmission measurements using a Beckman spectrophotometer [thi99].

8.3.2 Measurements with single crystals

Further studies of the light collection optics of the Crystal BPC were performed using a single crystal setup. The purpose was to simulate the spatial constraints in the Crystal BPC, but to render possible the installation of different lightguides and different crystal wrappings in order to measure the light yields of different arrangements.

The single crystal setup is shown in Fig. 8.5. The crystal is placed horizontally in front of a PMT R5600. The lightguide connecting both is exchangable, and it is possible to install different crystal wrappings. The crystal is excited by cosmic muons. The incidence of a muon is detected by two trigger counters installed above and under the crystal, respectively. A third trigger counter is placed under the setup covered by a lead shielding of 10 cm thickness. A muon which is not minimal ionizing is absorbed in the lead shielding and does not show a signal in the third trigger counter. Hence, if the three trigger counters are switched to coincidence, it is ensured that a trigger pulse is released only in case of minimal ionizing particles (MIPs).

A trigger pulse opens a gate with a length of 100 ns during which the analog–to–digital converter (ADC) integrates over the charge delivered by the PMT. The result is digitized

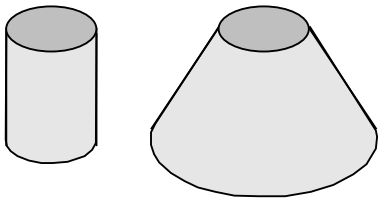

Figure 8.6: Cylindrical (left) and conical (right) lightguide tested to improve the light yield.

and read out by the PC which controls the setup. A detailed description of the readout system can be found in [hen99].

A calibration of the ADC in units of photoelectrons can be provided using LED flashes, see appendix E.

Studies using different lightguide shapes: The cross–sections of the crystals ($23.8 \times 23.8\,mm^2 = 566\,mm^2$) and the area of the PMTs' photocathodes (8 mm diameter, $50\,mm^2$) show a considerable disproportion. In order to provide a smooth transition between crystal and PMT, a conical shaped lightguide was built with a length of 10 mm and a diameter of 20 mm at the side attached to the crystal and 8 mm at the side connected to the PMT. The lightguide shape is shown in Fig. 8.6.

In Tab. 8.2 the measured light yield is compared to the light yield obtained with a cylindrical lightguide with a length of 10 mm and a diameter of 8 mm. The cylindrical lightguide shows a slightly superior result, which confirms results of light collection simulations using a ray–tracing monte carlo [dav97]. Most of the photons are lost through the sides of the conical lightguide. Consequently, the cylindrical lightguide shape was chosen for the construction of the Crystal BPC.

crystal	LG shape	PMT	light yield in p.e. per MIP
458 (7.1 p.e./MeV)	cylindrical ø8 mm × 10 mm	R5600	8.5 ± 0.2
	conical ø20/8 mm × 10 mm	R5600	7.0 ± 0.2

Table 8.2: Results of light yield measurements using differently shaped lightguides (LG) in a single crystal setup. The results cannot be compared directly to the results in Tab. 8.3 because different crystals were used. One MIP corresponds to an energy deposition of 25 MeV [wol97].

Studies using different wrappings: Scintillation light is produced isotropicly inside a crystal. A fraction of the light reaches the lightguide and the PMT after many reflections off the crystal faces. Another considerable fraction of the light leaves the crystal without being reflected and is thus lost. To reduce these losses, the crystal can be wrapped with different materials to reflect the escaping light.

Several measurements were performed using different wrappings, aluminium foil as mirror and Tyvek as diffuse reflector, for the crystal's four side faces and two front faces as well as the lightguide. The results are shown in Tab. 8.3. The best result, a light yield of

26 ± 0.5 p.e. per MIP corresponding to 1040 p.e./GeV, was achieved wrapping the crystal with Tyvek and the lightguide with aluminium foil.

Test of a new PMT type: In 1998, Hamamatsu released a new PMT (R7400U) with the same outer dimensions as the R5600U–03. Due to an improved dynode design, the p.e. collection efficiency is increased by 30% compared to the R5600U–03. Measurements under optimal conditions using this PMT show a p.e. yield of 31 ± 0.4 p.e. per MIP (Tab. 8.3) corresponding to about 1240 p.e./GeV. This would result in an even better energy resolution of the Crystal BPC as compared to the initial calorimeter design.

crystal	crystal wrapping		LG wrapping	PMT	light yield
	side faces	front faces			in p.e. per MIP
466 (13.0 p.e./MeV)	aluminium	aluminium	—	R5600	16 ± 0.3
	aluminium	Tyvek	—	R5600	18 ± 0.5
	Tyvek	Tyvek	—	R5600	22 ± 0.5
	Tyvek	Tyvek	aluminium	R5600	26 ± 0.5
	Tyvek	Tyvek	aluminium	R7400	31 ± 0.4

Table 8.3: Results of the studies of the effects of different wrappings on the light yield in a single crystal setup.

8.4 Measurements of the scintillation spectra of $PbWO_4$ crystals

It is known that the emission spectrum of $PbWO_4$ is rather complex and consists of several components whose relative contributions may differ from crystal to crystal [lum98]. This is discussed further in section 7.3.

In order to investigate the scintillation spectra of the crystals which were foreseen for the construction of the Crystal BPC, appropriate measurements were performed exciting the crystals with a ^{60}Co source. In section 9.5 the effect of irradiation on the scintillation spectra of $PbWO_4$ crystals is investigated.

8.4.1 The measurement setup

The aim of these measurements is to obtain the scintillation spectra of $PbWO_4$ crystals. Hence, the crystal light yield has to be measured in dependence of the wavelength, using a monochromator. This implies several problems. First, the intrinsic light yield of $PbWO_4$ crystals is rather low. Second, the scintillation light has to traverse the monochromator, which will cause further light losses. Due to these reasons, the setup used for these measurements had to be optimized for a good light collection. The setup is shown in Fig. 8.7.

The crystal is placed as close as possible to the entrance slit of the monochromator. It is excited to produce scintillation light by a ^{60}Co source (74 MBq, 2 mCi) which is located at the back face of the crystal opposite to the monochromator entrance slit. To optimize the light output of the crystal, it is completely wrapped with Tyvek, only leaving open a small area for the readout. A high–sensitive side window PMT of the type Hamamatsu 931A is installed directly behind the monochromator exit slit. Later, this PMT was exchanged by a PMT Hamamatsu R928 with an improved spectral range. The PMT signal is read out by a PC equipped with an ADC card of the type PC–Labcard 812PG, which contains an on–board amplifier. Switching the amplifier to maximum amplification, the dynamic range of the ADC is chosen to $0\,\mathrm{V} \leq U_{input} \leq 0.3\,\mathrm{V}$. This renders possible a measurement of the scintillation signal, which amounts to about 10 mV at maximum after pedestal subtraction, with a resolution of 0.15 mV. The PC also controls the monochromator using a stepping motor. Both control and readout are performed by a custom–made measurement program under the operating system Linux [mey95].

Optical devices, such as light sources, monochromators, lightguides, or PMTs, show a wavelength dependence of their optical behaviour, referred to as the apparatus function. The apparatus function of a measurement setup is given by the folding of the apparatus functions of all setup components. If the setup serves for the measurement of a spectrum S_{input}, the shape of the spectrum is changed according to the apparatus function A of the setup, and the spectrum S_{meas} obtained in the measurement is given by the folding

$$S_{meas} = S_{input} \otimes A \tag{8.9}$$

The measured spectrum must hence be corrected for the apparatus function of the setup, which can be obtained by measuring a known spectrum. In this case, S_{input} and S_{meas} are known, and the apparatus function can be calculated [dan96, gen96].

For the setup described above, the apparatus function was determined using the emission spectrum of a special tungsten lamp which can be calculated. The apparatus functions of the setup equipped with either of the two mentioned PMTs are shown in Fig. 8.8. The measured crystal spectra were corrected using the appropriate function.

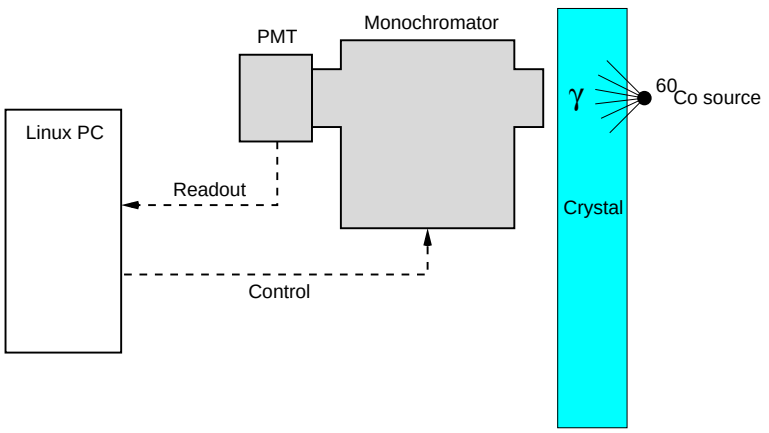

Figure 8.7: The setup used for measurements of $PbWO_4$ scintillation spectra.

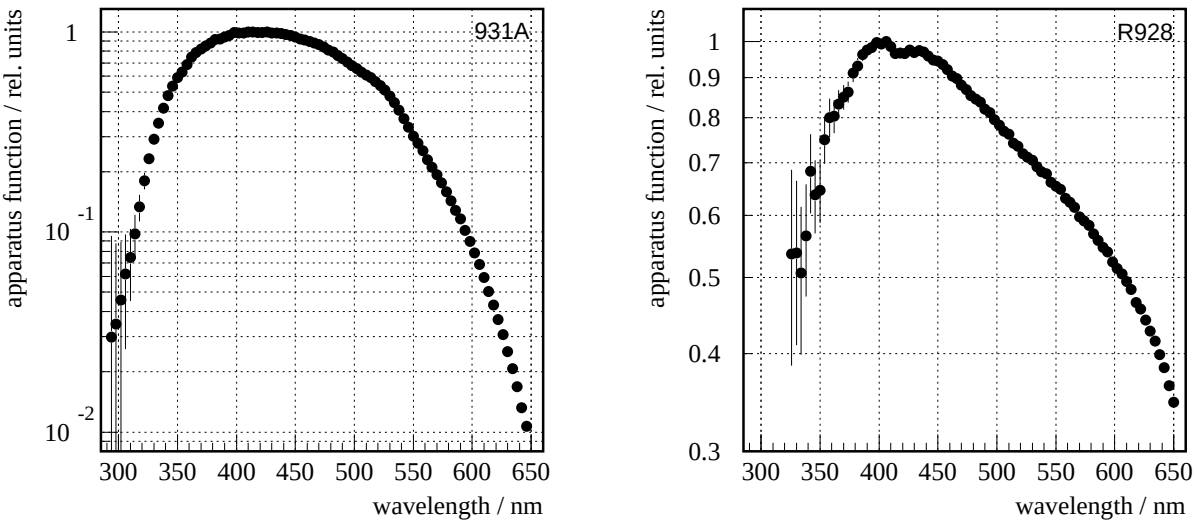

Figure 8.8: Apparatus functions of the scintillation spectrum measurement setup, equipped with PMTs Hamamatsu 931A (left) respectively R928 (right)

8.4.2 Typical scintillation spectra

The scintillation spectra of all 1997 crystals as well as of two 1995 crystals were measured using the setup described above. Typical spectra which are characteristic for the two types of crystal are shown in Fig. 8.9. Both spectra are normalized to unity. The two types of crystal clearly show a different emission spectrum. The 1995 crystals show an emission maximum at a wavelength of about 500 nm. This may explain the presence of a slow scintillation light component which was observed for these crystals (see section 8.5). According to [gen98b, lum98], the slow component can be identified with a green emission band.

The 1997 crystals reach their maximum of emission at a wavelength of 420 nm. This can be correlated with the La–doping applied to these crystals, which suppresses the slow green component. Nevertheless, there are still contributions of emission bands in the green and red spectral area.

All measured spectra are shown in appendix B. These spectra are not normalized. It is clearly visible that for the 1997 crystals the scintillation light yield depends on the azimuthal orientation of the crystals relatively to the setup. This effect is further investigated in the next section. See Fig. 8.10 for the orientation scheme of the crystals.

8.4.3 Dependence on the azimuthal orientation

As already mentioned, the scintillation light yield of the 1997 crystals depends on the azimuthal orientation of the crystals relatively to the setup. This effect is not observed with the 1995 crystals. In order to examine this effect, additional measurements on the 1997 crystals 466 and 388 were performed.

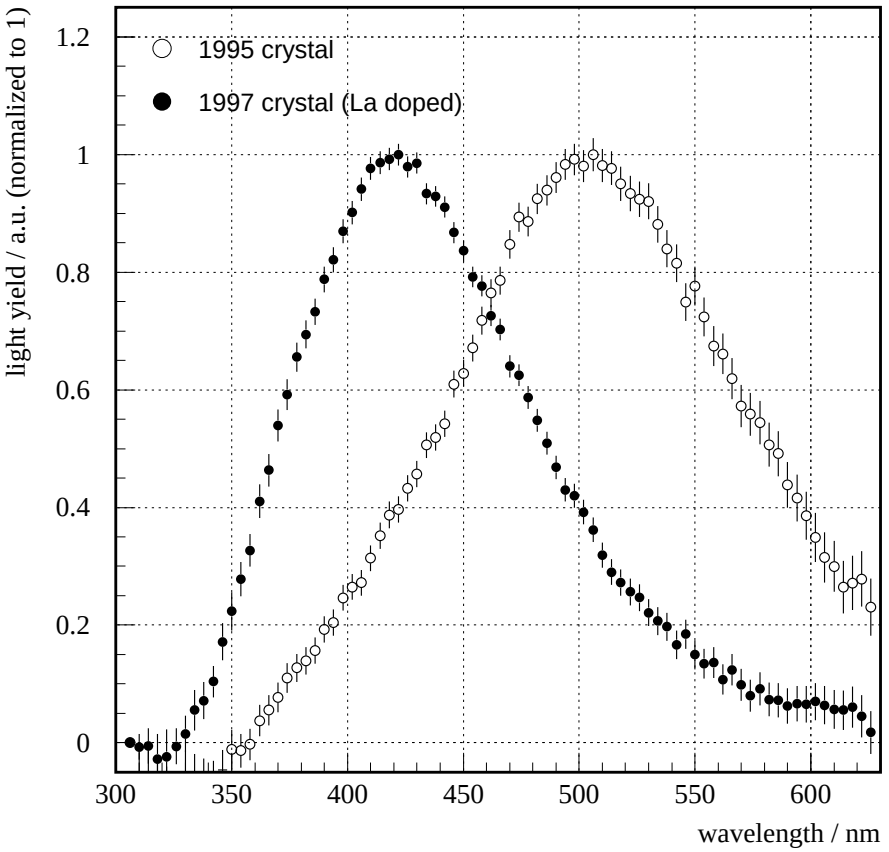

Figure 8.9: Typical scintillation spectra of 1995 and 1997 crystals. The spectra are normalized to 1. Whereas the emission maximum of the 1995 crystal is around 500 nm, emission of the 1997 crystal peaks around 420 nm.

First, measurements of the emission spectra were performed using all eight possible orientations of the crystals relative to the setup. An explanation of the orientation scheme of the crystals is given in Fig. 8.10. The results are shown in the upper plots of Fig. 8.11. There are exactly two groups of curves, equally shaped, but shifted by a factor of about 1.5. Obviously, the measured light yields are equal if the crystal label is oriented upwards or downwards. In the other cases, the other possible value for the light yield is obtained.

In addition, the crystals' transverse transmissions were measured in the Beckman spectrophotometer. The same orientation scheme as in the emission spectrum measurements was applied. The results can be observed in the middle plots of Fig. 8.11. Again, there are two groups of curves, indicating different transmissions in the two transverse directions. The lower transmission values for the orientations P2 and P4 of crystal 466 are caused by a slightly dirty crystal surface in the area of the Beckman beam spot.

In the bottom plots of Fig. 8.11, the clear correlation between the two measurements is shown. Comparing the two azimuthal orientations, a difference in transmission of about 3% and a difference in measured light yield of about 30% is obtained. This may be explained by the birefringent nature of the crystals, which affects light traversing different crystal surfaces in a different way. According to [chi98], the intensity of the

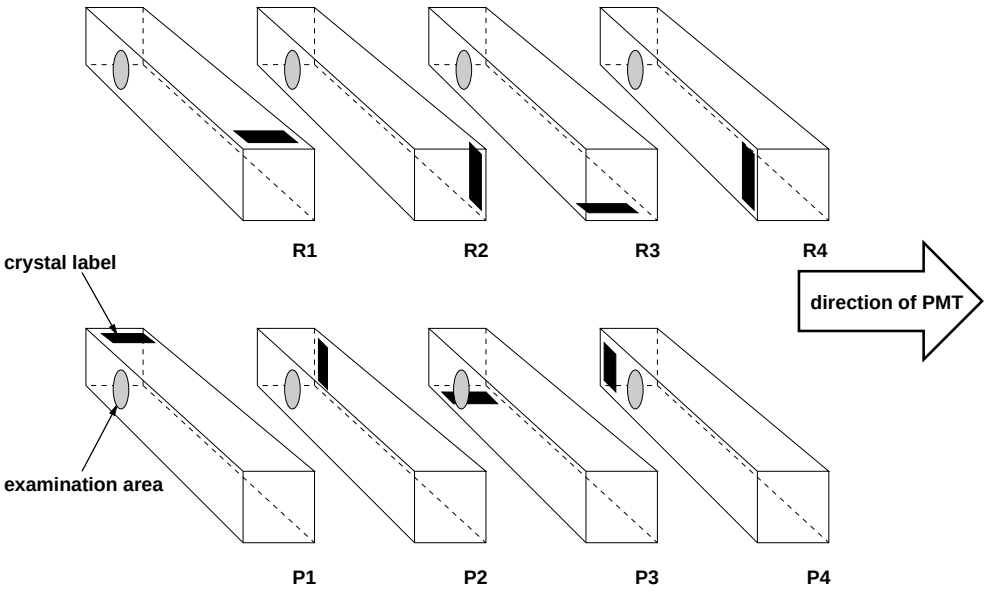

Figure 8.10: Orientation scheme of the crystals in the scintillation spectrum measurement setup and in the Beckman spectrophotometer for transverse transmission measurements

Fresnel reflections on the crystal surfaces depends on the orientation of the optical axis of the measured crystal and on the direction and polarization of the light ray. In addition, the intrinsic absorption of $PbWO_4$ crystals was found to be partially polarization dependent. Both effects may contribute to the observations described above.

The labels of the crystals, on which the orientation scheme is based, were put onto the crystals incidentally. Hence, there is a fraction of crystals where even numbers denote the direction of good transmission, whereas in case of the other crystals this direction is denoted by odd numbers.

8.5 Decay time of the scintillation signal

$PbWO_4$ crystals of the early stage of development are known to have a rather long signal decay time [nik95]. This is due to a slow green scintillation light component. The time between two HERA bunch crossings is 96 ns. Therefore it is required that less than 5% of the signal from the BPC be generated after this time. To investigate this issue, measurements were performed at the DESY 6 GeV test beam. The crystals were read out by a PMT Hamamatsu R580. The blue and green signal components were investigated with colour filters, which have transmission maxima at 400 nm (blue) and 550 nm (green). The waveforms were recorded using a fast digital oscilloscope LeCroy 9361. For each crystal and both colour filters, a typical waveform was obtained as an average over several single waveforms. The amount of light emitted within a certain time was calculated as the integral over time of each typical waveform. The results are shown in Fig. 8.12.

The slow green component (caused by molybdenum contaminations [cms97]) of the 1995 crystal is clearly visible. After 100 ns only 80% of the light is emitted, which makes this crystal unusable for the Crystal BPC. For the 1997 crystal the slow green component

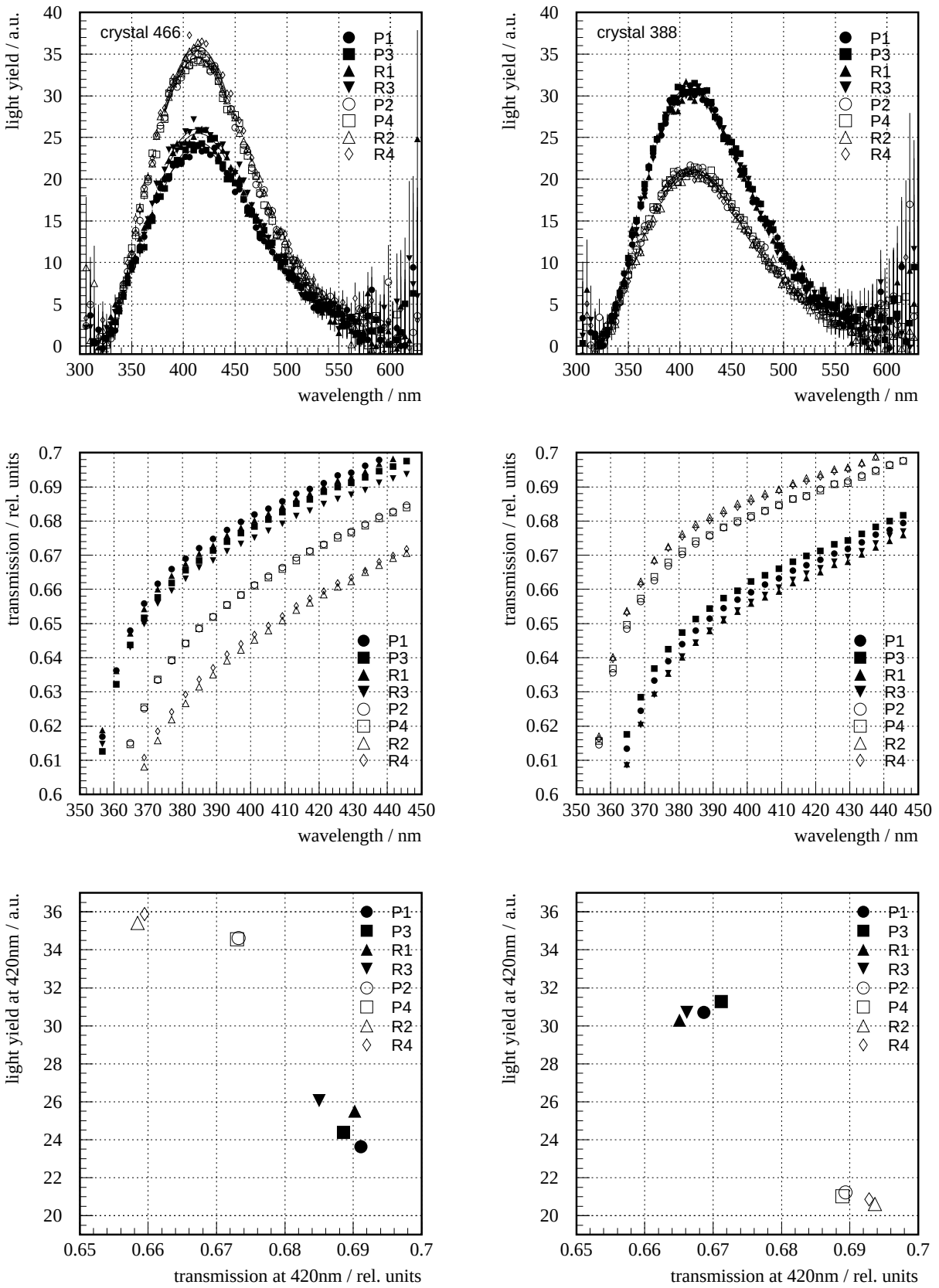

Figure 8.11: Scintillation spectra (up), transverse transmission spectra (middle) and their correlation at a wavelength of 420 nm (down) measured for crystals 466 (left) and 388 (right). A clear dependence on the azimuthal orientation of the crystal is visible.

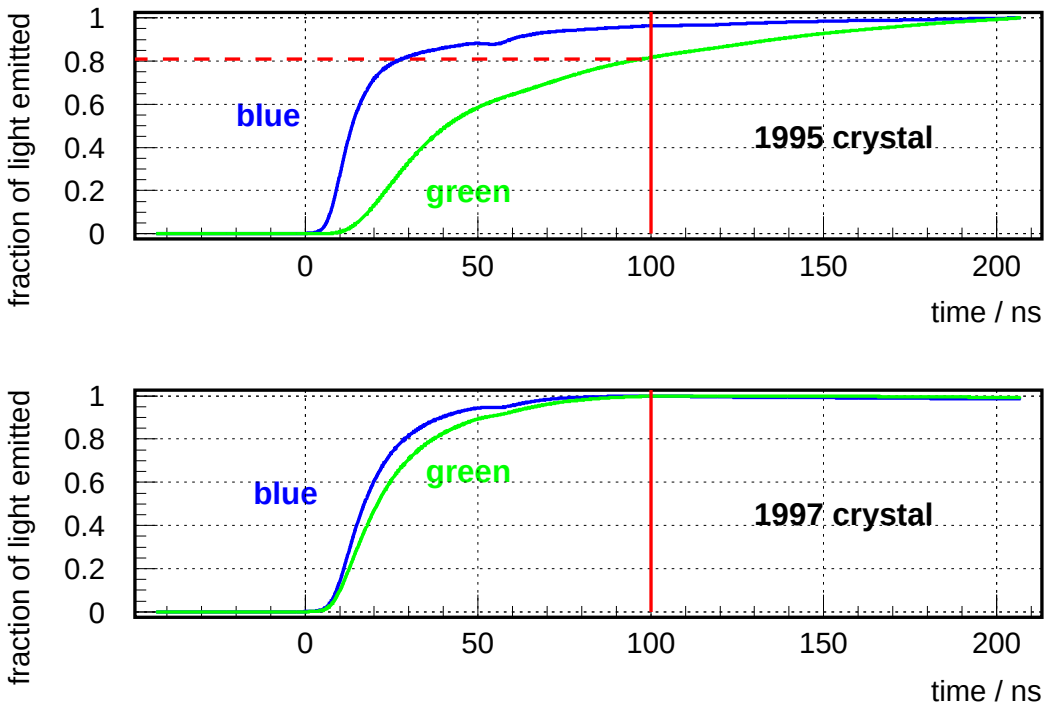

Figure 8.12: Integrated signal shapes of 1995 and 1997 crystals for blue and green components. The slow green component, seen with the 1995 crystal, is no longer observed with the 1997 crystal.

has disappeared. After 50 ns 90% and after 100 ns all of the scintillation light has been emitted. These crystals fit the requirements concerning signal decay time for the use in the Crystal BPC.

Chapter 9

Radiation damage effects of $PbWO_4$

Radiation tolerance is a major constraint of the Crystal BPC. The calorimeter will occupy a high radiation zone. The average dose rate in this region can reach several hundred Gy per month during beam–on periods. This is known both from a set of solid state diodes which monitor the radiation levels at various points of the calorimeter front face and from thermoluminescence dosimeters (TLD). The calorimeter must function and retain its calibration while being irradiated at this level.

9.1 Radiation damage processes in $PbWO_4$

The initial stages of a radiation damage in $PbWO_4$ caused by ionizing radiation consist of a three–step process [lum98, bac97b]:

1. the creation of electron–hole pairs (free carriers) by the interaction with a high energy γ
2. the separation of these electrons and holes during subsequent cooling down and diffusion processes
3. separate localisation of both electrons and holes at suitable lattice sites (traps), such as lattice distortions (dislocations, domain interfaces) and point defects (vacancies, impurity ions)

During the latter stage of the radiation damage process, the formation of metastable colour centers occurs, which cause additional absorption, the "radiation damage", in the crystal. This is caused by a local re–creation of the charge balance in the lattice. At a given dose and dose rate, the concentration of produced colour centers only depends on the concentration of lattice sites (traps) suitable for the localisation of radiation induced free carriers. The following colour centers were identified:

Pb^{3+} centre: This centre is formed by a Pb^{2+} ion which captured a hole. These centres absorb light at a wavelength of 340–360 nm [lum98, bac97b].

$(WO_4)^-$ or O^- centre: This centre is composed of a $(WO_4)^{2-}$ group which captured a hole, causing absorption at 410–430 nm [nik96, lum98, bac97b].

F centre: This centre consists of an oxygen vacancy which captured two electrons, absorbing at 520–575 nm [lum98, bac97b].

F^+ centre: This centre is formed by an oxygen vacancy which captured one electron. It absorbs light at 670–740 nm [lum98, bac97b].

The first two centers are hole centers, while the last two centers are electron centers. The hole centers play a dominant role in the radiation damage process with respect to electron centers because free hole charge carriers have a much higher mobility in the crystal lattice compared to free electrons [lum98]. The amplitude and intensity of each absorption band differ from crystal to crystal.

In $PbWO_4$ no irreversible radiation damage processes, such as the formation of Pb colloids known from PbX_2 compounds, were observed. The initial transmission of an irradiated crystal can always be restored by a heating procedure [lum98]. During this procedure, the crystal is slowly heated up to a temperature of 200°C.

The radiation damage of $PbWO_4$ also recovers at room temperature. This is a consequence of room temperature thermal annealing [zhu98]. Due to this reason, the production and the annealing of radiation damage in general compete with each other during irradiation, which causes a dose rate dependence of the radiation damage.

It was found that doping with trivalent ions, especially Lanthanum (La^{3+}), in the melt considerably improves the radiation resistance of $PbWO_4$ crystals. The radius of La^{3+} ions (1.15 Å) is very close to the radius of Pb^{2+} (1.20 Å) [kob97]. The La^{3+} ions replace divalent Pb^{2+} ions in the crystal lattice. The excess charge introduced by the La^{3+} ions reduces the concentration of sites in the lattice which are suitable for the localisation of holes created by irradiation. As a consequence, the concentration of stable and metastable hole centers decreases, and the crystal becomes more radiation–hard [lum98].

9.2 Online–Measurements of the radiation damage

9.2.1 The Online–Measurement setup

Irradiation tests of $PbWO_4$ crystals were performed at a ^{137}Cs source (150 GBq, 4 Ci). The optical transmission through the width of 23.8 mm was measured during irradiation with a mean dose rate of 1.8 Gyh^{-1}. The crystal is placed lying horizontally at a distance of 38 mm from the ^{137}Cs source (Fig. 9.1).

The setup can be equipped with one or two light emitting diodes (LEDs) as light sources. For the first measurements described in section 9.2.3, only one LED Nichia NSPB500 (blue, 470 nm) was installed. For further investigations described in section 9.2.4, the setup was equipped with one LED Nichia NSHU590 (uv, 380 nm) and one three–colour LED Nichia NSTM515S (blue, 470 nm, green, 535 nm, red, 650 nm). See appendix D

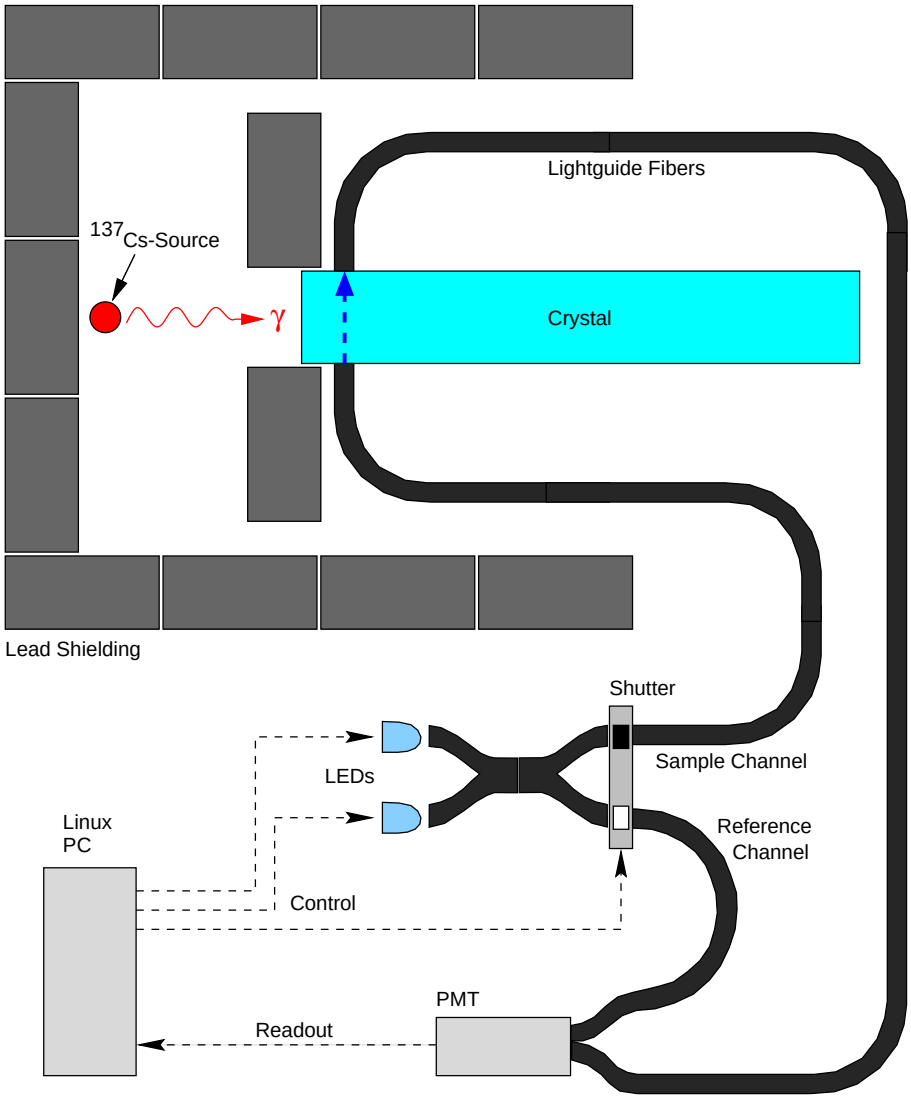

Figure 9.1: The setup used for online measurements of the transmission during irradiation (not to scale). The crystal is placed lying horizontally at a distance of 38 mm from a ^{137}Cs source. The LED light travels through the crystal vertically to the irradiation direction at a distance of 12 mm from the crystal's front face. It is detected by a PMT. The PMT signal is processed by a PC with an ADC card. Changes in the LED or PMT performance are corrected by a reference channel. The measurements are performed "online" every five minutes during irradiation and annealing phases.

for the emission spectra of the LEDs. The measurements were performed using the combinations uv–blue–red, respectively, in one case, uv–blue–green.

For a single measurement of the crystal's transmission, the LEDs are switched on consecutively and the shutter opens the sample channel and then the reference channel for each LED. The light from the LEDs travels transversally through the crystal and perpendicularly to the irradiation direction at a distance of 12 mm from the crystal's front face. It is detected by a PMT Hamamatsu R928, which has a spectral range of 185 to 900 nm.

The PMT signal is digitized by an analog-to-digital converter (ADC) plugged into a personal computer (PC) which also switches the shutter and the LEDs. Changes in the LED or PMT performance are corrected by a reference channel. Single measurements of

E_γ / keV	η'/ρ / $\mathrm{cm^2 g^{-1}}$		
	$PbWO_4$	LiF	Alanine
100	1.828	0.022	0.024
200	0.488	0.025	0.029
300	0.203	0.027	0.031
400	0.115	0.027	0.032
500	0.079	0.027	0.032
600	0.060	0.027	0.032
800	0.043	0.027	0.031
1000	0.035	0.026	0.030

Table 9.1: Mass energy–absorption coefficients for $PbWO_4$ and different dosimeter materials [aic95, hub81].

the crystal's transmission were performed "online" every five minutes during irradiation and annealing phases. A further description of the measurement setup together with an operating manual can be found in [gen00].

9.2.2 Dosimetry

Dosimetry at the ^{137}Cs irradiation facility was performed using alanine dosimeters. These dosimeters consist of a material in which stable free radicals are produced by irradiation. They are read out by a electron spin resonance (ESR) measurement device.

The indicated doses and dose rates have been calculated from alanine measurements for the centers of the crystals where the light ray of the LED is traversing. The following corrections were applied to the alanine doses.

The alanine dosimeters are located at the crystal face closest to the ^{137}Cs source at a distance of about 38 mm from the source. The light ray is traversing the crystal at a distance of about 50 mm from the source. Hence, a geometry correction factor k_{geom} must be applied to the dose rate:

$$k_{geom} = \frac{r^2_{alanine}}{r^2_{PWO}} \approx \frac{(38\,\mathrm{mm})^2}{(50\,\mathrm{mm})^2} = 0.58 \tag{9.1}$$

The crystal is inhomogenously damaged due to the fact that the 662 keV γ radiation is attenuated to about half its intensity in a depth of 12 mm behind the crystal's front face where the measurement light ray is traversing. A calculation according to [aic95] yields a shielding factor

$$k_{shield} \approx 0.45 \tag{9.2}$$

The energy absorption of a material exposed to radiation is described by the mass energy–absorption coefficient η'/ρ. Mass energy–absorption coefficients for $PbWO_4$ and different dosimeter materials are listed in Tab. 9.1. The relative energy absorption factor k_{abs} of

$PbWO_4$ and alanine for irradiation with ^{137}Cs is calculated as the ratio of the appropriate values at an energy of 600 keV:

$$k_{abs} = \frac{0.060\,\mathrm{cm^2 g^{-1}}}{0.032\,\mathrm{cm^2 g^{-1}}} \approx 1.9 \tag{9.3}$$

The energy dose which is absorbed by the crystal at the location of the traversing light ray can thus be calculated according to the dose rate

$$\dot{D}_{crystal} = k_{geom} \cdot k_{shield} \cdot k_{abs} \cdot \dot{D}_{alanine} \approx 0.50 \cdot \dot{D}_{alanine} \tag{9.4}$$

During an irradiation of 120 h, a dose of $D_{alanine}$=(435±37) Gy was detected, which corresponds to a dose rate of $\dot{D}_{alanine}$=(3.62±0.31) $\mathrm{Gyh^{-1}}$. Applying the corrections described above, a dose rate of $\dot{D}_{crystal}$=(1.8±0.15) $\mathrm{Gyh^{-1}}$ is obtained.

9.2.3 First measurements

In Fig. 9.2 the radiation induced absorption coefficient at 470 nm is plotted against the total absorbed dose for two $PbWO_4$ crystals. The 1997 crystal is about six times more radiation tolerant than the 1995 one and reaches the saturation level much earlier. The differences between the crystals are due to a finer tuned stoichiometric ratio during the growth process, Lanthanum doping and post-growth annealing [cms97].

The annealing of the radiation damage can be observed in Fig. 9.3, where a cycle of irradiation, annealing and re-irradiation of a 1997 crystal is shown. Here the induced absorption coefficient is plotted versus duration of measurement or, respectively, total absorbed dose.

During the initial irradiation a dose of 80 Gy is applied. The radiation damage of the crystal already reaches saturation after about 10 Gy. After blocking the irradiation, annealing of the radiation damage can be observed. After 100 h of annealing, the induced absorption coefficient has fallen by 36%. Finally, a second irradiation was applied at the same dose rate as the first irradiation. Similar to the first irradiation, the radiation damage of the crystal reaches saturation again after about 10 Gy.

At saturation level the induced absorption coefficient is 0.011 $\mathrm{cm^{-1}}$ corresponding to a decrease in transmittance of 20% through one crystal length (20 cm), which is still sufficient to allow proper operation of the Crystal BPC.

9.2.4 Systematic study of the radiation damage

The radiation damage was studied systematically for eight of our full-size crystals. For these measurements, the Online–Measurement setup described in section 9.2.1 was used. All crystal measurements proceeded according to a standard procedure: The crystal is installed in the setup and the measurement is started. At the beginning of each measurement, a drift of the measured transmission signals is observed, which is due to warming–up effects of the PMT and the LEDs. This effect is not shown in the plots of the results. If

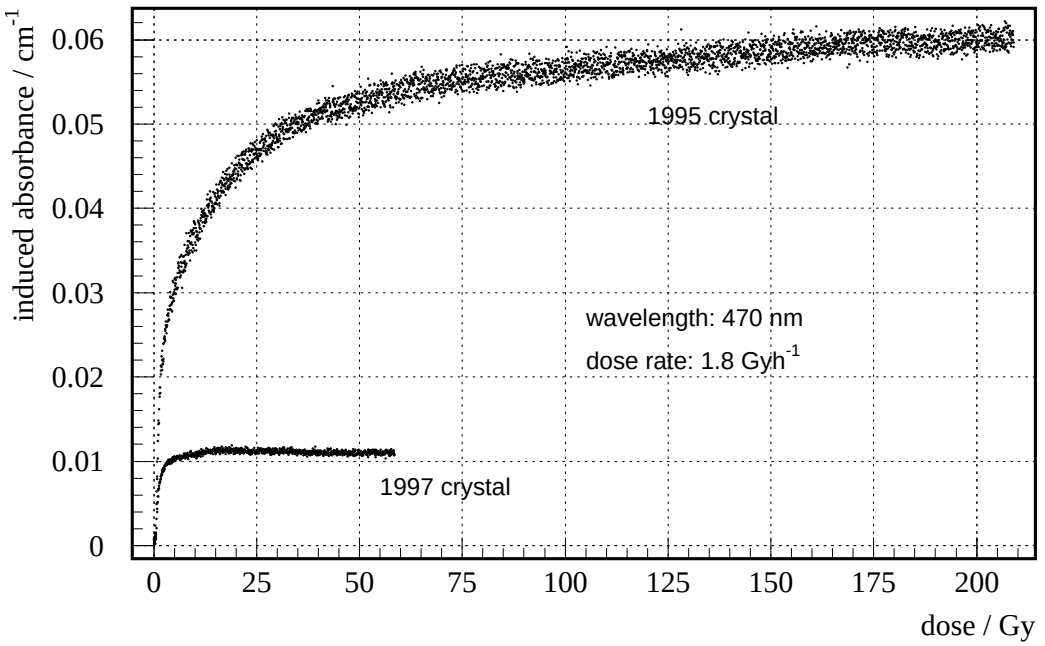

Figure 9.2: Comparison of online transmission measurements with two crystals. The 1997 crystal is six times more radiation tolerant than the 1995 one.

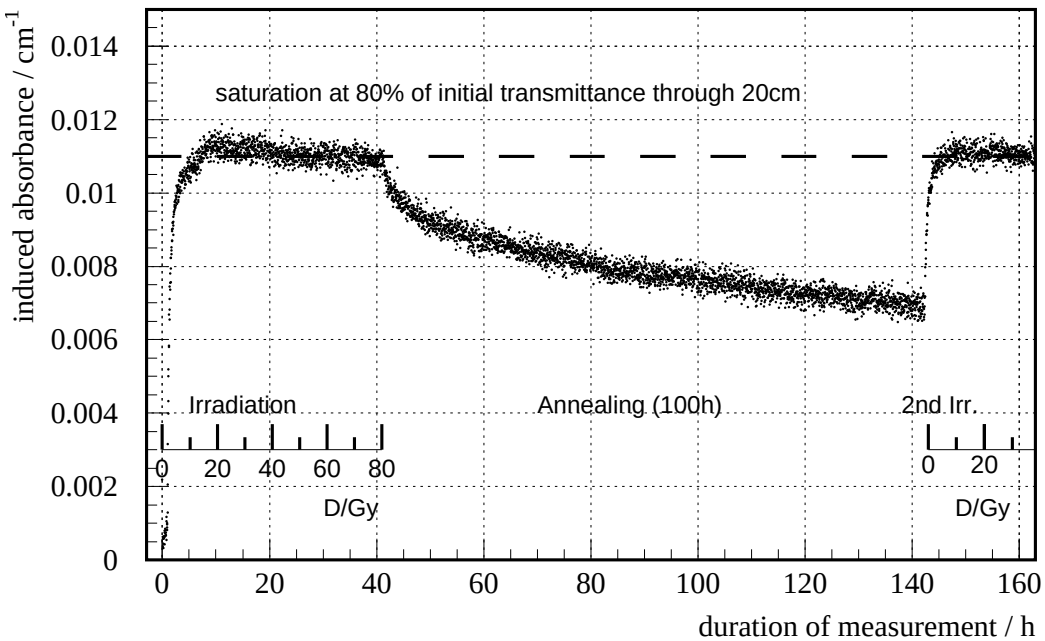

Figure 9.3: Online transmission measurement of a 1997 crystal. The crystal is irradiated with a dose of 80 Gy, then irradiation is switched off for 100 hours to observe annealing. Finally, a second irradiation is performed with the same dose rate.

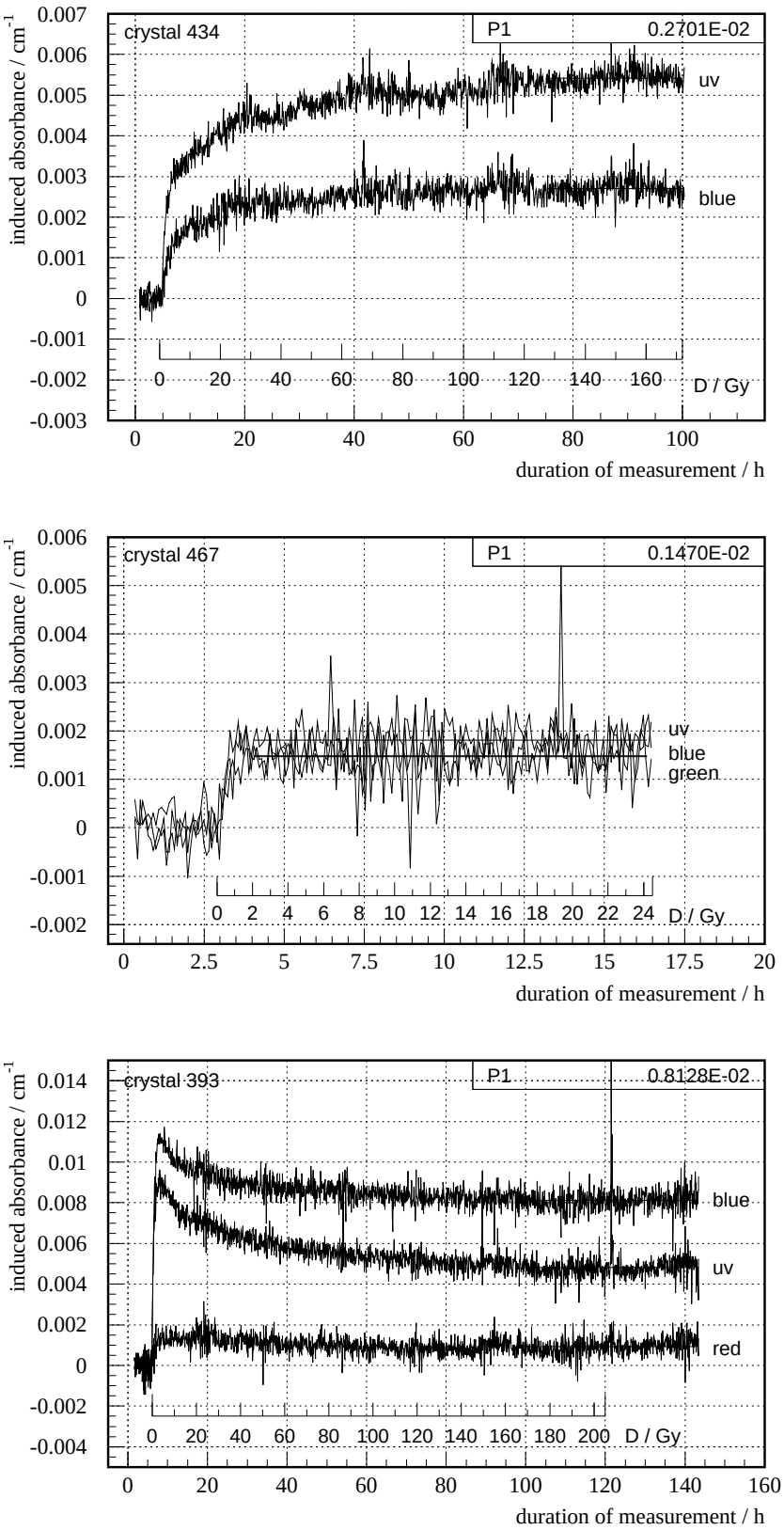

Figure 9.4: Online radiation damage measurements of crystals 434 (top), 467 (middle), 393 (bottom). Irradiation phases are denoted by an extra scale in the pictures which specifies the absorbed dose.

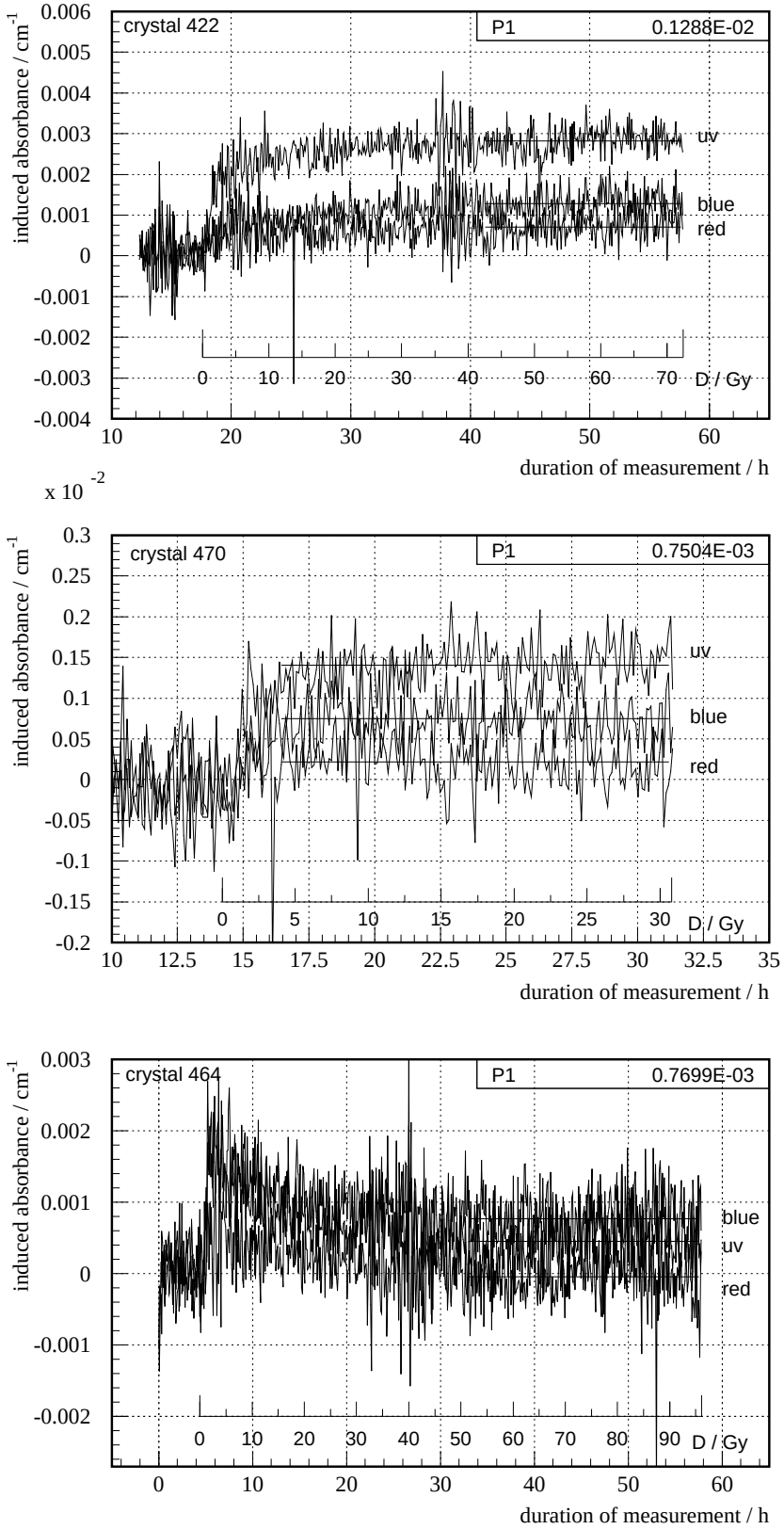

Figure 9.5: Online radiation damage measurements of crystals 422 (top), 470 (middle), 464 (bottom).

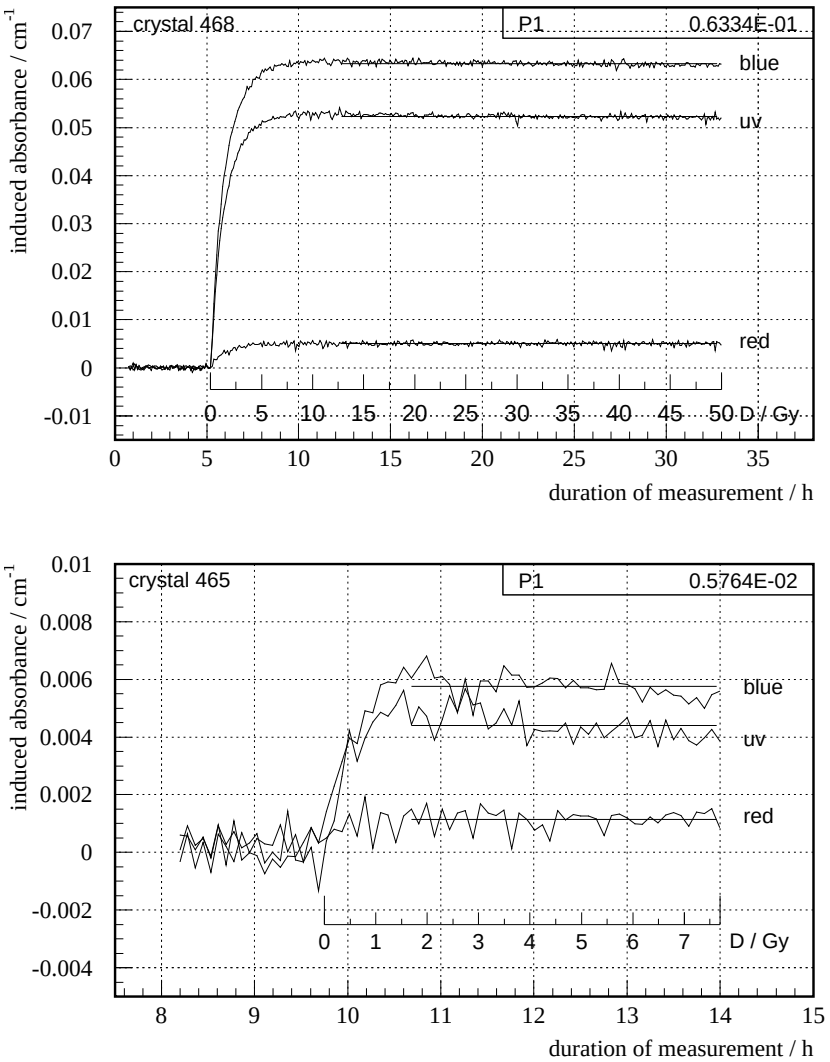

Figure 9.6: Online radiation damage measurements of crystals 468 (top), 465 (bottom).

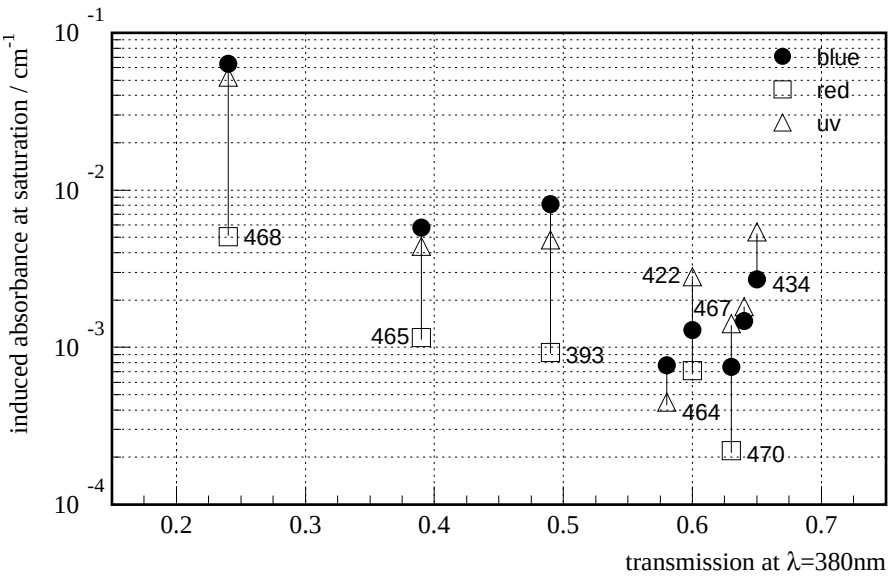

Figure 9.7: Induced absorption coefficient at saturation level plotted versus the longitudinal crystal transmission at a wavelength of 380 nm before irradiation. This picture shows the result for all LEDs. Vertical lines are drawn to connect the data points belonging to a particular crystal measurement.

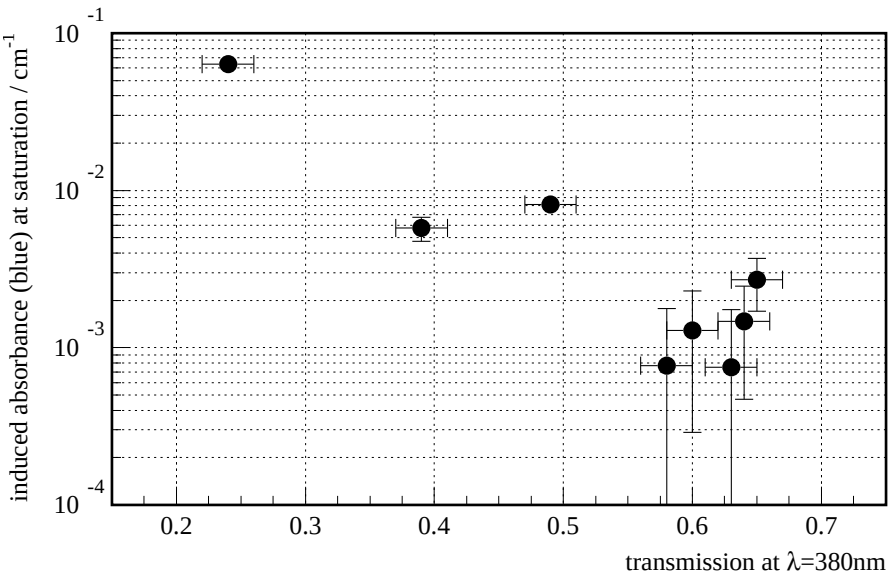

Figure 9.8: Same plot as above, but concentrating on the blue LED and showing error bars of the measurements.

crystal	induced absorbance at saturation / $10^{-2}\,cm^{-1}$				transmission
	blue	green	red	uv	at $\lambda = 380\,nm$
434	0.270±0.10	—	—	0.542±0.10	0.65±0.02
467	0.147±0.10	0.149±0.10	—	0.181±0.10	0.64±0.02
393	0.813±0.10	—	0.093±0.10	0.482±0.10	0.49±0.02
422	0.129±0.10	—	0.071±0.10	0.282±0.10	0.60±0.02
470	0.075±0.10	—	0.022±0.10	0.141±0.10	0.63±0.02
464	0.077±0.10	—	-0.004±0.10	0.045±0.10	0.58±0.02
468	6.334±0.10	—	0.504±0.10	5.234±0.10	0.24±0.02
465	0.576±0.10	—	0.115±0.10	0.440±0.10	0.39±0.02

Table 9.2: Result of the systematic study of the radiation damage of several crystals. The table contains the induced absorbance at saturation level in the examined spectral areas as well as the longitudinal transmissions of the crystals.

the measured signal is found to be sufficiently stable, the irradiation is switched on. The measurement proceeds until the radiation damage has reached its saturation level.

The results of the online measurements are shown in Figs. 9.4 to 9.6, where the radiation induced absorption coefficient is plotted versus time for each spectral region measured. The duration of the irradiation phases is denoted by an additional scale indicating the absorbed dose. The induced absorption values at saturation level for the different spectral regions are summarized in Tab. 9.2. The table also shows the longitudinal transmission value of each crystal at a wavelength of 380 nm.

Fig. 9.7 shows the induced absorption coefficients at saturation level plotted versus the longitudinal crystal transmission at a wavelength of 380 nm before irradiation for all spectral regions. Fig. 9.8 shows the same data, but concentrates on the blue LED and indicates measurement errors by error bars. A clear correlation between the radiation induced absorption coefficient and the crystal transmission at 380 nm can be observed. This result is confirmed by previous measurements, which revealed a better radiation resistance of crystals with a higher transmission value at a wavelength of 370 nm [zhu96]. It offers the possibility to recognize radiation–hard crystals without irradiation measurements.

9.2.5 Annealing of the radiation damage during irradiation

Two of the measured crystals, namely crystals 393 and 464, show an unexpected behaviour of the radiation damage. When switching on the irradiation, the radiation damage increases rapidly to a level of $0.011\,cm^{-1}$ (393) respectively $0.0018\,cm^{-1}$ (464). After an absorbed dose of less than 10 Gy, the damage decreases with another time constant although the irradiation is proceeding continuously. Finally, the radiation damage reaches a saturation level which is significantly lower ($0.008\,cm^{-1}$ respectively $0.0006\,cm^{-1}$) than the maximum damage. The irradiation of crystal 393 was stopped after an absorbed dose of about 205 Gy. Afterwards no annealing of the radiation damage can be observed, which is in contrast to the expectations. From the latter, it may be concluded that the crystal has reached a stage where it is insensitive to irradiation or annealing effects. The

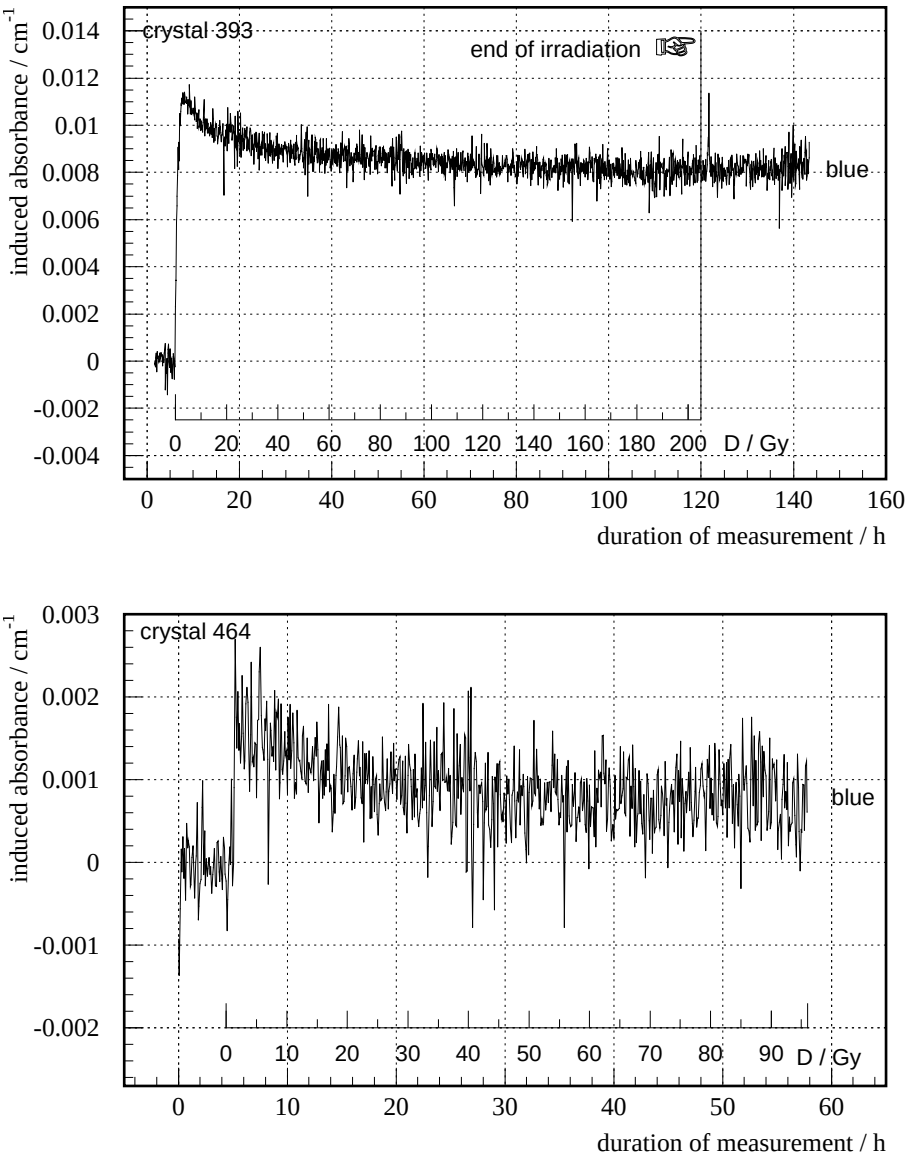

Figure 9.9: Radiation damage of crystals 393 and 464, measured with the blue LED. When switching on the irradiation, a damage occurs, decreasing in the following although the irradiation is proceeding. Finally, saturation is reached.

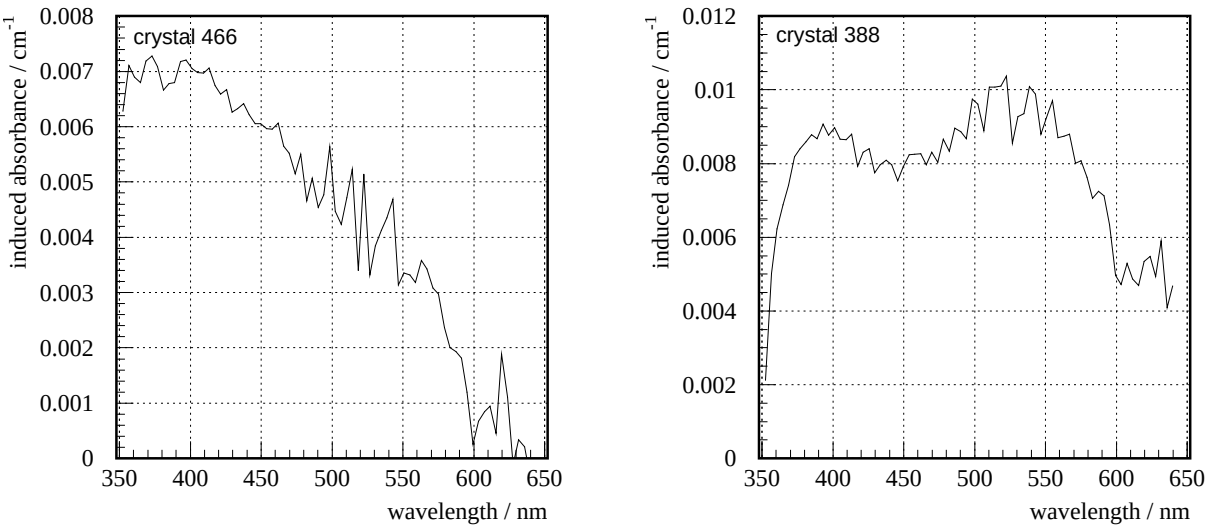

Figure 9.10: Induced absorption coefficient caused by a high dose irradiation (28 kGy) versus wavelength for crystals 466 (left) and 388 (right).

radiation damage of the two mentioned crystals can be observed in Fig. 9.9, showing the data for the blue LED.

Additional measurements have to be performed to further investigate this unexpected and very interesting behaviour of the radiation damage. If further measurements confirm the above described assumption of a permanent saturation of the radiation damage without showing annealing and a resulting insensitivity to further irradiation, it may be possible to construct radiation hard crystals. After pre–irradiation, such crystals would no more suffer from transmission changes due to radiation damage and retain a constant energy calibration.

9.3 Radiation damage at high doses

The online measurements described in section 9.2 were performed at a relatively low dose rate of 1.8 Gy/h. It was shown that the radiation damage of the crystals of good quality reaches saturation already after very small absorbed doses of a few up to a few ten Gy.

To investigate whether the saturation of the radiation damage is also preserved at higher absorbed doses, two crystals were irradiated at a ^{60}Co irradiation facility[1] at a dose rate of about 3 kGy/h to a dose of 28 kGy.

The irradiation facility is constructed such that the samples move on a conveyor belt between several ^{60}Co sources. Hence, it was not possible to install the online measurement setup which was used for the low dose irradiations. The radiation induced absorption coefficients $\Delta\mu$ of the crystals were determined by measuring the transverse transmissions

[1] Beiersdorf AG, Hamburg, Germany

of the crystals through 23.8 mm in a Beckman spectrophotometer (see section 8.1) before and after the irradiation and applying the following formula:

$$\Delta\mu = \frac{1}{d} \ln\left(\frac{T_0}{T_{irrad}}\right) \tag{9.5}$$

Here, d is the thickness of the sample, and T_0 and T_{irrad} denote the crystal's transmission before respectively after irradiation. The result of the measurements is shown in Fig. 9.10 for the two irradiated crystals. The radiation induced absorption coefficient is plotted versus wavelength.

Both crystals show a radiation damage of less then $0.01\,\mathrm{cm}^{-1}$. This damage amounts to the expected value from the online measurements. Obviously, the saturation behaviour is still valid for the large dose applied.

Nevertheless, the wavelength dependence of the radiation damage shows significant differences comparing the two crystals. This emphasizes the above mentioned fact that the contributions of the different radiation induced colour centers may differ significantly from crystal to crystal.

9.4 Radiation damage by neutrons

Chipaux et al. have studied the neutron damage resistance of $PbWO_4$. The radiation induced additional absorption caused by fast neutrons was found to be negligible. It is equal to $(0.00086 \pm 0.0005)\,\mathrm{cm}^{-1}$ per 10^{13} $\mathrm{n\,cm}^{-2}$ [chi94]. Another group irradiated a $PbWO_4$ sample at the Tapiro reactor in ENEA, Casaccia, Italy, by neutron fluxes from 1.9×10^{10} up to 4.72×10^{11} neutrons cm^{-2}. The observed transmission changes were within the experimental errors [lum98].

9.5 Effect of irradiation on scintillation

In order to examine a possible impact of irradiation on the scintillation mechanism of $PbWO_4$, the emission spectra of the two crystals which were subject to a high dose irradiation (see section 9.3) were measured before and after the irradiation. The dose rate of the irradiation was about 3 kGy/h, and the absorbed dose amounts to 28 kGy. These measurements were performed using the measurement setup described in section 8.4.

The results of the measurement are shown in Fig. 9.11. The spectra are arbitrarily normalized to provide a comparison of their shape. No significant change of the emission spectra before and after the irradiation can be observed. This indicates that the different scintillation processes which give rise to the spectral shape do not change their relative contributions. Hence, it may be concluded that the scintillation process remains unaffected at all [zhu96].

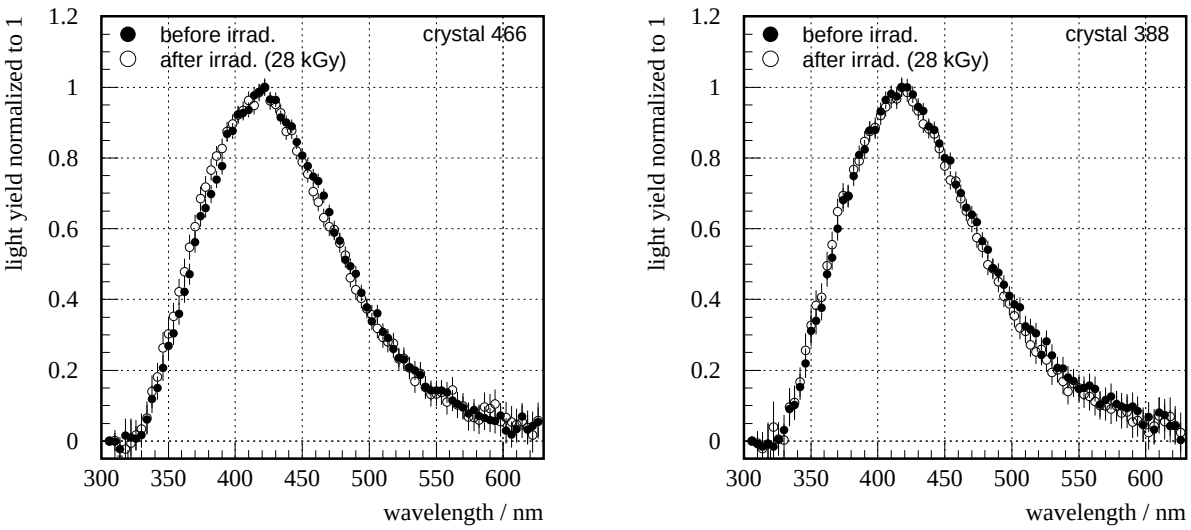

Figure 9.11: Effect of high dose irradiation on the scintillation spectra measured for crystals 466 (left) and 388 (right) before and after irradiation with a dose of 28 kGy. Each curve is normalized to one. It is clearly visible that the shape of the spectra remains unaffected.

Chapter 10

Measurements with the Crystal BPC prototype

In order to study the characteristics of a $PbWO_4$ calorimeter, a Crystal BPC prototype was built of crystals of the 1995 type. It was subject to several measurements at the DESY II test beam. See [mor98] for a detailed description of the test beam setup and the measurements.

10.1 Description of the prototype

The Crystal BPC prototype was designed to consist of nine $PbWO_4$ crystals of the 1995 type with dimensions $18 \times 18 \times 200\,\mathrm{mm}^3$, arranged in a 3×3 matrix. For the construction of the prototype, only eight undamaged crystals were available. As a consequence, one corner crystal of the calorimeter had to be omitted.

The optical readout of the prototype reflects an early Crystal BPC design study using a readout scheme with conventional PMTs. At the back of each crystal, a lightguide of PMMA with the same cross–section as the crystal, $18 \times 18\,\mathrm{mm}^3$, was attached using a silicone cookie. Shortly behind the crystals, the lightguides had a sharp bend of 90°, which would have been necessary in the Crystal BPC because of the limited space in the longitudinal direction inside the ZEUS detector. To provide a good light transmission, mirrors were installed. The lightguides were then bent smoothly to fit to the PMT housings and finally were coupled by silicone cookies to the PMTs. Their overall length was about 35 cm. The crystals and lightguides were wrapped with teflon to improve the light yield.

As PMT types, two Hamamatsu R580 and two Philips XP2008 as well as four Philips XP2012 tubes were installed inside iron tubes and equipped with magnetic shielding of mu metal.

The prototype was equipped with a transmission monitoring system used to detect radiation induced transmission changes of the crystals. Optical fibers were put into drills in the lightguides such that they injected the light of a light–emitting diode X–LED from the back into the crystals. The light traverses one crystal length, is reflected off the front face,

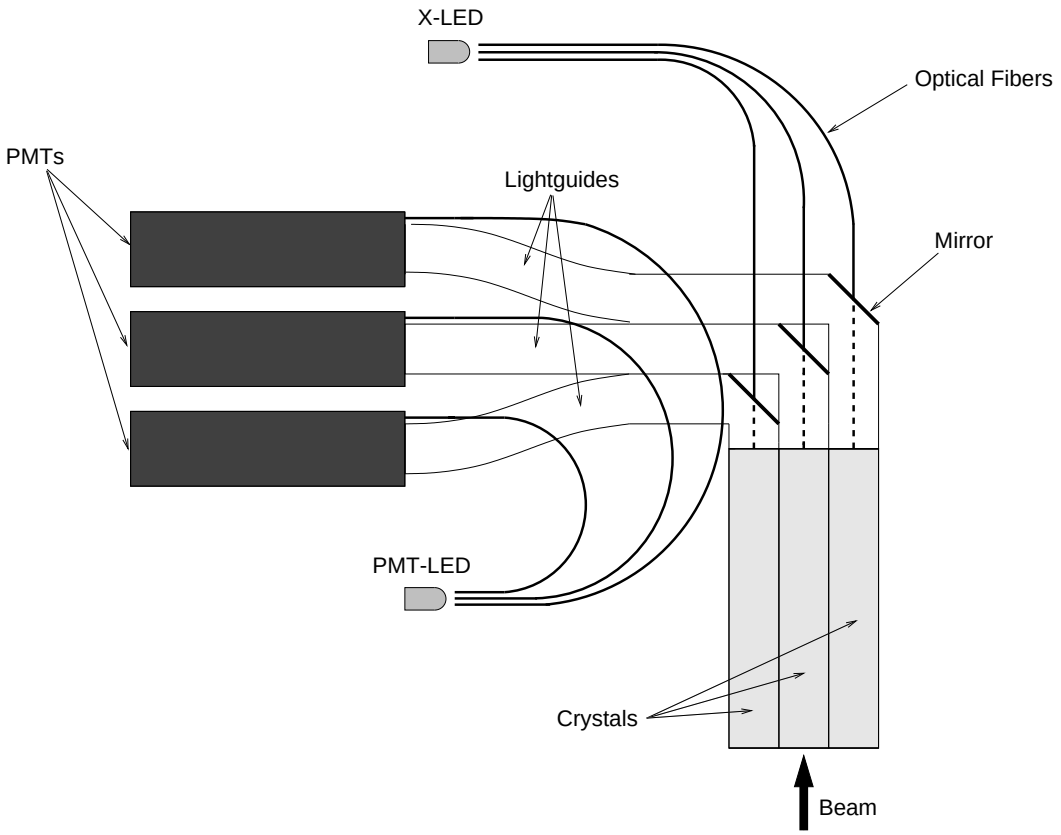

Figure 10.1: Top view of the Crystal BPC prototype.

traverses the crystal again and reaches the lightguides, which transport it to the PMTs, where it is detected. Another LED, the so–called PMT–LED, injects light directly into the PMTs for monitoring purposes using a different set of optical fibers. An overview of the Crystal BPC prototype is given in Fig. 10.1.

10.2 Measurements at the DESY II test beam

The DESY II test beam is a parasitic electron beam. A carbon fiber target moved into the electron halo of the DESY II electron storage ring is used to produce high energy photons, which in a copper conversion target convert into electron–positron pairs. The electrons are led by a dipole magnet into the test beam area. The momentum of the electrons reaching the area can be adjusted by setting the magnet current. The useful electron energies range from 1 to 6 GeV.

The readout of the prototype was CAMAC–based [hen99]. In the test beam area, trigger counters were installed, and a trigger logic was arranged to measure the energy deposit of single electrons in the prototype. The prototype was installed on a moving table, which made it possible to adjust its X and Y position relative to the beam.

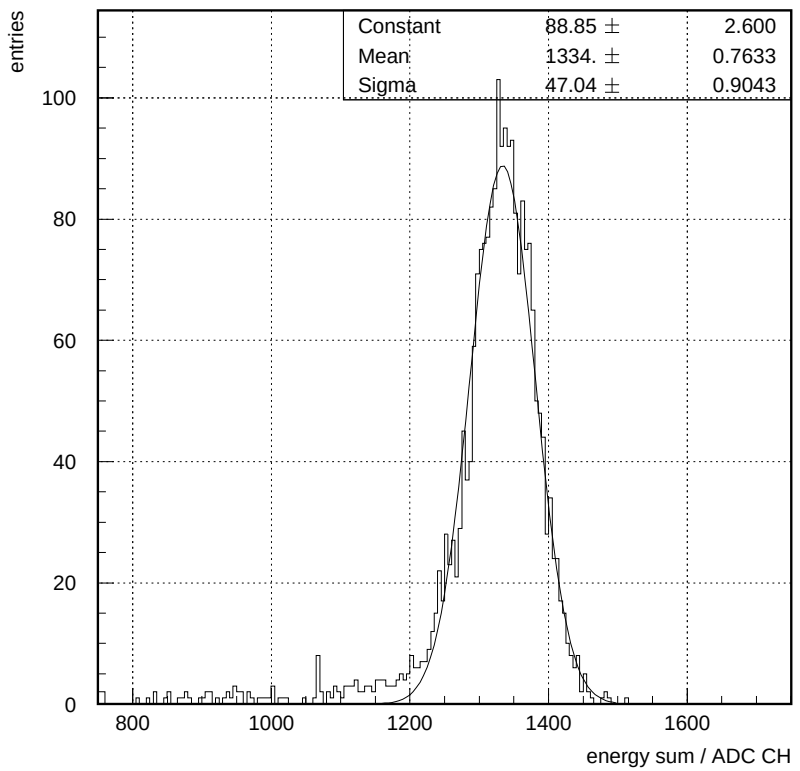

Figure 10.2: Energy resolution of the Crystal BPC prototype.

10.2.1 Energy resolution

In Fig. 10.2, a measurement of the energy resolution of the prototype is shown for an electron energy of 6 GeV. The number of hits is plotted versus the energy sum of all crystals. A Gaussian fit is applied to the measured energy distribution. Using the results of the fit, the energy resolution is calculated to be $8.6\%/\sqrt{\mathrm{E/GeV}}$. As the test beam energy spread was determined to 6.6% [mor98], the measured energy resolution must be corrected accordingly. A value of $5.5\%/\sqrt{\mathrm{E/GeV}}$ is obtained for the energy resolution of the prototype (see Eq.(5.19)).

10.2.2 Uniformity

In order to measure the uniformity of the prototype's energy response, a horizontal scan was performed. The electron beam was shot into the calorimeter at different horizontal positions in steps of 3 mm. The result of this measurement is shown in Fig. 10.3. The energy response deteriorates at the calorimeter edges due to lateral shower leakage. In the central region of the calorimeter, the energy response is stable to within about 2%, decreasing at the cracks between the crystals which are denoted by vertical lines at the

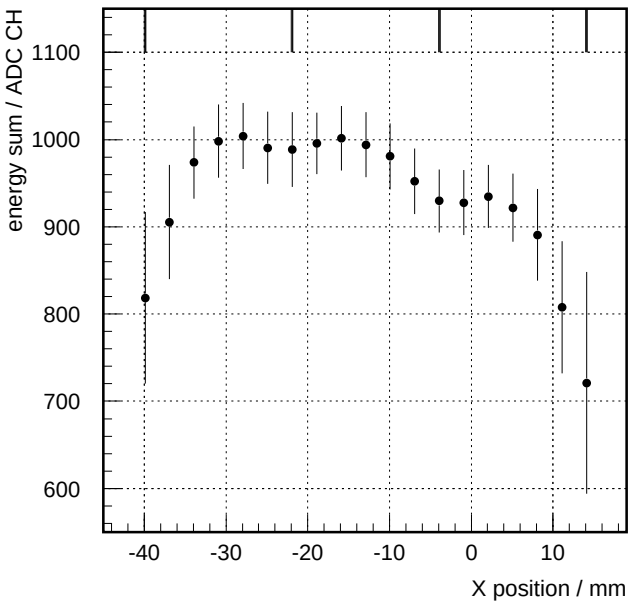

Figure 10.3: Energy response of the prototype as a function of the horizontal electron impact position.

top of the picture. The low energy response in the right part of the picture is caused by the missing corner crystal.

10.2.3 Temperature effect

The known temperature dependence of the light yield of $PbWO_4$ was tested by heating up the prototype in steps up to a temperature of 36°C. The prototype was equipped with temperature sensors which precisely recorded the temperature. Several runs with 6 GeV electrons were taken at different temperatures to measure the light yield dependence. The result is shown in Fig. 10.4. Six runs were taken at different temperatures from 20.5°C to 36°C. The decrease of the energy response is clearly visible. It corresponds to a temperature coefficient of the light yield of $-2\%/°C$, which is in agreement with previous measurements [rus97].

10.2.4 Radiation damage monitoring system

The transmission monitoring system of the prototype is expected to detect radiation induced transmission changes of the crystals. It was tested by removing the center crystal, irradiating it at a ^{60}Co source with a dose of 60 Gy and re–installing it in the prototype.

As the irradiated crystal was now subject to annealing, its transmission was expected to improve with time. Hence, it was expected that the energy response of the crystal, as well as the transmission signal delivered by the LED, should consequently show an increase.

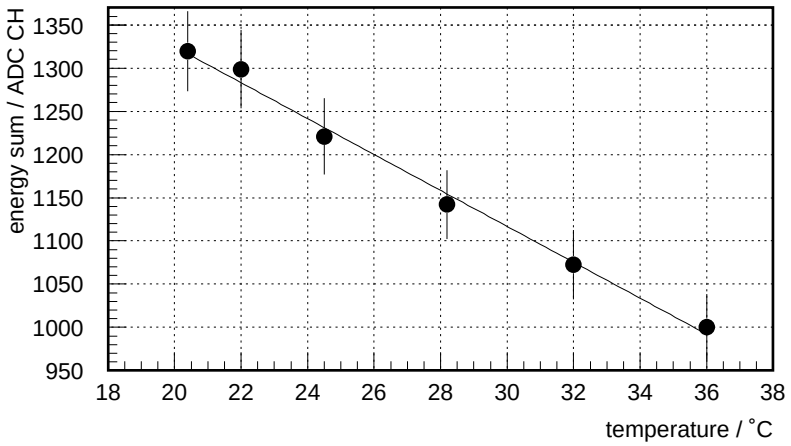

Figure 10.4: Temperature dependence of the energy response of the prototype.

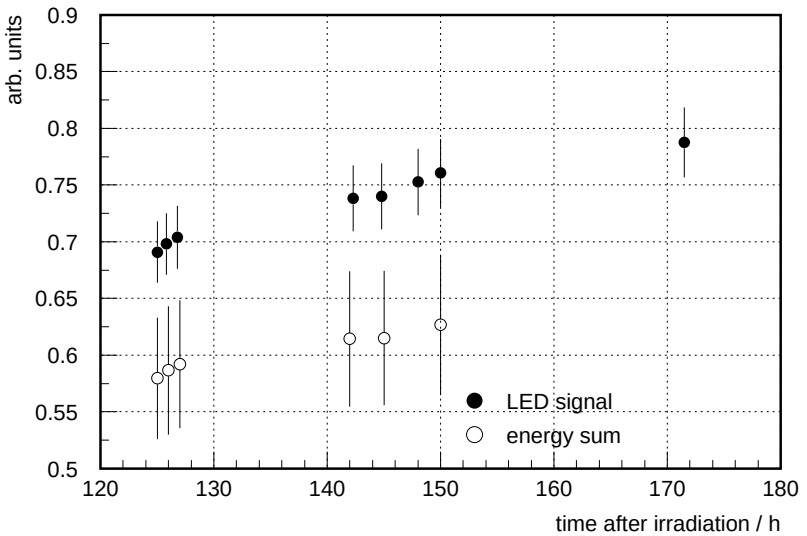

Figure 10.5: Test of the radiation damage monitoring system. As the irradiated crystal is annealing, the energy response as well as the LED signal show an increase with time.

The result is shown in Fig. 10.5. Both the energy response and the LED signal show a clear rise. Hence, it can be concluded that the transmission monitoring system can be used to monitor radiation induced transmission changes in the crystals. As the LED signal is correlated to the energy response, it is also possible to monitor the energy scale of the calorimeter.

Chapter 11

Description of the Crystal BPC

11.1 Mechanical Design of the Crystal BPC

The mechanical and optical design of the Crystal BPC is dominated by certain requirements and constraints. First, the available space is restricted. The position of the calorimeter at about 39 mm radial distance from the beam and 2937 mm downstream from the interaction point places it deep inside the ZEUS detector, where there is very little free volume. The space available allows a transverse extension of about 150 mm and 180 mm in the X and Y directions, respectively, and a total of 270 mm depth in the Z (electron) direction. This is the total available distance for the development of the electromagnetic shower and the detection of the scintillation light.

Furthermore, the Crystal BPC must operate in a magnetic field at the level of several hundred Gauss with a strong gradient which is caused by the ZEUS toroid and the compensator magnet.

Finally, temperature changes at the level of 2 K have been observed in the BPC area inside ZEUS, so that the Crystal BPC must be thermally stabilized (see section 11.4).

The Crystal BPC consists of a 4×4 matrix of crystals of $200 \times 23.8 \times 23.8\,\mathrm{mm}^3$, where the long dimension is parallel to the beampipe. The size of the crystals was close to the maximum obtainable at this time. The fiducial area of the front face of the calorimeter, that is the area which is the unimpeded projection of the interaction point through the beampipe window onto the calorimeter face, is $46 \times 51\,\mathrm{mm}^2$, so that the calorimeter dimensions provide more than one Molière radius around the three outside edges of the fiducial volume. The inner edge (adjacent to the beampipe) of the active part of the Crystal BPC will be about 44 mm away from the beam line.

The crystals are separated from each other by a layer of Tyvek [dup99] diffuse reflective paper. The wrappings create an inactive layer of about 200 μm thickness between the crystals. At the downstream end of each crystal there is an 8 mm diameter, 10 mm long acrylic lightguide (GS218, uv transparent) glued to the crystal which connects the rear face of each crystal to a Hamamatsu R5600U–03 PMT. The R5600U–03 is an 8 stage miniature PMT of only 12 mm length and 16 mm overall diameter with an 8 mm diameter photocathode. It has a spectral response of 185 nm to 650 nm. The lightguide, tube, custom-made base, and cables fit into the free space of 70 mm length.

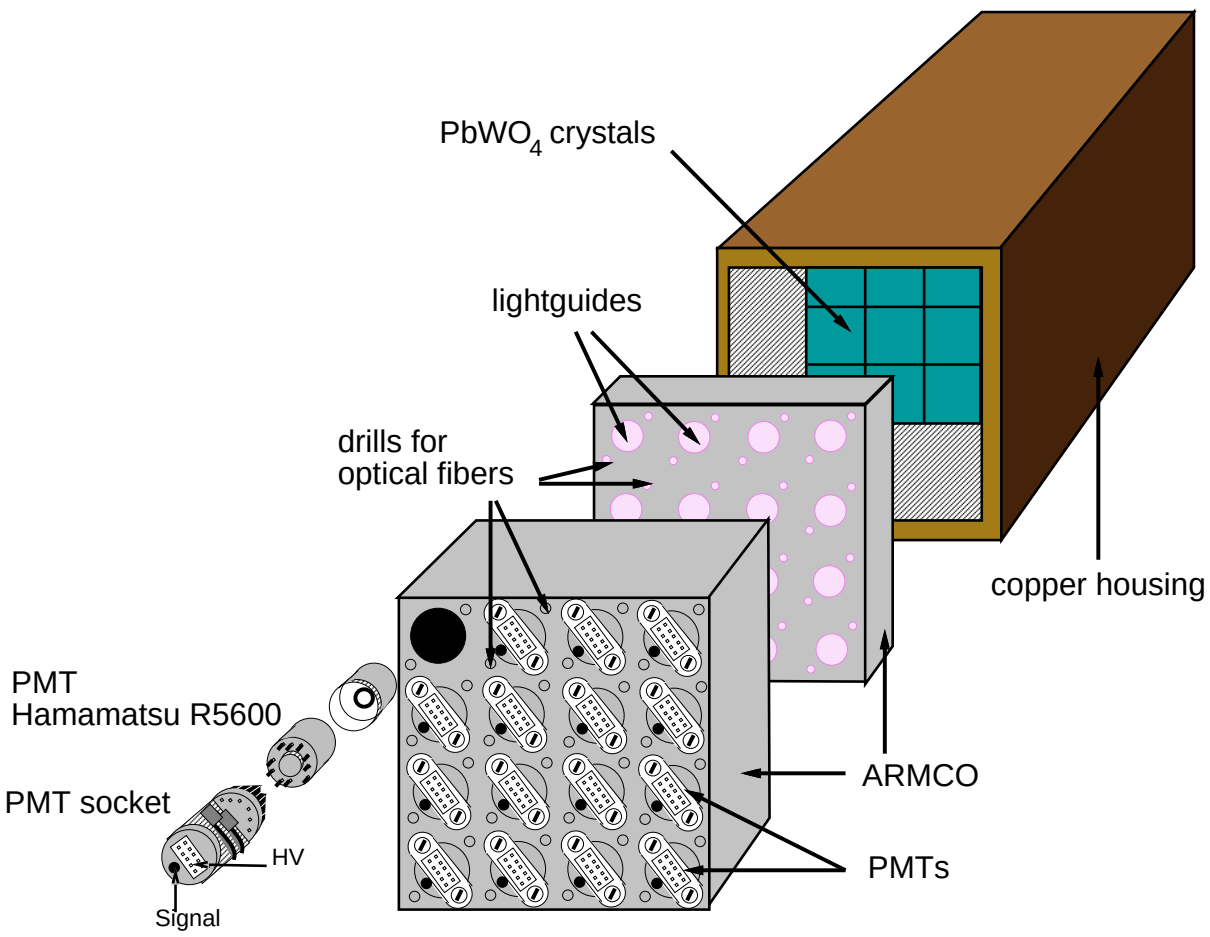

Figure 11.1: Exploded view of the Crystal BPC (from [mey99]).

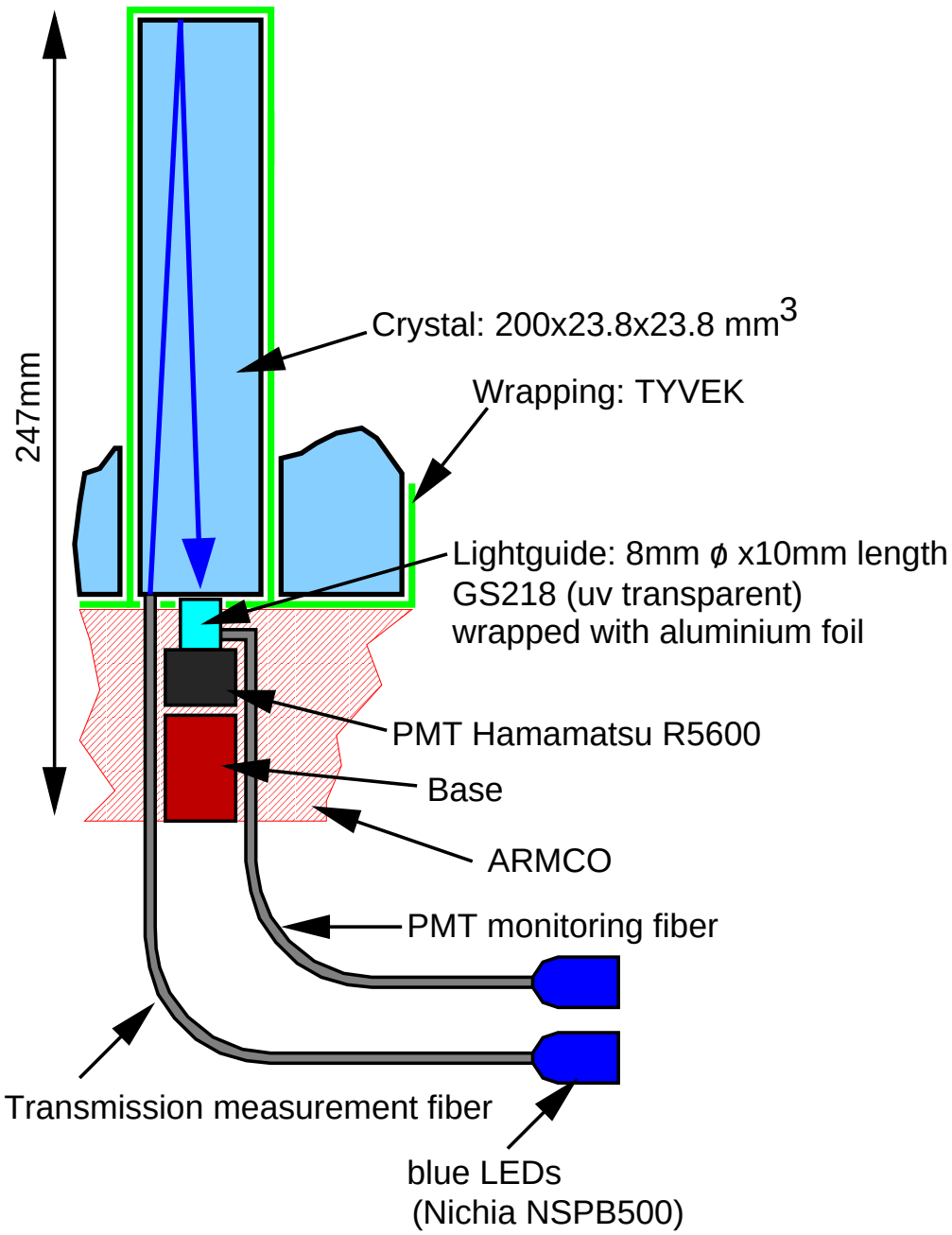

Figure 11.2: Schematic view of a crystal within the Crystal BPC. Each crystal is coupled by a cylindric lightguide to a PMT Hamamatsu R5600U–03. Two lightguide fibers inject light from behind into the crystal respectively directly into the PMT for monitoring purposes.

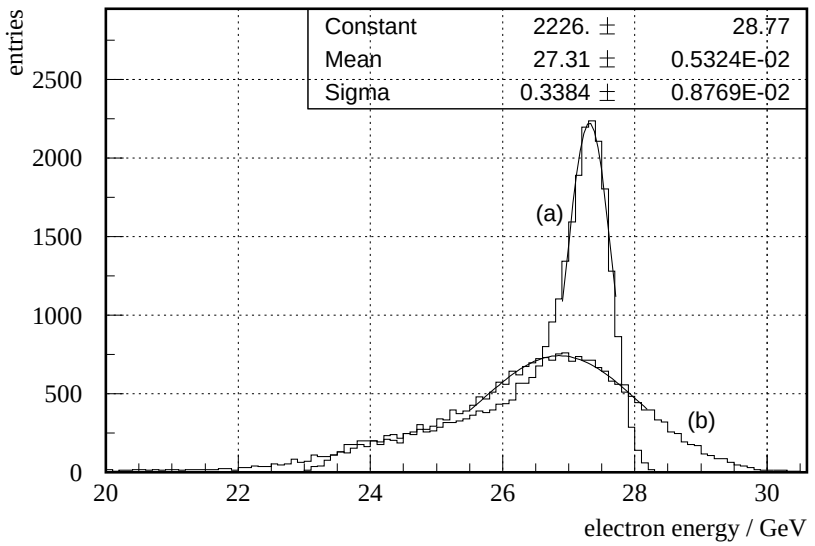

Figure 11.3: Histogram of kinematic peak events for energy scale calibration (Monte Carlo simulation). The narrow peak is composed of KP events, smeared by the Crystal BPC energy resolution of $5\%/\sqrt{E/GeV}$ (a). A fit to the peak locates it to within 0.005 GeV corresponding to a relative error of 0.019%. The fit parameters are shown in the plot. For comparison, the same data is shown smeared by the resolution of the previous BPC II ($17\%/\sqrt{E/GeV}$) (b).

11.2 Magnetic field

The BPC is located between the ZEUS toroid and the compensator magnet. These two magnets cause a magnetic field at the level of 500 Gauss [sur98] inside the BPC area. Tests have shown that conventional PMTs suffer from a significant degradation of their performance if they are exposed to the above mentioned conditions.

Hence, the PMT Hamamatsu R5600U–03 was chosen. Unlike conventional PMTs, it is rather insensitive to magnetic fields. There is no performance degradation in magnetic fields up to 100 G. To provide additional magnetic shielding, the PMTs are mounted inside a block of magnetic iron (ARMCO) [arm90]. As a consequence, the influence of the magnetic field can be neglected.

11.3 The radiation damage monitoring system

As discussed in section 9.2, $PbWO_4$ crystals exposed to ionizing radiation suffer from radiation damage. This causes changes in the crystals' transmissions, which affects the light yield of the calorimeter. A reduced light yield affects the energy measurement in two ways. The resolution becomes somewhat broader: a 15% decline will degrade a resolution of $5\%/\sqrt{E/GeV}$ which is limited by photostatistics to about $5.5\%/\sqrt{E/GeV}$. Far worse is that the energy scale is shrunk by 15%, that is, a 10 GeV electron would create the same number of p.e. as an 8.5 GeV electron before the damage occurs. In addition, the induced absorption would decrease again after the irradiation due to annealing of the

radiation damage, causing a continuous change of the calorimeter's energy calibration. Hence, in order to perform high precision measurements, this effect must be monitored and corrected.

The front face of the BPC is not uniformly irradiated; the crystals nearest to the beampipe get about five times the dose of the outside edges. Under these circumstances, it is impossible to predict the response of the crystals to irradiation with a precision approaching the necessary 0.5%. Instead, the calibration will be monitored with two separate systems, which are described in the following.

Variations in the transmissions of all crystals are monitored by an LED system. A bright, blue emitting (470 nm) LED (Nichia NSPB500) illuminates a bundle of 1.2 mm diameter double clad PS fibers [kur99], so that each fiber carries approximately the same intensity, and always the same fraction of light. One such fiber is affixed to the rear surface of each crystal. When the LED is pulsed, the fibers inject light into the crystal from the back. It traverses the length and is reflected off the front face back to the light guide and the PMT.

The purpose of the LED system is to follow changes in the crystals' transmissions between full calibrations (see further below) by flashing at frequent intervals. In addition, the LED system can be used to determine a dubious calibration state of the Crystal BPC. For example, an accidental beam dump into the BPC, which has happened several times with BPC II, would show up within one second as a sharp decline in the relative LED signals reported by the inner crystals, so that the specific run could be flagged for special consideration.

The LED system cannot produce an absolute energy calibration because a stability to the required 0.5% can not be guaranteed over long periods of time. The absolute energy calibration of the Crystal BPC in situ is possible by using kinematic peak (KP) events. Small angle, low y scattering of electrons off protons produces a narrow peak at the accurately known beam energy called the "kinematic peak". The beam energy is on the high energy side of the spectrum of scattered electrons. The position of this peak can be used as an energy calibration point. At typical HERA luminosities, the BPC will have about one KP event per second. After cuts to eliminate events with more than one electron, with additional gammas, or with energy outside the fiducial volume, about 10% to 30% of the events remain, depending on the HERA running conditions. Because of the drop–off of the cross–section with Q^2, the rate of KP electrons falls with increasing angle. The outer crystals have one fourth the rate of the inner ones.

A calibration to better than the required 0.5% can be done with about 1000 KP events per crystal, as can be seen in Fig. 11.3. The energy spectrum of KP events produced by a Monte Carlo simulation (30000 events) is smeared by the energy resolutions of the Crystal BPC ($5\%/\sqrt{E/GeV}$) and, for comparison, of the previous BPC II ($17\%/\sqrt{E/GeV}$), using a Gaussian random number generator. A Gaussian fit is applied to the peaks of the distributions to locate the mean values. The fit boundaries have been set to half of the maximum of the distributions. The mean value of the Crystal BPC simulation is determined with an error of 0.019% for 30000 events. As the error scales with the square root of the sample size, we end up with an error of 0.1%, better than the required 0.5%, for a sample of 1000 KP events. The simulation showed that an absolute calibration of

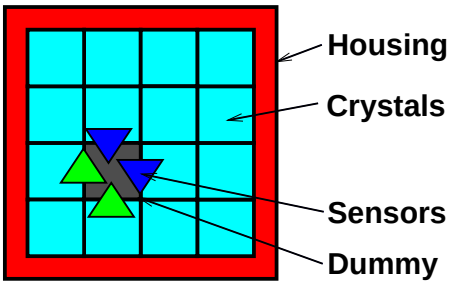

Figure 11.4: The crystal dummy and the temperature sensors inside the Crystal BPC, mounted for the heat conduction measurements.

the Crystal BPC to better than the required 0.5% could be performed in reasonable time intervals about once a day under nominal HERA beam conditions.

11.4 The temperature system

$PbWO_4$ has a distinct temperature dependence of the scintillation light yield. This effect is caused by thermal quenching of the excited states in the crystal which lead to the emission of scintillation light and amounts to $-2\%/°C$ [rus97] (see section 7.3). Without a correction of this temperature dependent light yield, precision measurements with a $PbWO_4$ calorimeter would be impossible. The energy calibration would change continuously because the crystal temperature of course follows changes of the ambient temperature.

There are two possibilities to avoid this constant drifting of the calibration:

- temperature stabilization of the calorimeter, e.g. using a temperature stabilized water cooling
- temperature dependent adaptation of the calorimeter's calibration constants

The best result can be expected if both approaches are used: The temperature could be stabilized to a certain extent using a water cooling circuit and the remaining small temperature changes caused by fluctuations of the water temperature could be monitored by precision temperature sensors and corrected for. This procedure of course presumes that the temperature coefficient of $PbWO_4$ is known to a sufficient accuracy.

11.4.1 Measurements of heat conduction in the Crystal BPC

It is not possible to measure directly the temperatures of the crystals if they are installed inside the Crystal BPC housing. Only the housing temperature can be measured. If the ambient temperature is subject to changes, the crystal temperature will follow the change with a certain delay depending on the heat conduction of the crystals and wrappings inside the calorimeter.

To investigate this issue, a measurement was performed. One central crystal was exchanged with a dummy crystal of plastic equipped with eight temperature sensors. Hence,

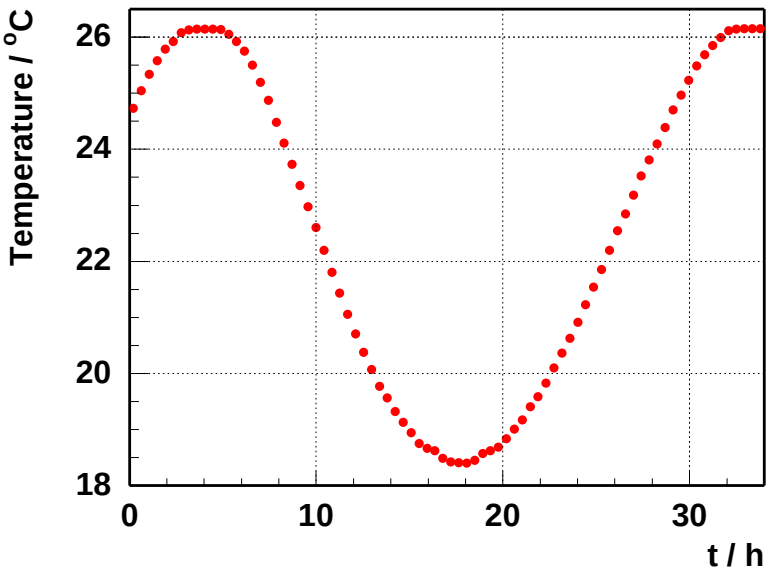

Figure 11.5: Example of a sine–shaped temperature change applied to the Crystal BPC by changing the water circuit temperature periodically.

the surface temperature of each of the four neighbouring crystals was measured by two sensors. The crystal dummy and the sensors inside the calorimeter are shown in Fig. 11.4. Simultaneously, the housing temperature was measured by five sensors. The housing was equipped with cooling water pipes, which were connected to a water circuit which could be cooled or heated. With the help of a custom–made gear unit [leg99] which controlled the water circuit temperature it was possible to apply sinusodial temperature changes to the Crystal BPC, as shown in Fig. 11.5. Measurements were performed with different frequencies of temperature changes from 4 h to 30 h and different temperature amplitudes of 4°C or 8°C. The resulting rapidities of the temperature changes were between 0.79°C/h to 6.9°C/h.

In all runs, a phase difference of the crystal temperature with respect to the housing temperature between 0.25 h and 0.35 h was observed. The mean value of the phase difference amounts to 0.3 h. A phase difference of the inner crystal temperature with respect to the outer crystal temperature of 0.04 h was neglected. This is shown in Fig. 11.6, where a cycle with increasing temperature (0.79°C/h) and a cycle with decreasing temperature (−0.94°C/h) are shown. The observed phase differences amount to 0.35 h and 0.25 h, respectively.

The delay of the temperature changes of the crystals with respect to the calorimeter housing was taken into account for the CERN test. Event–by–event temperature correction was applied by correcting a particular data point with the housing temperature which was measured 0.3 h ago.

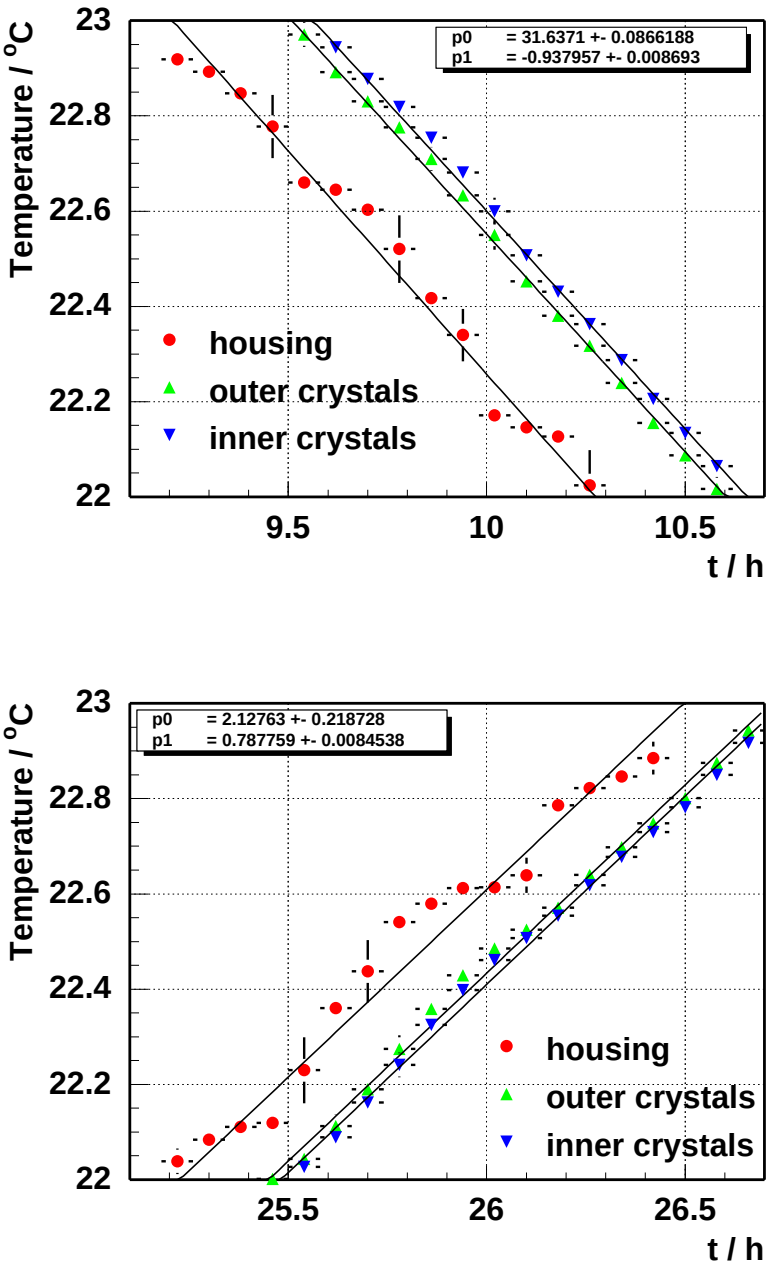

Figure 11.6: Temperature cycles with decreasing temperature ($-0.94°$C/h) and increasing temperature ($0.79°$C/h). The observed phase differences of the temperature changes of the crystals with respect to the calorimeter housing amount to 0.35 h and 0.25 h, respectively.

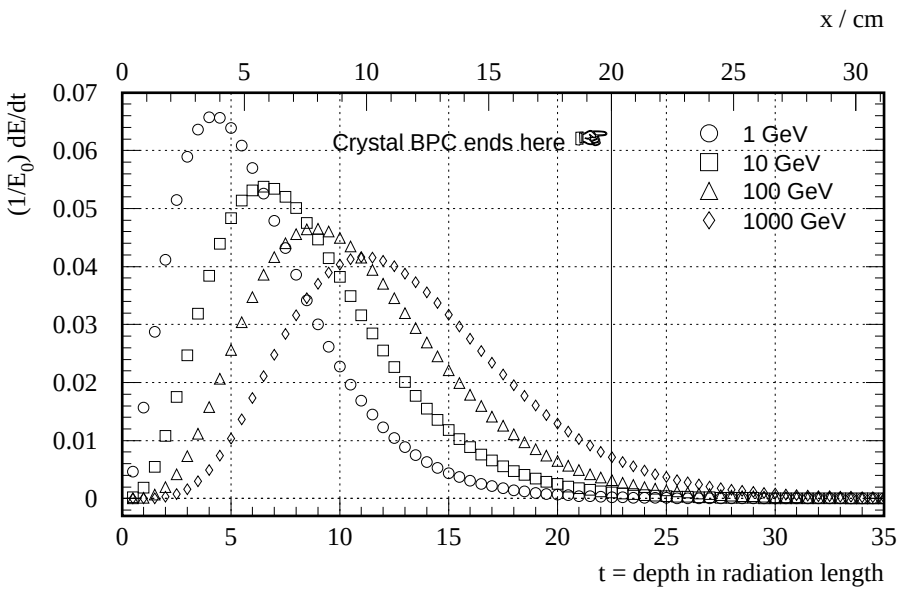

Figure 11.7: Simulated longitudinal shower shapes in $PbWO_4$ for energies of 1, 10, 100 and 1000 GeV. The length of the crystals used for the Crystal BPC, which amounts to 20 cm corresponding to 22.5 radiation lengths, is denoted by a vertical line.

11.5 Shower development in the Crystal BPC

In this section, Eq.(5.10) is used to simulate longitudinal shower shapes in the Crystal BPC for different electron energies.

The effective atomic number of $PbWO_4$ is determined to $Z_{eff} = 68.3$ using Eq.(5.5) and the composition of $PbWO_4$ shown in Tab. 7.1 on page 41. According to Eq.(5.6), the critical energy of $PbWO_4$ is calculated to $E_c = 8.8\,\mathrm{MeV}$. This value is compatible with values for the critical energy quoted in [gau97].

The scale factor b has to be determined from Fig. 5.1. As the densities of iron ($7.87\,\mathrm{gcm}^{-3}$) and $PbWO_4$ ($8.28\,\mathrm{gcm}^{-3}$) are comparable, we assume $b \approx 0.5$ independent of the electron energy. The parameter a can now be calculated for a particular electron energy using Eq.(5.12). The resulting shower shapes according to Eq.(5.10) for electrons hitting $PbWO_4$ are shown in Fig. 11.7 for different energies.

Taking the location of the shower maximum from Eq.(5.11), 98% of the electron energy is deposited within a calorimeter length of

$$L(98\%) = 2.5\,t_{max}, \quad t_{max} \text{ in units of } X_0 \tag{11.1}$$

for electron energies between 10 and 1000 GeV [gru93]. As an example, for a $PbWO_4$ calorimeter and an electron energy of 30 GeV, $L(98\%)$ amounts to 19.1 X_0.

The $PbWO_4$ crystals used in the Crystal BPC have a length of 20 cm corresponding to 22.5 radiation lengths. As can be seen in Fig. 11.7, the length is not sufficient to fully contain the electromagnetic shower, thus an energy–dependent fraction of the shower is lost due to longitudinal shower leakage, escaping detection. This effect increases at higher energies, deteriorating the linearity of the energy measurement, and hence must

be corrected for. This is done by determining energy dependent correction factors by integrating the appropriate shower shape over the calorimeter length (see section 12.4.4).

Chapter 12

Test Beam Measurements of the Crystal BPC at the CERN SPS

The beam test was carried out in May, 1998 at the X5 beam line of the CERN SPS with electrons of energies from 3 to 100 GeV, pions of 30 GeV and muons.

12.1 The CERN SPS X5 test beam facility

The X5 beam line in the West Area of CERN is a tertiary beam. It is derived from the CERN SPS proton synchroton via the H3 secondary beam.

Primary protons of momentum up to 450 GeV are slow–extracted from the SPS. Every SPS cycle, typically 2.58 s repeated every 14.4 s, a primary beam of about 1.5×10^{12} protons impinges on the T1 primary target. Secondary particles produced by interactions in this target, which consists of Beryllium and has a length of 40 cm, are momentum selected by the H3 beam optics and transported to two secondary targets X5 and X7. Most commonly, the H3 beam is adjusted to a momentum of -120 GeV, which allows the maximum flexibility in the derived test beams. In this mode, the H3 beam is composed to 90% of hadrons (83% $\pi^{\pm}$, 5.5% $K^{\pm}$ and 1.5% (anti)protons) and to 10% of $e^{\pm}$ [gat99].

The X5 target is the origin of the X5 beam line. A schematic view is shown in Fig. 12.1. The mentioned components are described in the following:

Secondary target: The secondary target units are motorised units that allow to put one out of four targets in the beam. The choices are the following:

- 4 mm of Lead, i.e. almost a radiation length, almost no interaction length
- 40 cm of Copper, i.e. more than 30 radiation lengths, 3 interaction lengths
- 40 cm of Beryllium, i.e. roughly one radiation and interaction length
- only air (X5 in secondary beam mode)

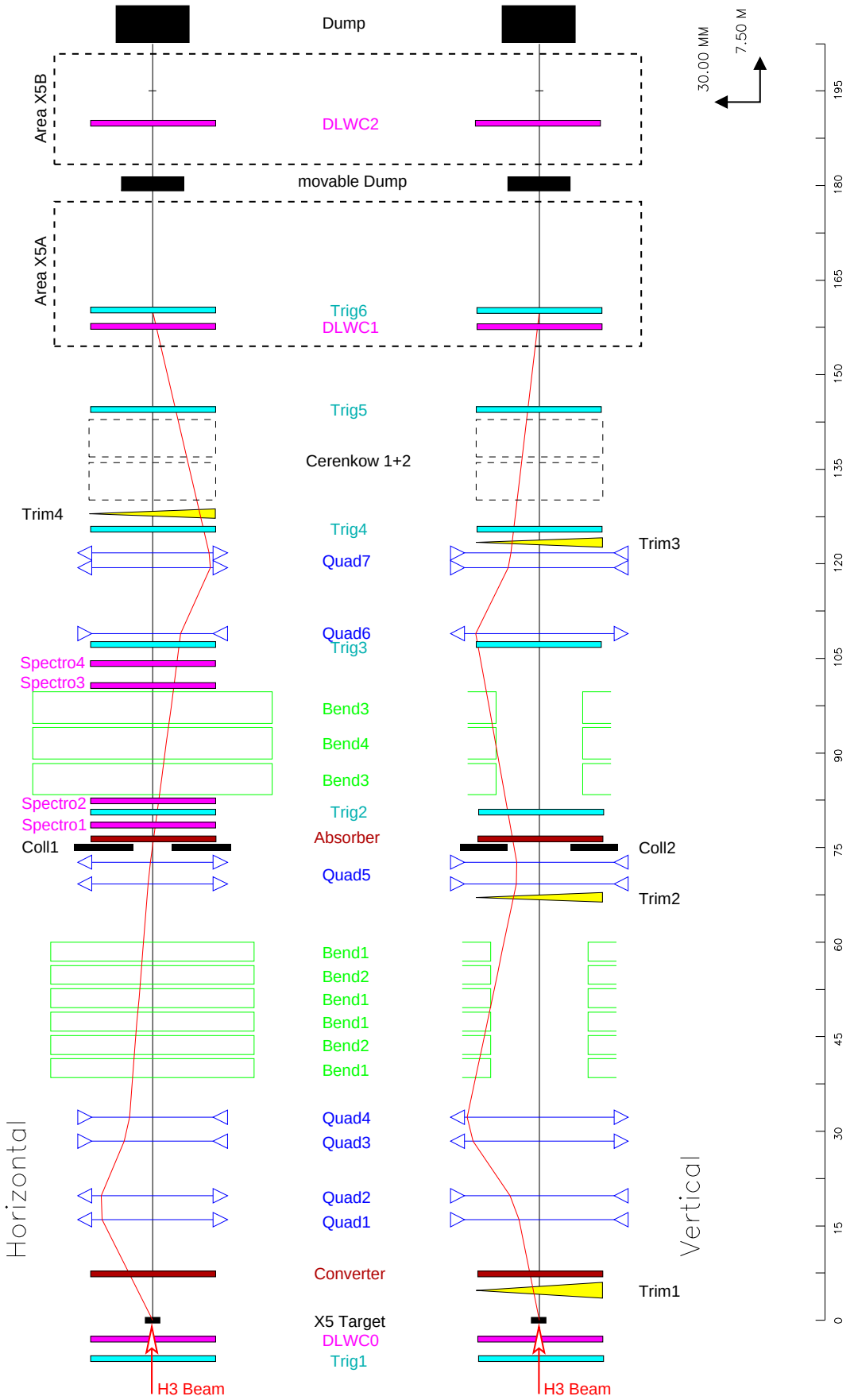

Figure 12.1: Overview of the CERN SPS X5 test beam optics. The beam is focused to area X5A.

Converter: A converter is a piece of material (normally a few mm of lead) that is situated after a production target and a sweeping magnet. The magnet removes all charged particles from the beam line and the photons remaining convert in the converter into e^+e^- pairs. The electrons (positrons) are picked up by the beam transport and are delivered to the experiment as if they were produced directly in the production target. This technique may lead to very clean electron beams.

Absorber: An absorber is a piece of material (normally a few mm of lead) that is brought into the beam passage to remove remaining electrons in the beam. Since the electrons lose energy in the material due to Bremsstrahlung, they will not be transported all the way down to the experiment and they are thus lost from the beam.

Quadrupole magnets: A quadrupole is a magnetic lens. Its purpose is to focus the beam in one of the principal planes. Contrary to an optical lens, which focusses normally in both planes, a quadrupole focusses in one plane but defocusses in the other.

Bending magnets: A bend is a magnet of the dipole type. Its purpose is to deviate a beam over an angle which is dependent on the beam momentum and the magnetic field.

Trim magnets: A trim is a small magnet of the dipole type. Its purpose is to correct the beam steering. Contrary to a main bend, its nominal field is exactly zero. Therefore these magnets are normally short and compact, as the required bending power is normally small.

Collimators: According to their position along the beam and depending on the optics chosen, collimators may have different roles:

- acceptance collimators control the beam flux
- momentum slits control the momentum band. Normally the flux transmitted is proportional to the momentum band.
- cleaning collimators clean up the debris produced by scattering off upstream elements

The collimator installed in the X5 beamline is a four–jaw collimator. It contains four independently motorised iron blocks of 1 m length each. Two blocks control the horizontal gap, the other two the vertical gap.

Trigger counters: Trigger counters are used for beam flux counting, beam tuning, and triggering purposes.

Delay line wire chambers: The delay line wire chambers (DLWC) are drift chambers that are read out through a delay line. The spatial resolution is about 200 μm, the sensitive area $10 \times 10\,\mathrm{cm}^2$. There are two types of DLWC:

- X/Y profile chambers provide measures of horizontal and vertical impact points of individual particles. Normally these are installed in the experimental areas, very close to the experimental apparatus.

- Spectrometer chambers have only a single plane readout. They are installed before and after bending magnets and allow a precise determination of the beam momentum.

Čerenkov counters: Threshold Čerenkov counters allow particle identification.

Dumps: Mobile dumps are used in the experimental halls to isolate a downstream area from an upstream one.

Every beam at CERN is terminated with a final fixed dump. The exact length and material of the dump depends on the intensity of the beam in question. Often the dump consists of 2.4 m of iron followed sometimes by some amount of concrete. For higher-intensity beams the dump is made re-entrant. This means that the particles are dumped in a hole. This helps to reduce the backsplash and skyshine from the dump.

The spectrometer chambers and Čerenkov counters were not functional during the Crystal BPC beam test.

The particle type is determined by the secondary target. An electron beam was obtained using the lead target. Electrons from the H3 beam are momentum degraded due to Bremsstrahlung processes in the target. Electrons with an energy which equals the energy to which the beam line is tuned are picked up by the beam transport, while the others are lost from the beam. For energies below 70 GeV, the beam consists to more than 99% of electrons. At higher energies, there is an unavoidable background of muons from decays of pions in the final straight section of the H3 beam. At an electron momentum of 100 GeV, the muon contamination amounts to more than 50%.

A hadron beam consisting of pions was produced using the copper target. Any remaining electrons due to conversion of photons from the π^0 decay were removed by inserting a 3 mm lead absorber plate at the location of the momentum slit. In the absorber, the electron momentum is degraded due to Bremsstrahlung processes and the electrons consequently are lost from the beam.

The total length of the H3 beam from the T1 target to the X5 target is about 700 m, whereas the overall length of the X5 beam from the X5 target to the experimental areas amounts to about 200 m.

A more detailed description of the X5 beam line together with with a description of the other beam lines in the CERN West Area can be found in [gat99].

12.2 The test beam setup

The beam test was performed in area X5A of the X5 beam line. An overview of the test beam area is shown in Fig. 12.2. The Crystal BPC was installed on a table which could be moved in X and Y directions relatively to the beam, making it possible to inject particles into different parts of the calorimeter.

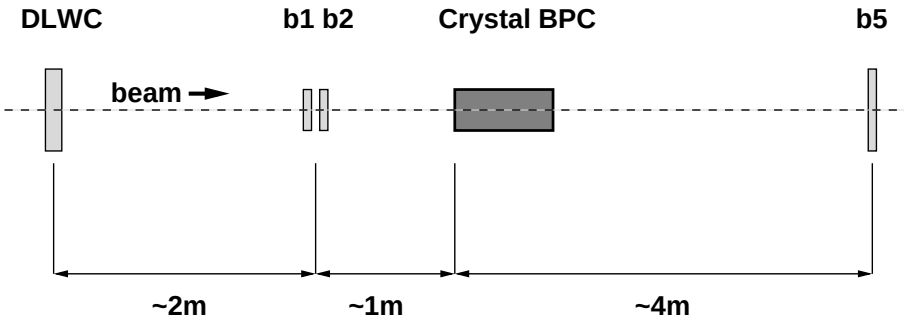

Figure 12.2: The test beam setup at the CERN SPS.

In front of the Crystal BPC at a distance of about 1 m, two trigger counters called b1 and b2 with active areas of $10 \times 10\,\mathrm{cm}^2$ were installed at a fixed position centered to the beam. The coincidence of these trigger counters served as trigger for the readout electronics. The analog signals of b1 and b2 were also read out to provide the possibility of offline cuts.

Further upstream, at a distance of about 3 m to the Crystal BPC, a delay–line wire chamber (DLWC) was installed measuring the impact position of beam particles in X and Y with a precision of 0.2 mm [gat99].

At a distance of about 4 m behind the Crystal BPC, another trigger counter called b5 with an active area of $20 \times 20\,\mathrm{cm}^2$ was located, similarly to b1 and b2 at a fixed position relative to the beam. The b5 counter was not included in the trigger decision, but served offline as an indicator for longitudinal energy leakage from the Crystal BPC, mainly caused by muons. Due to their low signal in b5, muons contaminating the electron beam could be removed from the data samples.

12.3 The readout system

An overview of the readout system which was used during the Crystal BPC test beam at CERN is shown in Fig. 12.3. The test beam data acquisition system was CAMAC based. The 16 calorimeter channels and three trigger counters b1, b2 and b5 were read out by LeCroy 2249A charge sensitive ADCs. The signals of the delay–line wire chamber (DLWC) which enabled us to determine the impact position of the particles with a precision of 0.2 mm were processed by a LeCroy 2228A TDC. The CAMAC crate was connected via a LeCroy 8901A GPIB interface to a GPIB bus and then via a National Instruments AT-GPIB interface board to a personal computer (PC) running the operating system LINUX. The readout software was custom-made and adapted to the test beam requirements. A description of the readout system can be found in [hen99].

In order to monitor temperature changes of the Crystal BPC, the calorimeter housing was equipped with four precision temperature sensors. In addition, one sensor was exposed to the ambient temperature. The sensors were read out by a separate PC equipped with an ADC card running a custom–made measurement program under the operating system Linux [mey95]. The temperatures were recorded once in a minute during the whole beam test time.

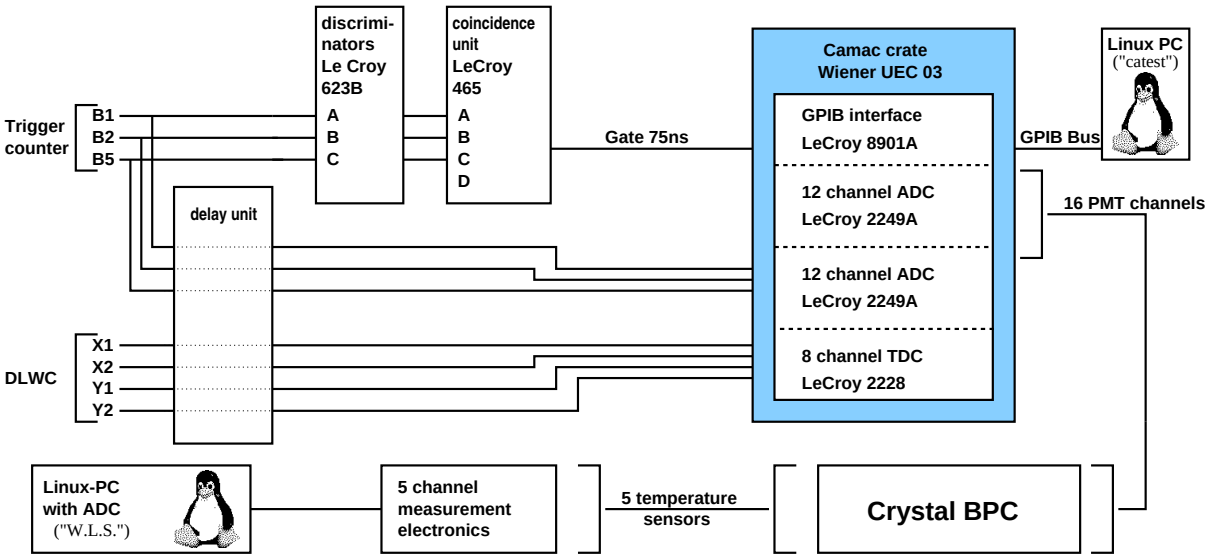

Figure 12.3: The test beam readout system (from [mey99]).

12.4 Reconstruction

The measurement of a single incoming particle using the Crystal BPC produces exactly 16 numbers, one for each readout channel. Each of them is correlated to the amount of light detected by the appropriate PMT and thus to the energy deposited in the appropriate crystal. Of course, there are many factors which influence the measurement results, such as electronic noise, electronic and optical differences between the calorimeter channels, temperature effects and leakage effects, to mention only a few. In order to perform precision energy and position measurements, all disturbing effects have to be evaluated and, if not classified as minor, corrected in the analysis.

The data obtained during the Crystal BPC CERN test was analysed using the ROOT data analysis system [bru97]. A listing of the program "cernnt.c", which was used to process the raw data, is shown in appendix F. In this section, the calibration and reconstruction methods are described which are used to obtain precision energy and position measurements from the raw data.

12.4.1 Pedestal subtraction

The pedestal is the number of ADC counts obtained in a measurement when no analog signal is applied to the ADC. Usually, it amounts to about 1% of the ADC's dynamic range and has to be subtracted from all ADC measurement results.

The pedestal of a particular ADC channel is determined by several factors. According to [lec95], the dominating factor is charge injection into the ADC channels within the ADC card, which assures proper operation of the ADC in case the quiescent DC level of the input should drift. Other factors influencing the pedestal values are grounding effects and quiescent currents from the PMTs, as well as the gate length. Hence, it is important to

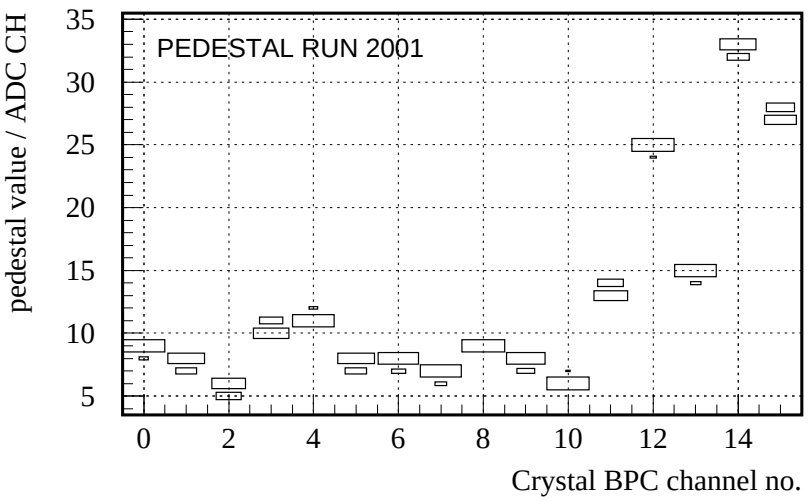

Figure 12.4: Typical pedestal run. The pedestal value is plotted versus the Crystal BPC channel number. The sizes of the boxes denote the number of entries in each bin. For each Crystal BPC channel, there are only entries in two bins. This very sharp pedestal distribution reveals very little noise in the readout chain.

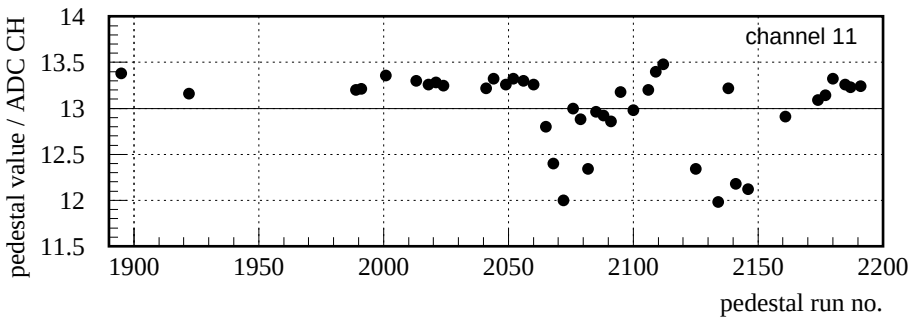

Figure 12.5: Summary of all pedestal runs taken during the CERN test. Only the Crystal BPC channel with the largest pedestal fluctuations is shown. Deviations from the mean value, which is denoted by a horizontal full line, amount to one ADC channel at maximum.

determine the pedestal values under same conditions as the actual measurement with the PMTs connected to the ADCs.

The pedestals of all ADC channels are measured in dedicated pedestal runs, where gates of the same length as in the actual measurement are initiated by a pulse generator at a frequency of about 100 Hz, independently of physics triggers.

In Fig. 12.4 the result of a typical pedestal run is shown for all Crystal BPC channels. The pedestal value is plotted against Crystal BPC channel. The sizes of the boxes denote the number of entries in each bin. For each Crystal BPC channel, there are only entries in two bins. This very sharp pedestal distribution indicates very little noise in the readout chain.

Fig. 12.5 shows a summary of all pedestal runs taken during the CERN test exemplarily

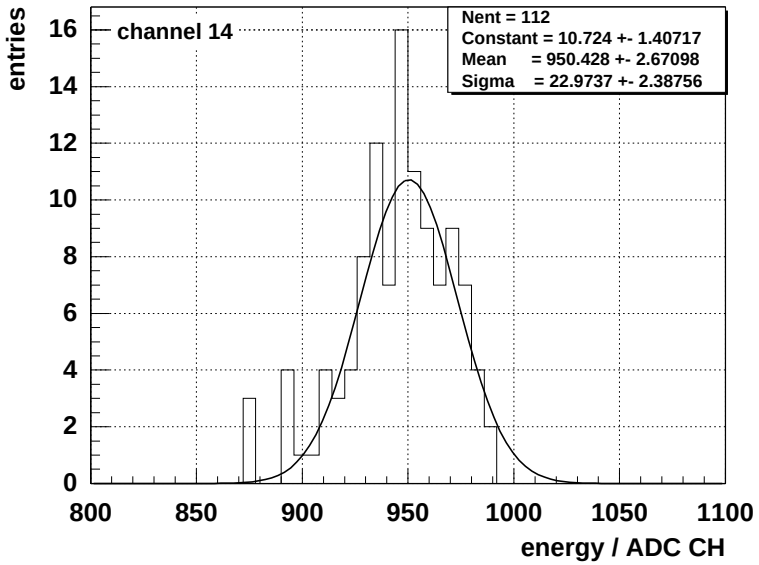

Figure 12.6: Channel-to-channel calibration of the Crystal BPC. The picture shows the energy spectrum of the Crystal BPC channel with the largest calibration error taken during a dedicated calibration run. A gaussian fit is applied to the spectrum, from which the calibration factor is calculated.

for the Crystal BPC channel with the largest pedestal fluctuations. Deviations from the mean value, which is denoted by a horizontal full line, amount to one ADC channel at maximum, demonstrating the good stability of the readout chain during the CERN test. As a consequence of this result, one mean pedestal value was determined for each readout channel averaging over all pedestal runs taken during the CERN test.

12.4.2 Channel-to-channel calibration

In order to perform a reliable energy measurement using the Crystal BPC, it must be ensured that all 16 channels of the calorimeter produce the same signal response if hit by electrons of the same energy, i.e. the calorimeter must be calibrated. The Crystal BPC was calibrated in two steps:

Coarse calibration: At the beginning of the test beam measurements, an iterative calibration procedure was performed during which electrons of defined energy (30 GeV) were shot consecutively into the centers of the crystals. For each crystal, short runs of 500 events were taken and the maximum of the energy spectrum of the current crystal was determined. The channel's HV was then adjusted in order to bring the maximum to a certain value and a new run was initiated. This procedure was repeated until the maximum of the channel's energy spectrum fitted within a range of 900 ADC CHs $\pm$ 2%. The determined nominal HV settings for all channels are shown in Tab. 12.1.

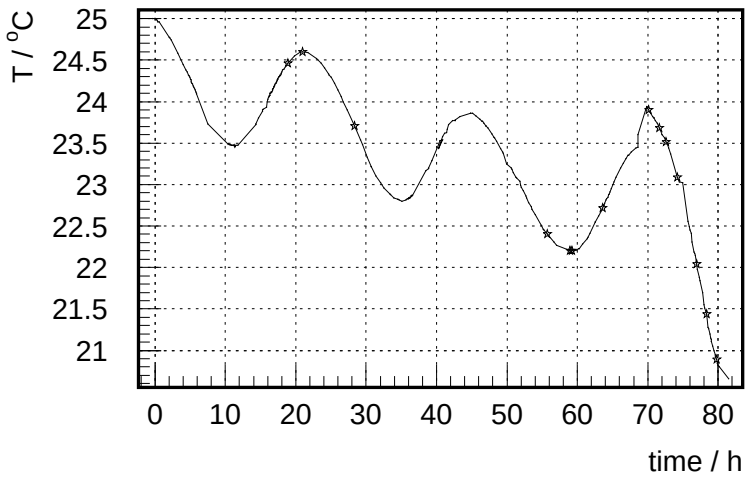

Figure 12.7: Temperature changes of the Crystal BPC housing during the CERN test. The temperature variation with a period of 24 hours is clearly visible.

Fine calibration: The fine tuning of the calibration was performed offline after the CERN test. For each Crystal BPC channel, a dedicated calibration run with the nominal HV setting (see Tab. 12.1) was analyzed. After pedestal subtraction (see section 12.4.1), a temperature correction (see section 12.4.3) was performed to correct for temperature changes. The calibration procedure required about three hours during which a rise of temperature of the calorimeter's housing of 0.8°C was observed. Without correction, this would lead to a miscalibration of about 1.6% at maximum between the first and the last calibrated channel.

A gaussian fit was then applied to the data. To avoid disturbing effects at the crystal edges, only electrons with an impact point on the calorimeter front plate within a circle of 5 mm radius centered upon the current crystal were included in the fit. The results of the fits, together with the calculated calibration factors, are shown in Tab. 12.1. Fig. 12.6 shows as an example the calibration of Crystal BPC channel 14, which is the channel with the largest calibration error. The energy spectrum shown already contains pedestal subtraction and temperature correction. The calibration factor is derived from the mean value of the gaussian fit applied to the spectrum. The fit is based on 112 out of 500 events which fulfil the above mentioned spatial cut.

12.4.3 Temperature correction

As mentioned in section 11.4, $PbWO_4$ has a distinct temperature dependence of the scintillation light yield which would influence the calorimeter's energy calibration if not corrected. It was planned to stabilize the temperature using a water cooling circuit and monitor the remaining temperature fluctuations by precision temperature sensors.

ch	HV / V	Pedestal / ADC CH	Channel-to-channel calibration			
			Run	Mean / ADC CH	Sigma / ADC CH	Calibration factor
low energy runs (3 ... 30 GeV)						
0	679	8.8 ± 0.3	1966	977.0 ± 2.6	19.02 ± 2.19	0.9211 ± 0.0025
1	644	7.5 ± 0.3	1968	983.3 ± 2.6	24.17 ± 2.63	0.9153 ± 0.0024
2	621	5.4 ± 0.3	1972	968.3 ± 1.7	16.57 ± 1.42	0.9295 ± 0.0016
3	645	10.1 ± 0.2	1974	975.4 ± 2.5	22.09 ± 2.23	0.9227 ± 0.0024
4	690	11.0 ± 0.1	1964	979.7 ± 2.3	20.46 ± 2.06	0.9187 ± 0.0022
5	635	7.5 ± 0.4	1962	957.7 ± 2.5	16.86 ± 2.50	0.9397 ± 0.0024
6	645	7.6 ± 0.4	1960	982.3 ± 2.2	19.51 ± 2.22	0.9162 ± 0.0021
7	624	6.7 ± 0.3	1956	972.1 ± 2.5	19.79 ± 1.27	0.9258 ± 0.0024
8	697	8.9 ± 0.2	1976	965.5 ± 2.7	22.70 ± 2.76	0.9322 ± 0.0026
9	643	7.6 ± 0.4	1949	975.9 ± 1.4	19.34 ± 1.06	0.9222 ± 0.0013
10	620	6.0 ± 0.2	1951	960.9 ± 1.7	21.76 ± 1.22	0.9366 ± 0.0017
11	640	13.0 ± 0.4	1953	967.2 ± 1.5	21.50 ± 0.97	0.9306 ± 0.0015
12	660	24.6 ± 0.4	1979	959.3 ± 1.6	16.33 ± 1.66	0.9382 ± 0.0016
13	721	14.8 ± 0.2	1981	968.1 ± 2.0	20.33 ± 2.01	0.9296 ± 0.0019
14	636	32.5 ± 0.3	1984	950.4 ± 2.7	22.97 ± 2.39	0.9469 ± 0.0027
15	660	27.3 ± 0.3	1986	973.4 ± 2.5	21.84 ± 2.36	0.9246 ± 0.0024
high energy runs (30 ... 100 GeV)						
10	520	see above	2130	233.3 ± 0.3	6.39 ± 0.22	3.8579 ± 0.0049

Table 12.1: Table of high voltage settings, pedestal values, and calibration related data for all Crystal BPC channels at the CERN test.

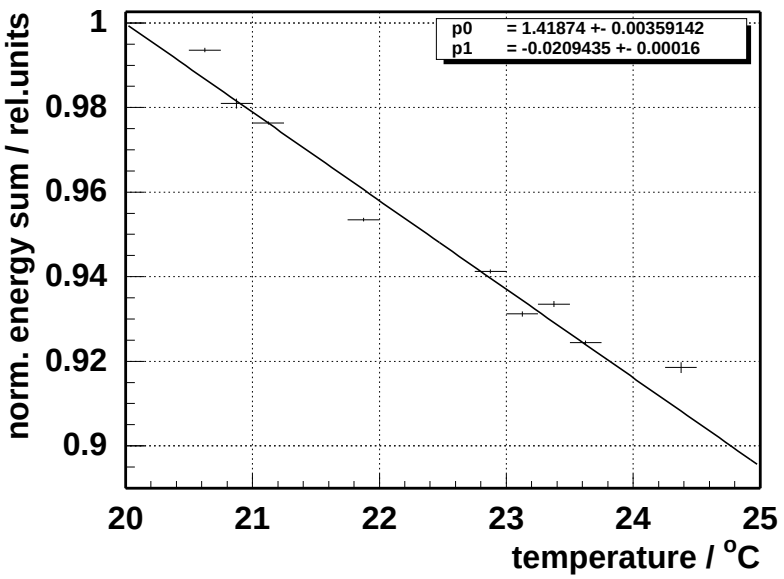

Figure 12.8: The temperature dependence of the Crystal BPC response to 30 GeV electrons. The energy response is normalized to a temperature of 20° C. A change in light yield of $-(2.09 \pm 0.02)\%/^{\circ}$C is obtained.

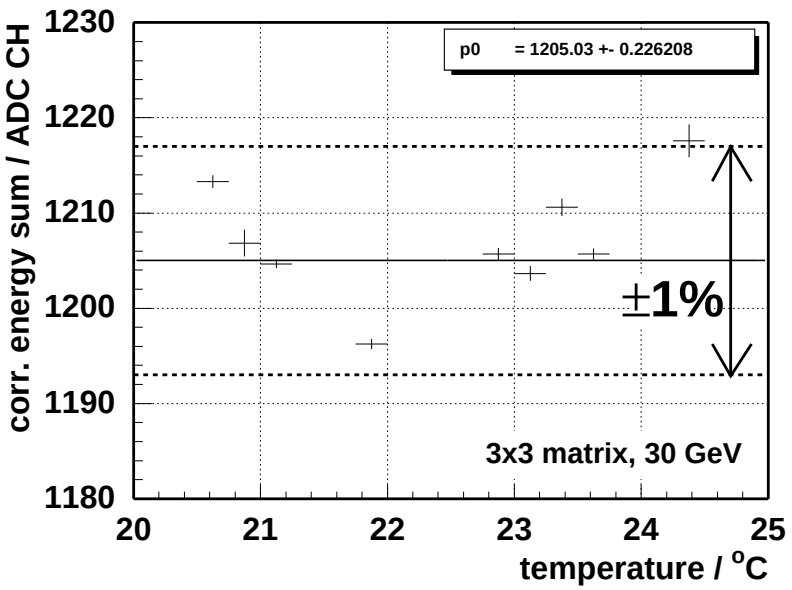

Figure 12.9: The results of all runs with 30 GeV electrons and the same running conditions after temperature correction. A correction accuracy of $\pm 1\%$ is achieved.

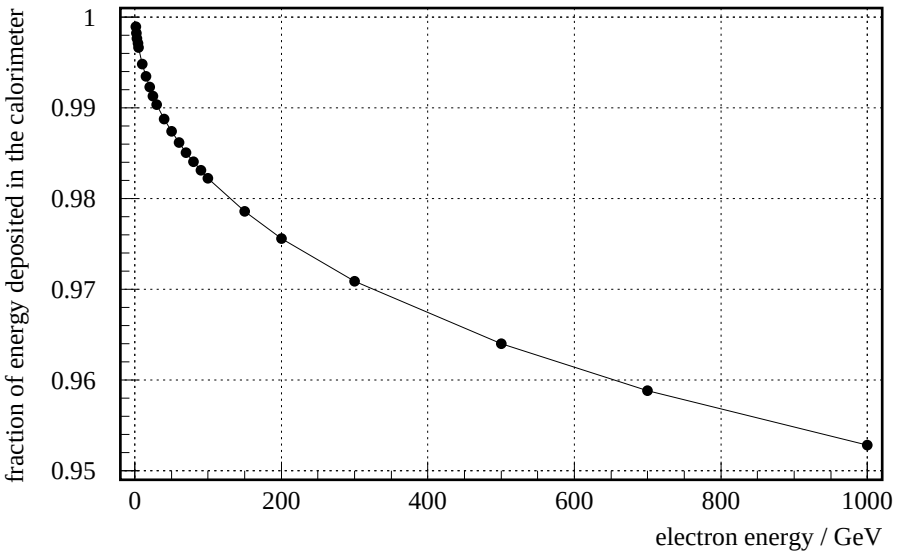

Figure 12.10: Simulated longitudinal shower leakage in the Crystal BPC for energies from 1 to 1000 GeV. The fraction of the electron energy which is deposited in the calorimeter is plotted versus electron energy.

During the Crystal BPC CERN test, the calorimeter's design was at an early stage of developement such that the foreseen water cooling pipes were not installed. Nevertheless, there were four precision temperature sensors attached to the calorimeter which recorded the housing temperature every minute. The calorimeter, packed in a box for thermal insulation, was exposed to temperature changes in the experimental area which were mainly caused by the diurnal cycle. The calorimeter housing temperature varied periodically with a period of 24 hours between 21°C and 24.5°C. This can be observed in Fig.12.7, where the housing temperature is plotted versus time.

To investigate the temperature coefficient of $PbWO_4$, dedicated runs were performed repeatedly where a 30 GeV electron beam was shot into the same central crystal, thus only varying the temperature. In Fig. 12.8 the Crystal BPC response to 30 GeV electrons is shown in dependence on the temperature. From these runs, a temperature coefficient of $-(2.09 \pm 0.02)\%/°C$ is obtained, which is compatible to previous measurements [rus97]. Using this information, the beam test data was corrected for the temperature effect. This is shown in Fig. 12.9, where the results of all runs with 30 GeV electrons and the same running conditions are displayed after the temperature correction. A correction accuracy of $\pm 1\%$ is achieved.

At ZEUS, temperature changes at the level of 2 °C were observed inside the BPC area. Significant changes occur when the RCAL, which surrounds the BPC hermetically, is opened or closed. To reduce the effect during data taking, the Crystal BPC will be surrounded by a housing of 10 mm thick copper which is temperature stabilized by a water cooling system. Temperature monitors are obligatory.

E_e	f_{BPC}	f_{leak}
3	0.998	0.002
5	0.997	0.003
10	0.995	0.005
15	0.993	0.007
20	0.992	0.008
25	0.991	0.009
30	0.990	0.010
50	0.987	0.013
70	0.985	0.015
100	0.982	0.018

Table 12.2: Fractions of the electron energy E_e deposited in the Crystal BPC f_{BPC} and lost due to longitudinal shower leakage f_{leak} in dependence of the electron energy.

12.4.4 Correction for longitudinal leakage

The $PbWO_4$ crystals used in the Crystal BPC have a length of 20 cm which corresponds to 22.5 radiation lengths. A simulation described in section 11.5 showed that the length is not sufficient to fully contain the electromagnetic shower. Due to this reason, an energy–dependent fraction of the shower is lost due to longitudinal shower leakage. This effect increases at higher energies, deteriorating the linearity of the energy measurement, and hence must be corrected for.

The fraction of the electron energy which is deposited in the calorimeter is determined by integrating the appropriate shower shape over the calorimeter length. These values are taken as energy dependent correction factors. Fig. 12.10 shows the energy fractions deposited in the calorimeter for energies from 1 to 1000 GeV. The correction factors which were used to correct the beam test data for longitudinal leakage are listed in Tab. 12.2.

12.5 Measurements

12.5.1 Electron identification

As far as the beam is concerned, there are several factors which might deteriorate the test beam measurements. The electron beam may be contaminated with other particles, such as hadrons ($\approx$1%) or muons (>50% for energies above 70 GeV). In addition, an incident electron might interact in material in front of the Crystal BPC (preshowered electron) or touch the boundary of the DLWC. A third effect are random coincidences which cause random triggers without the presence of an electron. All these events cause misleading energy deposits in the Crystal BPC. Hence, some criteria were established to identify these events and remove them from the data sample.

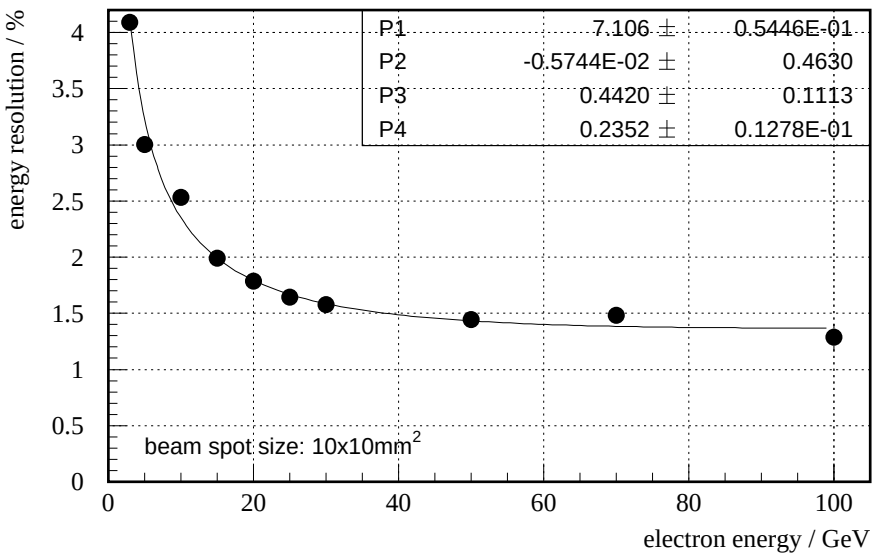

Figure 12.11: The energy resolution of the Crystal BPC, measured with electrons with energies from 3 to 100 GeV and a beam spot size of $10\times10\,\mathrm{mm}^2$. The fitting parameters denote the statistical, noise, constant, and leakage terms in this order (see text).

It was found that showers initiated by electrons in the Crystal BPC have a significant lateral shower width. Other particles, like muons, hadrons, or pre–showered electrons, show a significantly different shower width. Furthermore, the analog signal of the trigger counter b5 was found to be a good criterion for the detection of muons contaminating the electron beam.

The following offline cuts on the shower width SWR (see section 12.5.5) and the analog signal of trigger counter b5 (see section 12.2) were applied to ensure the selection of a "good electron":

$$12\,\mathrm{mm} < \mathrm{SWR} < 18\,\mathrm{mm} \qquad \text{and} \qquad \mathrm{b5} < 80\,\mathrm{ADC\ CH} \tag{12.1}$$

These standard cuts were performed on all electron runs for all energies from 3 to 100 GeV. In some cases, e.g. the energy resolution analysis, the data sample was further refined by spatial cuts on the DLWC coordinates.

12.5.2 Energy Resolution

An excellent energy resolution is the major requirement of the Crystal BPC. To allow higher precision measurements of the proton structure function F_2 and a further extension of the kinematic region, an improvement of the actual energy resolution from $17\%/\sqrt{E/GeV}$ to about $5\%/\sqrt{E/GeV}$ is necessary.

Fig. 12.11 shows a measurement of the energy resolution with electron energies from 3 to 100 GeV and a beam spot size of $10\times10\,\mathrm{mm}^2$. A fit according to Eq.(5.19) is applied to the data. The fitting parameters denote respectively the statistical, noise, constant, and leakage terms. The statistical, constant, and leakage terms are determined to be

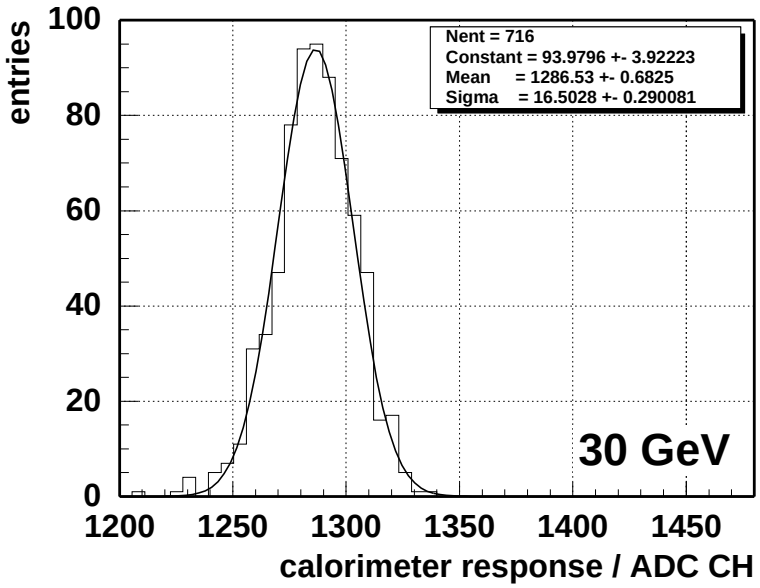

Figure 12.12: The energy resolution of the Crystal BPC, measured with 30 GeV electrons. The beam spot size measured $4\times6\,\mathrm{mm}^2$. An energy resolution of 1.28% is obtained. Taking into account the constant term of 0.4% and the leakage term of $0.24\%\cdot\ln(E/GeV)$, the statistical term is determined to be $4.9\%/\sqrt{E/GeV}$.

$(7.1\pm0.05)\%/\sqrt{E/GeV}$, $(0.4\pm0.1)\%$, and $(0.24\pm0.01)\%\cdot\ln(E/GeV)$, respectively. The contribution of the noise term is negligible.

In Fig. 12.12 the result of a measurement with a restricted beam spot size of $4\times6\,\mathrm{mm}^2$ is shown. A 30 GeV electron beam was injected into the center of an inner crystal of the Crystal BPC. The energy resolution results in 1.28%. According to Eq.(5.19) and taking into account the constant term of 0.4% and the leakage term of $0.24\%\cdot\ln(E/GeV)$, the statistical term is determined to be $4.9\%/\sqrt{E/GeV}$. This result is obtained assuming the hypothetical case of a monoenergetic electron beam. Taking into account the more realistic case of a spread beam energy (not much less than 1% [gat98]), which contributes to the uncertainty of the energy measurement, the result for the calorimeter's energy resolution would improve accordingly. Measurements of CMS at CERN resulted in an energy resolution of $4.2\%/\sqrt{E/GeV}\oplus\,0.34\%$ for a 3×3 array of $PbWO_4$ crystals read out by Avalanche photodiodes (APDs) [cms97].

The mean value of 1286.5 ADC channels corresponds to 16709 p.e. or 557 p.e./GeV of energy deposit. According to Poisson statistics, this p.e. yield contributes with $4.2\%/\sqrt{E/GeV}$ to the statistical term of the energy resolution. The p.e. yield observed in the test beam measurements is only about half the p.e. yield which was reached in the bench tests (see section 8.3). Those measurements were performed with optimal optical couplings of the lightguide to the single crystal and to the PMT whereas apparently the optical couplings are worse in the full Crystal BPC. Although the light yield is sufficient, it can still be improved by optimizing the assembly procedure.

12.5.3 Linearity

The linearity of the Crystal BPC was tested using electrons with energies of 3, 5, 10, 15, 20, 25, 30, 50, 70 and 100 GeV. The beam was injected into a central crystal. In Fig. 12.13 (left) the calorimeter response is shown in dependence on the beam energy for low energy (top) and high energy runs (bottom). This subdivision of the data was required because of a different energy calibration of the calorimeter for low energy and high energy runs. The data points represent the average calorimeter response to electrons hitting the calorimeter within a square of $10 \times 10\,\mathrm{mm}^2$ in horizontal and vertical dimension centered upon the crystal. The data are corrected for longitudinal leakage as described in section 12.4.4.

A linear fit to the low energy data shows an energy offset of 0.7 GeV which might be explained by a miscalibrated test beam energy at low energy. Similar effects have been observed by other experiments in the X5 beam line [goe98, wol98].

Fig. 12.13 (right) shows the deviation of the measured data from the fitted line. The deviation is smaller than $\pm 1\%$ for energies equal to or greater than 10 GeV. Only the 5 GeV and 3 GeV data, measured with a low intensity beam and very poor statistics, show larger deviations of 4.3% respectively 16.9%.

12.5.4 Uniformity

The response and energy resolution of the Crystal BPC will suffer from non-uniformities due to various effects. The first is simply that some fraction of the shower will leak into the surrounding dead material and not be converted into photoelectrons. This shows up as a reduced response at a given energy if an electron hits near the calorimeter edge. A second effect might be due to the coupling of the PMT to the crystals: the connecting lightguide covers only a center circle of 8 mm diameter of the crystals, which might cause an enlarged loss in light for electrons which hit near the crack between two crystals.

In Fig. 12.14 the calorimeter response to a 15 GeV electron beam is plotted versus horizontal electron impact position determined by the DLWC. The results are shown for one half of the calorimeter (two adjacent crystals). The histogram bins represent the average calorimeter response to electrons hitting the calorimeter perpendicularly within a square of 1.2 mm in horizontal and 6 mm in vertical dimension.

In [mey99], the beam test data is compared to an EGS4 Monte Carlo simulation. The Monte Carlo describes the real geometry of the Crystal BPC including the cracks between the crystals. The behaviour of the calorimeter response at the calorimeter edges and the cracks is in agreement with the Monte Carlo. Studies concerning the light collection efficiency showed that the non-uniform optical readout of the crystals using small cylindrical lightguides only has a negligible effect on the uniformity of the energy response. With the aid of the BPT, however, this specific, position dependent response can be measured, so that these effects are controllable.

The third effect is that shower fluctuations will randomly send more or less energy out of the crystal, resulting in a broadened resolution. This effect becomes more pronounced the closer the impact point is to the crystal edge. In Fig. 12.15 the energy resolution is plotted versus the horizontal electron impact position. Again, the results are shown for one half

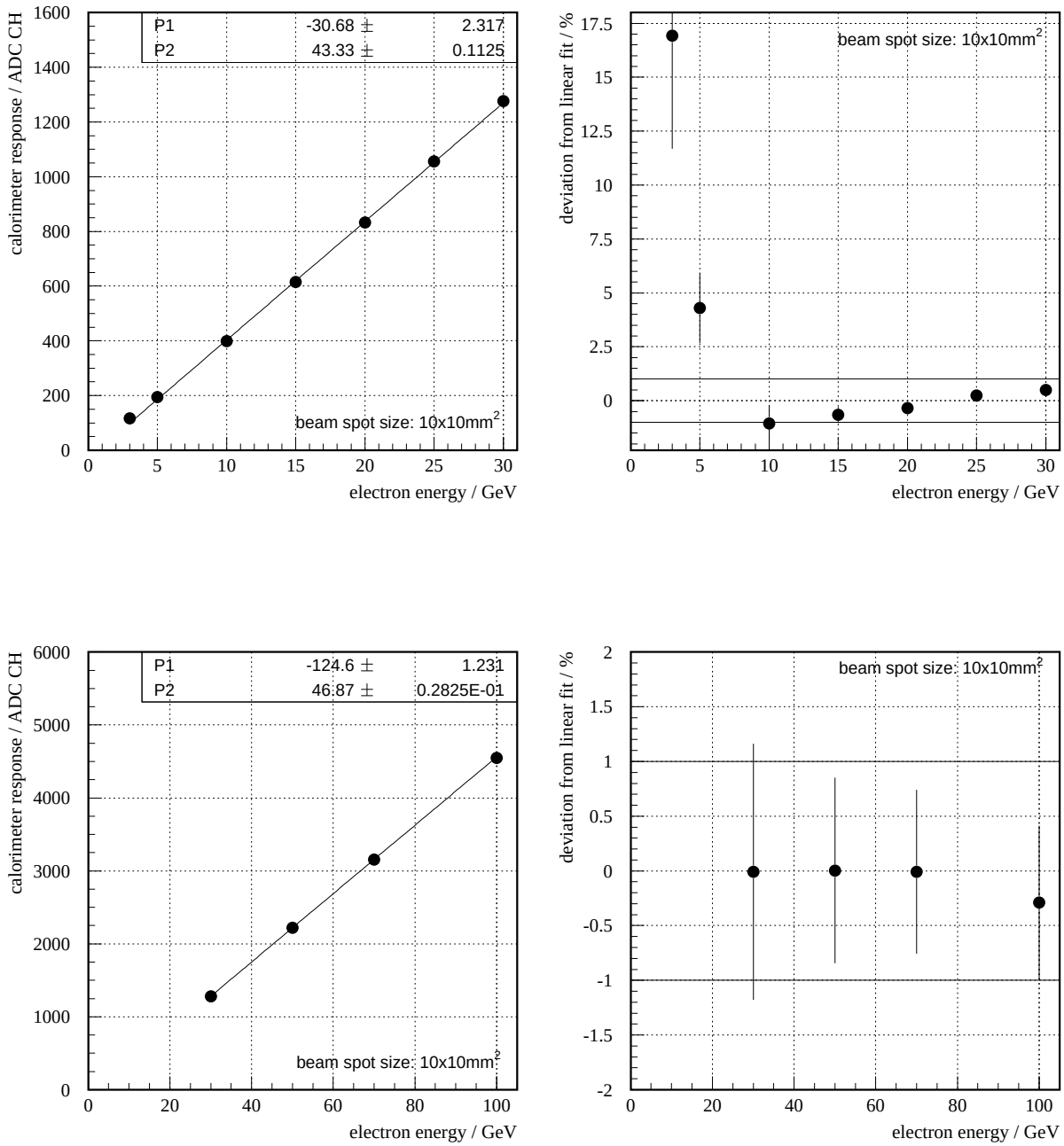

Figure 12.13: Linearity of the Crystal BPC, measured with electrons from 3 to 100 GeV. The plots show the calorimeter response versus beam energy (left) and the deviation from a linear fit to the data (right) for low energy runs (top) and high energy runs (bottom). The parameters P1 and P2 denote the offset and the slope of the fitted lines, respectively.

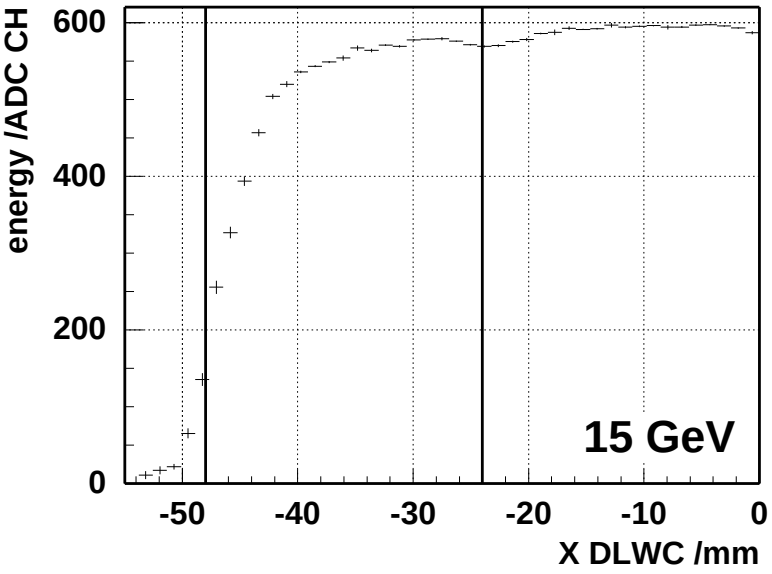

Figure 12.14: Uniformity of the Crystal BPC for vertical incidence of 15 GeV electrons. The beam is injected at different horizontal positions over one half of the calorimeter. The crystal boundaries are marked by vertical full lines at $X = -48$, -24, 0 mm. For values of $X < -48$ mm, the electrons hit the calorimeter housing.

of the calorimeter. Our measurements show that the resolution reaches $17\%/\sqrt{E/GeV}$, equal to the resolution which BPC II achieves inside its fiducial area, at 6 mm from the calorimeter edge.

12.5.5 Position and shower reconstruction

The X position X_{rec} of an incident particle is reconstructed according to the following procedure (see [awe92] for further details). The position is calculated by the formula

$$X_{rec} = \frac{\sum_{i=column\,1}^{column\,4} w_i\, X_i}{\sum_{i=column\,1}^{column\,4} w_i} \tag{12.2}$$

where X_i is the X coordinate of the center of crystal column i.

First, the energies of the four crystals arranged in a vertical column are summed up for each column:

$$E_i = \sum_{j=1}^{4} E_i^j, \qquad i = column\,1 \ldots column\,4 \tag{12.3}$$

E_i^j is the energy deposit in the jth crystal of crystal column i, and E_i is the total energy deposit in the crystal column i.

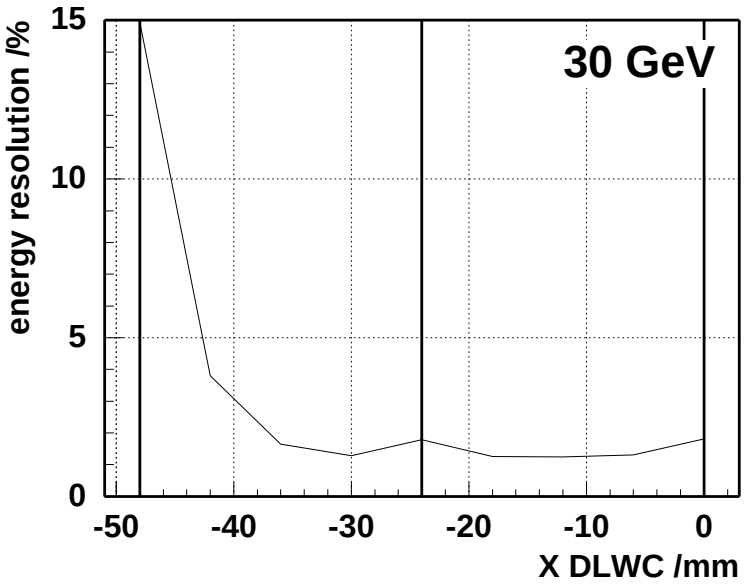

Figure 12.15: Energy resolution of the Crystal BPC in dependence on horizontal impact position for one half of the calorimeter, measured with 30 GeV electrons and a beam spot size of $10\times10\,\mathrm{mm}^2$. The beam energy spread of 1% [gat98] has been subtracted.

The weight factors w_i are calculated from the logarithm of the energy deposited in the crystal column in order to take into account the exponential falloff of the lateral shower energy distribution. They are given by the the expression

$$\begin{aligned} w_i &= W_0 + \ln\left(\frac{E_i}{E}\right) \quad \text{if} \quad W_0 + \ln\left(\frac{E_i}{E}\right) > 0 \\ &= 0 \quad \text{else}, \end{aligned} \tag{12.4}$$
$$i = column\,1 \ldots column\,4$$

Here, E_i is the energy deposit in the crystal column i, E is the total energy deposit in the calorimeter, and W_0 is a free parameter which has to be optimized.

The square of the dispersion of the shower is given by the formula

$$D_x^2 = \frac{\sum\limits_{i=column\,1}^{column\,4} w_i\, X_i^2}{\sum\limits_{i=column\,1}^{column\,4} w_i} - \left(\frac{\sum\limits_{i=column\,1}^{column\,4} w_i\, X_i}{\sum\limits_{i=column\,1}^{column\,4} w_i} \right)^2 \tag{12.5}$$

Again, X_i is the X coordinate of the center of crystal column i, and the weight factors w_i are calculated according to Eq.(12.4).

The Y position Y_{rec} of an incident particle is reconstructed accordingly, exchanging X by Y and columns by rows.

The total shower dispersion, referred to as shower width SWR, is given by

$$\mathrm{SWR} = \sqrt{D_x^2 + D_y^2} \tag{12.6}$$

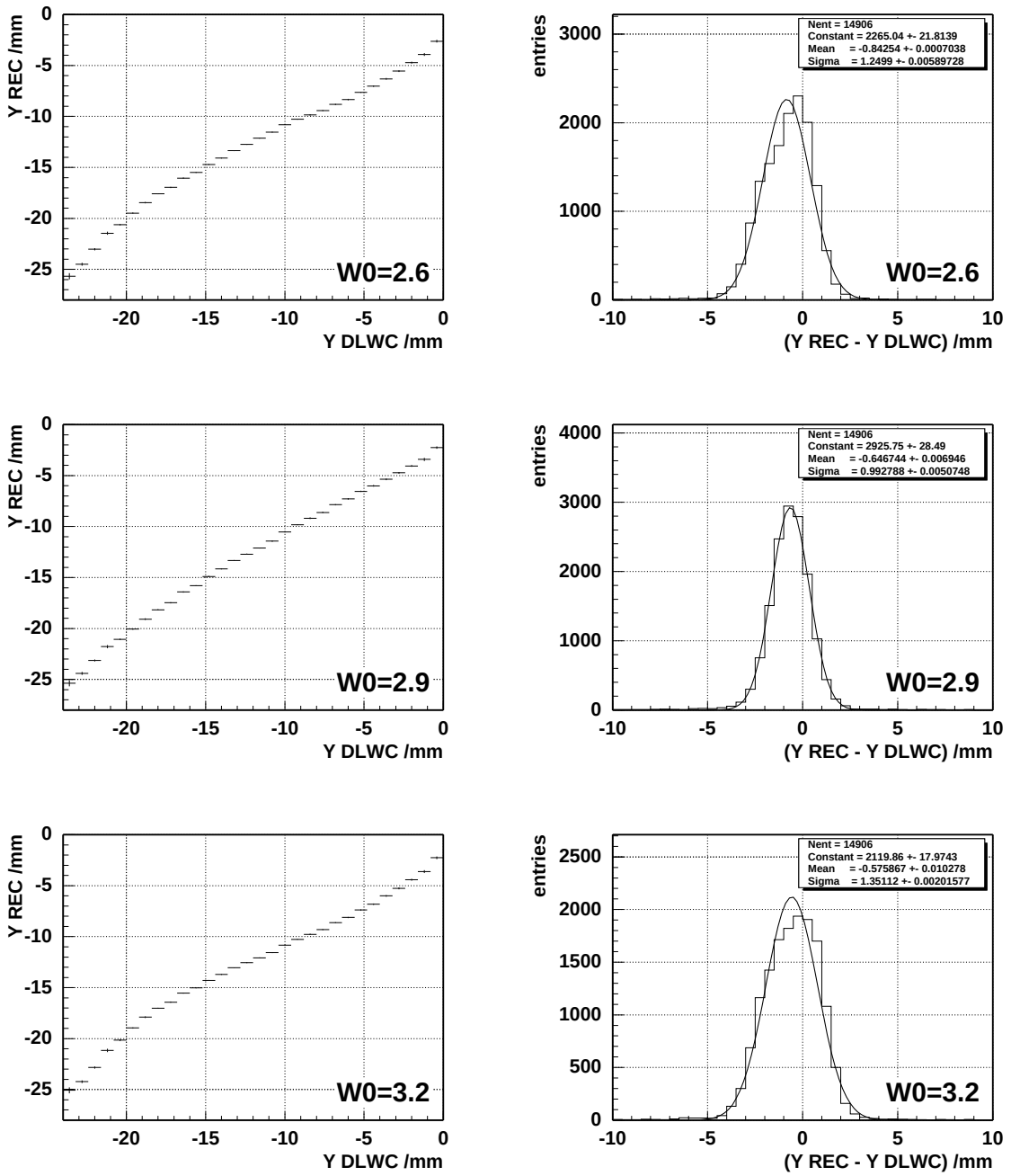

Figure 12.16: Determination of the free parameter W_0 for position reconstruction by means of experimental data at an electron energy of 30 GeV. The picture shows the reconstructed vertical electron position Y_{rec} versus the vertical position measured by the DLWC Y_{DLWC} (left) and the absolute measurement error $Y_{rec} - Y_{DLWC}$ (right) for $W_0 = 2.6$ (top), 2.9 (middle), 3.2 (bottom). The value $W_0 = 2.9$ was found optimal.

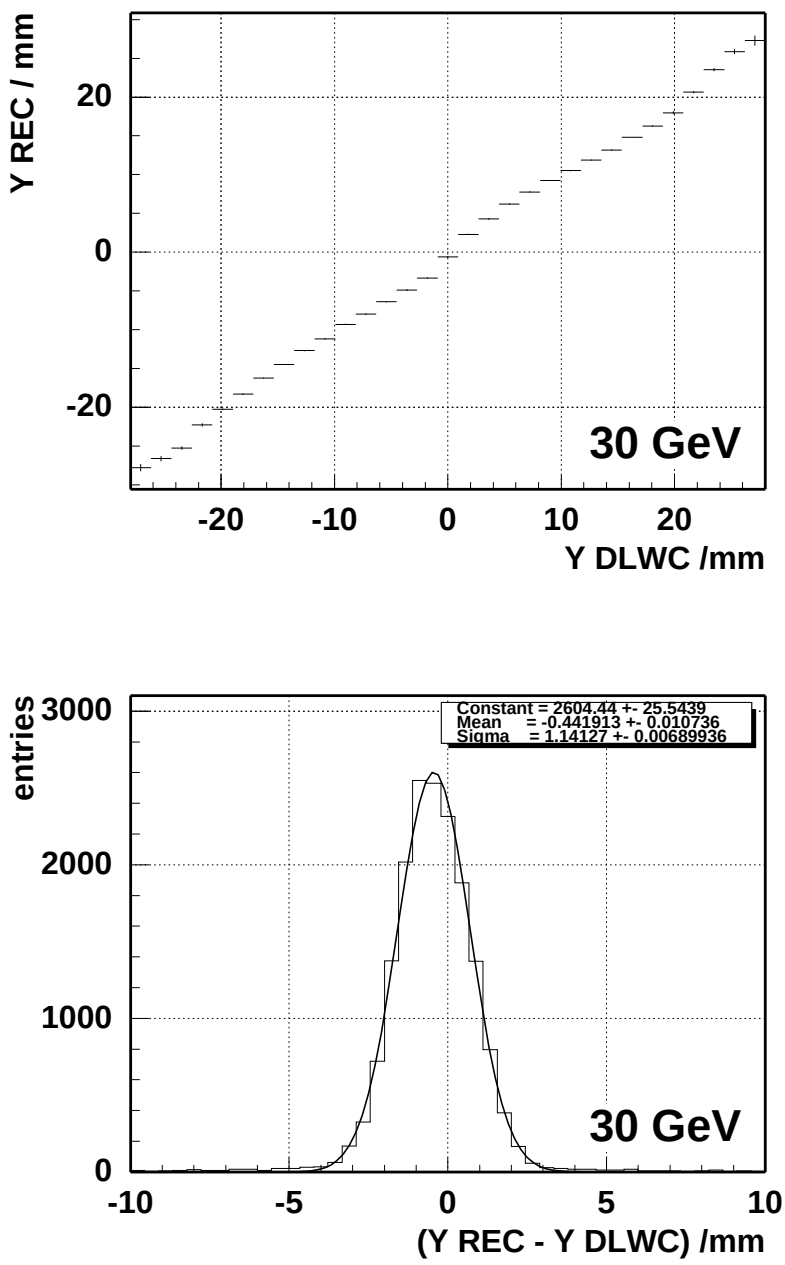

Figure 12.17: Position reconstruction in Y direction in two central crystals of the Crystal BPC (top) and the absolute error $Y_{rec} - Y_{DLWC}$ (bottom) of this measurement. A position resolution of (1.14±0.01) mm is obtained. The electron energy is 30 GeV.

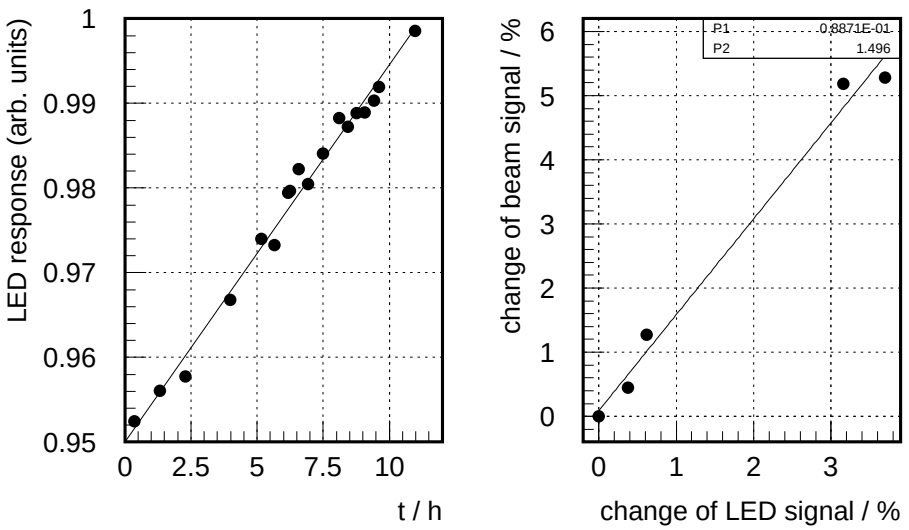

Figure 12.18: Recovery of the irradiated crystal. In the left figure the increasing signal of the LED radiation monitoring system with increasing time is shown. The right plot shows the correlation between LED signal and beam response.

In [awe92], Monte Carlo studies were performed simulating electron and pion showers in a 5×5 matrix of BGO crystals, each with dimensions $2.49 \times 2.49 \times 25\,\mathrm{cm}^3$. The radiation length of BGO amounts to 1.13 cm and the Molière radius is 2.44 cm. In this simulation, a value of $W_0 = 4.5$ was found optimal.

For the Crystal BPC, a study was performed to determine the optimum value for the parameter W_0. A set of CERN test data was analyzed using different values for W_0. Some of the results are shown in Fig. 12.16. In the left plots, the dependence of the reconstructed Y position on the Y position measured by the DLWC is shown. In the right plots, the error of the position measurement, calculated as the difference of the reconstructed position and the position measured by the DLWC, can be observed. Best results were achieved with a value of $W_0 = 2.9$.

In Fig. 12.17, the position reconstruction of the Crystal BPC in the Y direction is shown for two central crystals. The position resolution is found to be $(1.14 \pm 0.01)\,\mathrm{mm}$ at an electron energy of 30 GeV.

12.5.6 Test of the radiation damage monitoring system

The radiation damage monitoring system (see section 11.3) provides measurements of the crystals' transmissions in order to detect radiation induced transmission changes. It proved its functionality when two crystals were interchanged with irradiated crystals and the recovery was tracked. In Fig. 12.18 (left) a nearly linear rise of the LED signal of one recovering irradiated crystal with time can be observed. The correlation between the

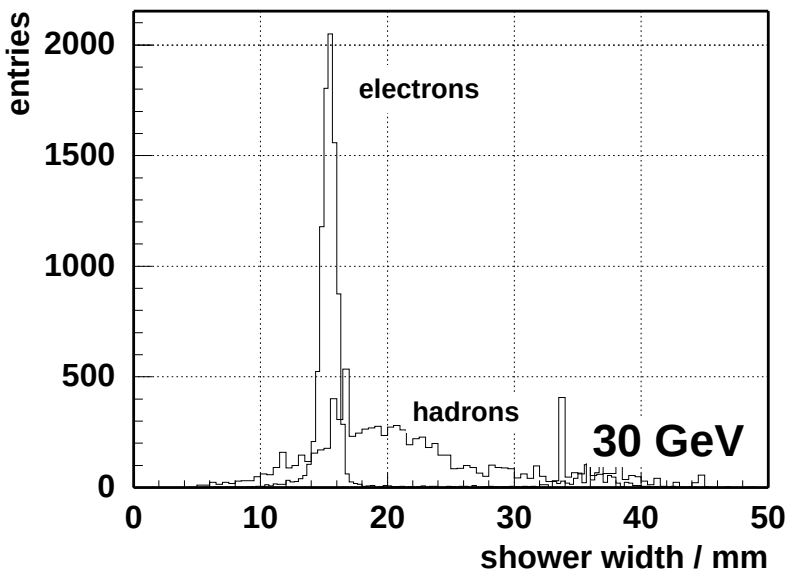

Figure 12.19: Shower width distributions for electrons and hadrons with energies of 30 GeV.

rise of the LED signal and of the crystal response to a 30 GeV electron beam is shown in Fig. 12.18 (right).

12.5.7 Hadron rejection

As mentioned in section 5.3, showers initiated by hadrons in general show a broadened lateral distribution compared to electromagnetic showers. Due to this fact, the shower width reconstructed according to Eq.(12.6) can be used to identify incident hadrons in the Crystal BPC.

In Fig. 12.19 the shower width distributions of an electron run and a hadron run, both with particle energies of 30 GeV, are compared. Electrons show a very sharp shower width distribution. Compared to this, the broadened shower width distribution of hadrons with a tendency to a greater lateral shower width is clearly visible. By applying cuts at appropriate boundaries on the shower width, a considerable fraction of hadrons can be removed from the data sample.

Chapter 13

Conclusions

Several measurements have been performed concerning the properties of $PbWO_4$ crystals. The light yield of the crystals was significantly improved by the manufacturer. Together with an optimized optical readout of the crystals, a photoelectron yield of 1240 p.e./GeV was achieved with single crystals. The decay time of the scintillation signal was also improved. More than 99% of the scintillation light is emitted within 100 ns. The radiation damage of the crystals was found to saturate after a low absorbed dose of a few Gy. The crystal transmission at saturation level of at least 80% of the initial value is still sufficient to allow proper operation of the calorimeter. The observed correlation between the radiation damage and the crystal transmission at 380 nm offers the possibility to recognize radiation–hard crystals without irradiation measurements. In summary, the measurements show that $PbWO_4$ crystals have reached a high quality level which makes it possible to use them for high precision calorimetry.

The Crystal BPC has been built in its final dimensions and proved its functionality during a CERN SPS beam test. The energy resolution was measured to be $4.9\%/\sqrt{E/GeV} \oplus 0.4\% \oplus 0.24\% \cdot \ln(E/GeV)$ with a restricted beam spot size of $4\times6\,\mathrm{mm}^2$ and neglecting the energy spread of the electron beam. As the energy resolution is dominated by photoelectron statistics, it can still be improved by optimizing the assembly procedure such that the photoelectron yield of 1240 p.e./GeV which was achieved with single crystals is reached with the calorimeter. The deviation from linearity is smaller than 1% for energies $10\,\mathrm{GeV} \leq E_e \leq 30\,\mathrm{GeV}$, and the uniformity of the calorimeter response is in agreement with a Monte Carlo simulation. A position reconstruction algorithm based on logarithmic weighting of the single crystal responses resulted in a position resolution of $(1.14\pm0.01)\,\mathrm{mm}$ at an electron energy of 30 GeV. Using an event–by–event temperature correction, it was possible to correct the calorimeter response to an accuracy of 1% although the calorimeter was not temperature stabilized. Together with a temperature stabilization a much better result can be expected. The radiation damage monitoring system proved its functionality when two crystals were interchanged with irradiated crystals and the recovery was tracked. All these results show that the high demands concerning the calorimeter performance can be satisfied.

The Crystal BPC will not be installed in the ZEUS detector. The main reasons are a lack of man–power for the implementation of the new calorimeter in the ZEUS detector and the improvements by the 1997 analysis of the BPC II data. Using alternative methods of

reconstruction, a significant extension of the kinematic range was already achieved with BPC II. Nevertheless, our studies concerning the Crystal BPC clearly demonstrate the practicability of the construction and the possibility of successful operation of a compact high precision calorimeter of $PbWO_4$ crystals.

Appendix A

Overview of Crystal BPC channels

Fig. A.1 shows an overview of the Crystal BPC channels (front view). The channel numbers, the crystal numbers, and the PMT serial numbers are depicted for each Crystal BPC channel. The letters "f" and "b" indicate the orientation of the crystals inside the calorimeter. The crystal labels point towards the calorimeter's front ("f") or the backward ("b") direction. The crystal numbers in brackets denote the crystals which were exchanged for the test of the radiation damage monitoring system (see section 12.5.6). Furthermore, the Crystal BPC coordinate system is shown together with the coordinates of the crystals.

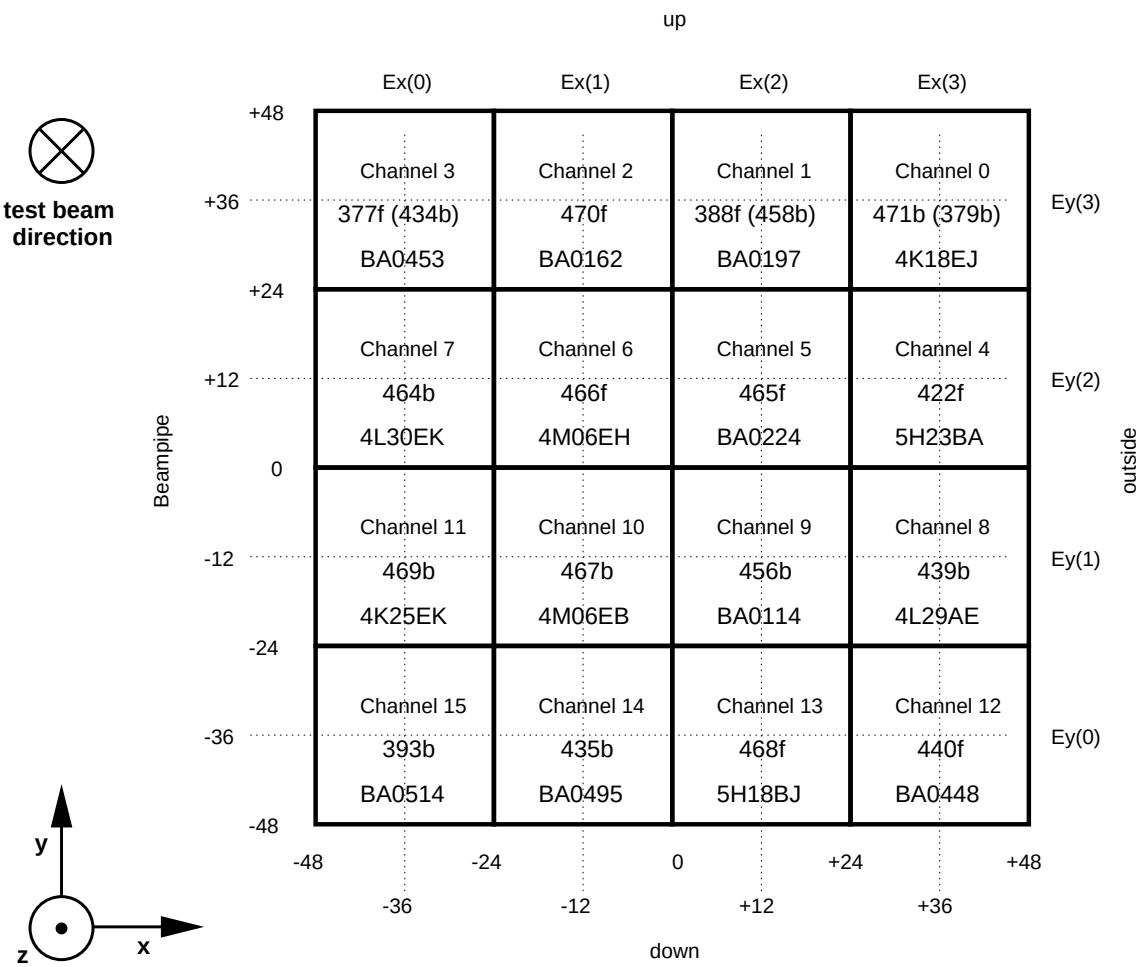

Figure A.1: Overview of the Crystal BPC channels. The picture shows the channel numbers, the crystal numbers, and the PMT serial numbers for each Crystal BPC channel.

Appendix B

Scintillation spectra of $PbWO_4$ crystals

This chapter shows the scintillation spectra of all twenty 1997 crystals and of two of the 1995 crystals. They were measured as described in section 8.4. The spectra are not normalized. It is clearly visible that for the 1997 crystals the scintillation light yield depends on the azimuthal orientation of the crystals relatively to the setup. This effect is investigated in section 8.4.3.

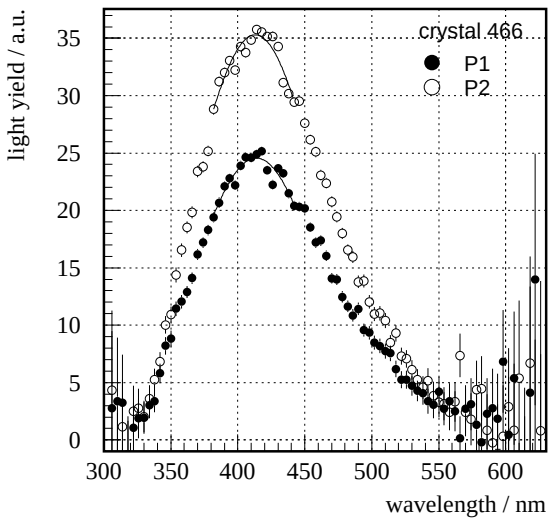
crystal 466
P1
P2
light yield / a.u.
wavelength / nm

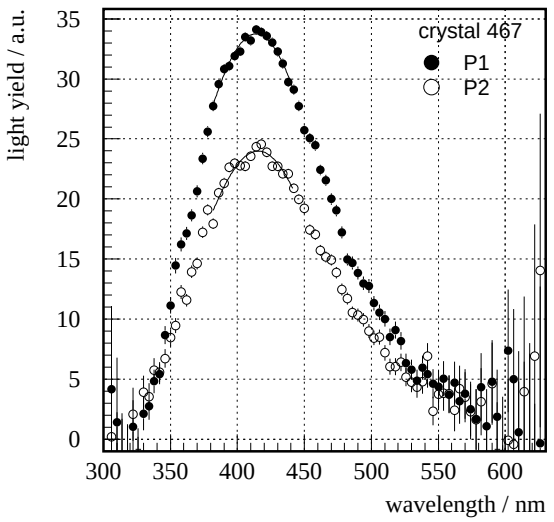
crystal 467
P1
P2
light yield / a.u.
wavelength / nm

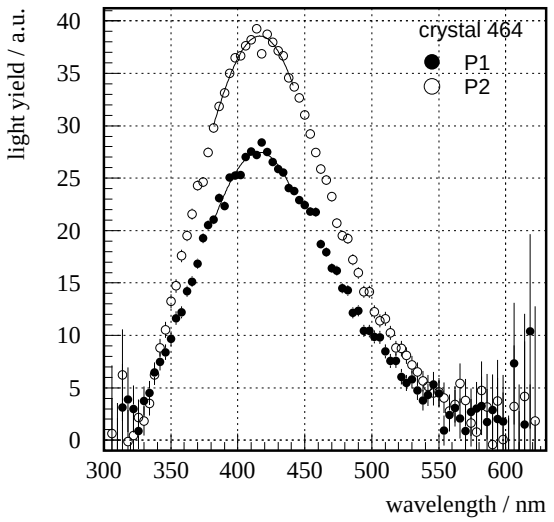
crystal 464
P1
P2
light yield / a.u.
wavelength / nm

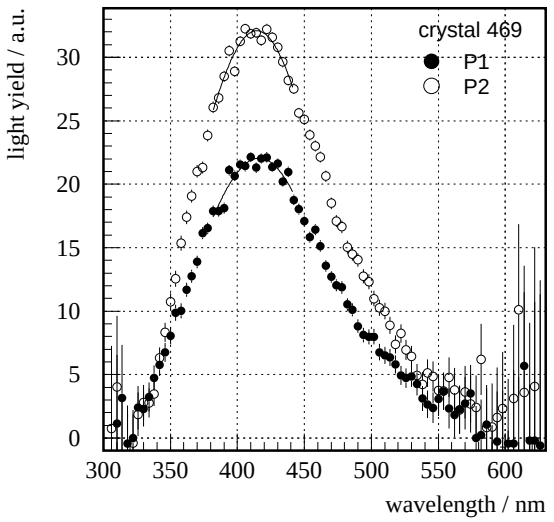
crystal 469
P1
P2
light yield / a.u.
wavelength / nm

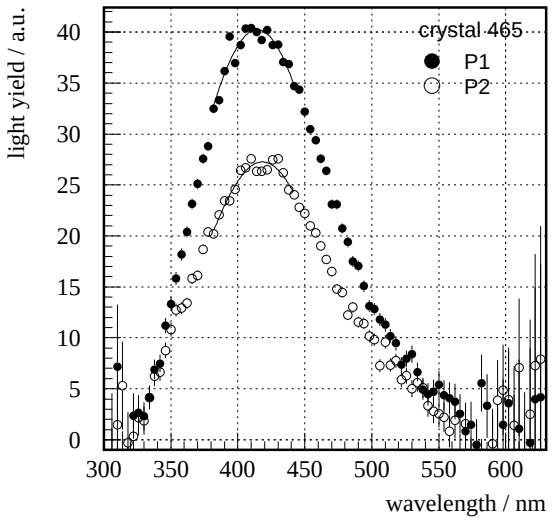
crystal 465
P1
P2
light yield / a.u.
wavelength / nm

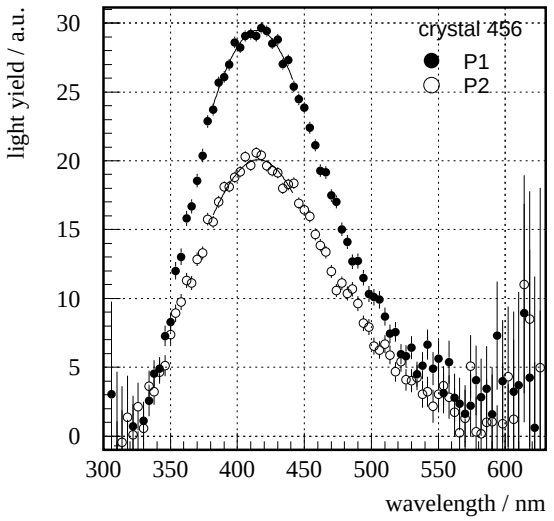
crystal 456
P1
P2
light yield / a.u.
wavelength / nm

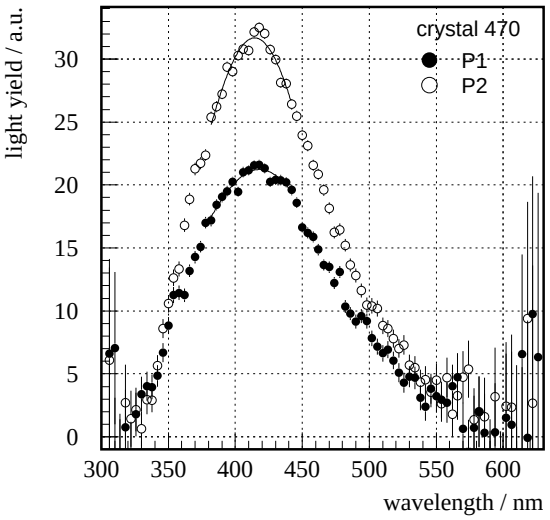
crystal 470
P1
P2
light yield / a.u.
wavelength / nm

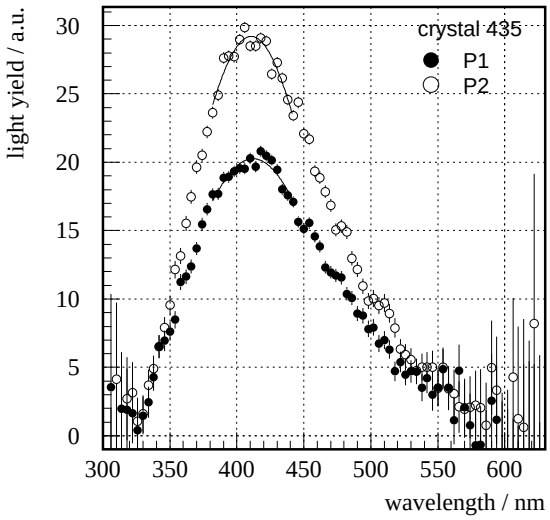
crystal 435
P1
P2
light yield / a.u.
wavelength / nm

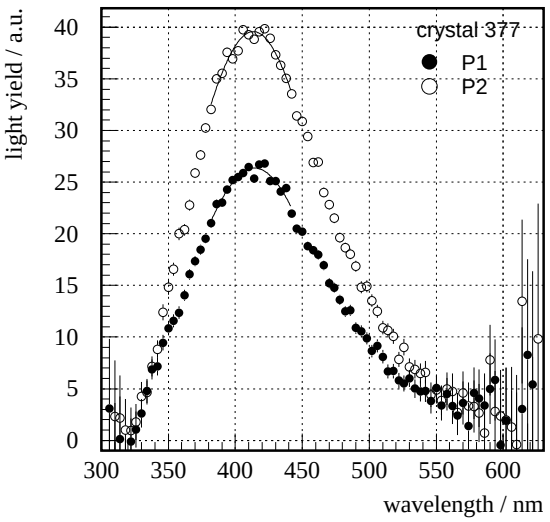
crystal 377
P1
P2
light yield / a.u.
wavelength / nm

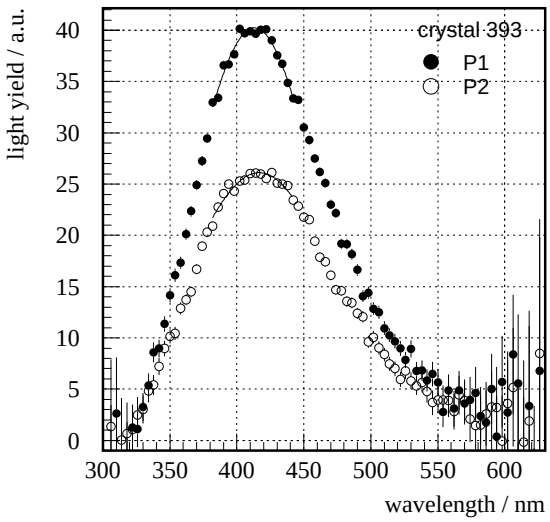
crystal 393
P1
P2
light yield / a.u.
wavelength / nm

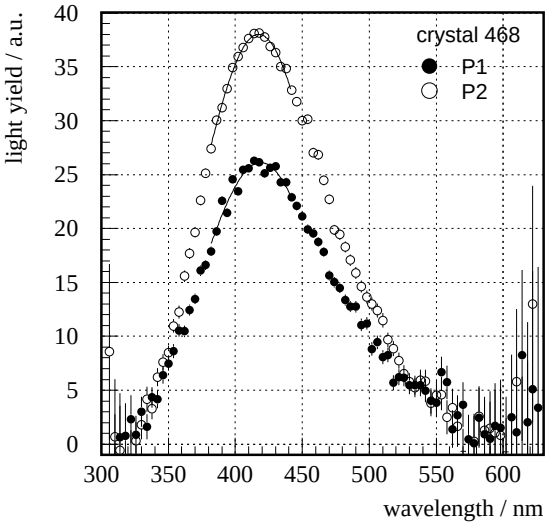
crystal 468
P1
P2
light yield / a.u.
wavelength / nm

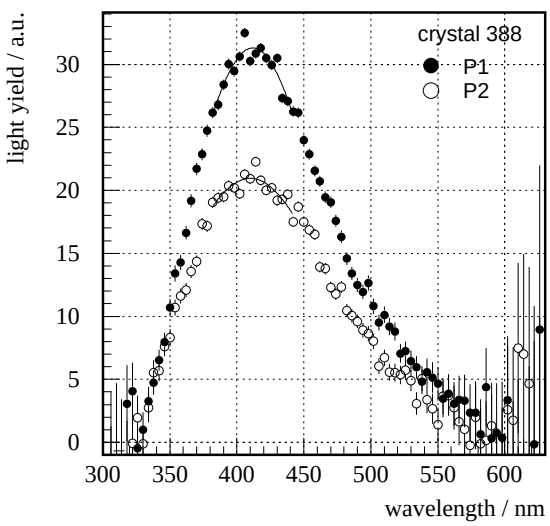
crystal 388
P1
P2
light yield / a.u.
wavelength / nm

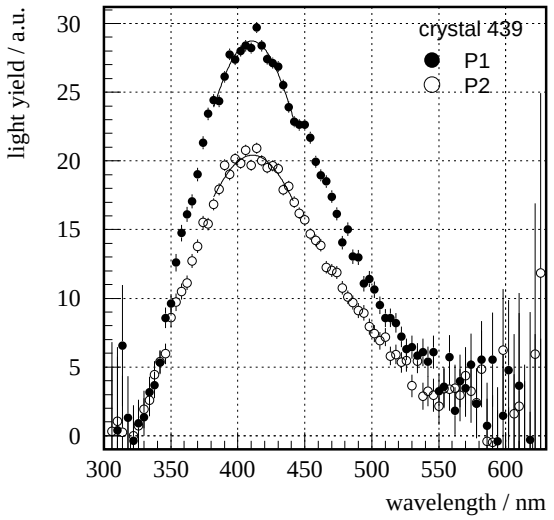
crystal 439
P1
P2
light yield / a.u.
wavelength / nm

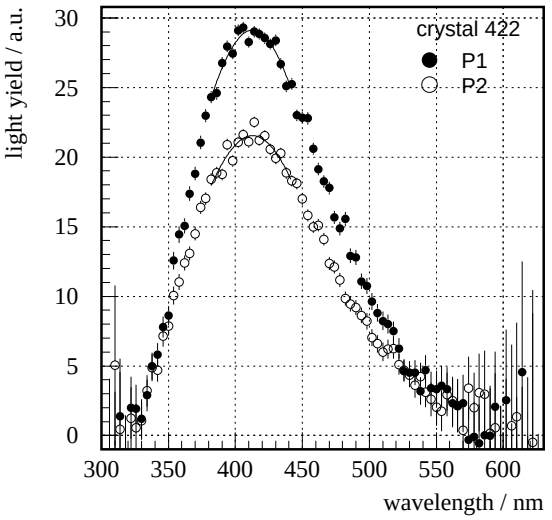
crystal 422
P1
P2
light yield / a.u.
wavelength / nm

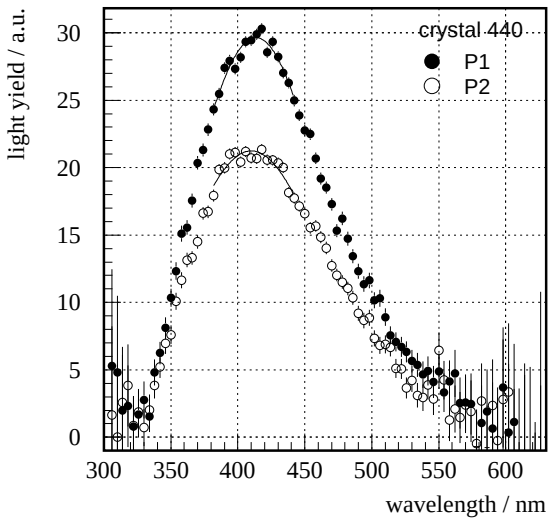
crystal 440
P1
P2
light yield / a.u.
wavelength / nm

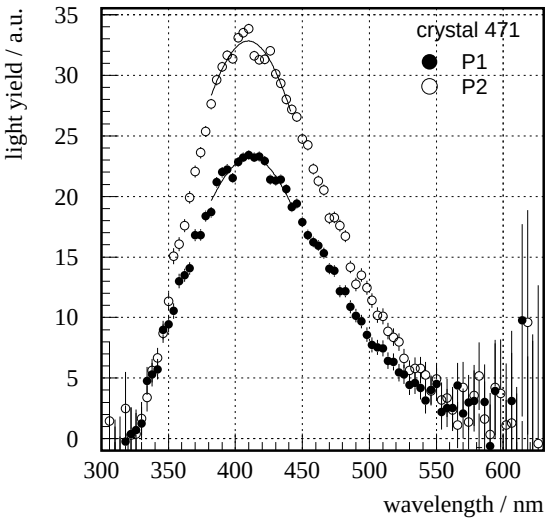
crystal 471
P1
P2
light yield / a.u.
wavelength / nm

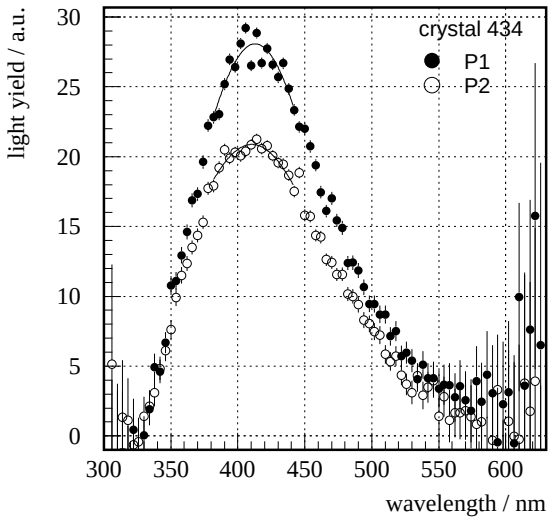
crystal 434
P1
P2
light yield / a.u.
wavelength / nm

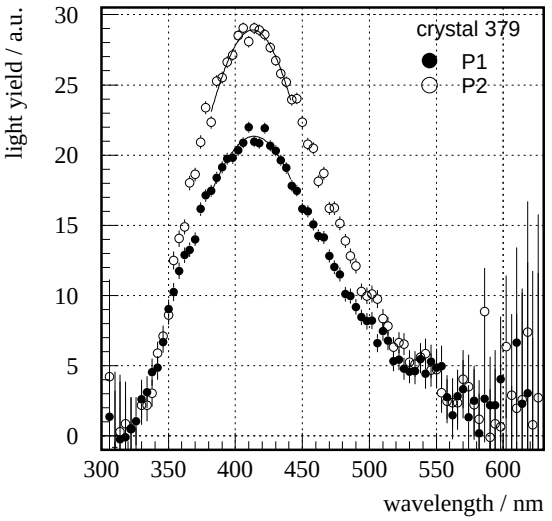
crystal 379
P1
P2
light yield / a.u.
wavelength / nm

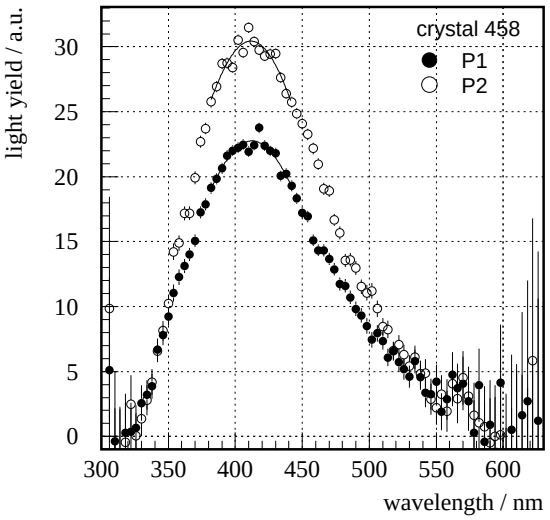
crystal 458
P1
P2
light yield / a.u.
wavelength / nm

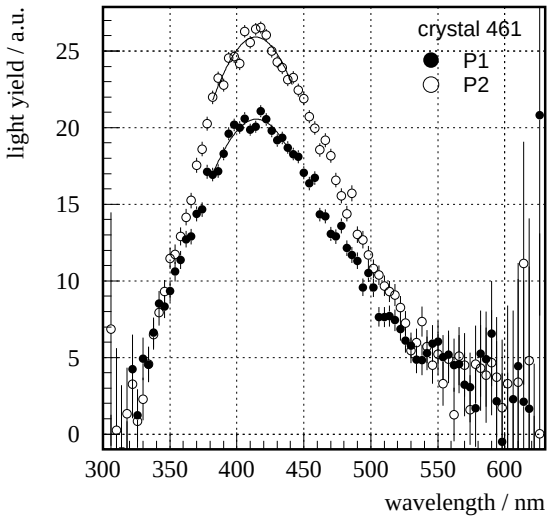
crystal 461
P1
P2
light yield / a.u.
wavelength / nm

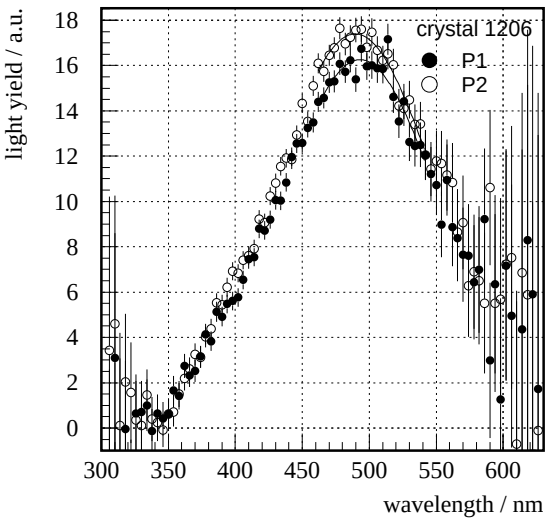
crystal 1206
P1
P2
light yield / a.u.
wavelength / nm

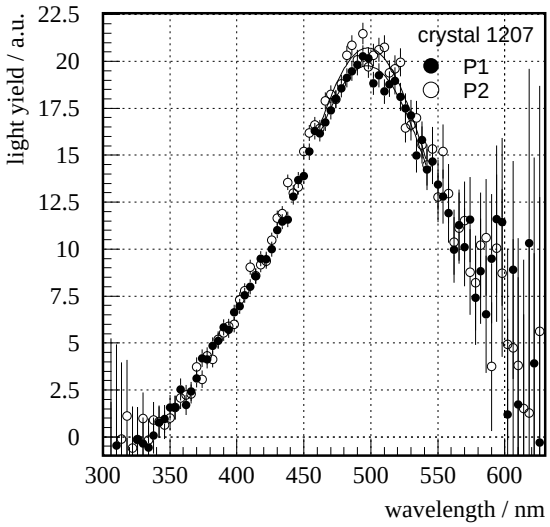
crystal 1207
P1
P2
light yield / a.u.
wavelength / nm

Appendix C

Longitudinal transmission spectra of $PbWO_4$ crystals

This chapter shows the longitudinal transmission spectra of all twenty 1997 crystals. They were measured according to the procedure described in section 8.1.3. In the plots the Fresnel transmission is also depicted, which denotes the highest possible transmission limited by losses due to Fresnel reflections.

The crystal transmission curves are normalized to the Fresnel transmission for wavelengths above 600 nm. The normalization was performed because the measured transmission curves were found to be shifted upwards or downwards by an absolute intensity offset varying from crystal to crystal and possibly caused by a normalization problem of the setup. This is further discussed in the section mentioned above.

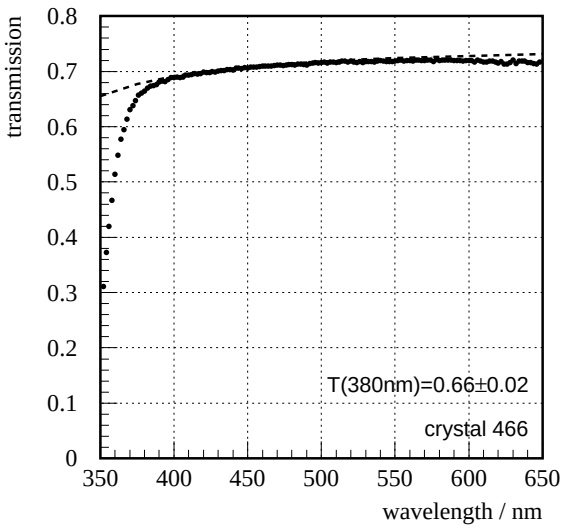
transmission
wavelength / nm
T(380nm)=0.66±0.02
crystal 466

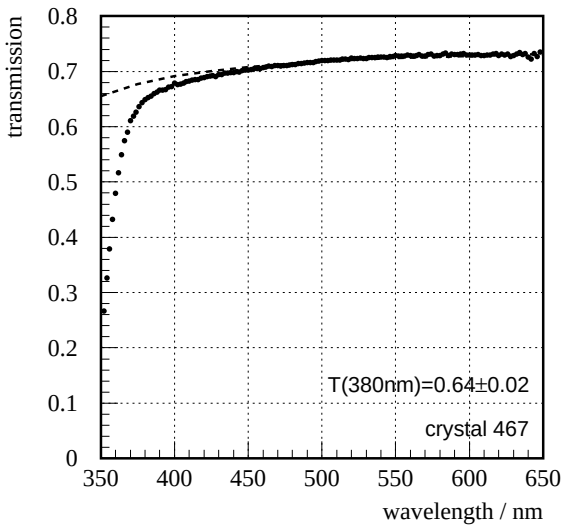
transmission
wavelength / nm
T(380nm)=0.64±0.02
crystal 467

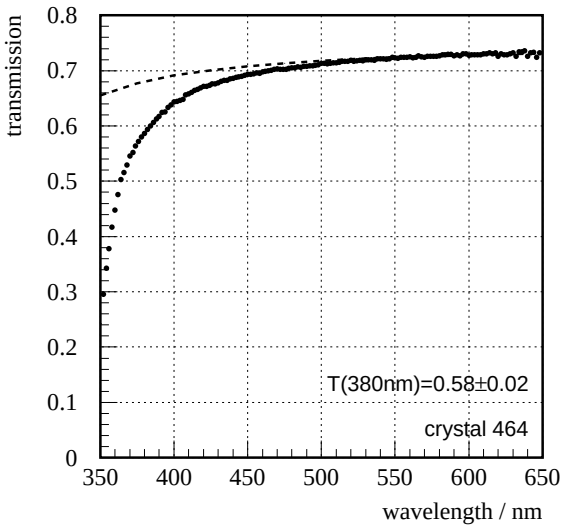
transmission
wavelength / nm
T(380nm)=0.58±0.02
crystal 464

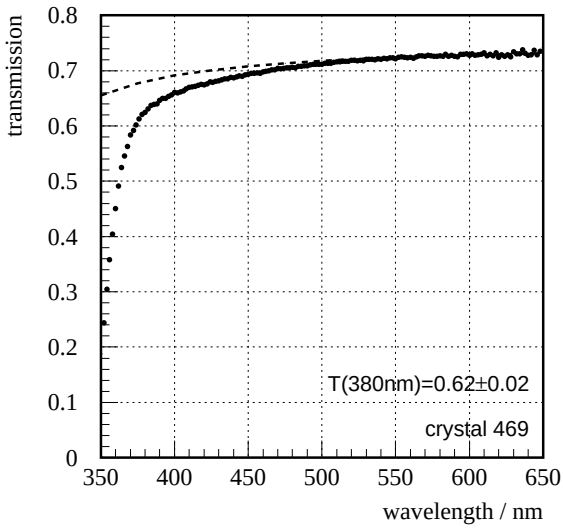
transmission
wavelength / nm
T(380nm)=0.62±0.02
crystal 469

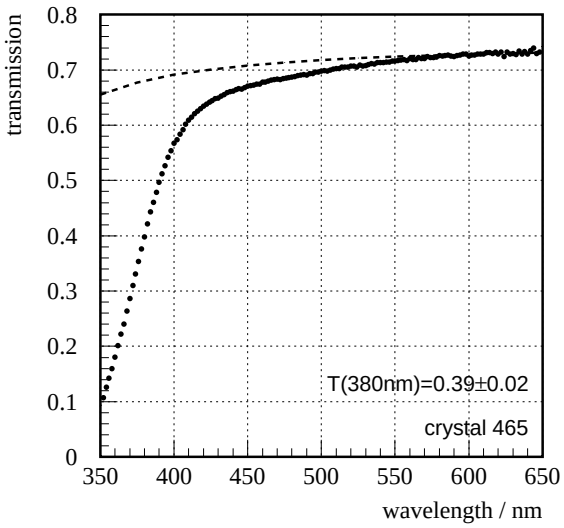
transmission
wavelength / nm
T(380nm)=0.39±0.02
crystal 465

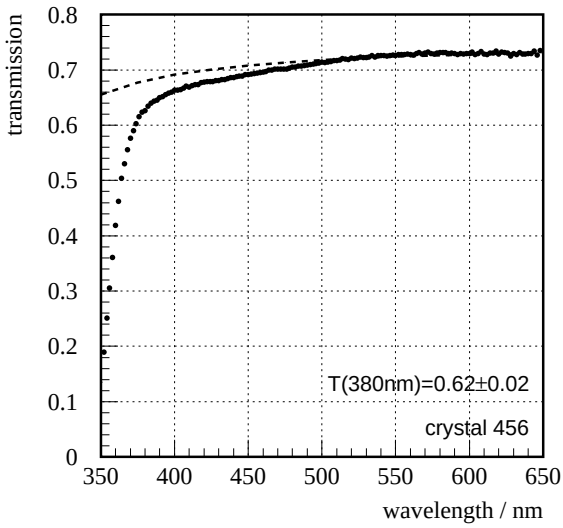
transmission
wavelength / nm
T(380nm)=0.62±0.02
crystal 456

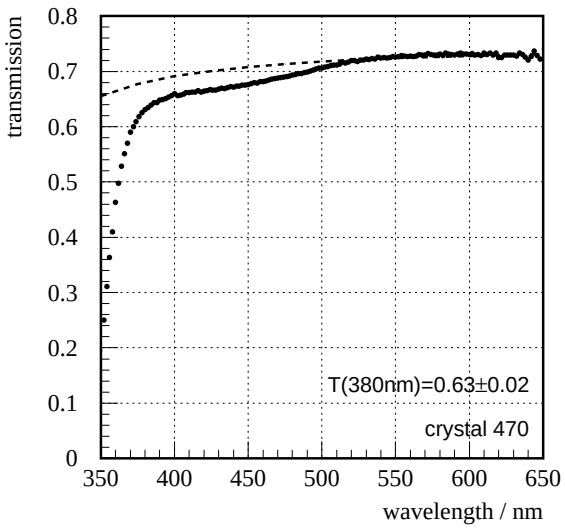
transmission
wavelength / nm
T(380nm)=0.63±0.02
crystal 470

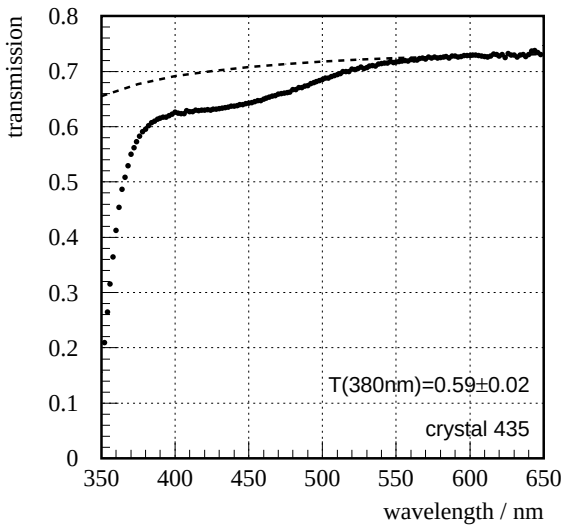
transmission
wavelength / nm
T(380nm)=0.59±0.02
crystal 435

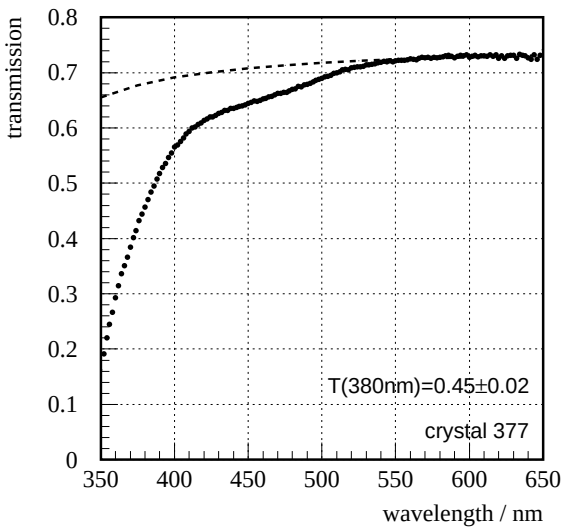
transmission
wavelength / nm
T(380nm)=0.45±0.02
crystal 377

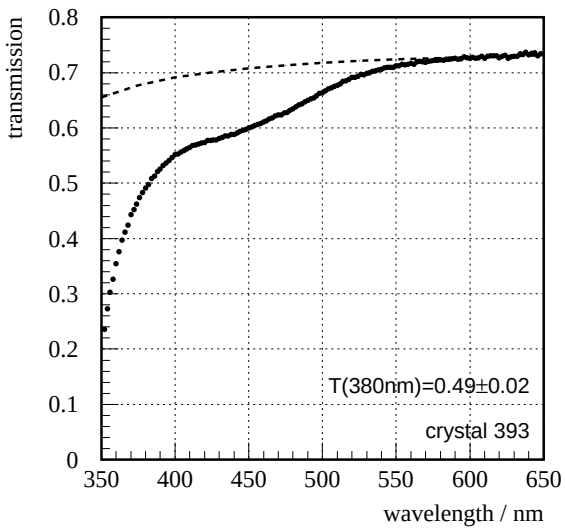
transmission
wavelength / nm
T(380nm)=0.49±0.02
crystal 393

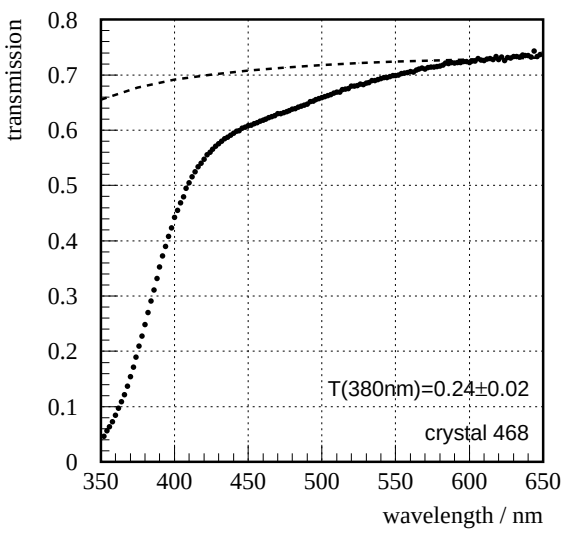
transmission
wavelength / nm
T(380nm)=0.24±0.02
crystal 468

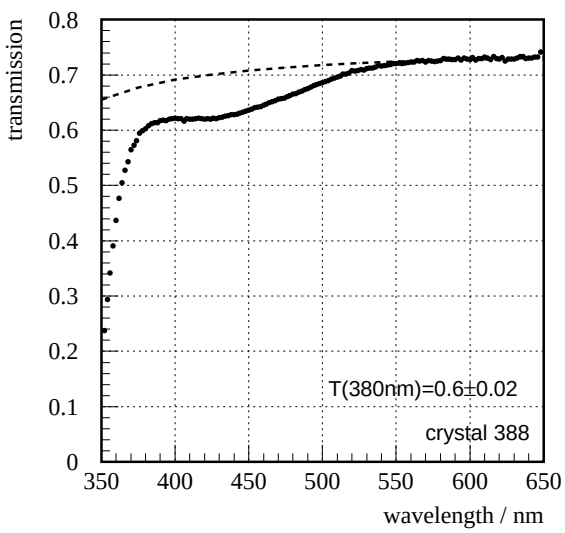
transmission
wavelength / nm
T(380nm)=0.6±0.02
crystal 388

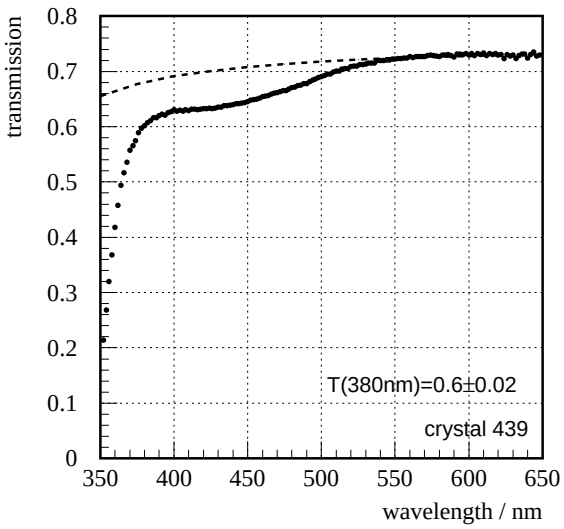
transmission
wavelength / nm
T(380nm)=0.6±0.02
crystal 439

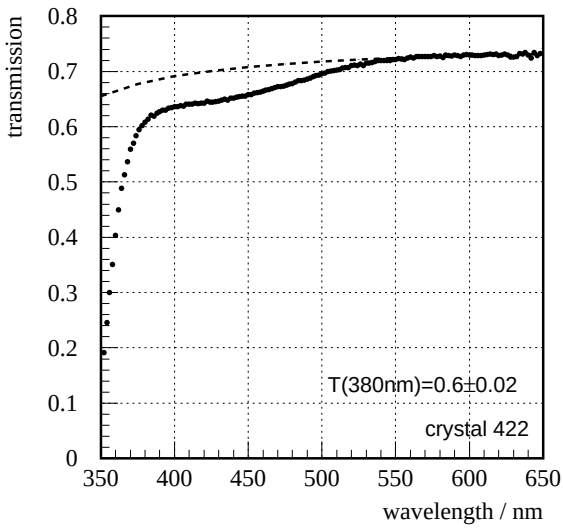
transmission
wavelength / nm
T(380nm)=0.6±0.02
crystal 422

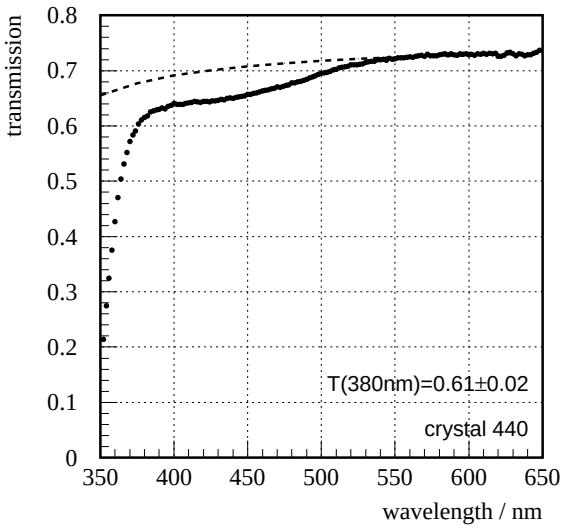
transmission
wavelength / nm
T(380nm)=0.61±0.02
crystal 440

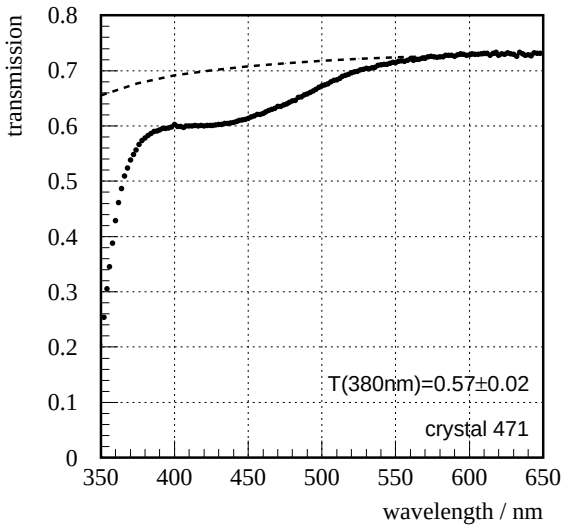
transmission
wavelength / nm
T(380nm)=0.57±0.02
crystal 471

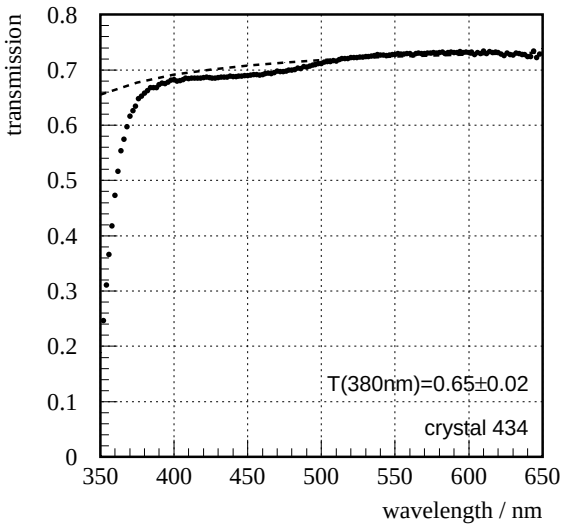
transmission
wavelength / nm
T(380nm)=0.65±0.02
crystal 434

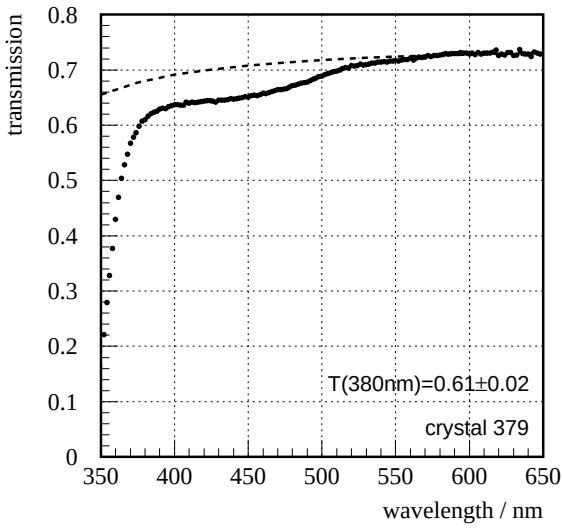
transmission
wavelength / nm
T(380nm)=0.61±0.02
crystal 379

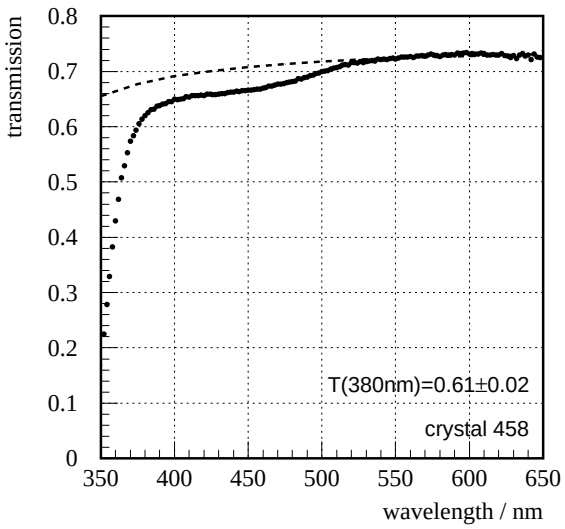
transmission
0.8
0.7
0.6
0.5
0.4
0.3
0.2
0.1
0
350
400
450
500
550
600
650
wavelength / nm
T(380nm)=0.61±0.02
crystal 458

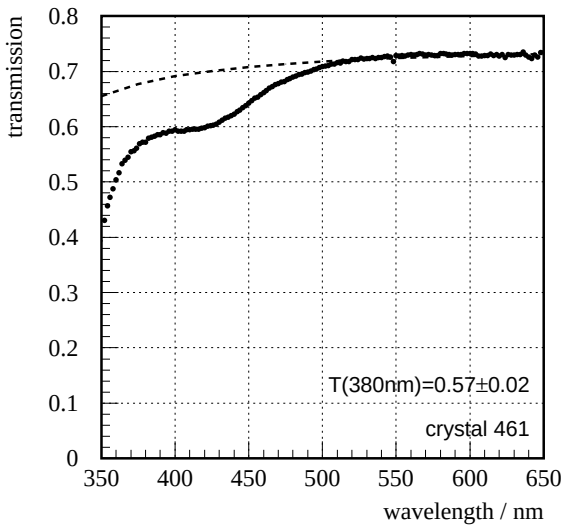
transmission
0.8
0.7
0.6
0.5
0.4
0.3
0.2
0.1
0
350
400
450
500
550
600
650
wavelength / nm
T(380nm)=0.57±0.02
crystal 461

Appendix D

Measurements of LED spectra

Light emitting diodes (LEDs) were used as light sources in several experimental setups described in this thesis. The radiation monitoring system of the CrystalBPC, which is described in section 11.3, is based on the blue emitting LED Nichia NSPB500. The measurement setup used for online measurements of the crystals' radiation damage was equipped with LEDs Nichia NSHU590, NSPB500, and NSTM515S. A description can be found in section 9.2.1.

Some effort was made to describe the operating characteristics of the LEDs used, especially their emission spectrum. For completeness, there were also LEDs included in these measurements which were not part of a setup described in this thesis such that spectra of LEDs throughout the visible spectrum from red to the near ultraviolet (uv) can be provided. The measured LED types are shown in Tab. D.1.

The measurement setup works as follows: The light of the LED under test is spectroscopically analyzed by a monochromator which is read out by a PMT. The measured spectra are corrected for the apparatus function of the setup, which is determined using the calculable emission spectrum of a special tungsten lamp [dan96, gen96]. The apparatus function is shown in Fig. D.1 (top left). The measured LED spectra can be observed in Fig. D.1 (top right) and (bottom).

Manufacturer	LED type	colour
Nichia	NSHU590	uv
	NSPB500	blue
	NSPE500	blue–green
	NSPG500	green
	NSTM515S	three–colour blue, green, red
Hewlett Packard	HLMP–DL08	amber
	HLMP–DJ08	orange
	HLMP–DH08	reddish orange
	HLMP–DG08	red

Table D.1: Table of measured LEDs

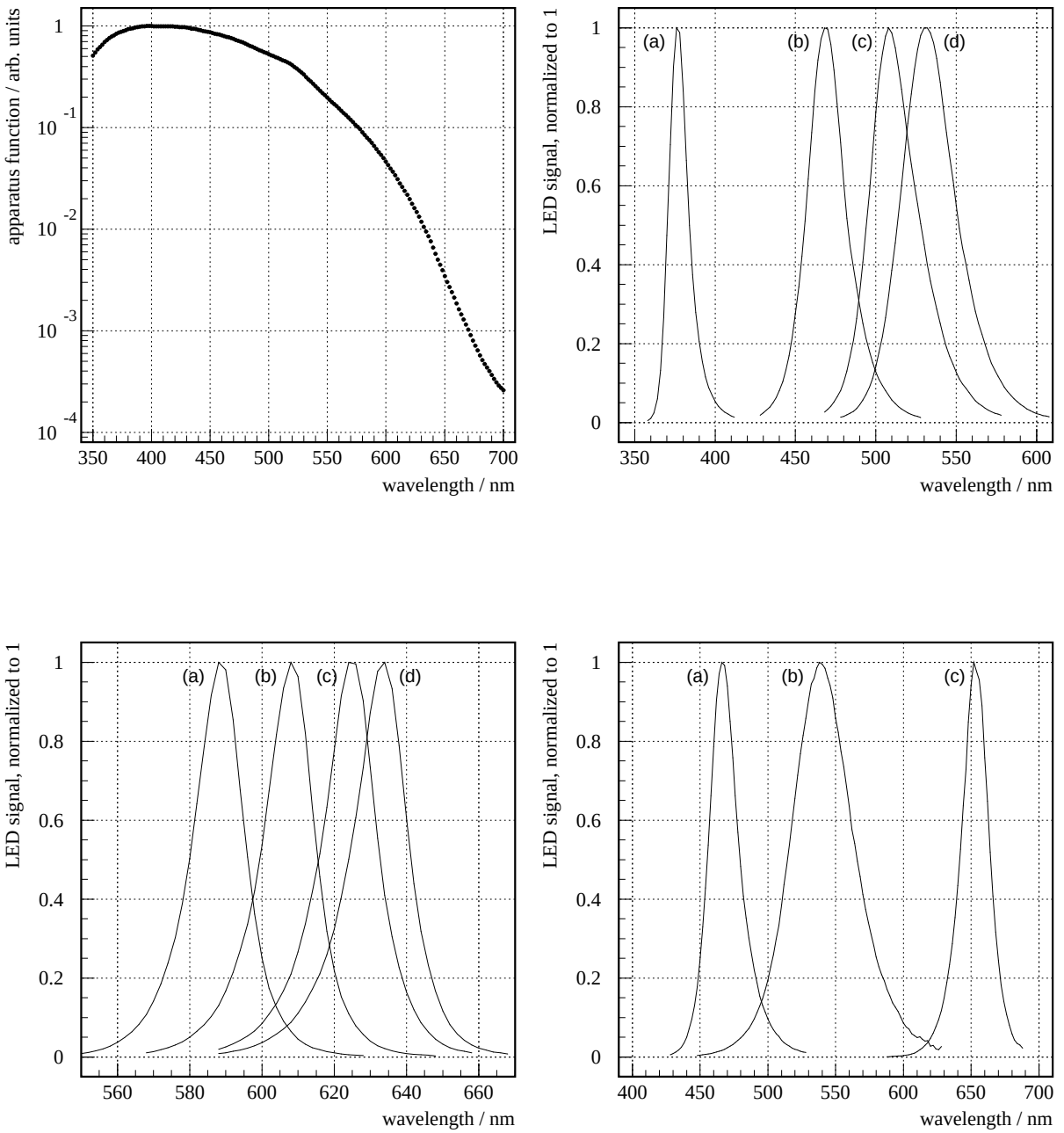

Figure D.1: (top left) Apparatus function of the setup used for measurements of LED spectra (top right) Spectra of Nichia LEDs: (a) NSHU590 (b) NSPB500 (c) NSPE500 (d) NSPG500 and (bottom left) of HP LEDs: (a) HLMP-DL08 (b) HLMP-DJ08 (c) HLMP-DH08 (d) HLMP-DG08 (bottom right) Spectra of the Nichia Full–Colour-LED NSTM515S: (a) blue (b) green (c) red

Appendix E

ADC calibration in units of photoelectrons

As many statistical processes are dominated by photoelectron statistics, it is convenient to calibrate the dynamic range of an analog–to–digital converter (ADC), usually expressed in units of ADC channels or delivered charge, in units of photoelectrons.

The calibration is done with the help of LED flashes. Using a high–precision LED driver, it can be assumed that the intensities of the LED flashes are very constant. Hence, the intensity distribution measured by an ADC is dominated by photoelectron statistics. The mean value μ of the distribution is given by

$$\mu = N_{p.e.} \cdot g \cdot e \cdot a \tag{E.1}$$

$N_{p.e.}$ denotes the number of photoelectrons produced at the PMT photocathode, g is the gain factor of the PMT, e is the electron charge and a is a calibration factor of the ADC and denotes the delivered charge which corresponds to one ADC channel. According to Poisson statistics, the standard deviation σ of the distribution can be calculated to

$$\sigma = \sqrt{N_{p.e.}} \cdot g \cdot e \cdot a \tag{E.2}$$

The number of photoelectrons corresponding to a particular distribution is given by the ratio

$$\frac{\mu^2}{\sigma^2} = N_{p.e.} \tag{E.3}$$

A calibration of the ADC in units of photoelectrons can be performed using the following equation:

$$\frac{\mu}{\sigma^2} = \left(\frac{N_{p.e.}}{\mu} \right) \tag{E.4}$$

The values μ and σ are measured in units of ADC channels. The factor $(N_{p.e.}/\mu)$ denotes the number of photoelectrons per ADC channel. It is determined by performing measurements at several different LED intensities. If the squared standard deviations σ^2 of the resulting distributions are plotted versus μ, the number of photoelectrons per ADC channel is given by the inverse slope of the resulting straight line.

Appendix F

The data analysis program "cernnt.c"

The data obtained during the Crystal BPC CERN test were analysed using the ROOT data analysis system [bru97]. The program "cernnt.c" written in the C/C++ programming language processes the raw data and produces a so–called ROOT tree, a data structure which provides a comfortable data analysis environment. A description of the ROOT tree data structure is given in Tab. F.1. A listing of the program "cernnt.c" is shown on the following pages.

branch description	branch name	type
run number	run	Int_t
run type	type	Int_t
beam energy	beam	Int_t
table X	tabx	Float_t
table Y	taby	Float_t
number of events in run	nevt	Int_t
global run temperature	gltemp	Float_t
day of run start	d	Int_t
hour of run start	h	Int_t
minute of run start	m	Int_t
collimator slit	slit	Float_t
LED amplitude	led	Float_t
event number	n	Int_t
seconds of running	sec	Int_t
absolute beam test time	asec	Int_t
event temperature	temp	Float_t
raw signal of channel	raw[16]	Float_t
p.e. in channel	pe[16]	Float_t
p.e. sum in cal	pesum	Float_t
calibrated signal	c[16]	Float_t
temperature corrected signal	t[16]	Float_t
leakage corrected signal	l[16]	Float_t
energy sum calibrated	ec	Float_t
energy sum temperature corr.	et	Float_t
energy sum leakage corr.	el	Float_t
energy sum in crystal column	ex[4]	Float_t
energy sum in crystal row	ey[4]	Float_t
reconstructed X coordinate	xrec	Float_t
reconstructed Y coordinate	yrec	Float_t
shower width in X	swrx	Float_t
shower width in Y	swry	Float_t
shower width	swr	Float_t
DLWC UP	up	Float_t
DLWC DOWN	down	Float_t
DLWC LEFT	left	Float_t
DLWC RIGHT	right	Float_t
DLWC X	dlx	Float_t
DLWC Y	dly	Float_t
DLWC WIDTH	dlw	Float_t
DLWC HEIGHT	dlh	Float_t
DLWC RADIUS	dlr	Float_t
absolute X coordinate	xabs	Float_t
absolute Y coordinate	yabs	Float_t
triggercounter B1	b1	Int_t
triggercounter B2	b2	Int_t
triggercounter B5	b5	Int_t

Table F.1: Description of the ROOT tree data structure used for the analysis of the CERN data.

```
{
/*************************************************************
  Cernnt.c
  reads raw ascii data file produced by pc camac readout
  and produces fancy root tree

  Time-stamp: <2000-02-02 18:23:16 nils>
  VERSION 00-02-02 with new shower reconstruction + new temp. corr.

  author : nils gendner

  raw data format: nr sec 16*bpc nix b1 b2 b5 left right up down
  *************************************************************/

/*
     view from behind, beam   /---\
                              | o |  (comes towards you)
                              \---/

                                      oben

                         ex[3]      ex[2]      ex[1]      ex[0]

yabs=taby=+48         ###############################################
                      #          #          #          #          #
                      #          #          #          #          #
                      #     1    #     2    #     3    #     4    #  ey[3]
                      # calib[0] # calib[1] # calib[2] # calib[3] #
                      #          #          #          #          #
                      #          #          #          #          #
           +24        ###############################################
                      #          #          #          #          #
                      #          #          #          #          #
                      #     5    #     6    #     7    #     8    #  ey[2]
                      # calib[4] # calib[5] # calib[6] # calib[7] #
                      #          #          #          #          #
                      #          #          #          #          #
 aussen      0        ###############################################       BP
                      #          #          #          #          #
                      #          #          #          #          #
                      #     9    #    10    #    11    #    12    #  ey[1]
                      # calib[8] # calib[9] # calib[10]# calib[11]#
                      #          #          #          #          #
                      #          #          #          #          #
           -24        ###############################################
                      #          #          #          #          #
                      #          #          #          #          #
                      #    13    #    14    #    15    #    16    #  ey[0]
                      # calib[12]# calib[13]# calib[14]# calib[15]#
                      #          #          #          #          #
                      #          #          #          #          #
           -48        ###############################################

                    xabs=tabx=+48        +24         0         -24        -48

                                      unten
*/

gROOT->Reset();                             /* reset root */


/* ---------- global variables ---------------------------------------------- */

/* globals for reading raw data */

Int_t raw_n;                                /* event number */
Int_t raw_sec;                              /* seconds since beginning of run */
Int_t raw_x[16];                            /* bpc raw data */
Int_t raw_nix;                              /* dummy, channel defective */
Int_t raw_b1,raw_b2,raw_b5;                 /* triggercounter */
Int_t raw_left,raw_right,raw_up,raw_down;   /* dlwc raw data */


/* globals for reading data file header */

Int_t head_run;                             /* run number */
Int_t head_day,head_mon,head_year;          /* start of run: day, month, year, */
Int_t head_h,head_m,head_s;                 /*               hour, min, sec */


/* globals for reading run info file */

Int_t info_run;                             /* run-number */
Int_t info_type;                            /* e=-1,mu=-2,Pi=1,PED=0,LED=2,PMLED=3 */
Int_t info_beam;                            /* beam energy */
Float_t info_tabx,info_taby;                /* table position x,y in mm */
Int_t info_nevt;                            /* number of events in run */
Float_t info_gltemp;                        /* global temperature in degrees */
Int_t info_d,info_h,info_m;                 /* start of run: day, hour, min */
Float_t info_slit;                          /* collimator slit in mm */
Float_t info_led;                           /* led intensity in skt */


/* globals for temperature measurement */

Float_t temp_mean;                          /* mean of temperature measurement */
Float_t temp_sigma;                         /* sigma of temperature measurement */
Float_t temp_asec;                          /* absolute time */


/* globals for root-tree */

Int_t nt_run;                               /* run number */
Int_t nt_type;                              /* e=-1,mu=-2,Pi=1,PED=0,LED=2 */
Int_t nt_beam;                              /* beam energy */
Float_t nt_tabx,nt_taby;                    /* table position x,y in mm */
```

```
Int_t nt_nevt;                              /* number of events in run */
Float_t nt_gltemp;                          /* global temperature in degrees */
Int_t nt_d,nt_h,nt_m;                       /* start of run: day, hour, min */
Float_t nt_slit;                            /* collimator slit in mm */
Float_t nt_led;                             /* led intensity in skt */
Int_t nt_n;                                 /* event number */
Int_t nt_sec;                               /* seconds since beginning of run */
Int_t nt_asec;                              /* absolute time */
Float_t nt_temp;                            /* temperature at event time */
Float_t nt_raw[16];                         /* bpc raw data */
Float_t nt_pe[16];                          /* number of photoelectrons */
Float_t nt_pesum;                           /* photoelectron sum of all xtals */
Float_t nt_c[16];                           /* calibrated data */
Float_t nt_t[16];                           /* temperature corrected data */
Float_t nt_l[16];                           /* longitudinal leakage corrected data */
Float_t nt_ec;                              /* energy sum of all calibrated xtals */
Float_t nt_et;                              /* energy sum of all temp.corr. xtals */
Float_t nt_el;                              /* energy sum of all leakage corrected xtals */
Float_t nt_ex[4];                           /* sum of 1 of 4 columns of xtals */
Float_t nt_ey[4];                           /* sum of 1 of 4 rows of xtals */
Float_t nt_xrec,nt_yrec;                    /* reconstructed x,y-coordinate */
Float_t nt_swrx,nt_swry;                    /* shower width in x,y */
Float_t nt_swr;                             /* shower width */
Float_t nt_up,nt_down,nt_left,nt_right;     /* raw data of dlwc */
Float_t nt_dlx,nt_dly;                      /* dlwc x,y-position in mm */
Float_t nt_dlw,nt_dlh;                      /* dlwc width and height in mm */
Float_t nt_dlr;                             /* radius to center of dlwc in mm */
Float_t nt_xabs,nt_yabs;                    /* absolute x,y-cordinate in mm */
Int_t nt_b1,nt_b2,nt_b5;                    /* triggercounter signals */
Int_t nt_coinc;                             /* b1+b2 in standard cut */
Int_t nt_muon;                              /* b5 in standard cut > 100 (=muon) */


/* misc. globals */

Int_t run;                                  /* run number */
Int_t i;
Int_t ntreelines=0;                         /* counter for events in tree */
Int_t nfilelines=0;                         /* counter for events in file */
Float_t tfactor;                            /* temperature correction factor */
Float_t lfactor;                            /* longitudinal leakage correction factor */
Float_t wx,wy;                              /* weighting factors for position rec. */
Float_t x_wsum,x_wxsum,x_wxxsum;            /* sums for position rec. in x */
Float_t y_wsum,y_wysum,y_wyysum;            /* sums for position rec. in y */
Float_t w0=2.9;                             /* parameter for position reconstruction */
char rawname[60];                           /* name of raw data file */
char rootname[60]="/opt/people/nils/root/n000202.root";   /* store all trees in this file */
char treeident[10];                         /* identifier of current tree */
char treename[20];                          /* name of current tree */

FILE *infofile;                             /* file pointer to run info file */
FILE *tempfile;                             /* file pointer to temperature data file */
FILE *rawfile;                              /* file pointer to raw data file */


/* pedestals of all 16 channels */

Float_t ped[16]={8.8,
                 7.5,
                 5.4,
                 10.1,
                 11.0,
                 7.5,
                 7.6,
                 6.7,
                 8.9,
                 7.6,
                 6.0,
                 13.0,
                 24.6,
                 14.8,
                 32.5,
                 27.3};

/* calibration factors of all 16 channels */

Float_t cal[16]={0.9211,
                 0.9153,
                 0.9295,
                 0.9227,
                 0.9187,
                 0.9397,
                 0.9162,
                 0.9258,
                 0.9322,
                 0.9222,
                 0.9366,
                 0.9306,
                 0.9382,
                 0.9296,
                 0.9469,
                 0.9246};

/* calibration factors of all 16 channels, high energy runs */

Float_t calhi[16]={0.9211,
                   0.9153,
                   0.9295,
                   0.9227,
                   0.9187,
                   0.9397,
                   0.9162,
                   0.9258,
                   0.9322,
                   0.9222,
                   3.8579,
```

```
                    0.9306,
                    0.9382,
                    0.9296,
                    0.9469,
                    0.9246};

/* photoelectron calibration factors */

Float_t pec[16]={7.95,
                 1.40,
                 9.66,
                 9.57,
                 12.45,
                 10.46,
                 13.83,
                 9.91,
                 6.89,
                 11.20,
                 11.81,
                 10.96,
                 7.91,
                 7.54,
                 7.57,
                 9.80};

Int_t xmid[4]={-36,-12,12,36};

Int_t ymid[4]={-36,-12,12,36};

/* ---------- create new root file ---------------------------------------- */

TFile *myfile = new TFile(rootname,"RECREATE");
myfile->Close();

/* ---------- loop over all cern test runs -------------------------------- */

for (run=1895;run<=2192;run++)
{
  printf( "\nprocessing run %d\n", run );

  /* ---------- reopen existing root file for append ------------------------ */

  TFile *myfile = new TFile(rootname,"UPDATE");
  printf("opening root file for append...OK\n");

  /* ---------- create root tree, one for each run -------------------------- */

  sprintf(treeident,"t%d",run);
  sprintf(treename,"000202 R%d",run);
  TTree *mytree = new TTree(treeident,treename);

  mytree->Branch("RUN",            &nt_run,     "run/I");
  mytree->Branch("TYPE",           &nt_type,    "type/I");
  mytree->Branch("BEAM ENERGY",    &nt_beam,    "beam/I");
  mytree->Branch("TABLE X",        &nt_tabx,    "tabx/F");
  mytree->Branch("TABLE Y",        &nt_taby,    "taby/F");
  mytree->Branch("NO. EVT",        &nt_nevt,    "nevt/I");
  mytree->Branch("GLOBAL TEMP",    &nt_gltemp,  "gltemp/F");
  mytree->Branch("DAY",            &nt_d,       "d/I");
  mytree->Branch("HOUR",           &nt_h,       "h/I");
  mytree->Branch("MINUTE",         &nt_m,       "m/I");
  mytree->Branch("COLL. SLIT",     &nt_slit,    "slit/F");
  mytree->Branch("LED AMPLITUDE",  &nt_led,     "led/F");
  mytree->Branch("EVENT NUMBER",   &nt_n,       "n/I");
  mytree->Branch("RUN SEC.",       &nt_sec,     "sec/I");
  mytree->Branch("ABS. SEC.",      &nt_asec,    "asec/I");
  mytree->Branch("EVENT TEMP.",    &nt_temp,    "temp/F");
  mytree->Branch("RAW",            &nt_raw,     "raw[16]/F");
  mytree->Branch("PHOTO EL.",      &nt_pe,      "pe[16]/F");
  mytree->Branch("PHOTO EL. SUM",  &nt_pesum,   "pesum/F");
  mytree->Branch("CALIBRATED",     &nt_c,       "c[16]/F");
  mytree->Branch("TEMP. CORR.",    &nt_t,       "t[16]/F");
  mytree->Branch("LEAK. CORR.",    &nt_l,       "l[16]/F");
  mytree->Branch("ESUM CALIB.",    &nt_ec,      "ec/F");
  mytree->Branch("ESUM TEMP.KOR.",&nt_et,       "et/F");
  mytree->Branch("ESUM LEAK.KOR.",&nt_el,       "el/F");
  mytree->Branch("COLUMN ENERGY",  &nt_ex,      "ex[4]/F");
  mytree->Branch("ROW ENERGY",     &nt_ey,      "ey[4]/F");
  mytree->Branch("X RECONSTR.",    &nt_xrec,    "xrec/F");
  mytree->Branch("Y RECONSTR.",    &nt_yrec,    "yrec/F");
  mytree->Branch("SHOWER WIDTH X",&nt_swrx,     "swrx/F");
  mytree->Branch("SHOWER WIDTH Y",&nt_swry,     "swry/F");
  mytree->Branch("SHOWER WIDTH",   &nt_swr,     "swr/F");
  mytree->Branch("DLWC UP",        &nt_up,      "up/F");
  mytree->Branch("DLWC DOWN",      &nt_down,    "down/F");
  mytree->Branch("DLWC LEFT",      &nt_left,    "left/F");
  mytree->Branch("DLWC RIGHT",     &nt_right,   "right/F");
  mytree->Branch("DLWC X",         &nt_dlx,     "dlx/F");
  mytree->Branch("DLWC Y",         &nt_dly,     "dly/F");
  mytree->Branch("DLWC WIDTH",     &nt_dlw,     "dlw/F");
  mytree->Branch("DLWC HEIGHT",    &nt_dlh,     "dlh/F");
  mytree->Branch("DLWC RADIUS",    &nt_dlr,     "dlr/F");
  mytree->Branch("ABSOLUTE X",     &nt_xabs,    "xabs/F");
  mytree->Branch("ABSOLUTE Y",     &nt_yabs,    "yabs/F");
  mytree->Branch("TC B1",          &nt_b1,      "b1/I");
  mytree->Branch("TC B2",          &nt_b2,      "b2/I");
  mytree->Branch("TC B5",          &nt_b5,      "b5/I");
  mytree->Branch("COINC. B1+B2",   &nt_coinc,   "coinc/I");
  mytree->Branch("MUON B5",        &nt_muon,    "muon/I");


  /* ---------- read information from run info file ------------------------- */

  if (!(infofile = fopen( "/baby/l-z/nils/root/logs/runinfo_000126.log", "rb" )))
    {
      printf("ERROR: can't read from run info file\n");
```

```
    return(1);
  }
printf("GetRunInfo: searching for run %d\n", run );

while (info_run != run)
  {
    fscanf( infofile,"%d %d %d %f %f %d",
            &info_run,
            &info_type,
            &info_beam,
            &info_tabx,
            &info_taby,
            &info_nevt );

    fscanf( infofile,"%f %d %d %d %f %f\n",
            &info_gltemp,
            &info_d,
            &info_h,
            &info_m,
            &info_slit,
            &info_led );

    if (feof(infofile))
      {
        printf("ERROR: reached EOF of run info file\n");
        return(1);
      }
  }

fclose(infofile);

printf( "%d %d %d %f %f %d %f %d %d %d %f %f\n",
        info_run,
        info_type,
        info_beam,
        info_tabx,
        info_taby,
        info_nevt,
        info_gltemp,
        info_d,
        info_h,
        info_m,
        info_slit,
        info_led);


/* ---------- open raw data file ------------------------------------------- */

sprintf(rawname,"/opt/people/nils/cernraw/data.%d",run);

if (!(rawfile = fopen( rawname, "rb" )))
  {
    printf("ERROR: can't open raw data file data.%d ...skipping!\n",run);
  }
else
  {
    printf("opening raw data file...OK\n");


    /* ---------- open temperature data file ----------------------------------- */

    if (!(tempfile = fopen( "/usr/people/nils/root/logs/cerntemp.vec","rb" )))
      {
        printf("ERROR: can't open temperature file\n");
        return(1);
      }
    printf("opening temperature file...OK\n");


    /* ---------- read header line from raw data file -------------------------- */

    if (fscanf( rawfile,"%d %d:%d:%d %d:%d:%d\n",
                &head_run,
                &head_day,
                &head_mon,
                &head_year,
                &head_h,
                &head_m,
                &head_s) != 7)
      {
        printf("ERROR: error reading data file header\n");
        return(1);
      }
    printf("run %d started on %d.%d.%d at %d:%d:%d\n",
           head_run,
           head_day,
           head_mon,
           head_year,
           head_h,
           head_m,
           head_s);


    /* ---------- eventloop ---------------------------------------------------- */

    ntreelines=0;

    while(!feof(rawfile))
      {

        /* read one line from raw data file */

        ntreelines++;
        nfilelines++;

        fscanf( rawfile,"%d %d ",&raw_n, &raw_sec );
```

```
for (i=0;i<=15;i++)
  fscanf( rawfile,"%d ",&raw_x[i] );
fscanf( rawfile,"%d %d %d %d ",&raw_nix, &raw_b1, &raw_b2, &raw_b5 );
fscanf( rawfile,"%d %d %d %d\n",&raw_left, &raw_right, &raw_up, &raw_down );

/* put data into ntuple struct */

nt_run    = run;
nt_type   = info_type;
nt_beam   = info_beam;

if (nt_run >= 2099)                          /* error in x after run 2098 */
  nt_tabx   = info_tabx-6;
else
  nt_tabx   = info_tabx;

nt_taby   = info_taby;
nt_nevt   = info_nevt;
nt_gltemp = info_gltemp;
nt_d      = info_d;
nt_h      = info_h;
nt_m      = info_m;
nt_slit   = info_slit;
nt_led    = info_led;
nt_n      = raw_n;
nt_sec    = raw_sec;
nt_asec   = raw_sec+86400*info_d+3600*info_h+60*info_m;

/* look up current temperature; note the heat conduction correction:
   we take the housing temperature from 17.16mins ago  */

while ( temp_asec < (nt_asec - 1030) )
  {
    fscanf( tempfile,"%f %f %f\n",&temp_mean, &temp_sigma, &temp_asec );

    if (feof(tempfile))
      {
        printf("ERROR: reached EOF of temperature file\n");
        return(1);
      }
  }

nt_temp = temp_mean;

/* calculate temperature correction factor, reference temperature is 20 degrees */
tfactor = 1.41965 - nt_temp * 2.09824e-02;

/* calculate longitudinal leakage correction factor from beam energy */
/* not an elegant procedure, but simple and working :) */

if (nt_beam == 0)   lfactor=1;
if (nt_beam == 3)   lfactor=0.99764;
if (nt_beam == 5)   lfactor=0.996668;
if (nt_beam == 10)  lfactor=0.994849;
if (nt_beam == 15)  lfactor=0.993453;
if (nt_beam == 20)  lfactor=0.992287;
if (nt_beam == 25)  lfactor=0.99127;
if (nt_beam == 30)  lfactor=0.990361;
if (nt_beam == 50)  lfactor=0.987399;
if (nt_beam == 70)  lfactor=0.98508;
if (nt_beam == 100) lfactor=0.982263;

/* energy calibration and correction, calculate energy sums */

nt_pesum = (float)0;
nt_ec = (float)0;
nt_et = (float)0;
nt_el = (float)0;

if (nt_run>=2122 && nt_run<=2138)        /* high energy runs with electrons*/
  for (i=0;i<=15;i++)
    {
      nt_raw[i] = (float)raw_x[i];
      if ((nt_raw[i]-ped[i]) > 0)
        nt_c[i] = (nt_raw[i]-(float)ped[i]) * (float)calhi[i];
      else
        nt_c[i] = (float)0;              /*avoid negative energies*/
      nt_pe[i] = (float)0;
      nt_ec += nt_c[i];
      nt_t[i] = nt_c[i] / tfactor;
      nt_et += nt_t[i];
      nt_l[i] = nt_t[i] / lfactor;
      nt_el += nt_l[i];
    }
else                                     /*other runs*/
  for (i=0;i<=15;i++)
    {
      nt_raw[i] = (float)raw_x[i];
      if ((nt_raw[i]-ped[i]) > 0)
        {
          nt_pe[i] = (nt_raw[i]-(float)ped[i]) * (float)pec[i];
          nt_c[i]  = (nt_raw[i]-(float)ped[i]) * (float)cal[i];
        }
      else                               /*avoid negative energies*/
        {
          nt_pe[i] = (float)0;
          nt_c[i]  = (float)0;
        }
      nt_pesum += nt_pe[i];
      nt_ec += nt_c[i];
      nt_t[i] = nt_c[i] / tfactor;
      nt_et += nt_t[i];
      nt_l[i] = nt_t[i] / lfactor;
      nt_el += nt_l[i];
    }
```

```
          /*sum of xtal rows and columns */

          nt_ex[0] = nt_t[3]+nt_t[7]+nt_t[11]+nt_t[15];
          nt_ex[1] = nt_t[2]+nt_t[6]+nt_t[10]+nt_t[14];
          nt_ex[2] = nt_t[1]+nt_t[5]+nt_t[9]+nt_t[13];
          nt_ex[3] = nt_t[0]+nt_t[4]+nt_t[8]+nt_t[12];
          nt_ey[0] = nt_t[12]+nt_t[13]+nt_t[14]+nt_t[15];
          nt_ey[1] = nt_t[8]+nt_t[9]+nt_t[10]+nt_t[11];
          nt_ey[2] = nt_t[4]+nt_t[5]+nt_t[6]+nt_t[7];
          nt_ey[3] = nt_t[0]+nt_t[1]+nt_t[2]+nt_t[3];

          /* position reconstruction */

          nt_xrec = 0;
          nt_yrec = 0;
          nt_swrx = 0;
          nt_swry = 0;
          nt_swr = 0;

          x_wsum=(float)0;
          x_wxsum=(float)0;
          x_wxxsum=(float)0;
          y_wsum=(float)0;
          y_wysum=(float)0;
          y_wyysum=(float)0;

          if (nt_et > 0)
            {
              for (i=0;i<=3;i++)
                {
                  if (w0 + log(nt_ex[i]/nt_et) > 0)
                    wx = w0 + log(nt_ex[i]/nt_et);
                  else
                    wx = 0;

                  x_wsum += wx;
                  x_wxsum += wx * xmid[i];
                  x_wxxsum += wx * xmid[i]**2;

                  if (w0 + log(nt_ey[i]/nt_et) > 0)
                    wy = w0 + log(nt_ey[i]/nt_et);
                  else
                    wy = 0;

                  y_wsum += wy;
                  y_wysum += wy * ymid[i];
                  y_wyysum += wy * ymid[i]**2;
                }
              if (x_wsum>0 && y_wsum>0)
                {
                  nt_xrec = x_wxsum / x_wsum;
                  nt_yrec = y_wysum / y_wsum;

                  /* shower width */

                  nt_swrx = sqrt( (x_wxxsum / x_wsum) - (x_wxsum / x_wsum )**2 );
                  nt_swry = sqrt( (y_wyysum / y_wsum) - (y_wysum / y_wsum )**2 );

                  nt_swr = sqrt( nt_swrx**2 + nt_swry**2 );
                }
            }

          /* delay line wire chamber related data */

          nt_up = (float)raw_up;
          nt_down = (float)raw_down;
          nt_left = (float)raw_left;
          nt_right = (float)raw_right;
          nt_dlx = (nt_right-nt_left)/(float)20;
          nt_dly = (nt_down -nt_up  )/(float)20;
          nt_dlw = (float)2*abs(nt_dlx);
          nt_dlh = (float)2*abs(nt_dly);
          nt_dlr = (float)sqrt(nt_dlx*nt_dlx + nt_dly*nt_dly);
          nt_xabs = nt_dlx + nt_tabx;
          nt_yabs = nt_dly + nt_taby;

          /* trigger counter related data */

          nt_b1 = raw_b1;
          nt_b2 = raw_b2;
          nt_b5 = raw_b5;
          nt_coinc = (400<nt_b1) && (nt_b1<1000) && (100<nt_b2) && (nt_b2<600);
          nt_muon = (nt_b5>80);

          /* fill data into tree */

          mytree->Fill();

        }

      /* ---------- end of eventloop ---------------------------------------------- */


      printf("%d events put to tree, %d to root file.\n",ntreelines, nfilelines);


      /* ---------- close files --------------------------------------------------- */

      fclose(rawfile);
      fclose(tempfile);
    }
  myfile->Write();
  myfile->Close();
}
}
```

List of Figures

2.1 Feynman diagrams of deep inelastic electron–proton scattering 5
2.2 The final state in NC electron–proton scattering 7
2.3 F_2 for several assumptions of proton substructures 14

3.1 Overview of the HERA accelerator complex 20

4.1 Overview of the ZEUS detector 22
4.2 Sketch of an FCAL module 23

5.1 Scale factor b for energy deposition profiles for several elements 27

6.1 The rear beampipe with the two BPC modules 32
6.2 Picture of BPC II and BPT 33
6.3 Estimated extension of the kinematic region by the Crystal BPC 36
6.4 Kinematic region covered in the 1997 BPC II and BPT analysis 37
6.5 Kinematic regions covered by several experiments 38

7.1 Scheme of energy transfer processes in $PbWO_4$ scintillator 44
7.2 Temperature dependence and temperature coefficient of $PbWO_4$ light yield 44

8.1 Overview of the Beckman spectrometer 47
8.2 The setup used for longitudinal transmission measurements 48
8.3 Light yield of crystal 388 vs. distance from source to PMT 49
8.4 Fresnel transmission of the crystal–lightguide interface 52
8.5 The single crystal setup 53
8.6 Lightguide shapes 54
8.7 Setup for scintillation spectra measurements 56
8.8 Apparatus functions 57

8.9 Scintillation spectra of $PbWO_4$ crystals 58
8.10 Orientation scheme of the crystals 59
8.11 Dependence of light yield and transmission on azimuthal orientation 60
8.12 Integrated signal shapes for blue and green emission components 61

9.1 Setup used for online measurements of the transmission during irradiation 64
9.2 Comparison of online transmission measurements with two crystals 67
9.3 Online transmission measurement of a 1997 crystal 67
9.4 Radiation damage of crystals 434, 467, 393 68
9.5 Radiation damage of crystals 422, 470, 464 69
9.6 Radiation damage of crystals 468, 465 70
9.7 Induced absorption coefficient versus crystal transmission 71
9.8 Induced absorption coefficient for the blue LED versus crystal transmission 71
9.9 Radiation damage of crystals 393 and 464 73
9.10 Radiation damage caused by a high dose irradiation 74
9.11 Effect of high dose irradiation on scintillation spectra of crystals 76

10.1 Top view of the Crystal BPC prototype 78
10.2 Energy resolution of the prototype 79
10.3 Uniformity of the prototype 80
10.4 Temperature dependence of the energy response 81
10.5 Test of the radiation damage monitoring system 81

11.1 Exploded view of the Crystal BPC 84
11.2 Schematic view of a crystal within the Crystal BPC 85
11.3 Kinematic peak events for energy scale calibration 86
11.4 Crystal dummy and the sensors inside the Crystal BPC 88
11.5 Sine–shaped temperature change applied to the Crystal BPC 89
11.6 Temperature cycles with increasing and decreasing temperature 90
11.7 Simulated shower shapes in $PbWO_4$ 91

12.1 Overview of the CERN SPS X5 test beam 94
12.2 The test beam setup at the CERN SPS 97

12.3 The test beam readout system 98
12.4 Typical pedestal run 99
12.5 Summary of pedestal runs 99
12.6 Channel-to-channel calibration of the Crystal BPC 100
12.7 Temperature changes of the Crystal BPC housing during the CERN test . 101
12.8 Temperature dependence of the Crystal BPC response to 30 GeV electrons 103
12.9 Temperature correction of the CERN data 103
12.10 Simulated longitudinal shower leakage in the Crystal BPC 104
12.11 Energy resolution measured with electron energies from 3 to 100 GeV . . . 106
12.12 Energy resolution measured with a restricted beam spot size 107
12.13 Linearity of the Crystal BPC 109
12.14 Uniformity of the Crystal BPC 110
12.15 Energy resolution in dependence on horizontal impact position 111
12.16 Determination of the free parameter W_0 112
12.17 Position reconstruction 113
12.18 Recovery of the irradiated crystal in the Crystal BPC 114
12.19 Shower width distributions for electrons and hadrons 115

A.1 Overview of the Crystal BPC channels 119

D.1 Several LED spectra 131

List of Tables

2.1 Fundamental particles in the Standard Model 3

7.1 Properties of $PbWO_4$ crystals 41

7.2 Refractive index of $PbWO_4$ at different wavelengths 42

8.1 Results of light yield measurements of the crystals 51

8.2 Measurements with different lightguide shapes 54

8.3 Effect of different wrappings on the light yield 55

9.1 Mass energy–absorption coefficients 65

9.2 Result of the systematic radiation damage study 72

12.1 Table of calibration related data 102

12.2 Energy fractions deposited in the Crystal BPC 105

D.1 Table of measured LEDs 130

F.1 Description of the ROOT tree data structure 134

Bibliography

[abr96] H. Abramowicz et al., in *Proceedings of the Workshop on Future Physics at HERA*, ed. G. Ingelman et al., Hamburg (1995).

[abr97] H. Abramowicz and A. Levy, *DESY 97–251* (1997).

[abt93] H1 Collaboration, I. Abt et al., *Nucl. Phys.* **B 407** (1993) 515.

[abt97] H1 Collaboration, I. Abt et al., *Nucl. Instr. and Meth.* **A 386** (1997) 310-347 and 348-396.

[ada96] M. Adams et al., *Phys. Rev.* **D 54** (1996) 3006.

[aic95] *PHOTCOEF — a nuclear physics utilities program*, AIC Software, Grafton, Massachusetts (1995).

[ame99] Ch. Amelung, *Measurement of the Proton Structure Function F_2 at Very Low Q^2 at HERA*, BONN-IR-99-14, Univ. of Bonn (1999).

[and91] A. Andresen et al., *Nucl. Instr. and Meth.*, **A 309** (1991) 101.

[and92] J. Andruszków et al., DESY 92–066 (1992).

[arm90] ARMCO EISEN GmbH, *Technical Information*, Köln, Germany (1990).

[awe92] T.C. Awes et al., *Nucl. Instr. and Meth.* **A 311** (1992) 130–138.

[bac97a] S. Baccaro et al., *Nucl. Instr. Meth. A* 385 (1997) 209–214.

[bac97b] S. Baccaro et al., *Radiation damage mechanism in $PbWO_4$ crystal and radiation hardness quality control of PWO scintillators for CMS*, CMS Note 1997/038, CERN, Geneva (1997).

[bad90] B. Badelek and J. Kwiecinski, *Phys. Lett.* **B 295** (1992) 263.

[bam99] A. Bamberger et al., *The ZEUS Forward Plug Calorimeter with Lead–Scintillator Plates and WLS Fiber Readout*, DESY 99–194, DESY, Hamburg (1999).

[bar96] Particle Data Group, R.M. Barnett el al., *Phys. Rev.* **D 54** (1996) 1.

[bas94] U. Bassler, G. Bernardi, *On the Kinematic Reconstruction of Deep Inelastic Scattering at HERA: the Σ Method*, DESY Note 94-231, DESY, Hamburg (1994); U. Bassler, G. Bernardi, *Nucl. Instr. Meth. A* 426 (1999) 583.

[bas97] U. Bassler, G. Bernardi, DESY Note 97-137, DESY, Hamburg (1997).

[bat70] G. Bathow et al., *Nucl. Phys.* **B 20** (1970) 592.

[ben92] S. Bentvelsen, J. Engelen and P. Koijman, *Reconstruction of x, Q^2 and Extraction of Structure Functions in Neutral Current Scattering at HERA*, in: Proceedings of the 1991 Workshop on Physics at HERA, ed. W. Buchmüller and G. Ingelman, DESY, Hamburg, Vol. 1 (1992) 23.

[ber93] B. Bernstein et al., *Nucl. Instr. and Meth.* **A 336** (1993) 23.

[bet34] H. Bethe, W. Heitler, *Proc. Roy. Soc.* **A 146** (1934) 83.

[bjo67] J.D. Bjœrken, *Phys. Rev.* **163** (1967) 1767.

[bjo69] J.D. Bjœrken, *Phys. Rev.* **179** (1969) 1547.

[bre97] ZEUS collaboration, J. Breitweg et al., *Measurement of the Proton Structure Function F_2 and $\sigma_{tot}^{\gamma^* p}$ at Low Q^2 and Very Low x at HERA*, DESY 97–135 (1997).

[bru97] R. Brun and F. Rademakers, *ROOT — An Object Oriented Data Analysis Framework*, Proceedings AIHENP96 Workshop, Lausanne, Sep. 1996, Nucl. Inst. & Meth. in Phys. Res. A 389 (1997) 81-86. See also `http://root.cern.ch/`.

[cal69] C.G. Callan and D. Gross, *Phys. Rev. Lett.* **22** (1969) 156.

[cal96] A. Caldwell, R. Klanner, S. Ritz, Q. Zhu, *A Silicon Tracker for BPC and a possible Upgrade to BPC III*, ZEUS Note 96–044, DESY, Hamburg (1996).

[cap94] A. Capella et al., *Phys. Lett.* **B 337** (1994) 358.

[cas98] C. Caso et al., The European Physical Journal **C3** (1998) 1 and *1999 off-year partial update for the 2000 edition* available on the PDG WWW pages (URL: `http://pdg.lbl.gov/`).

[chi94] R. Chipaux et al., *Study of neutron damage resistance of some scintillating crystals and associated photodetectors with the nuclear reactor ULYSSE*, Symposium "Scintillator and Phosphor Materials", Materials Research Society 1994 Spring Meeting, San-Francisco (1994).

[chi98] R. Chipaux, M. Géléoc, *Optical anisotropy effects in lead tungstate crystals*, CMS Note 1998/090, CERN, Geneva (1998).

[cms97] CMS EMC Group, *The EMC Project*, Technical Design Report, CERN/LHCC 97-33, CERN, Geneva (1997).

[col70] R.D.B. Collins, *An Introduction into Regge Theory and High Energy Physics*, Cambrige University Press, Cambrige (1977).

[dan96] A. Dannemann, *Untersuchungen zur Strahlenresistenz polymerer Materialien für den Einsatz in Experimenten der Hochenergiephysik*, DESY–F35D–96–06, Hamburg (1996).

[dav97] G. Davies et al., *Studies of the efficiency of scintillation light collection from $PbWO_4$ crystals*, CMS internal Note 1997/027 (1997).

[der91] M. Derrick et al., *Nucl. Instr. and Meth.* **A 309** (1991) 77.

[der93] ZEUS Collaboration, M. Derrick et al., *Phys. Lett.* **B 316** (1993) 412.

[dre64] S.D. Drell and J.D. Walecka, *Amn. Phys. (N.Y.)* **28** (1964) 18.

[don92] A. Donnachie and P.V. Landshoff, *Phys. Lett.* **B 296** (1992) 227.

[dup99] E.I. du Pont de Nemours and Company, USA.

[fey69] R.P. Feynman, *Phys. Rev. Lett.* **23** (1969) 1415.

[fos93] B. Foster et al., *Nucl. Instr. and Meth.* **A 338** (1993) 254.

[fri98] U. Fricke, Deutsches Elektronen–Synchroton DESY, Private Communication.

[fri99] U. Fricke, *Precision Measurement of the Proton Structure Function F_2 at Low Q^2 and Very Low x at HERA*, DESY-THESIS-1999-043, Hamburg (1999).

[gae89] K.J.F. Gaemers, M. Van Der Horst, *Nucl. Phys.* **B 316** (1989) 269; M. Van Der Horst, *Nucl. Phys.* **B 347** (1990) 149.

[gat98] L. Gatignon, CERN, Private Communication.

[gat99] L. Gatignon, *The West Experimental Area at the CERN SPS*, CERN SL–99–013 EA (1999).

[gau97] F. Gautheron and A. Givernaud, *About the electromagnetic shower lateral profile in the lead tungstate*, CMS Note 1997/037, CERN, Geneva (1997).

[gel62] M. Gell–Mann, *Phys. Rev.* **125** (1962) 1067.

[gel64a] M. Gell–Mann, *Phys. Lett.* **8** (1964) 214.

[gel64b] M. Gell–Mann and Y. Ne'eman, *The Eightfold Way*, W.A. Benjamin Inc., New York (1964)

[gen96] N. Gendner, *Messungen an strahlengeschädigten Bleiglasfasern und Konstruktion eines Online-Dosimeters auf Basis dieser Fasern für die Verwendung im ZEUS-Detektor*, Diploma Thesis, Hamburg (1996).

[gen98a] N. Gendner, U. Holm, A. Meyer–Larsen, M. Moritz, S. Thies, K.F. Johnson, *A PWO Beampipe Calorimeter for ZEUS at HERA*, Proc. Int. Workshop on Tungstate Crystals, Roma (1998), ed. S. Baccaro et al., Univ. La Sapienza, Roma (1999) 307.

[gen98b] N. Gendner, U. Holm, A. Meyer–Larsen, M. Moritz, S. Thies, K.F. Johnson, *A $PbWO_4$ Beampipe Calorimeter for ZEUS (I)*, ZEUS Note 98–072 (1998).

[gen99] N. Gendner, U. Holm, K.F. Johnson, A. Meyer–Larsen, S. Thies, *A PWO Crystal Calorimeter for High Energy Physics*, Proc. Vth Int. Conf. on Inorganic Scintillators and their Applications, Moscow (1999).

[gen00] N. Gendner, *The Fiber Online Dosimeter FRODO*, University of Hamburg, Hamburg (2000).

[gil72] F.J. Gilman, *Phys. Rev.* **129** (1968) 1365.

[goe98] F. Goebel, Deutsches Elektronen–Synchroton DESY, Private Communication.

[gru93] C. Grupen, *Teilchendetektoren*, BI–Wissenschaftsverlag, Mannheim, Leipzig, Wien, Zürich (1993).

[hai99] D. Haidt, *Log–Log behaviour of F_2 at low x in the Q^2 range from 0.1 to 35 GeV^2*, Proceedings of the DIS99 Workshop (1999).

[hal84] F. Halzen and A.D. Martin, *Quarks and Leptons*, John Wiley Sons Inc., New York (1984).

[ham94] Hamamatsu, *Technical Information*, Tokyo, Japan (1994).

[han63] L.N. Hand, *Phys. Lett.* **B 129** (1963) 1834.

[hen99] A.P. Henkel, U. Holm, N. Gendner, R.P. Feller, A. Meyer–Larsen, *A PC Based Readout System for Fast CAMAC Electronics*, ZEUS Note 99–069, DESY, Hamburg (1999).

[her93] HERMES collaboration, *Technical Design Report*, DESY (1993).

[her95] HERA–B collaboration, *Technical Design Report*, DESY–PRC 95/01 (1995).

[hof53] R. Hofstadter et al., *Phys. Rev.* **91** (1953) 422.

[hof55] R. Hofstadter and R.W. McAllister, *Phys. Rev.* **98** (1955) 217.

[hof57] R. Hofstadter, *Ann. Rev. Nucl. Part. Sci.* **7** (1957) 458.

[hol99] U. Holm, N. Gendner, A. Meyer–Larsen, S. Thies, K.F. Johnson, *A Small Compact Electromagnetic Lead Tungstate Calorimeter*, Proc. VIIIth Int. Conf. on Calorimetry in High Energy Physics, Lisbon/Portugal (1999).

[hub81] J. H. Hubbell: *Photon Mass Attenuation and Energy–absorption Coefficients from 1 keV to 20 MeV*, in: Int. J. Appl. Radiat. Isot. Vol. 33, pp. 1269 to 1290 (1982).

[inu99] M. Inuzuka: *Measurement of the Diffractive Cross Section in Low Q^2 ep scattering at HERA*, Ph.D. thesis, Univ. of Tokyo (1999).

[jac79] F. Jacquet and A. Blondel, in: Proceedings of the Study of an *ep* Facility for Europe, ed. U. Amaldi, DESY Report 79/48, Hamburg (1979) 391.

[jac82] J.D. Jackson, *Klassische Elektrodynamik*, de Gruyter (1982).

[joh97] K.F. Johnson, N. Gendner, U. Holm, A. Meyer–Larsen, *The ZEUS Crystal Beampipe Calorimeter*, INFN Eloisatron Project, 36^{th} Workshop: New Detectors, Erice (1997), World Scientific (1999) 407–415.

[kam83] T. Kamon et al., *Nucl. Instr. and Meth.* **213** (1983) 261.

[kob97] M. Kobayashi et al., *Improvement in Transmission and Decay Time of $PbWO_4$ Scintillating Crystals by La–doping*, KEK Preprint 96–183 (1997).

[kor96] M.V. Korzhik et al., *Phys. Stat. Sol. (a)* **154** (1996) 779.

[kur99] Kuraray Co., LTD, Tokyo.

[lec94] P. Lecoq et al., *Lead Tungstate ($PbWO_4$) Scintillators for LHC EM-Calorimetry*, CERN–PPE/94-225, CERN, Geneva (1994).

[lec95] LeCroy, *Model 2249A 12–Channel ADC Operator's Manual* (1995).

[lec96] P. Lecoq, *Development of lead tungstate crystals for high performance calorimetry*, in: Proceedings of the Sixth International Conference on Calorimetry in High Energy Physics, Frascati, Italy (1996).

[lec97] P. Lecomte, *Radiation Hardness of doped and undoped Lead Tungstate Crystals produced in China for the CMS Collaboration*, Proceedings of the Seventh International Conference on Calorimetry in High Energy Physics, Tucson (1997).

[leg99] LEGO Deutschland GmbH, Munich.

[loe94] M. Löwe, *The Hard– and Software of the Beampipe Calorimeter*, ZEUS Note 94–32 (1994).

[loh96] E. Lohrmann et al., *The ZEUS Beam Pipe 1995/1996*, ZEUS Note 96–089 (1996).

[lon75] E. Longo and I. Sestili, *Nucl. Instrum. Methods* **128** (1975) 283.

[loo75] W. van Loo, *Phys. Stat. Sol. (a)* **27** (1975) 565; W. van Loo, *Phys. Stat. Sol. (a)* **28** (1975) 227.

[lum98] S. Baccaro et al., *Activity of LUMEN (1996-97): understanding of $PbWO_4$ scintillator characteristics and their optimisation*, CMS Note 1998/067, CERN, Geneva (1998).

[mey95] A. Meyer–Larsen, *Bedienungsanleitung W.L.S. Command Interpreter*, University of Hamburg, Hamburg (1995).

[mey99] A. Meyer–Larsen, *Konstruktion, Aufbau und Kalibration eines strahlrohrnahen Bleiwolframatkalorimeters zur Verwendung im ZEUS–Experiment*, DESY-THESIS-1999-035, Hamburg (1999).

[mnc98] V. Monaco, *Measurement of the proton structure function F_2 at low Q^2 and low x with the Beam Pipe Tracker and the Beam Pipe Calorimeter of ZEUS at HERA*, Ph.D. thesis, Univ. of Turin (1998).

[mon98] T. Monteiro, *Study of Exclusive Electroproduction of ρ^0 Mesons at Low Q^2 Using the ZEUS Beam Pipe Calorimeter at HERA*, DESY-THESIS-1998-027, Hamburg (1998).

[mor98] M. Moritz, *Voruntersuchungen zum Bau eines Kalorimeters aus Bleiwolframat-($PbWO_4$)-Kristallen*, Diploma Thesis, Hamburg (1998).

[nee61] Y. Ne'eman, *Nucl. Phys.* **26** (1961) 222.

[nel66] W.R. Nelson et al., *Phys. Rev.* **149** (1966) 201.

[nik95] M. Nikl et al., *Slow Components in the Photoluminescense and Scintillation Decays of $PbWO_4$ single Crystals*, CMS TN/95-187, CERN, Geneva (1995).

[nik96] M. Nikl et al., *Phys. Stat. Sol. (b)* **196**, K7 (1996).

[pio93] K. Piotrzkowski, DESY F35D–93–06 (1993).

[pla94] Metallwerk Plansee GmbH, *Technical Information*, Lechbruck, Austria (1994).

[reg59] T. Regge, *Nuovo Cimento* **14** (1959) 951.

[ros50] M.N. Rosenbluth, *Phys. Rev.* **79** (1950) 615.

[ros52] B. Rossi, *High Energy Particles*, Prentice–Hall, Inc., Englewood Cliffs, NJ (1952).

[rut11] E. Rutherford, *Phil. Mag.* 211 (1911) 669.

[rus97] R.W. Rusack, *The CMS Lead Tungstate Electromagnetic Calorimeter*, Proceedings of the Seventh International Conference on Calorimetry in High Energy Physics, Tucson (1997).

[sak60] J.J. Sakurai, *Ann. Phys.* **11** (1960) 1.

[sak72] J.J. Sakurai and D. Schildknecht, *Phys. Lett.* **B 40** (1972) 121.

[sch94] S. Schacht, *Bedienungsanleitung zum Programm "beckman" zur Steuerung des Beckman–Spektrometers*, University of Hamburg, Hamburg (1994).

[sch97] D. Schildknecht and H. Spiesberger, *BI–TP 97/25* (1997).

[sur98] B. Surrow, *Measurement of the Proton Structure Function F_2 at Low Q^2 and Very Low x with the ZEUS Beam Pipe Calorimeter at HERA*, DESY-THESIS-1998-004, Hamburg (1998).

[thi99] S. Thies, *Untersuchungen an Komponenten eines kompakten elektromagnetischen Kalorimeters aus $PbWO_4$-Kristallen*, Diploma Thesis, Hamburg (1999).

[wol97] S. Wölfle, *Program for the calculation of the energy deposit of muons in matter*, Universität Freiburg i.Br., Germany (1997).

[wol98] S. Wölfle, Universität Freiburg i.Br., Private Communication.

[wu84] S.L. Wu, *Phys. Rep.* **107** (1984) 1.

[zeu93] ZEUS Collaboration, *The ZEUS Detector*, Status Report, ed. U. Holm, DESY, Hamburg (1993).

[zeu97] ZEUS Collaboration, J. Breitweg et al., *Phys. Lett.* **B 407** (1997) 432..

[zhu96] R.Y. Zhu et al., *A study on the properties of lead tungstate crystals*, Nucl. Instr. and Meth. **A 376** (1996) 319-334.

[zhu98] R.Y. Zhu, *Radiation Damage in scintillating Crystals*, Nucl. Instr. and Meth. **A 413** (1998) 297-311.

[zwe64] G. Zweig, *CERN–8192/TH401* (1964); G. Zweig, *CERN–8419/TH402* (1964).

Acknowledgements

A physicist's work, from my experience, is (and has to be) mostly teamwork. During my work at the Hamburg I group of the Hamburg University and within the ZEUS collaboration, I got into touch with many people who strongly supported me and contributed to the completion of this thesis.

First I want to thank Prof. Dr. Klaus Wick and Dr. Uwe Holm for the opportunity to work on the Crystal BPC. Many discussions and suggestions supported my work in a very fruitful way.

I would like to thank the ZEUS BPC group, especially Prof. Dr. Robert Klanner, for many useful discussions and support. Special thanks to Ulli Fricke for his help in many, many things and his believe in the Crystal BPC.

Many thanks to the Crystal BPC group, which consisted of Dr. Uwe Holm, Dr. Kurtis F. Johnson, Dr. Armin Meyer–Larsen, Matthias Moritz, and Stefan Thies. They were the main "team" mentioned above.

I also want to thank the other members of the Hamburg I group, as there are Bernd Bodmann, Dr. Ilja Bohnet, Dr. Wolfgang Busjan, Dr. Andreas Dannemann, Sadegh Faghihi, Rainer Peter Feller, André Henkel, Dr. Dieter Horstmann, Sönke Jacobs, Dietmar Kummerow, Martin Kunz, Andreas Kunze, Ralf Ladwig, Nicolas Latuske, Ernst Möller, Thomas Neumann, Marian Nowoczyn, Heinz Prause, Dr. H. Salehi, Arzu Yildirim, and Thomas Zoufal. It was a pleasure to work with them in the very friendly and inspiring atmosphere within our working group.

I would also like to thank P. Lecoq for his help in purchasing the crystals and E. Auffray for her help in irradiating the crystals and measuring the crystals' light yields.

Special thanks to Maike Carstensen, Ulli Fricke, and Levent Demirörs for reading my thesis draft, M. von Hurter from Beiersdorf AG, Hamburg for the high dose irradiations, M. Kasemann and the ZEUS FPC group for borrowing us PMTs, H. Krause for providing us with a sample UV–LED, A. Maniatis for the construction of our PMT bases, B. Racky for the opportunity of irradiations at the DESY Cs–source, and K.-H. Sulanke for the construction of our LED–Driver.

And, of course, there are the staffs of the mechanical workshop and the electronics workshop, who always did their best in constructing the equipment which we needed for our measurements.

Finally, I would like to thank my family and friends for their encouragement and support and, of course, my girlfriend Ortrud, whose love, support, and loving criticism helped me a lot during the recent years and prevented me from getting lost in physics.

This work has been supported by the German Bundesminister für Bildung und Forschung (BMBF) under contract 057HH19P.